Assessment of mesoscale eddy parameterizations for coarse resolution ocean models

by

Mikhail A. Solovev

M.Sc. Moscow State University, Russia (1993)

Submitted in partial fulfillment of the
requirements for the degree of
Doctor of Philosophy
at the
MASSACHUSETTS INSTITUTE OF TECHNOLOGY
and the
WOODS HOLE OCEANOGRAPHIC INSTITUTION
September 1999

Signature of Author ....
Joint Program in Physical Oceanography
Massachusetts Institute of Technology
Woods Hole Oceanographic Institution
July 23, 1999

Certified by ....
Paola Malanotte-Rizzoli
Professor
Massachusetts Institute of Technology
Thesis Supervisor

Accepted by ....
W. Brechner Owens
Chairman, Joint Committee for Physical Oceanography
Massachusetts Institute of Technology
Woods Hole Oceanographic Institution

[redacted]

Assessment of mesoscale eddy parameterizations for coarse resolution ocean models

by

Mikhail A. Solovev

Submitted in partial fulfillment of the requirements for the degree of
Doctor of Philosophy at the Massachusetts Institute of Technology
and the Woods Hole Oceanographic Institution
July 23, 1999

Abstract

Climate simulation with numerical oceanic models requires a proper parameterization scheme in order to represent the effects of unresolved mesoscale eddies. Even though a number of schemes have been proposed and some have led to improvements in the simulation of the bulk climatological properties, the success of the parameterizations in representing the mesoscale eddies has not been investigated in detail. This thesis examines the role of eddies in a 105–years long basin scale eddy resolving simulation with the MIT General Circulation Model (GCM) forced by idealized wind stress and relaxation to prescribed meridional temperature; this thesis also evaluates the Fickian diffusive, the diabatic Green-Stone (GS) and the quasi–adiabatic Gent-McWilliams (GM) parameterizations in a diagnostic study and a series of coarse resolution experiments with the same model in the same configuration.

The mesoscale eddies in the reference experiment provide a significant contribution to the thermal balance in limited areas of the domain associated with the upper $1000M$ of the boundary regions. Specifically designed diagnostic tests of the schemes show that the horizontal and vertical components of the parameterized flux are not simultaneously downgradient to the eddy heat flux. The transfer vectors are more closely aligned with the isopycnal surfaces for deeper layers, thus demonstrating the adiabatic nature of the eddy heat flux for deeper layers. The magnitude of the coefficients is estimated to be consistent with traditionally used values. However, the transfer of heat associated with time–dependent motions is identified as a complicated process that cannot be fully explained with any of the local parameterization schemes considered.

The eddy parameterization schemes are implemented in the coarse resolution configuration with the same model. A series of experiments exploring the schemes' parameter space demonstrate that Fickian diffusion has the least skill in the climatological simulations because it overestimates the temperature of the deep ocean and underestimates the total heat transport. The GS and GM schemes perform better in the simulation of the bulk climatological properties of the reference solution, although the GM scheme in particular produces an ocean that is consistently colder than the reference state. Comparison of the eddy heat flux divergence with the parameterized divergences for typical parameter values demonstrates that the success of the schemes in the climatological simulation is not related to the representation of the eddy heat flux but to the representation of the overall internal mixing processes.

Thesis Supervisor: Paola Malanotte-Rizzoli
Title: Professor
Massachusetts Institute of Technology

Acknowledgements

First and foremost, my sincere gratitude goes to my advisor, Paola Rizzoli. I greatly appreciate her encouragement, trust and advice in every aspect surrounding my graduate study and the thesis research. I would like to acknowledge the help and support at each stage of the thesis project from the members of my Thesis Committee: Jochem Marotzke, Breck Owens, Mike Spall and Peter Stone. Thanks to Glenn Flierl, the Thesis Defense Chairman, for valuable suggestions about the thesis.

I am indebted to Chris Hill and Alistair Adcroft for their help in mastering the MIT General Circulation Model; all members of the support staff, especially Linda Meinke, for help with computer systems; Lisa McFarren for reading the final version of the thesis.

The financial support for this research was provided by ONR grant number N00014-98-1-0881, Alliance for Global Sustainability and American Automobile Manufactures Association.

Grateful thank you and dedications to my parents, Alexei and Galina, and to Kris, *lux mea mundi*; without these people I would not have been able to finish this work.

Contents

List of Figures

List of Tables

Chapter 1

Introduction

Our understanding of climate dynamics and the ability to make forecasts relies to some extent on the numerical models. Complex climate models include the comprehensive representation of physical processes that drive the coupled Atmosphere-Ocean system. Given that a wide range of temporal and spatial scales must be resolved in order to construct a reliable forecast, there are a number of conceptual and technical problems that need to be solved. Although computer technology during the last two decades has sustained an almost exponential growth in computer power and ability to handle large volumes of data, execution of a comprehensive three–dimensional climate model that spans all energetic scales is still not feasible now or in the near future. Thus, current models will have to take into account the important processes on the unresolved scales with the help of parameterization schemes.

One of the most important problems of oceanic modelling on the climatic time scales is poor representation of mesoscale eddies. A number of eddy parameterization schemes have been proposed to represent the transport properties of eddies in complex General Circulation Models (GCMs). Although important, the nature of the eddy momentum flux is not well understood and until recently has been explored only in simple models. The major focus of research in the development of the eddy parameterizations presently aims to represent the eddy flux of tracers, including the active tracers such as temperature and salinity.

The purpose of this thesis is to explore the proposed eddy heat flux parameterizations in a comprehensive project combining a reference eddy resolving numerical experiment in simplified geometry with a series of coarse resolution experiments using several popular parameterization schemes. The assessment of the schemes in diagnostic and climatological analyses will address the validity of the parameterization schemes and the potential implementational and conceptual problems in improving the representation of the mesoscale eddies in coarse resolution calculations.

1.1 Motivation

The ocean plays a double role in the climate system. First, it is a giant thermal reservoir with the total mass 270 times greater (*Gill, 1982* [24]) and with a heat capacity thousands of times larger than the whole atmosphere. The heat content of only $2.5M$ of water equals to that of a whole vertical column of air (*Gill, 1982* [24]). Second, it transports heat poleward in an amount equal for some latitudes to the atmospheric heat transport (Figure 1-1). Thus, all climatological simulations must reproduce these two major roles correctly.

Nevertheless, experiments with the climatological models tend to have serious problems simulating the oceanic component of the climate. The coupled simulation by *Manabe and Stouffer, 1988* [38] showed that this coupled model can not reproduce the current climate without some artificial flux adjustment. In addition, the majority of coarse resolution experiments in a realistic geometry tend to underestimate the northward heat flux by as much as 50%. What are the apparent problems with the oceanic component of these coupled climate models?

One of the potential candidates for this deficiency in the ocean component is the representation of the unresolved processes. Because of finite resources, numerical simulations with a horizontal grid sufficiently small enough to resolve the most energetic component of the oceanic circulation (Figure 1-2) can not be integrated over the required time to

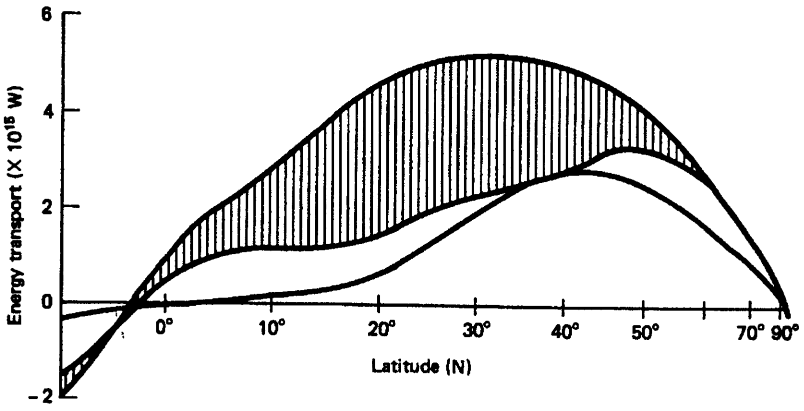

Figure 1-1: The northward transport of energy, $[10^{15}W]$ as a function of latitude. The white area is the part transported by the atmosphere and the shaded area the part transported by the ocean. The lower curve denotes the part of the atmospheric transport due to transient eddies. Adopted from *VonderHaar and Oort, 1973* [59].

achieve an equilibrium state for the density field. Thus, the mesoscale eddies need to be represented in terms of large–scale quantities. While it is a well–established fact that transports due to transient eddies provide a significant direct contribution to the heat transport by the atmosphere (Figure 1-1, the lower curve), it is still unknown what is the role of eddies in the heat transport by the ocean.

Oceanic mesoscale eddies can either transport heat directly by advecting water in the meridional direction where they exchange heat with the atmosphere, or indirectly by modifying the large–scale density distribution and, respectively, the heat transport. *Cox, 1985* [13] and *Böning and Budich, 1992* [4] identified in a series of basin scale experiments with varying horizontal resolution from 1° down to 1/6° that the explicitly resolved eddy field does not increase the total heat transport but rather modifies the transport by the mean circulation such that the sum of two is a constant. In a recent study by *Fanning and Weaver, 1997* [21], a similar experimental set–up performed for a much longer time and using lower order horizontal mixing, it was shown that by increasing the resolution and effectively permitting eddies in the model, the total heat transport is indeed increased

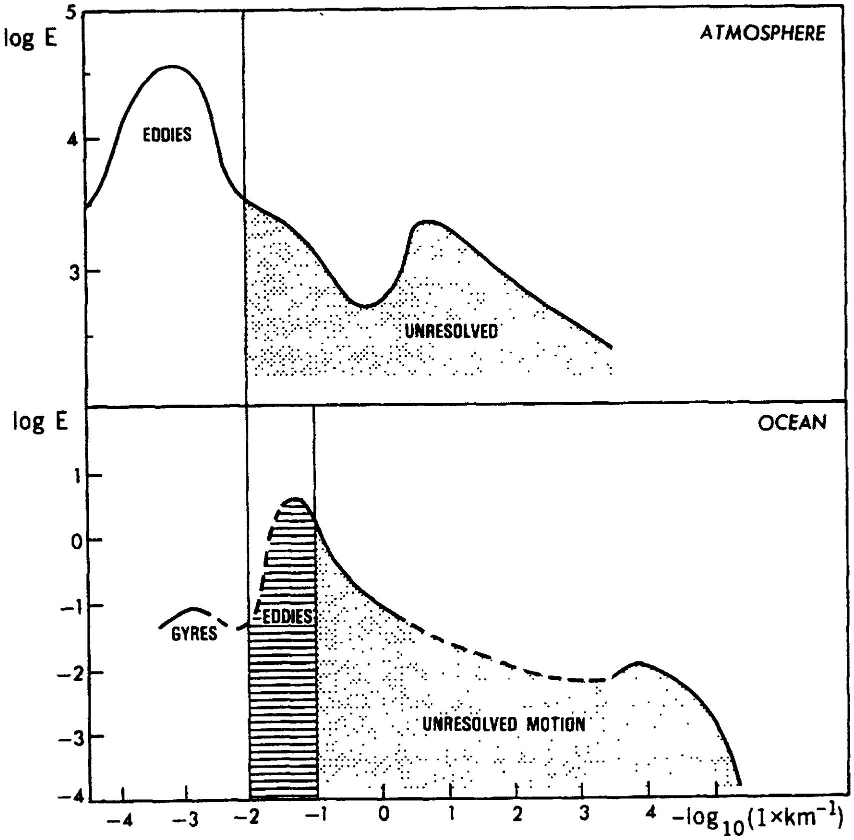

Figure 1-2: Kinetic energy spectrum, $[M^2 \cdot \mathrm{sec}^{-1}]$, as a function of horizontal wave number, $\left[{}^{cycles}/_{KM}\right]$, for the atmosphere and the oceans. Adopted from *Woods, 1985* [61].

by as much as 50%. This enhancement was observed when the horizontal resolution was increased from that typical for climate models 4° to 1/4°. In addition, they identified that the increase occurs because of the steady currents, thus demonstrating the importance of the fine resolution in representing the baroclinic gyre component of the total heat transport. The contradiction of these studies suggests that the understanding of the role of eddies in the establishment of climate state of the model is still an open question and requires a consistent representation in the coarse resolution models.

First, it is necessary to perform a climate simulation for millennia time scales as determined by the time scale of adjustment of the thermohaline circulation. Thus, it is only possible to carry out calculations with a horizontal resolution of a few degrees. The experiment requires a proper parameterization of the effects of time–dependent motions on the transport of properties. All of coarse resolution experiments carried out to date employ one of the proposed eddy heat flux parameterization schemes.

Traditionally, the transfer of heat by mesoscale eddies was assumed to occur in the opposite direction to the gradient of the time mean temperature distribution. The diffusive or the Fickian scheme, named after the nineteenth–century German physiologist, Adolf Fick, has been extensively used in ocean modelling (e.g., *Sarmiento and K. Bryan, 1982* [49], *F. Bryan, 1987* [7]). The scheme assumes that the mesoscale eddies act to decrease the local gradients of temperature.

The representation of eddy transport as the transfer of heat by eddies excited by baroclinic instability was proposed for the zonally averaged modelling of the atmospheric flows by *Green, 1970* [26] and *Stone, 1972* [55] and adopted for the potential vorticity flux by *Marshall, 1981* [41] in a study of a zonally averaged model of the Antarctic Circumpolar current. The schemes based on a similar concept had a considerable success in the atmospheric modelling (e.g., *Stone and Yao, 1990* [56]). So far, the scheme has not been implemented in a primitive equation oceanic GCM.

One of the recently proposed eddy heat flux parameterization schemes is based on a set of different assumptions. While the schemes mentioned earlier rely on the diabatic eddy transfer, the Gent–McWilliams scheme (*Gent and McWilliams, 1990* [23]) represents the eddy heat flux by a quasi–adiabatic process similar to Stokes drift. A non–divergent velocity is added to the time mean Eulerian flow forming a modified advective velocity. The scheme is based on the transformed Eulerian–mean equations originally formulated in atmospheric modelling (*Andrews and McIntyre, 1976* [1]; *Plumb and Mahlman, 1987* [45]). Following its implementation in the framework of a coarse resolution GCM (*Danabasoglu et al., 1994* [15]), the scheme is very popular today and is implemented in the majority of the primitive equation oceanic GCMs. The most attractive part of the scheme is its quasi–adiabatic nature, as the largest part of the ocean is essentially adiabatic and mixing occurs predominantly in the isopycnal direction.

While the more sophisticated schemes provide some improvements in the simulation of the climatological state of the ocean compared to a simple Fickian diffusion (*Danabasoglu et al., 1994* [15]; *Duffy et al., 1997* [17]; *England and Hirst, 1997* [20]), it has not been demonstrated that the improvements are indeed a result of better representation of the eddies. This important question is the major goal of this thesis project.

The published studies in the area of the assessment of the parameterization schemes can be divided into three major groups. The first group evaluates the schemes in process models. The physical mechanism underlying the parameterization is being reproduced in some framework as the conceptual modelling. The second type of experiments deals with eddy resolving simulations that allow the direct evaluation of necessary fluxes and components of the scheme, thus providing the most consistent evaluation. The third group contains a variety of coarse resolution experiments that can only identify some improvements in the representation of bulk climatological properties. By design, the coarse resolution experiments do not contain explicit information about eddies.

When evaluating a scheme in the framework of a process model, the experimental set–up is the closest reproduction of the physical model originally used for the scheme's development. Therefore, the majority of studies (*Marshall, 1981* [41]; *Lee et al., 1997* [35]; *Visbeck et al., 1997* [58]; *Killworth, 1998* [33]; *Gille and Davis, 1999* [25]; *Treguier, 1999* [57]) consider either zonally averaged or channel model configurations. By construction, this set–up is the oceanic analog of the atmospheric models; thus, the relative success of the schemes in the atmospheric modelling is usually repeated here. These studies investigate use of the parameterization schemes in the ocean regions where indeed the flow can be approximated by a periodic channel model, such as the Antarctic Circumpolar current. On the other hand the conclusions of these studies may not be valid in the areas where the flow is intrinsically three–dimensional, such as western boundary currents and gyre circulations.

The only experimental set–up that allows the direct evaluation of the eddy heat flux properties is the framework of eddy resolving calculations with a GCM. Only in these experiments a realistic eddy representation can be obtained with the minimum of simplifications and the eddy heat flux can be evaluated directly from the simulated data. In addition, all of the details of the parameterization schemes can also be evaluated from the numerical data. Unfortunately, because of the computational difficulties, there is a limited number of such large–scale calculations performed so far. Among the most widely analyzed are the idealized simulation of the North Atlantic (*Cox, 1985* [13]; *Böning and Budich, 1992* [4]); an eddy resolving model simulation of the southern ocean (*FRAM Group, 1991* [22]); a realistic simulation of the North Atlantic ocean by the *Community Modelling Effort (*CME*)* group, *1992-1996* ([5], [6]); and a Global Eddy Resolving model simulation (*Semtner and Chervin, 1992* [51]). The primary goals of the experiments were the reproduction of the observed features of the ocean general circulation and the most basic eddy activity. The evaluation of the eddy parameterization schemes was not explored. In addition, the length of the experiments was too short, measured in few years (e.g., the individual runs in CME experiments were about 5 years long); thus, the resulting eddy statistics were potentially not stable. Moreover, some of the information required for the evaluation of the eddy parameterization schemes were not collected; for example, in some of the CME experiments the required flux of salinity was not accumulated, so the buoyancy flux was estimated on the basis of the T–S relation. The only study published to date that has attempted to infer the quality of eddy parameterizations from a large–scale eddy resolving simulation is by *Rix and Willibrand, 1996* [47] in which the mixing coefficient corresponding to the Gent–McWilliams scheme is identified of $10^3\,[M^2 \cdot \mathrm{sec}^{-1}]$. However, they did not succeed in describing the spatial patterns of the mixing nor did they assess the quality of the scheme that was due to the insufficient length of the integration.

The coarse resolution experiments simulating aspects of ocean climate are less computationally intensive. Thus, there is a large body of research addressing the climatological properties of these solutions: total heat transport, strength and structure of the overturning cell, water mass properties (e.g. *Sarmiento and Bryan, 1982* [50]; *F. Bryan, 1987* [7]; *Danabasoglu et al., 1994* [15]; *England, 1995* [19]; *Robitaille and Weaver, 1995* [48]; *Duffy et al., 1997* [17]). All of these experiments use one of the proposed parameterization schemes so they can only evaluate how well the bulk climatological properties are being reproduced compared with observations (*Levitus, 1982* [36] and *1994* [37]). These experiments can not compare the implied divergence of the parameterized flux with the observations, as the Levitus climatology does not provide observations suitable to evaluate the eddy heat flux and its divergence.

1.2 Outline of the Thesis

The thesis examines the proposed eddy heat flux parameterization schemes in a comprehensive numerical experiment. The study includes two major parts. The first part addresses the eddy resolving simulation providing necessary numerical data for the estimation of the local properties of the parameterizations. The second part of the project deals with the implementation of the schemes in the coarse resolution experiments and the assessment of their skills. All of the simulations are performed with the same numerical model in the same experimental set–up, thus providing a consistent framework for the analysis. Chapters 2, 3, 4 and 5 consider the eddy resolving simulation and present a diagnostic evaluation of the eddy heat flux parameterization schemes. Chapter 6 addresses the assessment of the schemes in the coarse resolution experiments.

The reference eddy resolving experiment is described in Chapter 2. A necessary description of the MIT GCM is presented at the beginning of the chapter followed by a detailed description of the fine resolution experiment. The major criteria for a successful eddy resolving simulation are stated in the following section. The chapter presents a detailed description of the model's forcing, internal and external parameters. The model is initialized with a climatology obtained with a coarse resolution experiment for typical values of internal parameters. The evolution of the eddy resolving simulation is presented in the last section of the chapter by analyzing the time series of horizontal kinetic energy and average layers' temperature.

Chapter 3 presents the climatological analysis of the reference experiment by evaluating major climatological properties of the simulation. The purpose of the chapter is to demonstrate improvements in the simulated climatological state introduced by explicit representation of the mesoscale processes. The thermal structure of the solution, the total heat transport and the main meridional overturning cell are compared with some published studies and with two coarse resolution experiments. The improved climatology is a basis of the subsequent comparisons with the coarse resolution experiment using different eddy heat flux parameterization schemes.

The role of mesoscale eddies in the time–averaged thermal balance is evaluated in Chapter 4. The analysis concentrates on a series of meridional cross–sections through the depth of the main thermocline by plotting various terms contributing to the thermal balance. It identifies the areas of the domain where eddies are important by estimating the eddy heat flux divergence and comparing its magnitude to the other terms of the equation. In the western mid–latitudinal area, where the eddy heat flux divergence is the largest, the diagnostic analysis of the eddy heat flux parameterizations is performed and presented in the following chapter.

The detailed properties of the Fickian, the Green–Stone and the Gent–McWilliams schemes are studied in Chapter 5. After the description of the isopycnal framework specifically designed for the diagnostic assessment of the schemes, the three considered parameterizations are analyzed. The diagnostic tests of the parameterization schemes are developed according to the physical mechanisms underlying each of them and evaluated in the following sections. For a typical values of the specific parameters the local divergence of the parameterized flux are computed and compared with the eddy heat flux divergence. The comparison allows evaluation of the schemes' skills in reproducing the geographical distribution of the eddy forcing in the thermal balance.

Chapter 6 evaluates the eddy parameterization schemes in a series of coarse resolution experiments. The simulations are designed in the same framework as the reference experiment. The Green–Stone parameterization scheme is implemented in the MIT GCM. The other two schemes are part of the model's code. First, the climatological analysis is performed for the experiments by testing the schemes' skills in reproducing the bulk climatological quantities of the reference simulation. Second, the implied divergence of parameterized flux is evaluated for the best performing experiments and then compared with the divergence of the eddy heat flux of the reference calculation averaged on the grid of the coarse resolution experiments. The analysis helps to answer the question of whether the improvements in the climatological simulations with some of the eddy heat flux parameterization schemes can be actually attributed to the correct representation of mesoscale eddies.

Chapter 2

Reference Numerical Experiment

This chapter presents the experimental set–up of the project. Due to the importance of the high–resolution numerical experiment, which I will call the "reference" experiment, I provide a comprehensive description. In the following sections I present the numerical model and all the successive steps required for the execution of the reference simulation.

2.1 Introduction

The research project is based upon two major parts: a reference fine resolution simulation and a number of coarse resolution experiments employing different eddy heat flux parameterization schemes. The reference fine resolution calculation is an eddy resolving simulation of a numerical model of a basin scale ocean forced by climatological fluxes. The calculation is carried out starting from a prescribed initial conditions and letting the model evolve until an energetic mesoscale eddy field is developed.

The problem in carrying out such an experiment lies in the length of computational time required for an eddy resolving ocean model to reach a fully equilibrated state. It is well known that the adjustment process of the deep ocean thermal state is controlled in most areas of the domain by advection. This process is very slow below the main thermocline, so it requires thousands of years to reach an overall statistical steady state.

Until that time the model deep circulation preserves the memory of the initial state. The situation is different for the upper ocean, where there is a shorter adjustment time due to faster advective time scale of O (10years) and the presence of faster propagating planetary and other waves. These two different adjustment time scales require a mechanism to accelerate the convergence of the integration.

There are two ways which can be used to accomplish this task. The first is the initialization of the model with a field that is close to the expected final steady state. The second is the distorted physics approach (*Bryan, 1984* [10]) in which two different time steps are used. The shorter one is for the dynamical variables, the longer for the thermodynamical variables. The method distorts the physics of the instantaneous state while converging, with some limitations, to the true final steady state.

The majority of ocean climate models use a combination of both methods. They are usually initialized with some a priori known climatology for the density field. Subsequently, the integration of the models employes small time step for the dynamic variables, of the order of an hour, and a much larger time step for the thermodynamical variables, of the order of a day. There are some further variations, such as an even larger time step for the deeper layers. Overall, this method works only if the final state of the model is truly steady, and is appropriate for coarse resolution simulations. It is not correct to employ this method for eddy resolving models due to the presence of mesoscale variability, in which a "truly" steady state $\left(\frac{\partial}{\partial t}(\cdots) = 0 \text{ for all variables}\right)$ does not exist.

The goal of the experiment is to simulate the mesoscale motions and how they influence the climatological state of the model ocean; thus, it is inappropriate to use the distorted physics approach. To accelerate the convergence to the statistical steady state I initialize the experiment with a carefully simulated climatology. In the following sections I present the detailed description of the initialization procedure.

The set of parameters and integration procedures define the solution of the numerical model. The steps in the process following the initialization are the spin–up and the actual solution of the model's equation, that I call the data period.

2.2 Numerical Model

The model used is the MIT General Circulation Model (MIT GCM). The complete description of this model can be found in *Marshall et. al* (1997a [43], 1997b [42]). In this section I present a short description of the model that is relevant to my experiment.

The MIT GCM solves Navier Stokes equations in a very general set–up. It can be used for simulations of three–dimensional turbulent flows in basins of varying sizes and shapes: from the symmetrical laboratory tank experiments to the global ocean with realistic profiles of coast line and bottom topography. The model differs from other GCMs mainly by the flexibility of its numerical algorithm, both in terms of formulation and the method of numerical solution. It is possible to use the model in the non–hydrostatic mode; therefore, it can simulate ocean convection and processes occurring in very fine scales such as three–dimensional flows in laboratory tanks. For the larger scale flows, it can be switched to the hydrostatic formulation, that significantly simplifies the calculations.

The original formulation of the model has been designed specifically for the calculations on the massive parallel computer Connection Machine (CM-5). The complexity of the parallel implementation of the numerical algorithm is offset by the significant improvement in the speed of execution (*Hill and Marshall, 1995* [29]). Unfortunately the CM-5 computer is no longer available. I performed the reference fine resolution experiment from February 1997 to March 1998, when there were still available computers.

The model is formulated in the finite volume discretization scheme using height as the vertical coordinate. Time–stepping is performed through the quasi-second-order Adams-Bashforth scheme. The model is prognostic in some variables and diagnostic in others.

The numerical algorithm of the model is expressed by the pressure method, where the dynamical equations are transformed into an elliptic equation for pressure, followed by the prognostic time–stepping for the horizontal components of velocity. The next step is the diagnostic calculation of the vertical component of velocity through the non–divergence of the velocity field. The last step is the prognostic calculation of temperature and salinity. All of the above calculations take into account the finite volume configuration of the grid and the requirements for time–stepping. For the compete formulation of the numerical algorithm see *Marshall et. al* (1997a [43], 1997b [42]).

2.2.1 Equations

The general form of the MIT GCM belongs to a class of primitive equation ocean models. It solves Navier-Stokes equations of motion

$$\begin{aligned} \frac{\partial \vec{v}_h}{\partial t} &= \vec{G}_{vh} - \nabla_h p, \\ \frac{\partial w}{\partial t} &= G_w - \frac{\partial p}{\partial z}, \end{aligned} \tag{2.1}$$

continuity

$$\nabla \cdot \vec{v} = 0, \tag{2.2}$$

heat

$$\frac{\partial T}{\partial t} = G_T, \tag{2.3}$$

salt

$$\frac{\partial S}{\partial t} = G_S, \tag{2.4}$$

talking into account the equation of state

$$\rho = \rho\left(T, S, p\right), \tag{2.5}$$

where $\vec{v} = (\vec{v}_h, w)$ is the three–dimensional velocity, subscript h means horizontal components, p is pressure, as the deviation from that of a resting stratified ocean, and

$\vec{G}_v = (G_u, G_v, G_w)$ represents the forcing terms for the dynamical variables, G_T and G_S are the forcing of the temperature and salt equations. The forcing include both the internal dynamical and thermodynamical mechanisms (inertial, Coriolis, metric, gravitational, dissipation) and external forcing due to the interaction with the surrounding environment, such as the atmosphere.

In the reference experiment, the equations (2.1) - (2.5) are simplified according to the following assumptions:

- Salinity is fixed at $S_0 = 35^0/_{00}$; thus, $G_S = 0$,
- The equation of state is linear $\rho = \rho_0 \cdot (1 - \alpha T + \beta S_0)$, where α is the thermal expansion coefficient, β is the coefficient of saline contraction,
- The hydrostatic approximation is used.

The resulting system of equation in the spherical planetary coordinate system (λ, ϕ, r) has the following form

$$\begin{aligned}
\frac{\partial u}{\partial t} &= -\frac{1}{a\cos\phi}\frac{\partial p}{\partial \lambda} - \vec{v}\cdot\nabla u + \frac{uv\tan\phi}{a} + 2\Omega v\sin\phi + F_u, && (2.6a)\\
\frac{\partial v}{\partial t} &= -\frac{1}{a}\frac{\partial p}{\partial \phi} - \vec{v}\cdot\nabla v - \frac{u^2\tan\phi}{a} - 2\Omega u\sin\phi + F_v && (2.6b)\\
0 &= -g\frac{\delta p}{\rho_0} - \frac{\partial p}{\partial r}, && (2.6c)\\
\nabla\cdot\vec{v} &= 0, && (2.6d)\\
\frac{\partial T}{\partial t} &= -\nabla\cdot(\vec{v}T) + F_T, && (2.6e)\\
\frac{\partial S}{\partial t} &= 0, && (2.6f)
\end{aligned}$$

where $p = \frac{\delta p}{\rho_0}$ is the perturbation pressure, i.e. the ratio of the deviation of pressure from the resting hydrostatically balanced ocean to the reference density; a is the radius of the Earth.

2.2.2 Boundary Conditions

The set of boundary conditions for the large–scale ocean simulation is the following:

- No flow is allowed through the boundaries, $\vec{v} \cdot \vec{n} = 0$, where $\vec{n}$ is the normal vector to the boundary,
- The surface of the ocean is a rigid lid; thus, all fast surface gravity waves are filtered out, $w|_{z=0} = 0$,
- The tangental velocity component is zero, or no–slip boundary conditions are used at side walls, $\vec{v}|_{\tau} = 0$,
- A constant drag is used at the bottom, $\frac{\partial u}{\partial t}\big|_{z=H} \sim \lambda_B \, u|_{z=H}$,
- No diffusive flux of heat and salt are allowed normal to the solid boundaries, $K_n \frac{\partial}{\partial n} (T, S) = 0$,
- The wind stress at the surface is constant in time, $K_{Vw} \frac{\partial}{\partial z} (u, v)\big|_{z=0} = \frac{1}{\rho_0} \left(\tau^{\lambda}, \tau^{\phi}\right)\Big|_{z=0}$,
- The heat flux at the surface is set by the relaxation towards an apparent atmospheric temperature profile,
- No fresh water flux is allowed through the surface, $K_{Sw} \frac{\partial}{\partial z} S\big|_{z=0} = 0$.

2.2.3 Domain of the Experiment

The spherical domain of the experiment extends for a few degrees north of the equator to the polar ocean. The longitudinal extent of the basin is 36°, which roughly corresponds to the width of the midlatitudinal part of the Atlantic ocean. The coast lines are straight, the assumptions simplifying the computations and formulation of the boundary conditions. The bottom of the model ocean is flat.

2.3 Specifications of the Numerical Experiment

The continuous Navier Stokes equations (2.1)-(2.5) describe the behavior of all hydrodynamical systems. The choice of parameters makes the experiment a unique one. I divide the total number of the required parameters into two sets. The first set contains the internal parameters such as diffusivity and viscosity coefficients. The second set contains external parameters, which are independent of the particular numerical representation such as the atmospheric forcings.

2.3.1 Internal Parameters

The main criteria for the choice of sub–grid mixing parameters is the necessity for the solution to support the process of baroclinic instability and the associated formation of mesoscale eddies. The forcing terms of (2.6) (F_u, F_v and F_T) depend on the internal parameters. The horizontal sub–grid mixing is chosen to be biharmonic. It allows the development of small–scale horizontal motions. The mechanical energy input to the model ocean is removed with the help of bottom drug, a linear function acting on the zonal component of velocity. In a series of preliminary experiments with the model testing the sensitivities to values of internal parameters it was identified that it is not necessary to add the bottom drag for the meridional component of velocity. The magnitude of the zonal bottom drag λ_B is a constant value everywhere in the domain. It represents the moderate roughness of the observed bottom topography. The form of the forcing terms depending on the internal parameters is the following

$$\begin{aligned}
F_u &= K_{Vw} u_{zz} - K_{Vbh} \Delta^2 u + \lambda_B \, u\big|_{z=H}, \\
F_v &= K_{Vw} v_{zz} - K_{Vbh} \Delta^2 v, \\
F_T &= K_{Tw} T_{zz} - K_{Tbh} \Delta^2 T + Q_T\big|_{z=0},
\end{aligned}$$

where K_{Vbh} - horizontal biharmonic viscosity, K_{Vw} - vertical Laplacian viscosity, K_{Tbh}

Coefficient	**Value [dimensions]**
K_{Vbh}	$2.5 \cdot 10^{11}$ $[M^4 \cdot \text{sec}^{-1}]$
K_{Vw}	10^{-3} $[M^2 \cdot \text{sec}^{-1}]$
K_{Tbh}	$2.5 \cdot 10^{11}$ $[M^4 \cdot \text{sec}^{-1}]$
K_{Tw}	$0.3 \cdot 10^{-4}$ $[M^2 \cdot \text{sec}^{-1}]$
λ_B	$1.2 \cdot 10^{-7}$ $[\text{sec}^{-1}]$
α	$2 \cdot 10^{-4}$ $[{}^\circ C^{\ -1}]$
β	$7.4 \cdot 10^{-4}$ $[{}^0/_{00}{}^{\ -1}]$

Table 2.1: Internal parameters of the reference experiment

- horizontal biharmonic diffusivity, K_{Tw} - vertical Laplacian diffusivity and $Q_T|_{z=0}$– external forcing for temperature in the form of relaxation to some prescribed temperature profile.

The simplest form of the equation of state used in the experiment is a linear function of temperature. Effects of changes in salinity are neglected by keeping it constant through the whole length of the integration, $S = 35^\circ/_{00}$. This value represents an average ocean salinity.

The values of the coefficients are given in Table 2.1.

2.3.2 External Parameters

The sources of energy for the model ocean are the wind stress acting at the surface, and thermal forcing, i.e. the relaxation to an apparent atmosphere for the upper layer. Both components of the forcing are constant in time and vary only meridionally. They represent an approximation to the climatological conditions in the northern hemisphere. The profiles of the forcing are similar to the functions that were widely used in coarse resolution climate simulations (*Bryan, 1987* [7], *Marotzke and Willebrand, 1991* [40]).

The model is forced through the direct interaction with atmosphere. It exchanges momentum through the action of wind on the surface. The density structure is modified by the heat flux at the surface.

The shape of the wind stress profile (Figure 2-1(a)) captures the major features of the observed zonally averaged wind stress. Its curl supports the formation of three major wind–driven gyres: the subtropical and subpolar circulations and a tropical gyre maintaining the horizontal circulation in the vicinity of the southernmost boundary. The profile is slightly non–symmetrical with respect to the mid–latitude line of the zero wind stress curl.

The thermal forcing acts on the surface of the ocean. The upper layer of the model ocean is in thermal equilibrium with an apparent atmospheric temperature (*Haney, 1971* [28]). The profile of the temperature (Figure 2-1(b)) is a simple sinusoidal function of latitude:

$$T_a = \frac{1}{2}\left(T_E + T_P\right) + \frac{1}{2}\left(T_E - T_P\right)\cos\left(\frac{18}{7}\phi\right),$$

where the equator temperature is $T_E = 27°C$ and the polar one is $T_P = 0°C$. The corresponding heat flux into the ocean is

$$F_H = \rho_0 C \frac{(T_a - T|_{z=0})}{\tau_D} \Delta h_1,$$

where C the specific heat of water, τ_D the relaxation constant and Δh_1 the upper layer thickness. The relaxation constant is chosen to be 30 days, equivalent for the upper layer of $50M$ to a heat flux of about $70\,[W \cdot M^{-2}]$ for $1°C$ difference between the upper layer of the model and the apparent atmospheric temperature. Although this value is about two times larger than the standard value estimated by Haney, it provides a reasonable diabatic forcing in the energetic parts of the basin. The expected equivalent surface heat flux is about $300[W \cdot M^{-2}]$ for the areas where the deviation of surface layer isotherms from the apparent atmospheric temperature the largest.

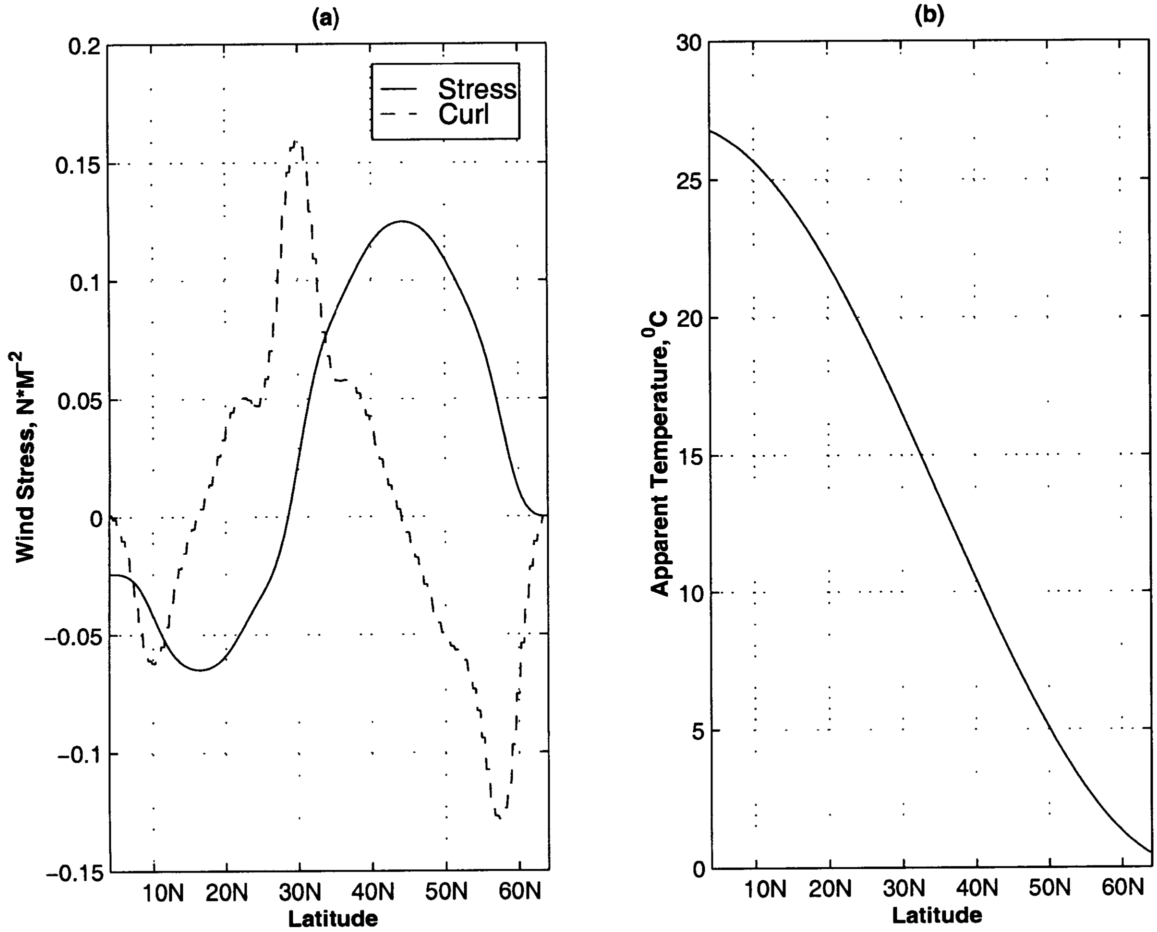

Figure 2-1: Forcing of the model as functions of latitude: (a) wind stress, $[N \cdot M^{-2}]$ and wind stress curl, $10^{-5}\,[N \cdot M^{-3}]$, (b) apparent atmospheric temperature, $[^{\circ}C]$.

2.3.3 Domain and Discretization

Horizontal Dimensions

The northern Atlantic ocean is mimicked by the idealized model configuration. In the northern Atlantic the ocean gains heat in the tropical and subtropical areas and loses heat in the Polar one. When it loses heat to the atmosphere in the northern areas vertical convection occurs and to maintain a stable state heat must be transported from the southern to the northern areas. The basin scale wind–driven circulation further modifies the transport. These processes represent a general oceanic contribution to the climate system and must be represented in the climate simulation.

The numerical domain must comprise all of the above areas in meridional direction. That is, it must span at least one hemisphere. In the zonal direction, the major features of the wind–driven general circulation are reproduced: quiescent interior of mid-latitude gyres, fast western boundary currents and tropical circulation. The breaking of the geostrophic balance right at the equator requires a very small time step to overcome numerical instabilities, thus making the whole simulation more computationally expensive. In order to keep the time step reasonably large it was decided to move the southern boundary to $4°N$. The northern boundary is located approximately at the area of the possible ice formation at $64°N$.

The selection of horizontal discretization is mainly due to two factors. The satisfactory simulation of eddies requires the horizontal resolution to be small compared to the radius of deformation since I expect that the mesoscale eddies are the result of baroclinic instability. The definition of the radius of deformation I use is connected with the local quasi–geostrophic approximation. The radius of deformation varies in magnitude with the location in the ocean. The reference value for the mid–latitude ocean is of the order of 50 kilometers. It is smaller in the northern parts and larger for the southern areas due to the increase in the stability of the vertical stratification for the lower latitudes and the decrease in the value of the Coriolis parameter. On the other hand, the smaller

Dimension	**Degrees**	**min, Km**	**max, Km**	**mean, Km**
L_x	$0°E - 36°E$	1763.5	3970.0	3156.7
L_y	$4°N - 64°N$	6648.4	6648.4	6648.4
Resolution				
Δ_x	0.2°	9.8	22.2	17.6
Δ_y	0.2°	22.4	22.4	22.4

Table 2.2: Horizontal dimensions of the domain and horizontal resolution

Layer	1	2	3	4	5	6	7	8	9	10	11	12	13	14	15
Thickness, M	50	75	100	125	150	200	250	300	400	450	450	500	500	500	500
Mid-depth, M	25	88	175	288	425	600	825	1100	1450	1880	2320	2780	3250	3750	4250

Table 2.3: Vertical discretization

the horizontal resolution the higher the requirements for the computer resources. For the most powerful computers available today, it is impossible to perform a climate simulation on basin scales with the resolution of the order of a fraction of the radius of deformation. Thus, I choose the horizontal resolution to be 0.2°. It is uniform in both meridional and zonal directions. This value is smaller than the radius of deformation in the most areas of the model domain, except some local marginally stable deep convective regions, and at the same time given the appropriate closure coefficients allows the simulation of the mesoscale motions.

The horizontal dimensions and resolution are given in the Table 2.2. The following notations are used in the table: L_x and L_y - West-East and South-North dimensions of the basin, Δ_x and Δ_y - the corresponding horizontal resolution.

Vertical Dimension

The vertical structure of the flow has a non–uniform distribution. The numerical algorithm allows one to choose vertical layers of varying thickness. The largest number of layers spans the upper part of the water column, in and above the main thermocline. The deep ocean is represented with a small number of thick layers. Table 2.3 shows the vertical discretization.

The size and discretization of the model ocean domain are comparable to those for the basin scale pioneering eddy resolving simulation by *Cox, 1985* [13] and the North Atlantic simulations by the "community modelling effort" (CME) of the World Ocean Circulation Experiment (WOCE) *Bryan and Holland, 1989* [8], *Böning and Budich, 1992* [4], *Böning et. al, 1995* [6], *1996* [3].

2.3.4 Initialization

The solution method of the numerical model is time–stepping from an initial state until the model reaches a statistical steady state. This final state is characterized by a balance between the input of energy and dissipation and the generation of eddies and their decay. Due to the non–linear nature of the dynamical equations, there is no guarantee in the uniqueness of the final state. Unfortunately, the modern computational resources do not allow to perform an ensemble of fine resolution experiments to explore the uniqueness of a final state. Thus, it is important to have some a priori knowledge about the nature of expected final state, so the initial state can be chosen in its vicinity and the solution converges within the limits of the projects resources. In realistic simulations the initial state is usually an observed climatology, compiled from oceanic observations. The most popular data set is the atlas by Levitus, see e.g. *Levitus, 1982* [36], [37].

The reference experiment is idealized, with straight coast line and flat bottom topography. There are two ways to carry out the initialization. One is the initialization with some transformed version of the Levitus climatology. The other is a preliminary simulation of an artificial climatology obtained by performing a coarse resolution simulation. In the latter case the parameters of climatological simulation can be chosen in such a way as to allow for a unique steady solution. The linear equation of state and constant salinity with the combination of large mixing coefficients guarantees the uniqueness of the climatological simulation (*Marotzke and Willebrand, 1991* [40]). The final state of the calculation is interpolated on the fine grid of the eddy resolving simulation.

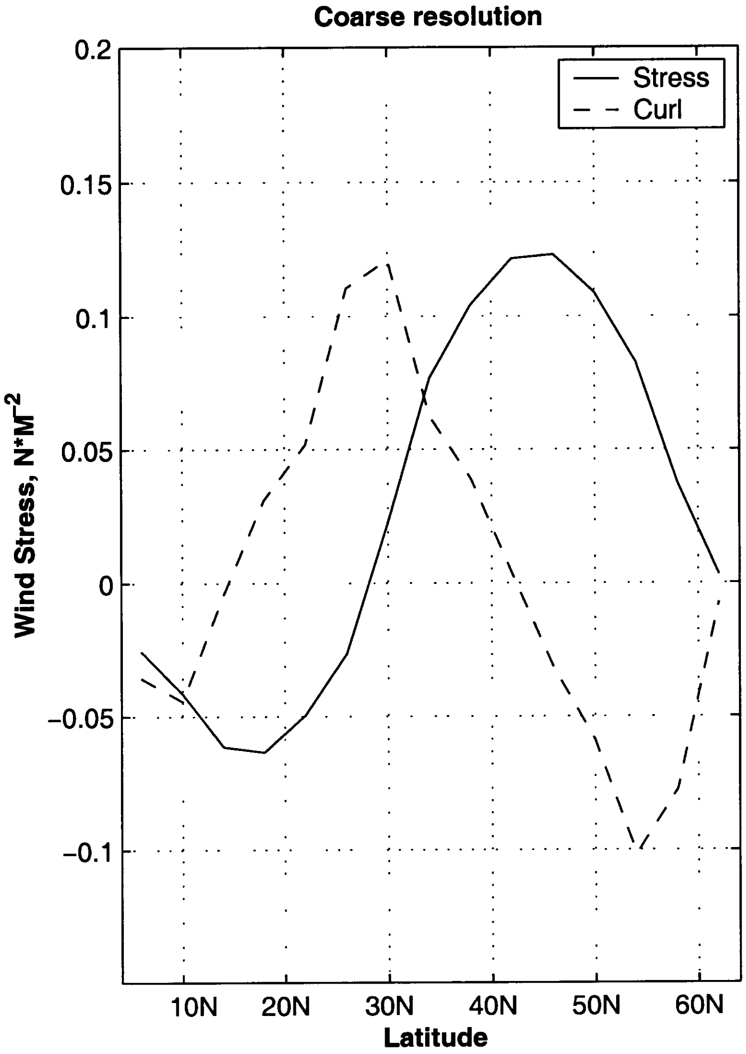

Figure 2-2: Wind stress, $[N \cdot M^{-2}]$, and wind stress curl, $10^{-5}\,[N \cdot M^{-3}]$, in the coarse resolution experiment simulating the initial conditions for the reference experiment.

This interpolated state is used as the initial condition for the reference run. By adopting this approach, I am not only accelerating the convergence, but also observing the modifications of the coarse climatological state due to the explicit resolution of mesoscale eddies.

Coarse Resolution Climatological Experiment

The coarse resolution climatological run with the MIT GCM simulates the larger scale features of the climatology. The horizontal resolution of the run is 4°, a standard value for coarse resolution climate simulations, while the number of vertical layers, 15, is the same as in the eddy resolving calculation. The forcing of the model (Figure 2-2) is the forcing of the eddy resolving reference experiment interpolated on the coarse grid ($4^\circ \times 4^\circ$) (Figure 2-1). Due to a larger horizontal grid in performing spatial derivatives of the wind stress profile, the magnitude of the wind stress curl is weaker in the coarse resolution simulations by about 30% at the maximum values observed around $30^\circ N$. The horizontal sub-grid scale mixing is parameterized in its simplest form as Laplacian viscosity and diffusivity with the conventional values of parameters. The vertical mixing and bottom drag are the same as in the eddy resolving experiment. The coarse resolution, the linear equation of state and the absence of fresh water influx assure the uniqueness and the steadiness of the final state. Thus, it is possible to apply the acceleration of convergence technique (*Bryan, 1984* [10]) to perform an integration of a few thousand years measured on a tracer time scale. The time step for temperature is 24 times larger that for the dynamical prognostic variables. Specific parameters of the idealized simulation are presented in Table 2.4. In the table $P_{u,v}$ and P_T are the dynamical and tracer total integration lengths, K_{Vh} - horizontal Laplacian viscosity, K_{Th} - horizontal Laplacian diffusivity, all other notations are the same as in Tables 2.1 and 2.2.

	Parameter	**Value[dimensions]**
Resolution	Δ_x	4°
	Δ_y	4°
Time step	$\tau_{u,v}$	1[hour]
	τ_T	24[hour]
Integration	$\mathrm{P}_{u,v}$	480[year]
	P_T	9600[year]
Mixing	K_{Vh}	$5 \cdot 10^5\,[M^2 \cdot \mathrm{sec}^{-1}]$
	K_{Vw}	$10^{-4}\,[M^2 \cdot \mathrm{sec}^{-1}]$
	K_{Th}	$10^3\,[M^2 \cdot \mathrm{sec}^{-1}]$
	K_{Tw}	$5 \cdot 10^{-5}\,[M^2 \cdot \mathrm{sec}^{-1}]$

Table 2.4: Specific parameters of the climatological coarse resolution experiment

Simulated Climatology

The final fields of u, v, w and T evaluated in the coarse resolution experiment are used as the initial state of the eddy resolving calculation. The experiment is similar to the other coarse resolution climate simulations cited above in an idealized geometry with steady forcing. I present a concise analysis of the climatological state and some diagnostics that are most relevant to climate analysis.

Thermal State Figure 2-3 presents the temperature distributions for three layers. The upper layer (Figure 2-3 (a)) is strongly forced by the apparent atmospheric temperature; thus, it reproduces the forcing almost exactly. The modifications occur in the dynamically active western boundary current area and in the southern part of the domain. The subsurface layer (Figure 2-3 (b)) shows a strong signature of the deepening thermocline in the subtropical gyre. The thermocline layer (Figure 2-3 (c)) shows the expected presence of closed contours of the isotherms in the sub–tropical gyre and deep convection in the northernmost part of the domain.

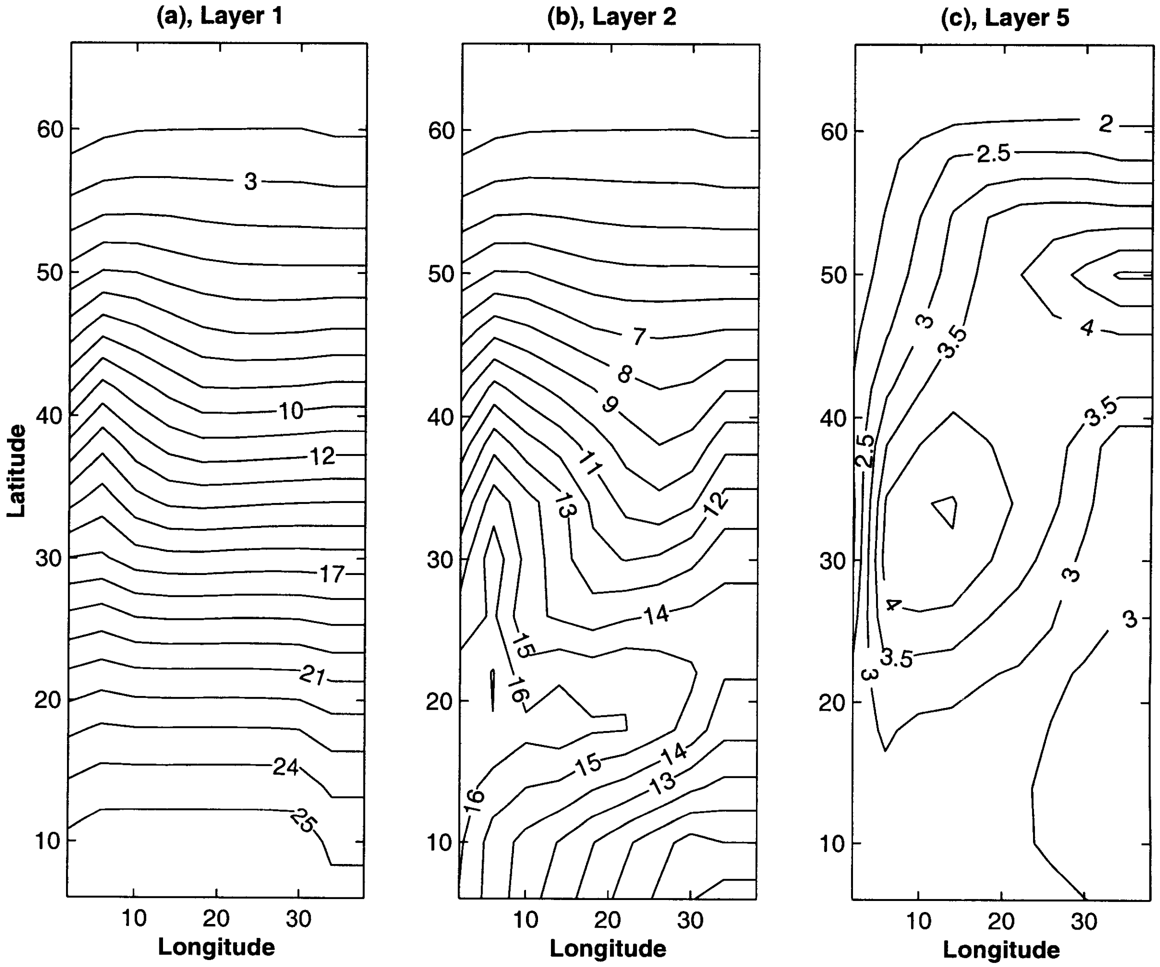

Figure 2-3: Temperature fields [°C] used in the initialization procedure: (a) upper surface layer, (b) second sub–surface layer, (c) 5^{th} thermocline layer.

Barotropic transport function One of the measures of the simulation's horizontal flow is the barotropic transport. I compute it according to:

$$\Psi_{bar}^{i,j} = -\sum_{j}^{Ny-j} \Delta_y \cdot \sum_{k=1}^{15} u^{i,j,k} \cdot \Delta_z^k,$$

where k indicates the k^{th} layer and Δ_z^k is the thickness of k^{th} layer. The value of the wind–driven barotropic transport in the coarse resolution experiment of $10Sv$ (Figure 2-4(a)) is weaker than the one estimated according to Sverdrup dynamics. In the assumption of a homogeneous model on the β plane driven by steady wind stress τ, the barotropic transport ψ_{bar} is

$$\psi_{bar} = \int_E^W \frac{\nabla \times \tau|_z}{\beta \rho_0} dx = \frac{\nabla \times \tau|_z \cdot L_x}{\beta \rho_0}.$$

For the model's values of $\nabla \times \tau|_z \approx 0.12 \cdot 10^{-6} [N \cdot M^{-3}]$ at $30°N$, $L_x = 36°$, $\beta = 2 \cdot 10^{-11} [M^{-1} \cdot \sec^{-1}]$ and $\rho_0 = 995 [kg \cdot M^{-3}]$, the Sverdrup transport ψ_{bar} is about $20Sv$. The baroclinic structure of the circulation and the thermohaline circulation can be accounted for the weaker transport. In addition, due to the numerical implementation of the no–slip boundary conditions in the model, the velocity is set to zero in the near boundary grid points. Thus, the effective width of the domain, where the wind stress forces the model, is smaller by two grid points (8°) than the geographic zonal bounds. The weakness of the wind–driven circulation is one of the features of numerical simulations with the uniform horizontal resolution of 3° to 4° for a limited domain in the East–West direction. Although a weaker wind–driven circulation affects the climatological state by underestimating the heat transport associated with intense western boundary currents (*Kamenkovich et al., 1999* [32]), it is not the scope of the present work to address the role of the horizontal resolution in the simulation of the wind–driven circulation. The wind stress (Figure 2-1(a)) forms three barotropic gyres with the boundaries between them corresponding to the zero wind stress curl lines.

Meridional overturning transport function. A very important diagnostic measure is the total meridional overturning transport function (Figure 2-4(b)), defined as

$$\Psi^{j,k}_{over} = \sum_{i}^{Nx-i} \Delta_x \cdot v^k \cdot \Delta_z^k.$$

The maximum transport is about 7 Sv and occurs near the northern boundary in the area of deep convection. About 2 Sv crosses the 30°N latitude at the thermocline depth. There are two wind–driven cells in the upper part of the domain.

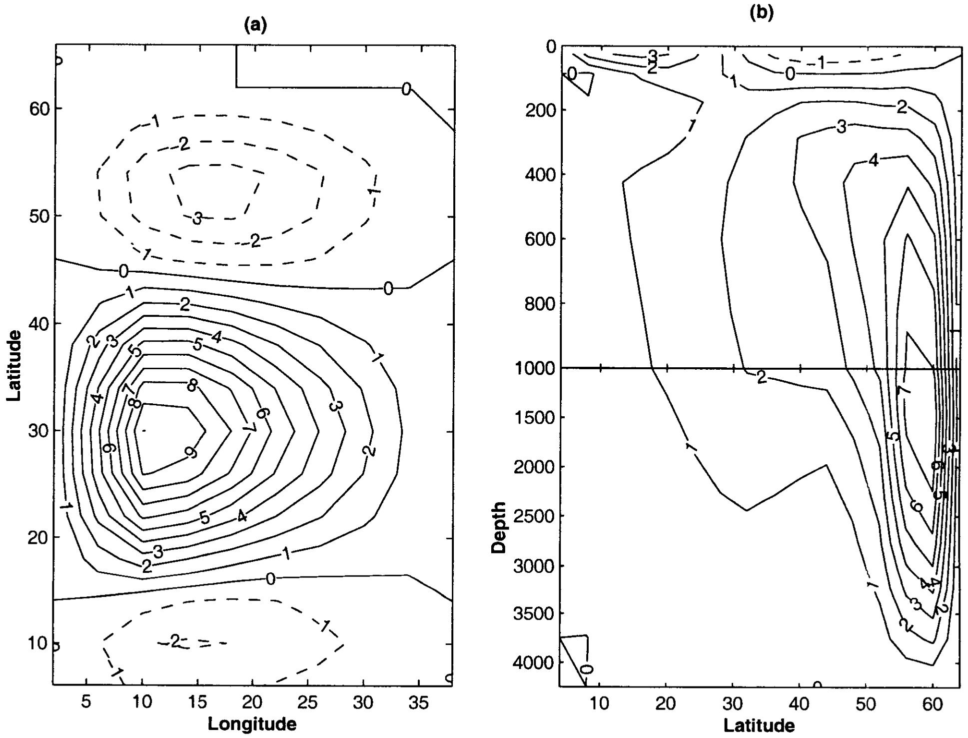

Figure 2-4: Flow diagnostics of the climatologycal simulation: (a) barotropic transport, Sv, (b) overturning transport, Sv.

Northward Integrated Heat Transport The simulated ocean transports heat from the warmer southern part to the colder northern (Figure 2-5). Due to some compromises taken in designing the experiment, mainly the limited zonal width of the basin and repositioning of the southern boundary to 4°N, the model ocean transports only $0.16PW$ of heat at the maximum. The location of the largest transport is in the Subtropical gyre around 20°N. This value is one order of magnitude smaller than the observations about the ocean transport of $1.2PW$ at 24°N (*Hall and Bryden, 1982* [27]).

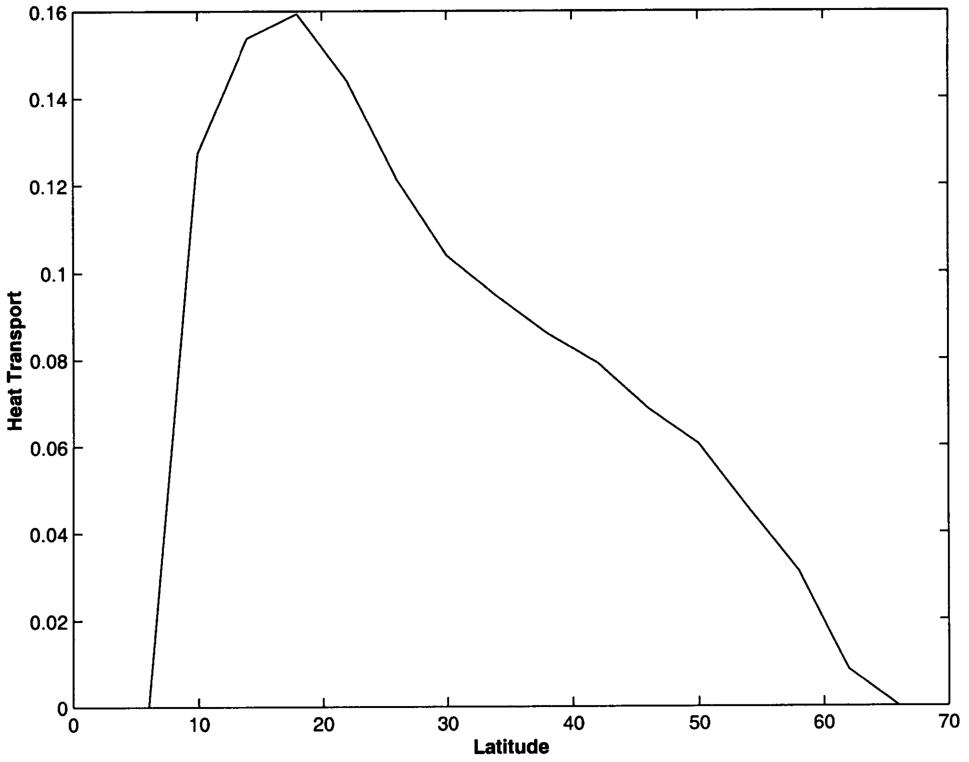

Figure 2-5: Northward integrated heat transport in the climatological simulation, $[PW]$.

2.4 Eddy Resolving Calculation

2.4.1 Initialization Period

The flow of the simulated climatology in the coarse resolution experiment is weak. The maximum values are about few centimeters per second for the upper ocean. The values are nearly two orders of magnitude smaller than expected values of $\backsim 1\,[M \cdot \mathrm{sec}^{-1}]$ in the fast western boundary currents and tropical return flows. The temperature field on the other side is expected to undergo only moderate modifications.

I use the following procedure to obtain an initial state consistent with the climatology. A relaxation term is added to the right hand side of the prognostic equations for the horizontal velocity components and temperature

$$\begin{aligned} \frac{\partial u}{\partial t} &= F_u - \lambda_c\,(u - u_c)\,, \\ \frac{\partial v}{\partial t} &= F_v - \lambda_c\,(v - v_c)\,, \\ \frac{\partial T}{\partial t} &= F_T - \lambda_c\,(T - T_c)\,, \end{aligned}$$

where F_u, F_v and F_T contain all terms from the right hand side of the corresponding equations in (2.6), $\lambda_c = \frac{1}{\tau_c}$ is a relaxation coefficient with $\tau_c = 1$ day. The strong nudging guarantees that after some period of time longer than τ_c, the fields u, v and T of the fine resolution calculation will be exactly equal to the climatology. The w field and all other fields adjust to local balances. The length of the initialization period is of 1.2 years. After this period the relaxation is turned off, and the model evolves only according to the dynamical equations (2.6).

2.4.2 Spin–up Period

During next 50 years of integration the model undergoes a complicated process of internal adjustment. The fine resolution allows the development of time–dependent motions on a scale of the radius of deformation. The flow adjusts relatively fast according to the geostrophic adjustment process. Then it advects the temperature, modifying the density structure and thus the flow itself through the same relation. In addition the mesoscale eddies transport heat locally and change the distribution of temperature. Again, the upper layer of the model is in direct contact with the atmospheric forcing. All these processes lead to a complex non–linear internal adjustment.

The time scale of the dynamical adjustment is of the order 10 years. This fact was shown by a number of eddy resolving calculations (*Holland and Rhines, 1980* [31], *Drijfhout, 1994* [16]). An integration of about 50 years is performed, after which the flow has no memory of the initial dynamical conditions and evolves only in response to much slower varying density field. This period is the so–called the spin–up period. After the completion of the spin–up, the actual fine resolution experiment is started.

The evolution of the spin–up is monitored using two diagnostic measures collected once every 14 days, dynamical adjustment by computing the total horizontal kinetic energy of the flow and the evolution of the density field through the changes in the average temperature of layers. The two weeks collection period provides a sufficient coverage on a hundred year time scale of the integration. The layer's horizontal kinetic energy measures the relation between input and output of mechanical energy to each particular layer. The average temperature of each layer gives an estimate of the time drift, that is the overall heating or cooling of each layer. Upon reaching a statistically steady state, both curves become flat on a time scale larger than the time scale of the mesoscale variability.

Figure 2-6 shows the plots of the diagnostic quantities as a function of time during the spin–up period. After a short nudging period (years 0-1.2 Figure 2-6(a)), the model quickly develops strong horizontal flows. At about year 10 all layers are in a statistical steady state as the kinetic energy for each layer fluctuates around some constant value. During years 10 to 50 the time–dependent motions become in balance with the thermal structure.

The evolution of the density structure occurs on a different time scale. After the 50 years of the spin–up period the averaged temperature of the layers is still in a transient state. There is an obvious presence of thermal drift for each depth. The moment to start collecting the data for the simulation is given by decrease in the drift, in particular for the lower thermocline depths (700M to 1000M), that is after 50 years. The drift is small and has a linear structure, that can be accounted for during the later stages of analysis.

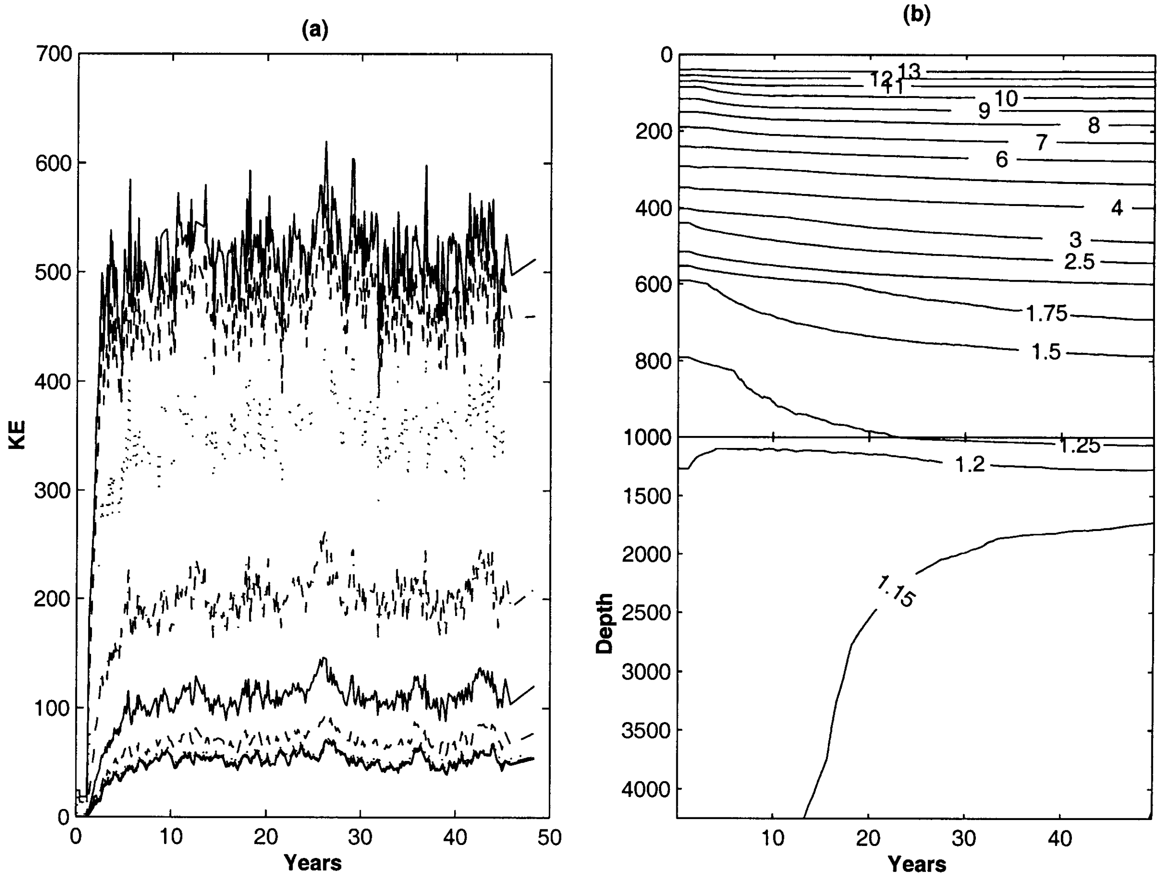

Figure 2-6: Spin–up stage of the eddy resolving simulation: (a) horizontal kinetic energy for each layer (upper layers at the top), (b) horizontally averaged temperature. Note: upper 1000M are stretched and varying contour intervals.

2.4.3 Data Period

The data is collected during the successive 55 years of integration after the 50 years of spin up period. The strategy for the data collection is a trade–off between accumulating the necessary data to evaluate eddy processes and the evolution in response to the slowly varying thermal fields and the limitations in the computer resources. The comprehensive analysis of the solution will be presented in the subsequent chapters.

Data Acquisition

Four major points must be taken into account for the data collection:

- Periodic and sufficiently frequent sampling of the flow evolution and associated density structure,
- Collection of climatological and time–dependent data necessary to diagnose eddy effects on the climate state of the model ocean,
- Fast frequency observations for the estimation of statistical properties of the climatological and time–dependent variables,
- Additional data for monitoring of particular processes related to the instantaneous and climatic states of the model, such as the zonally integrated northward heat flux.

The easiest and the most straightforward way of collecting the data would be a periodical collection of state variables with the subsequent off–line calculation of all diagnostic quantities. Unfortunately, it is technically impossible. Even saving only four necessary state variables: u, v, w and T every day for 50 years of integration, requires a solid storage exceeding $0.5\,TB$ $(1\,TB = 10^{15}B)$. It is impossible to store and subsequently analyze such an amount of data given the resources of the project. Thus, the data collection is restricted according to the four above requirements.

Monitoring The periodic monitoring of the solution is performed in the same manner as during the spin–up phase. Biweekly values of kinetic energy and layer averaged temperature are stored.

Climatological and Eddy Quantities The diagnostics of the climatological quantities, or first moments, are computed by accumulating state variables at each iteration. Division by the length of the period P at the end of the experiment provides the time mean quantities for each prognostic or diagnostic variable, e.g. for zonal component of velocity

$$\bar{u} = \frac{1}{P}\sum_{m=1}^{P} u_i.$$

At the same time I estimate the eddy diagnostics by measuring the temperature flux for each elementary volume, cross–correlation products of dynamical variables and the product of state variables with themselves. Consider the computation of the zonal component of eddy flux of temperature $\overline{u'T'}$. Given the definition of eddies as the deviation from the time mean properties, $u^{'} = u - \bar{u}$ and $T^{'} = T - \bar{T}$,the zonal component of eddy heat flux is computed as

$$\overline{u'T'} = \overline{uT} - \bar{u}\bar{T}.$$

The procedure is similar for the meridional and vertical components of the eddy heat flux, and all other second moments: $\overline{u'^2}$, $\overline{u^{'}v^{'}}$, $\overline{u^{'}w^{'}}$, $\overline{v'^2}$, $\overline{v^{'}w^{'}}$, $\overline{w'^2}$ and $\overline{T'^2}$.

Statistical Properties The high frequency data about state variables were collected as a daily averages for 40 selected locations for each layer during the whole length of the integration. The position of these stations is presented in Figure 2-7. The high frequency data allows to estimates of the uncertainties of the statistical properties of the climatological and eddy quantities. Due to the limitations of the experiment this data also helps to identify different dynamical regions of the numerical domain. The data can be used for the evaluation of additional processes, that are important for the local balances, such as mixed layer dynamics and convection processes.

Additional Diagnostics Instantaneous snapshots of the model state are periodically saved. This data set samples the time–dependent processes such as wave propagation,

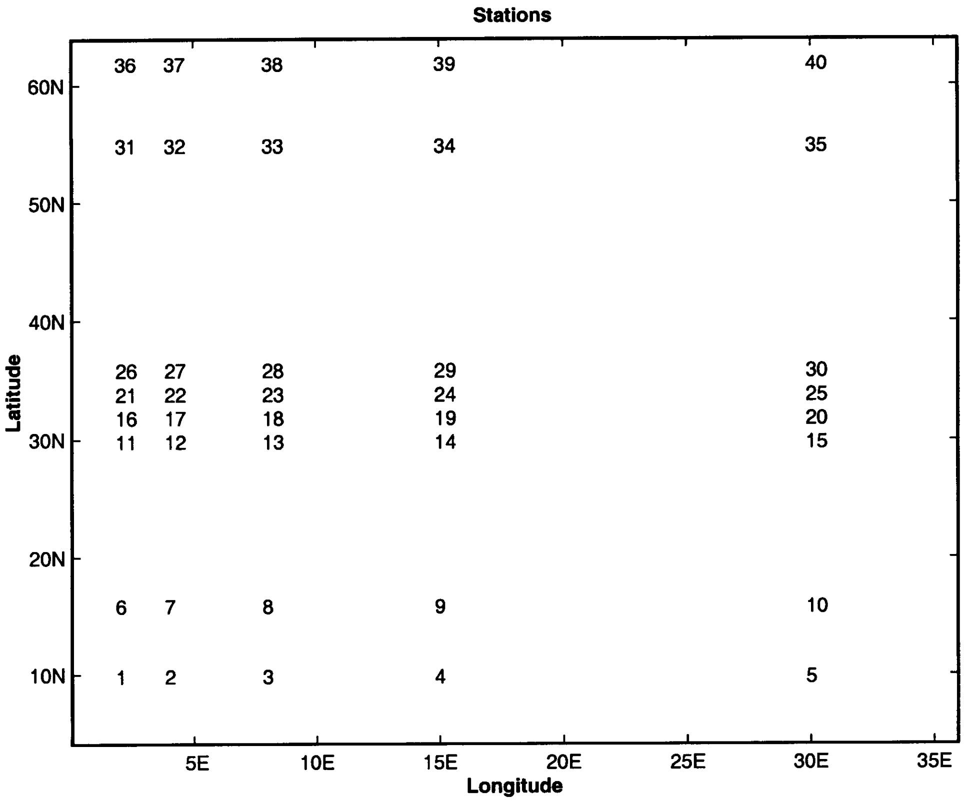

Figure 2-7: Geographical location of stations.

meandering, isolated eddies dynamics, patterns in the density structure.

To monitor the variability of the northward zonally integrated heat flux the daily, averaged values are saved during the whole length of the integration.

Table 2.5 summarizes the data acquisition strategy for the experiment.

Evolution of the Model During Data Period

After the spin–up, the model is integrated for a further 55 years. The horizontal flow is in a statistical steady state (Figure 2-8(a)). The signature of the mesoscale eddies is reflected in the presence of high frequency variability through the whole length of the simulation. The averaged thermal state continues to evolve with a slow time drift (Figure

Data	Description	Period	Location
Horizontal kinetic energy	Monitoring	every 14 days	each layer
Average temperature	Monitoring	every 14 days	each layer
Time mean quantities	Time mean diagnostics	sum over iterations	each grid point
Eddy quantities	Eddy diagnostics	sum over iterations	each grid point
Time series	High frequency observations	daily averaged	40 stations
Instantaneous data	Fine resolution observations	5 snapshots	each grid point
Northward heat flux	Variability of heat flux	daily averaged	zonally integrated

Table 2.5: Data acquisition strategy for the reference experiment

2-8(b)). The upper thermocline ocean gets warmer, the deeper ocean becomes cooler. The depths between $800M$ and $1000M$, that is roughly at the base of the thermocline, are in an equilibrium state. The same is true for the uppermost layer. The temperature evolution suggests that on average the thick deep ocean is losing heat to the thinner upper thermocline ocean.

During this 55 years period the state variables and their respective fluxes were accumulated in order to obtain an estimate of the eddy heat flux at the end of the simulation. Is the length of the data period sufficient for a stable estimate of the eddy quantities? This question was posed since the first eddy resolving experiments with numerical oceanic models. *Holland and Rhines, 1980* [31] showed that averaging over at least 3600 days was necessary to obtain a stable average in their two layer quasi–geostrophic simulation forced by a steady wind stress. A similar analysis is performed here by evaluating the stability of the time–averaging procedure for the meridional velocity (v), temperature (T) and the meridional heat flux $\left(\overline{v'T'}\right)$. The following function of the length of integration τ is evaluated for the quantities

$$\overline{A}(\tau) = \frac{1}{\tau} \int_{t_0}^{t_0+\tau} A(t)dt,$$

where A is a variable and t_0 is the beginning of averaging period. Figures 2-9 and 2-10 present the evaluation for stations 27 $(36°N, 4°E)$ and 29 $(36°N, 15°E)$ in the second layer, respectively. The stations are located in the midlatitudinal area (Figure 2-7) where

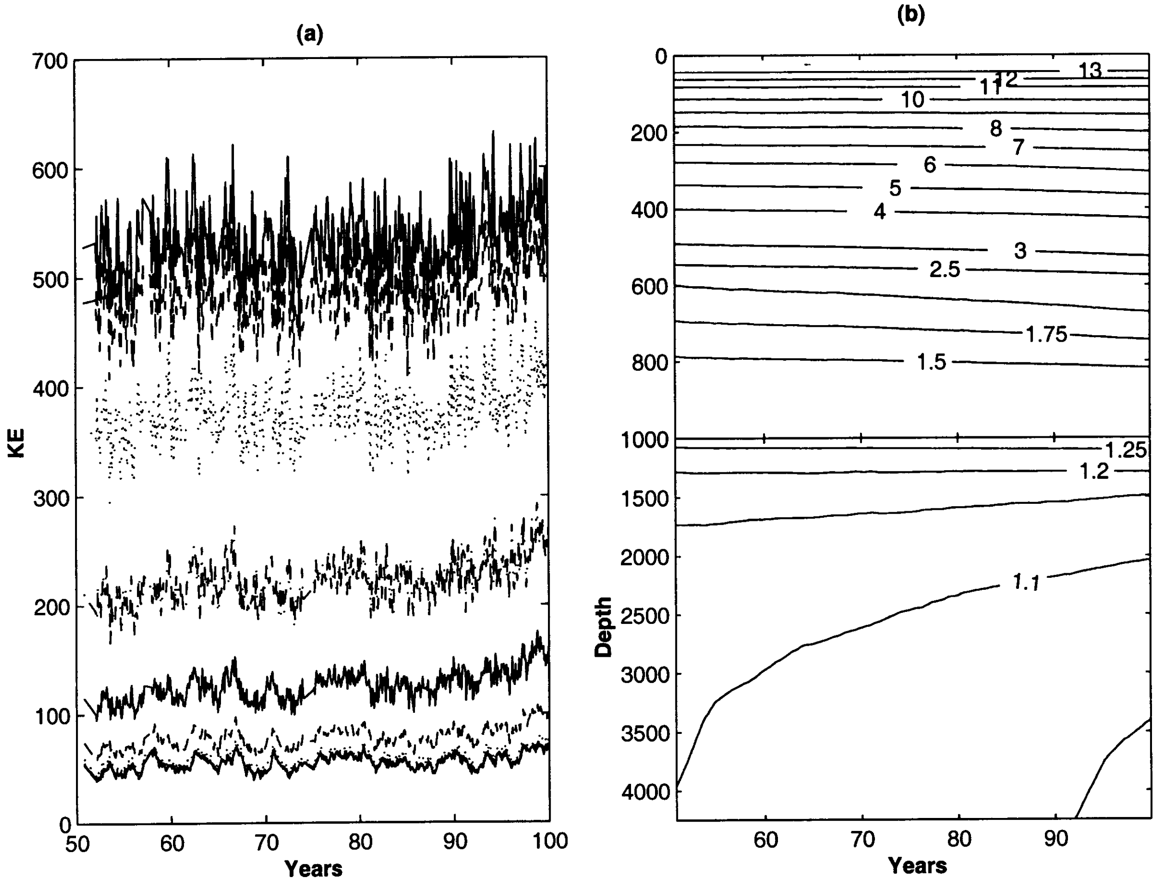

Figure 2-8: Data period of the eddy resolving simulations: (a) horizontal kinetic energy for each layer (upper layers at the top), (b) horizontally averaged temperature. Note: upper $1000M$ are stretched and varying contour intervals.

the eddy heat flux divergence is anticipated to be the strongest.

For station 27 (Figure 2-9), in the immediate vicinity of the western boundary current, about 10 years is required to obtain a stable estimate of all considered variables and fluxes. An even longer period, about 30 years, is necessary for the interior station 29 (Figure 2-10). Thus, the total length of the data period of 55 years is sufficient for the accurate estimation of eddy quantities. This result is consistent with the study by *Rix and Willebrand, 1996* [47] where they showed that the 4 to 5 years length of an individual experiment in CME calculations is insufficient to obtain a stable estimate of the eddy

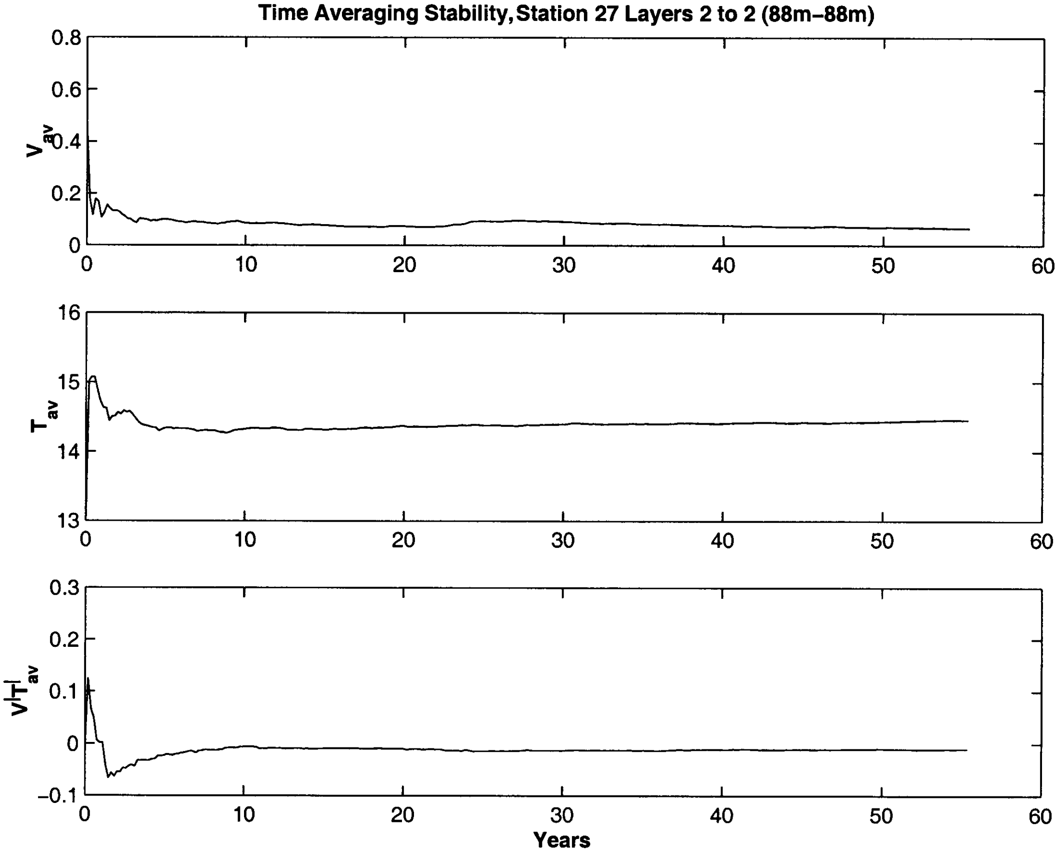

Figure 2-9: Stability of the time average quantities: upper plot: v, meridional velocity; middle plot: T, temperature; lower plot: $\overline{v'T'}$, meridional heat flux. Station 27. Layer 2.

heat flux.

The magnitude of the barotropic transport in the eddy resolving simulation (Figure 2-11) is larger than in the coarse resolution experiment (Figure 2-4(a)) generating the initial conditions. There are two reasons that can account for the difference. First, as it was pointed out when discussing the climatology of the initial state, the finer horizontal grid of the eddy resolving simulation allows the no–slip boundary conditions to be satisfied in narrow regions of 0.2°; thus, the effective width of the domain is 99.9% of the geographical extent vs. 77.8% in the coarse resolution simulation. Second, the mesoscale eddies in the reference simulation significantly enhance the wind–driven circulation in the western

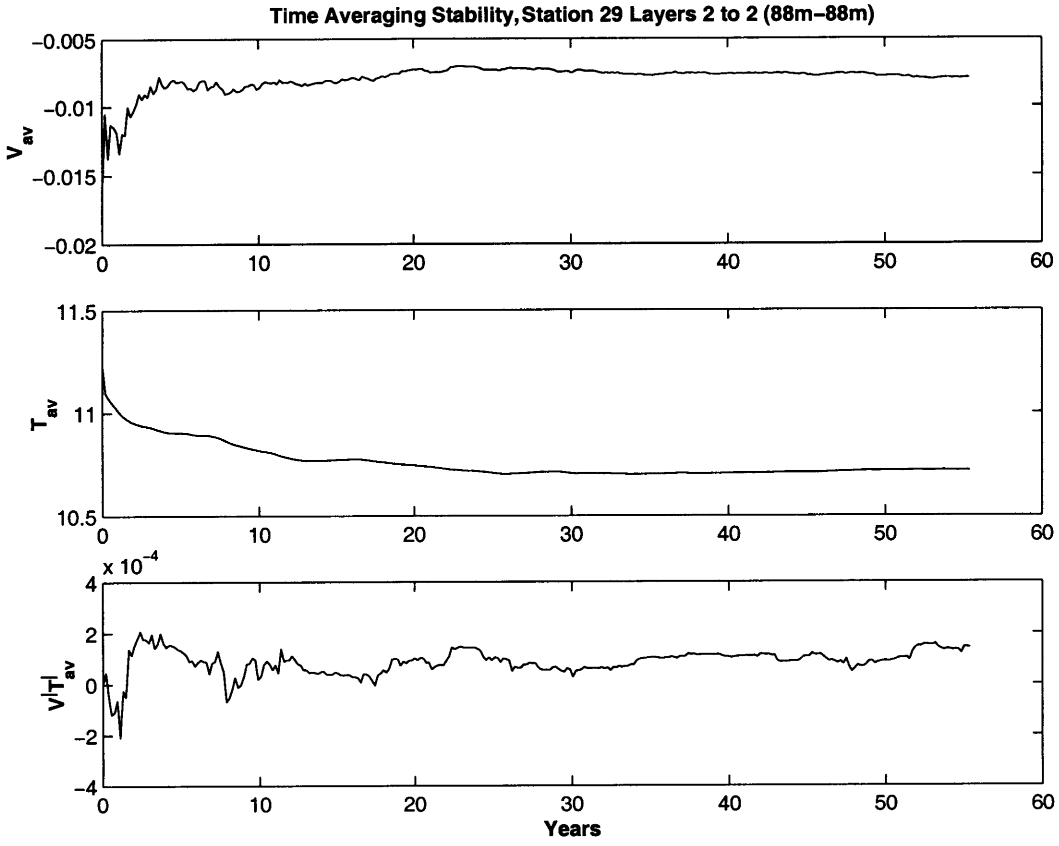

Figure 2-10: Stability of the time average quantities: upper plot: v, meridional velocity; middle plot: T, temperature; lower plot: $\overline{v'T'}$, meridional heat flux. Station 29. Layer 2.

boundary region through the non-linear eddy-mean flow interactions (*Hogg, 1988* [30]), thus effectively modifying the purely wind-driven Sverdrup balance.

2.5 Summary

The chapter deals with the specifications and implementation of the reference fine resolution experiment. The simulation was performed from the ground up using the MIT GCM on the parallel computer CM-5.

The total number of wind- and buoyancy-driven eddy resolving/eddy permitting simulations on the basin and global scales is still small (e.g. *CME* [5], [4], [3]; U.K. Fine Resolution Antarctic Model (FRAM) [22]; *Semtner and Chervin, 1992* [51]). So researchers can not possibly foresee all potential problems when they originally design a fine resolution climatological experiment. One needs to make a compromise between the formulation of the experiment and the corresponding requirements for the computer resources. For the former the natural tendency is to describe all known processes resulting in an overwhelming requirements for the computer resources. The ideas about the set up of the experiment, data accumulation strategy and monitoring of the reference simulations are important for the future large–scale ocean modelling.

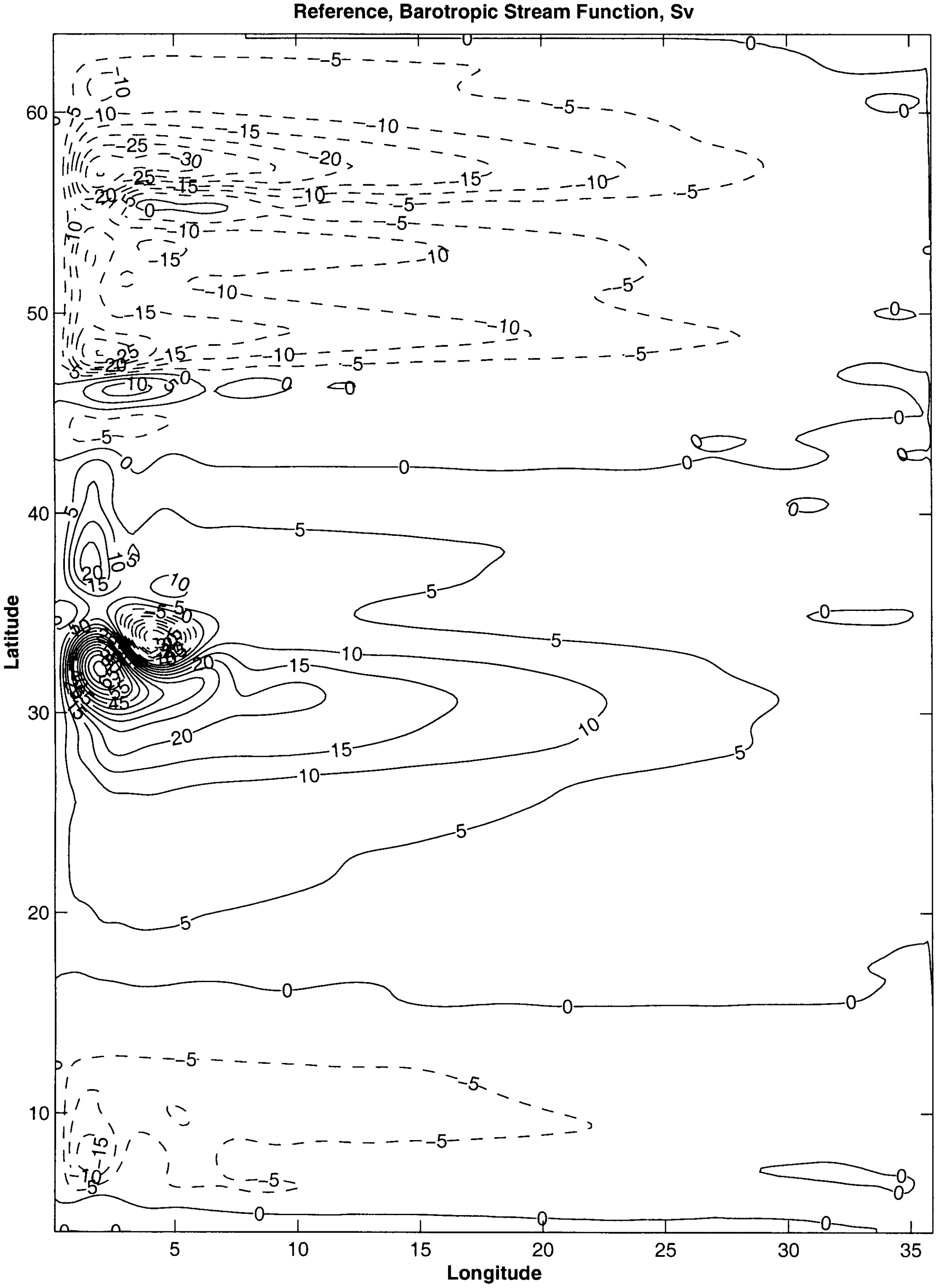

Figure 2-11: Barotropic transport, $[Sv]$ in the reference experiment averaged over 55 years.

Chapter 3

Climatological Analysis

3.1 Introduction

The *climatological state* of an eddy resolving simulation is defined as the time average of all intermediate model states during the data period[1] of the experiment. The major diagnostic quantities to be considered in this chapter are those which are usually evaluated in climate simulations with coarse resolution models.

The assessment of the climatological state of the model is presented in two different ways. First, I analyze the climatology (i.e. the average of 55 years) of the eddy resolving reference experiment by averaging the climatological fields over a $4^\circ \times 4^\circ$ horizontal area. In such a way smoothed, coarse resolution distributions are obtained which can be compared with coarse and fine resolutions climatological simulations published in the recent literature. Second, I compare the same climatology again averaged on a $4^\circ \times 4^\circ$ square, with two coarse resolution experiments. The first one is *the initial condition* that was prescribed as coarse resolution fields obtained in the initialization process discussed in the previous Chapter 2. The second experiment is a coarse resolution simulation with the coefficients of vertical diffusivity and viscosity equal to the values used in the reference

---

[1] The definition of the data period is given in Chapter 2.

fine resolution experiments. Below, this experiment is referred to as *the coarse resolution experiment.*

Coarse resolution simulations demonstrate better skills in the reconstruction of the gross density structure and overturning transport (e.g. *Cox, 1985* [13], *Bryan, 1987* [7]) than in reproducing the cumulative effects of mesoscale eddies and instability processes. Therefore in the chapter, I concentrate predominantly on diagnosing thermodynamical quantities and the associated transports.

3.2 Climatological Diagnostics

The following sections present a climatological analysis of the reference fine resolution calculation. The first part shows an analysis of the temperature field. Due to the linearity of the equation of state, temperature uniquely defines the density structure. The second part concentrates on the transport properties.

The direct analysis of the results is based on the comparison with some of the already performed experiments. It is important to understand the relationship between the reference simulation and the already published research. The scope of the comparison is limited by the availability of the plots from the recently published papers corresponding to the climatological diagnostic quantities which are evaluated from the reference experiment. The majority of the climate simulations (e.g. *Bryan, 1987* [7], *Danabasoglu and McWilliams, 1995* [14], *England, 1995* [19], *Robitaille and Weaver, 1995* [48], *Duffy et. al, 1997* [17], *Fanning and Weaver, 1997* [21]) has been performed using the Modular Ocean Model (MOM) version of the Bryan-Cox ocean general circulation model developed at the Geophysical Fluid Dynamics Laboratory (GFDL) (*Bryan, 1969* [9]; *Cox, 1984* [12]; *Pacanowski et. al, 1991* [44]). The MIT GCM belongs to a similar type of primitive equations models, hence the results can be compared directly. In a case of significant differences in the formulations of the experiments only a qualitative evaluation will be discussed.

Prior to the analysis, the projection on the coarse grid is performed for all fine resolution diagnostics. The details of the procedure are presented in the Appendix A.

3.2.1 Density Structure

The density distribution defines the overall heat storage of the system. The heat capacity of sea water is much larger than of the atmosphere. The heat content of the upper $2.5M$ of the ocean equals the heat content of the entire atmosphere (*Marotzke, 1994* [39]). Therefore, a small difference in the density can result in large variations of the total heat content of the combined system. Second, through the thermal wind relation, the density distribution affects the geostrophic component of the horizontal flow. This property connects the general circulation of the ocean with the thermal structure.

Most of the above cited coarse resolution climate simulations use the traditional Fickian diffusive closure for the eddy heat flux and show some deficiencies in reproducing the observed climate system. The assessment of the simulation is often based on the comparison with some climatological dataset. Often, the experiments were initialized with one of those datasets. The major problems of the solutions from the point of view of simulating the density structure can be identified as:

- The deep ocean tends to be warmer than the comparison climatology by as much as $4°C$,
- The upper ocean is cooler, resulting in a less sharp thermocline,
- The strong diapycnal mixing in the regions of steeply sloping density surfaces leads to the unrealistic structure of the thermocline,
- The deep convective mixing is too strong, leading to the greater vertical exchange of water in the high latitude ocean, resulting in local warming of the deeper ocean.

The success of the reference simulation is judged on the grounds of how well the simulation succeed in improving the above stated deficiencies of the climatological simulations.

The time mean thermal state of the reference simulation is presented in Figure 3-1. The following three diagnostic sets were computed. The surface heat flux (Figure 3-1 (a)) shows the interaction between the atmosphere and the ocean. The diabatic forcing in the form of the relaxation of the upper layer temperature to the prescribed apparent atmospheric temperature provides a linear relationship between the surface heat flux and the upper layer temperature anomaly. The zonally averaged temperature (Figure 3-1 (b)) portrays the structure of the thermocline and the depth of the deep convection. The horizontally averaged temperature profile (Figure 3-1 (c)) provides an overall measure of how sharp (or smooth) is the climatological thermocline.

Surface Heat Flux

The surface heat flux provides a measure of the interaction between atmosphere and ocean. The restoring boundary condition at the surface (*Haney, 1971*[28]) does not prescribe a fixed heat flux. The magnitude of the flux is modified in response to the changes in temperature of the upper layer.

Ocean gains heat in the southern and the interior of the central parts of the basin, and loses heat in the western boundary current and the northern areas (Figure 3-1(a)). The maximum heating of $+75\,[W \cdot M^{-2}]$ is observed in the southern area of the domain. The strongest heat loss to the atmosphere occurs in the area of the western boundary current. Warm water, brought from the South, actively loses heat to the atmosphere with a maximum of about $-150\,[W \cdot M^{-2}]$. The upper layer of the model is in a nearly statistical steady state with an apparent atmosphere (Figure 2-8). Even though the absolute magnitude of heat loss is larger than the maximum heat gain, the area integral of the surface heat flux over the whole basin is small. The ocean on average losses heat at the rate of about $0.2[W \cdot M^{-2}]$. This value corresponds to the heat flux from the ocean

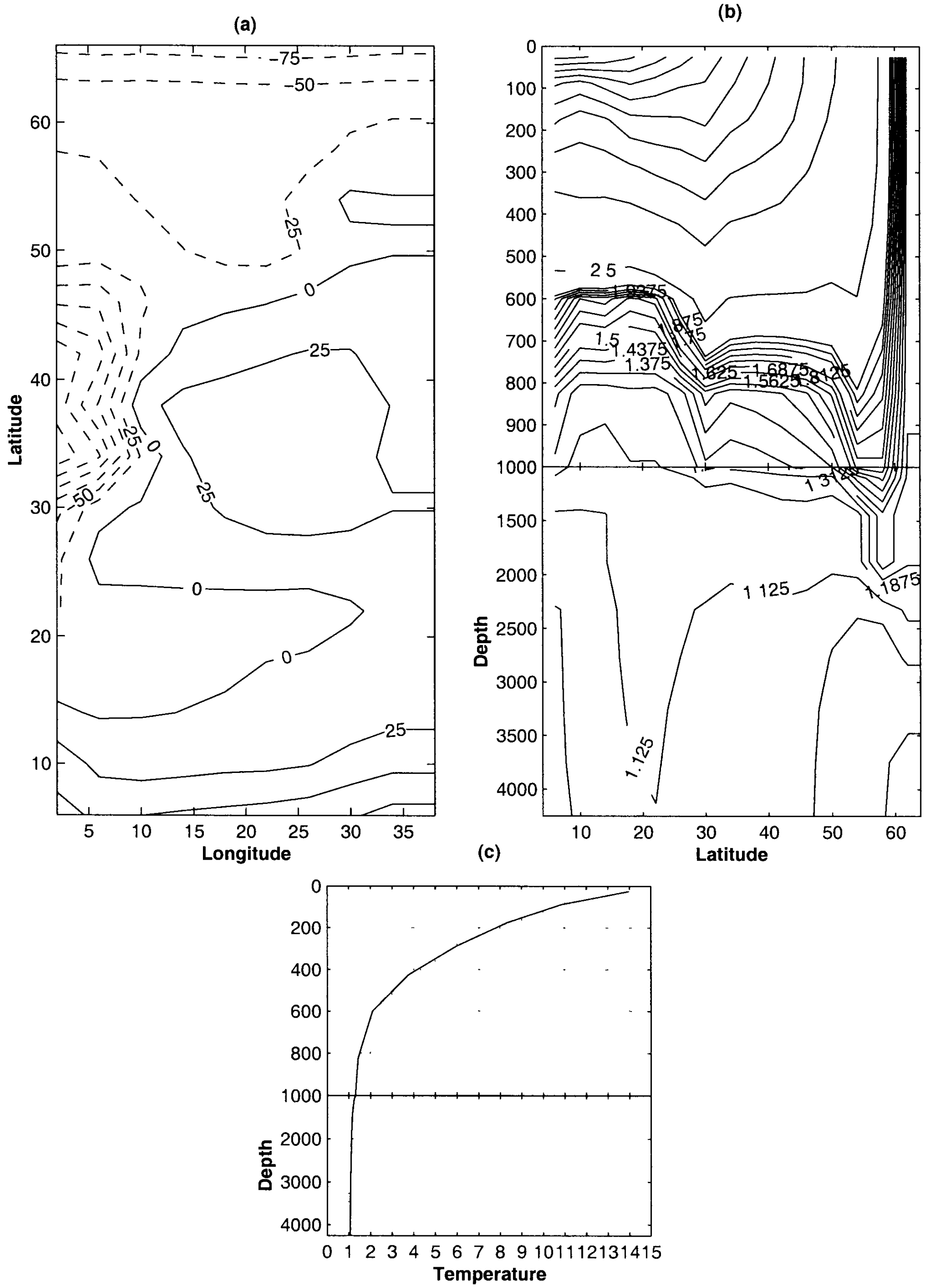

Figure 3-1: Thermal structure of the reference simulation: (a) surface heat flux, $[W \cdot M^{-2}]$; (b) zonally averaged temperature, $[°C]$, stretched upper $1000M$, variable contour intervals of $0.0625°C$ between $1°C$ and $2°C$, $0.25°C$ between $2°C$ and $3°C$, $2.5°C$ between $3°C$ and $25°C$; (c) horizontally averaged temperature, $[°C]$, as a function of depth, stretched upper $1000M$.

to the atmosphere in the amount of $0.005[PW]$. Figure 3-1(a) is a rectangular projection of a spherical surface; thus, the southern part of the domain occupies a larger area than the northern part.

The direct comparison with *Bryan, 1987* [7] (Figure 3-2) shows the similarity between the distribution of the surface heat flux in his coarse resolution equilibrium experiments and the reference simulation: strong cooling in the western boundary current and warming in the southern part of the domain. The profile of the apparent atmospheric temperature and the relaxation coefficients are similar in both experiments leading to consistent upper layer temperature distribution.

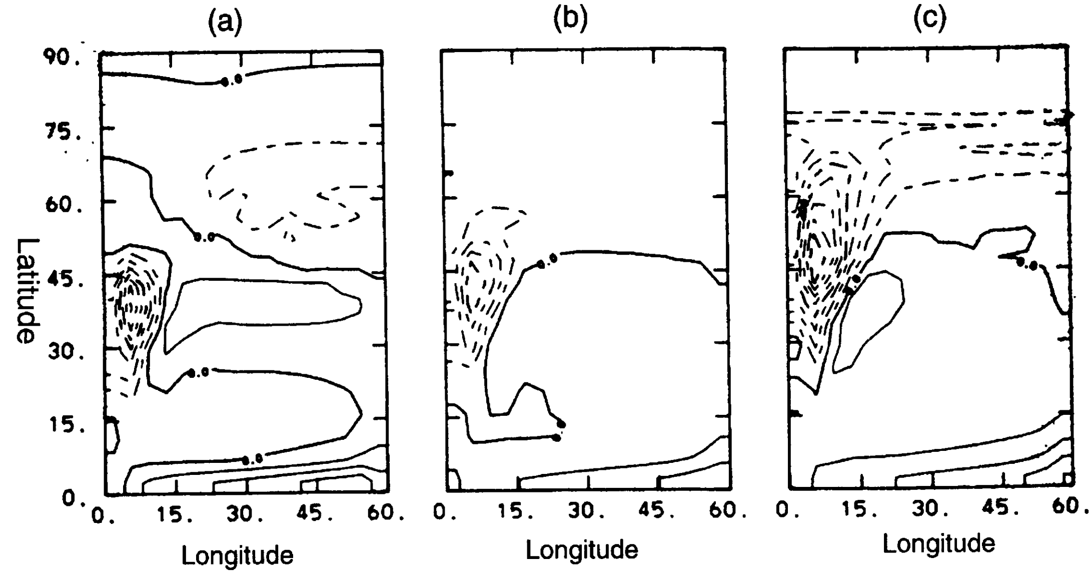

Figure 3-2: Surface heat flux, $[W \cdot M^{-2}]$, adopted from *F. Bryan, 1987* [7] for experiments with different vertical diffusivity: (a) $0.1 \cdot 10^{-4}\,[M^2 \cdot \mathrm{sec}^{-1}]$, (b) $2.5 \cdot 10^{-4}\,[M^2 \cdot \mathrm{sec}^{-1}]$, (c) $5.0 \cdot 10^{-4}\,[M^2 \cdot \mathrm{sec}^{-1}]$. Contour intervals (a) 25 $[W \cdot M^{-2}]$, (b) and (c) 50 $[W \cdot M^{-2}]$.

The difference in the magnitude is due to the value of vertical diffusivity. Bryan observed that a larger vertical diffusivity coefficient leads to a stronger western boundary current. Stronger advection of temperature in this area causes the isotherms in the

Bryan's experiments to deviate significantly from the apparent temperature. This larger difference leads to the stronger surface heat flux. The value of the vertical diffusivity in the reference eddy resolving calculation is $0.3 \cdot 10^{-4}\,[M^{-2} \cdot \sec^{-1}]$, which is 3 times larger than the value in the Bryan's experiment that is shown in Figure 3-2(a). In this particular Bryan's simulation, the value of the vertical diffusion coefficient is $0.1 \cdot 10^{-4}\,[M^{-2} \cdot \sec^{-1}]$.

Zonally Averaged Temperature

To resolve some fine features in the thermal structure, variable contour intervals are used in plotting isotherms. The processes in the upper ocean sustain the largest temperature variations. They span the temperature range from $1°C$ to $25°C$. The contour interval used for these depths is $2.5°C$. The deep ocean is uniform in temperature. A contour interval of $0.0625°C$ is used for the range of $1°C$ to $2°C$. The mid–depths, that are usually associated with the thermocline, are covered with the interval of $0.25°C$ over the temperature range from $2°C$ to $3°C$. Although the variable contouring produces some artificial convergence of isotherms, it allows to resolve the features within adjacent regions.

An important property of the zonally integrated temperature (Figure 3-1(b)) is a strong thermocline, identified as the range in depth corresponding to the sharp gradient in temperature. It is located between $500M$ and $1000M$ depending on the latitude. There is a step structure in the profile: the thermocline depth remain relatively constant from the southern boundary to about $25°N$, with a sudden deepening of $\backsim 100M$ of all isotherms between $20°N$ and $30°N$. The subsequent deepening around $52°N$ changes into strong deep convective regions in the northernmost part of the domain. Strong deep convection occurs around $60°N$ with the depth of penetration of about $2000M$. It brings water of about $1.18°C$ from the surface to the deep ocean.

The distribution of the zonally averaged temperature is generally consistent with the simulations by *Cox, 1985* [13] and *Böning and Budich, 1992* (Figure 3-3 shows an averaged between $40°E$ and $50°E$ potential density, or a linear function of temperature).

The differences arise in the depth of the mixed layer between 35°N and 50°N, that penetrates almost uniformly to the depth of 200M in Cox and Böning experiments, with their thermocline deepening to the South of 40°N. In the reference experiment the thermocline has an interior plateau at 700–800M (Figure 3-1(b)).

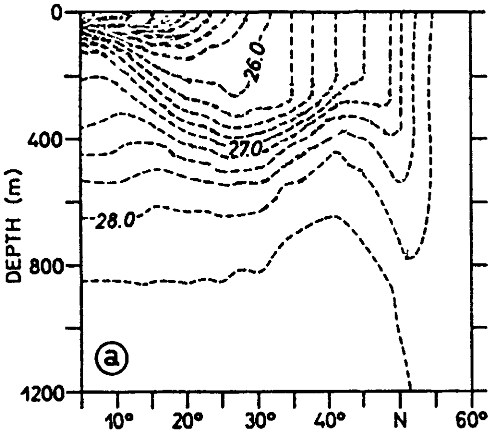

Figure 3-3: Time mean density for (a) 1/3° (*Cox, 1985* [13]) and (b) 1/6° (*Böning and Budich, 1992* [4]) averaged between 40°E and 50°E. Adopted from *Böning and Budich, 1992* [4].

Horizontally Averaged Temperature

The horizontally averaged temperature presents the overall temperature contrast between the upper and deep ocean, that demonstrates the model skill in overcoming the deficiency of producing solutions with unrealistically warm deep layers.

The shape of the profile (Figure 3-1(c)) corresponds to the generally observed density profiles: rapid changes in the upper layer, sharp drop in the thermocline and nearly constant, almost neutrally stratified deeper ocean. The upper temperature is about 14°C decreasing to about 1°C in the abyss.

Robitaille and Weaver, 1995 [48] computed this property in a series of global climatological experiments (Figure 3-4). Even though they computed the global ocean value, it can be directly compared with the reference simulation, due to the general symmetry in vertical distribution of temperature in both Hemispheres. As I pointed out, the overall profiles are similar: warm upper ocean, thermocline and cold deep ocean. The difference arises in the slope of curves. The temperature drop between the depths of $500M$ and the abyssal ocean is about $2°C$ in the reference simulation (Figure 3-1(c)). *Robitaille and Weaver, 1995* [48] produced much larger changes over the same depth interval, ranging from $6°C$ for Levitus climatology to $11°C$ for the experiment employing the Gent-McWilliams parameterization scheme. The larger value indicates less sharp thermocline. Therefore, the reference simulation produces a more realistic, sharper thermocline, closer to the Levitus climatology.

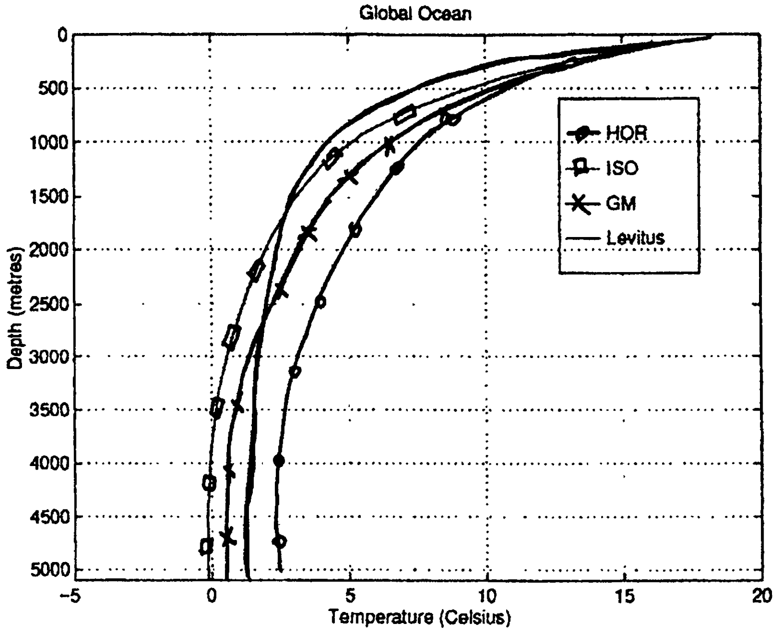

Figure 3-4: Horizontally averaged vertical profile of potential temperature [$°C$] for coarse resolution experiments using different eddy parameterization schemes: HOR - Laplacian mixing, ISO - isopycnal, GM - Gent-McWilliams parameterization [23], Levitus - observed climatology. Adopted from *Robitaille and Weaver, 1995*[48].

3.2.2 Transport

Among possible integral properties of the solution, the two that are considered to be of outmost importance to climate simulations, are the meridional overturning transport and meridional zonally integrated heat transport.

The meridional overturning circulation provides an estimate of the large–scale South/North exchange of properties in different vertical layers. There are a number of important passive tracers, such as CFCs, which are advected by the thermohaline circulation.

The other important role of the ocean in climate is the transport of heat from Equatorial regions to the polar ones. In nature, this contribution is of the same order as the atmospheric transport. Thus, the skill of the model in simulating this quantity is of the greatest importance for the simulations

These diagnostics are evaluated on a 4° coarse resolution grid that corresponds to the standard resolution of climate simulations in the ocean. In the climatological analysis of this chapter I do not consider horizontal properties of the flow, such as the barotropic circulation. The modifications of the horizontal circulation due to the explicit resolution of the mesoscale eddies are significant and the discussion of the diagnostics of the reference experiment evaluated over the fine resolution grid will be presented in later chapters when analyzing the transport properties of eddies.

Overturning Transport

The dominant feature of the overturning circulation (Figure 3-5(a)) is a large–scale cell located near the northern boundary. It is associated with the localized sinking of water due to the cooling at the surface and deep convection. The water returns to the upper layers in a large–scale interior return flow from about $60°N$ to the vicinity of the southern boundary. The maximum transport of the cell is about $7Sv$ with almost 3 Sv reaching $30°N$ latitude.

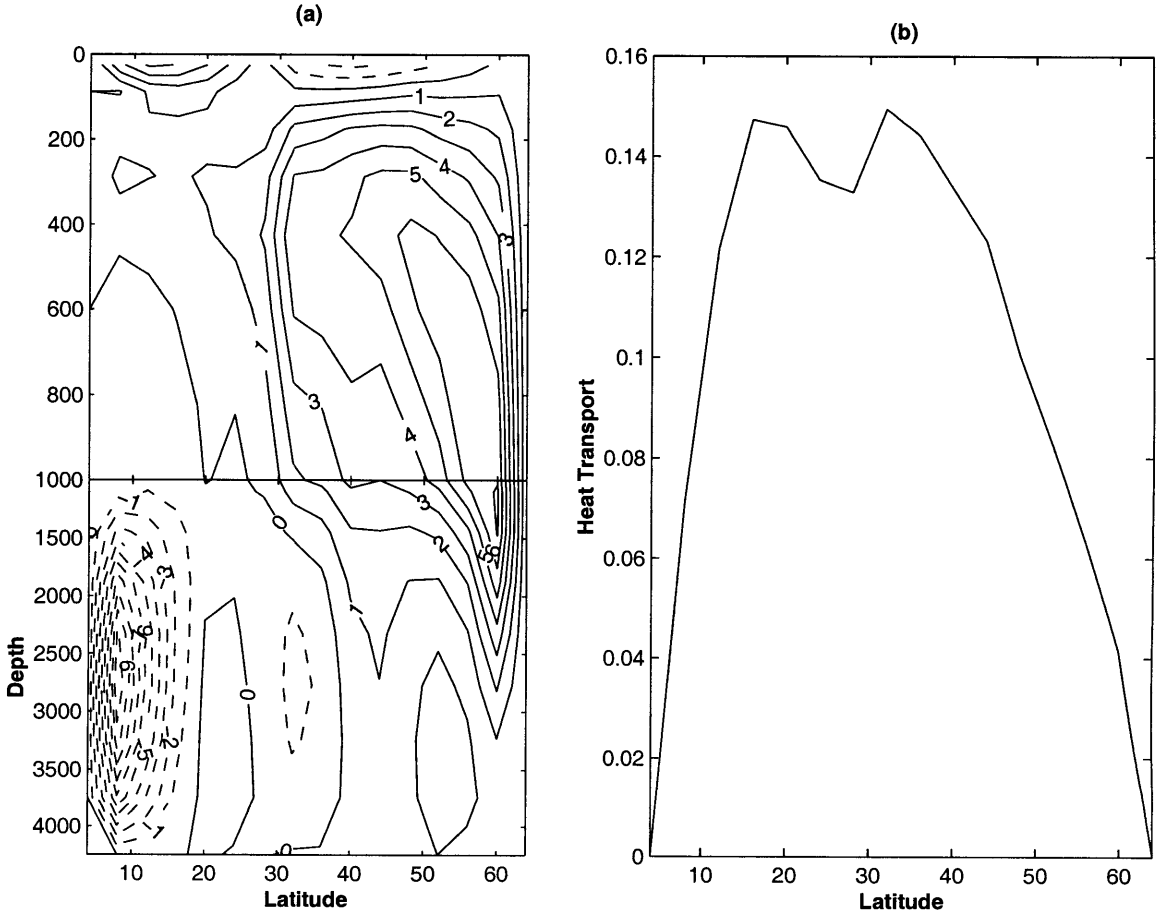

Figure 3-5: Transport properties of the reference simulation: (a) meridional overturning transport, $[Sv]$, stretched upper $1000M$; (b) total Northward heat flux, $[PW]$.

There are two wind–driven cells in the upper ocean. The stronger one, that transports about 3 *Sv,* is formed due to the combined effects of the upwelling in the regions adjacent to the southern boundary, where the strongest heating of the surface ocean (Figure 3-1(a)) occurs, and near equatorial trade wind supports the surface outflow. Equatorward Ekman transport forms another wind–driven cell in the middle latitudes. The strength of this cell[2] is about -2 *Sv.* It can be considered part of the main meridional circulation, acting primarily to reduce the total transport.

A fourth cell is present in the deep ocean near the southern boundary. Similar structures consisting of strong overturning cells centered around $3000M$ have been observed in a number of calculations with both coarse (e.g. *Bryan, 1987* [7], *Cox, 1985* [13]) and fine (e.g. *Böning and Budich, 1992* [4], *Semtner and Chervin, 1992* [51]) resolutions. Figure 3-6 from *Böning and Budich, 1992* [4] also shows the presence of a deep overturning cell of -4Sv near the Equatorial boundary.

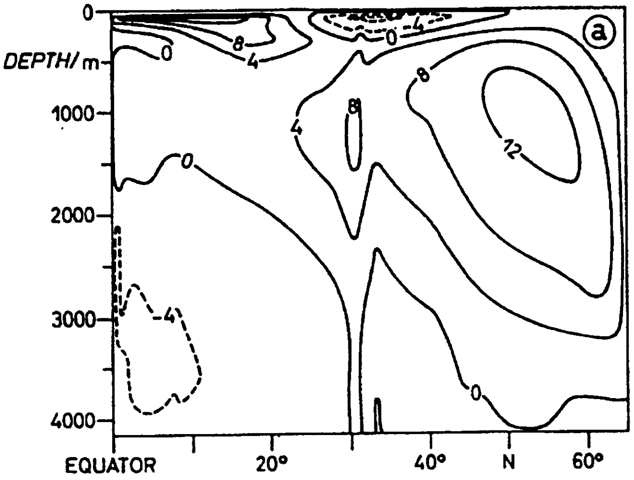

Figure 3-6: Meridional overturning stream function, $[Sv]$, in a fine resolution experiment by *Böning and Budich, 1992* [4].

---

[2] Negative value indicates counter-clockwise direction of the mass transport in the cell.

It is unknown what is the nature of this cell. The most common explanation is that the cell is an artifact of the insufficient vertical resolution in combination with low vertical diffusivity and viscosity. *Weaver and Sarachik, 1990* [60] define this cell as spurious and present the criteria on grid Reynolds and Peclet numbers that are necessary to be satisfied in order to remove it. On the other hand the fact that similar equatorial structures consistently occur in a variety of different simulations suggests that there might be some physical mechanism responsible for the formation of the strong deep cells.

Heat Transport

The northward heat flux is the primary quantity of interest in the establishment of the ocean climate. The total time mean heat transport H_{Total} is given by

$$H_{Total} = \rho_0 C_P \int_{-H}^{0} dz \int_{W}^{E} dx \cdot \overline{vT}, \tag{3.1}$$

where the second integral is computed from the western to the eastern boundaries and the overbar represents time–averaging over 55 years of the data period.

Figure 3-5(b) presents the meridional heat flux averaged on a 4° grid. An feature is the presence of two maximum in the profile. The first is located around $18°N$. Strong warming in the southern ocean requires an efficient removal of an excess heat. The strong southern upper ocean cell (Figure 3-5(a)) transports heat to the North. The deep southern cell does not contribute to the formation of this maximum, since temperature of water for this regions is distributed nearly uniformly (Figure 3-1(b)); thus, the local fluxes of heat are small.

The decrease in heat flux in the northern latitudes is due to the compensation between the northward transport by the main overturning cell and the Equatorward transport by the upper wind–driven Ekman cell (Figure 3-5(a)).

The distinguished feature of this particular simulation is the presence of the second maximum around $35°N$ and overall increase in the northward integrated heat flux to the North of this latitude. It transports heat of comparable amount to the southern maximum. In the simulations by *Cox, 1985* [13] and *Böning and Budich, 1992* [4], the second peak is absent from the total northward heat transport (Figure 3-7). The slight modulation at around 30°N is not developed into a strong local maximum. *Fanning and Weaver, 1997* [21] performed a simulation in the configuration of *Cox, 1985* [13]. The profile of the total heat flux in their experiments exhibits a local maximum in the midlatitude region between 25°N and 50°N (Figure 6 in *Fanning and Weaver, 1997* [21]). Due to the horizontal Laplacian mixing and larger horizontal resolution, which they employed in the experiments, the profile is smoother compared with the reference simulation. The midlatitudinal maximum develops with the decrease in the horizontal resolution from 4° to 0.5°. The nature of the increase in the heat flux will be analyzed in the latter section when I compare the reference fine resolution simulation with two coarse resolution experiments.

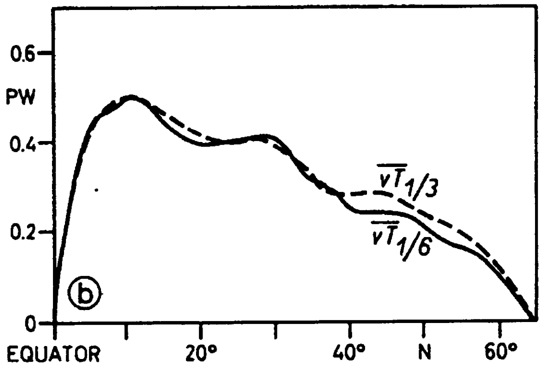

Figure 3-7: Total northward heat transport in the simulations by *Cox, 1985* [13] (dashed line, 1/3° resolution) and *Böning and Budich, 1992* [4] (solid line, 1/6° resolution). Adopted from *Böning and Budich, 1992* [4].

The magnitude of the heat transport is about $0.15PW$, rather small in comparison with the observations for the North Atlantic of $1.2PW$ at 24°N (*Hall and Bryden, 1982* [27]). The value is determined by the external factors of the model, such as the width of the domain and the contrast in apparent atmospheric temperature between the southern- and northernmost locations.

3.3 Comparison with the Coarse Resolution Experiments

The fine resolution of the reference experiment allows the development of mesoscale eddies. This section addresses the modifications to the initial state of the reference simulation due to the presence of these time–dependent motions. In addition it compares the reference simulation with a coarse resolution experiment that was performed with vertical diffusivity and viscosity of the reference fine resolution simulation. The differences between the time mean state over the last 55 years of the reference experiment evaluated over the coarse resolution grid of 4° × 4° and two coarse resolution experiments is analyzed according to the climatological diagnostic quantities: the simulation of the density field and the associated transports.

Initial State

A coarse resolution simulation is used to produce the initial state of the reference experiment. The description and parameters of this 4° × 4° horizontal resolution, equilibrium simulation are presented in Table 2.4. Figure 3-8 shows the climatological diagnostic quantities describing the density field. All subplots and contour intervals are the same as in the Figure 3-1. The associated transport properties of the initial state are presented in Figure 3-9. All subplots and contour intervals are the same as in the Figure 3-5.

Coarse Resolution Experiment

Another coarse resolution experiment was performed in a set–up that was similar to the one used in the simulation of the initial state. The differences are in the values of the

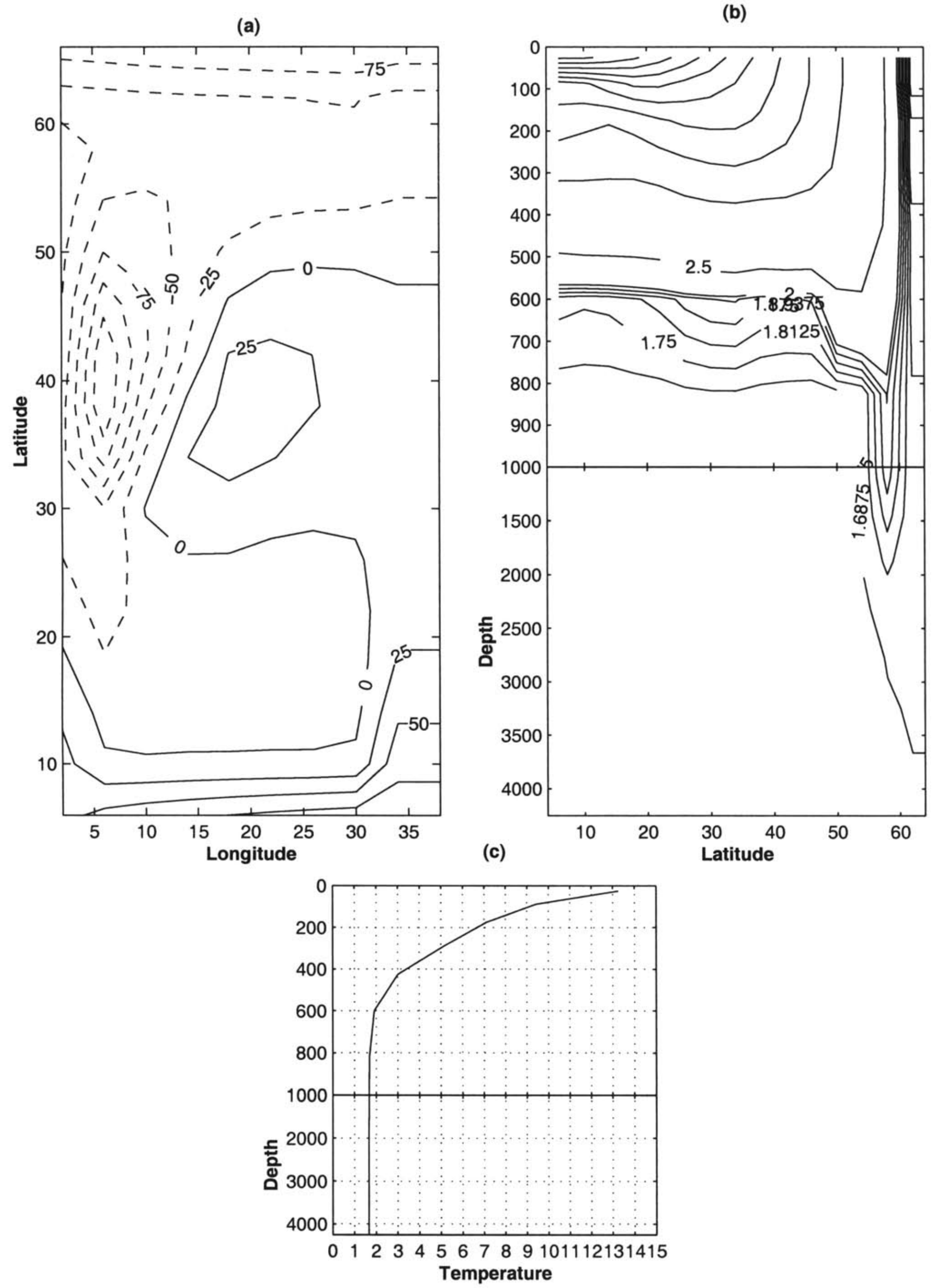

Figure 3-8: Thermal structure of the initial state: (a) surface heat flux, $[W \cdot M^{-2}]$; (b) zonally averaged temperature, $[^{\circ}C]$, stretched upper $1000M$, variable contour intervals of $0.0625^{\circ}C$ between $1^{\circ}C$ and $2^{\circ}C$, $0.25^{\circ}C$ between $2^{\circ}C$ and $3^{\circ}C$, $2.5^{\circ}C$ between $3^{\circ}C$ and $25^{\circ}C$; (c) horizontally averaged temperature, $[^{\circ}C]$, as a function of depth, stretched upper $1000M$.

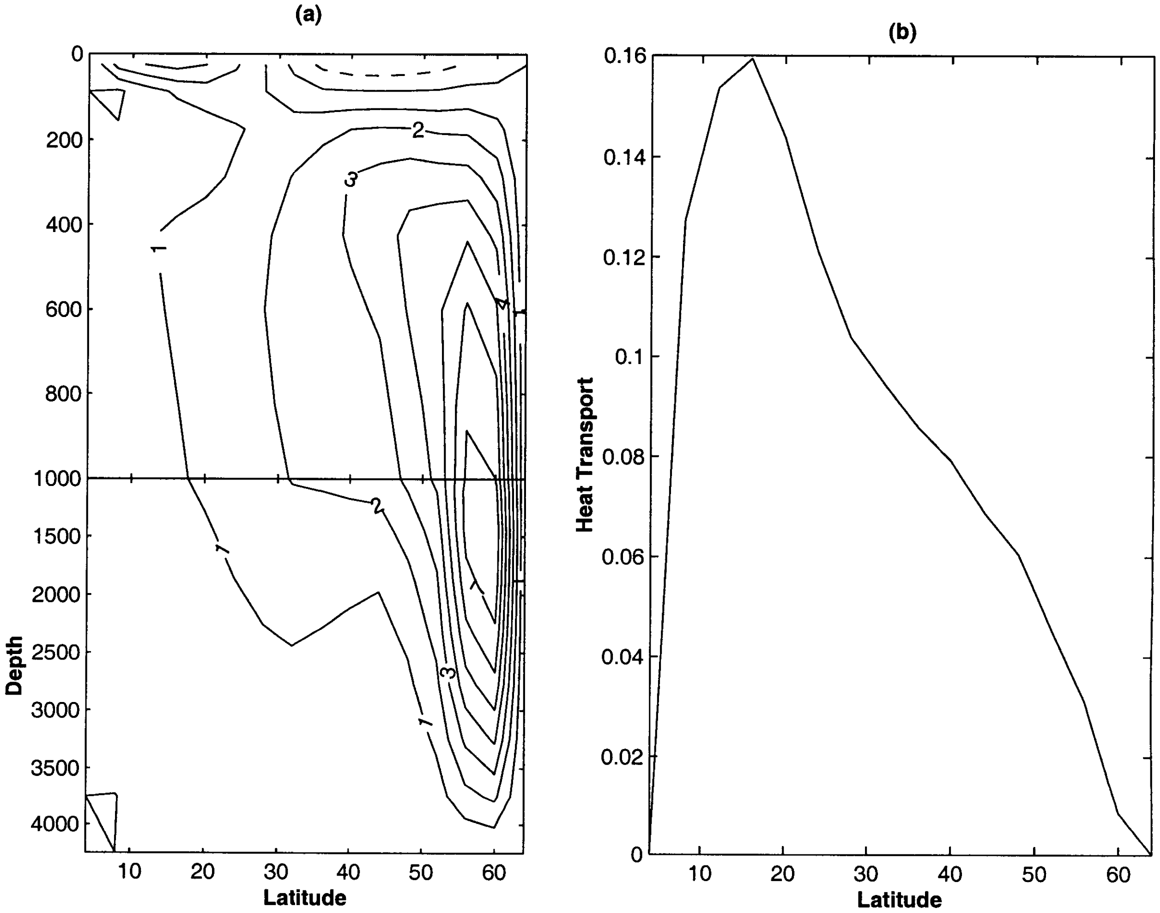

Figure 3-9: Transport properties of the initial state: (a) meridional overturning transport, $[Sv]$, stretched upper $1000M$; (b) total Northward heat flux, $[PW]$.

vertical mixing. The smaller vertical diffusivity of $0.3 \cdot 10^{-4}$ $[M^2 \cdot \sec^{-1}]$ and larger vertical viscosity 10^{-3} $[M^2 \cdot \sec^{-1}]$ are used in the experiment. These parameters are identical to the values used in the reference experiment. Figure 3-10 shows the thermal diagnostic quantities. Figure 3-11 shows the transport properties of the coarse resolution simulation. All subplots and contour intervals are the same as in the Figure 3-1.

3.3.1 Density Structure

Surface Heat Flux

The distribution of the surface heat flux in the climatological mean of the reference simulation (Figure 3-1(a)), the initial state (Figure 3-8(a)) and the coarse resolution experiment (Figure 3-10(a)) are similar: heating in the southern and Interior parts and cooling in the northern and western boundary regions. The general similarity of the distributions suggests that the interaction between the atmosphere and ocean on 4° horizontal scale is well reproduced by a coarse resolution simulation. The effects of eddies have local influence on this diagnostic quantity and are averaged out on the 4° horizontal scale.

The surface heat flux is modified mainly in the mid–latitudinal area of the domain. The strongest cooling in the reference experiment is located in the immediate vicinity of the western boundary. This location can be explained by the development of narrow and fast western boundary currents advecting warmer water to the North. The interior warming area is larger for the fine resolution simulation. The slight decrease in the area of the midlatitudinal cooling in the coarse resolution experiment is consistent with the observation made by *Bryan, 1987* [7] that the magnitude of the surface heat flux in the western boundary current area increases with the increase in vertical diffusivity.

The area integral of the surface heat flux is small in all cases. The solutions are in statistical equilibrium with the apparent atmospheric temperature (Figure 2-8).

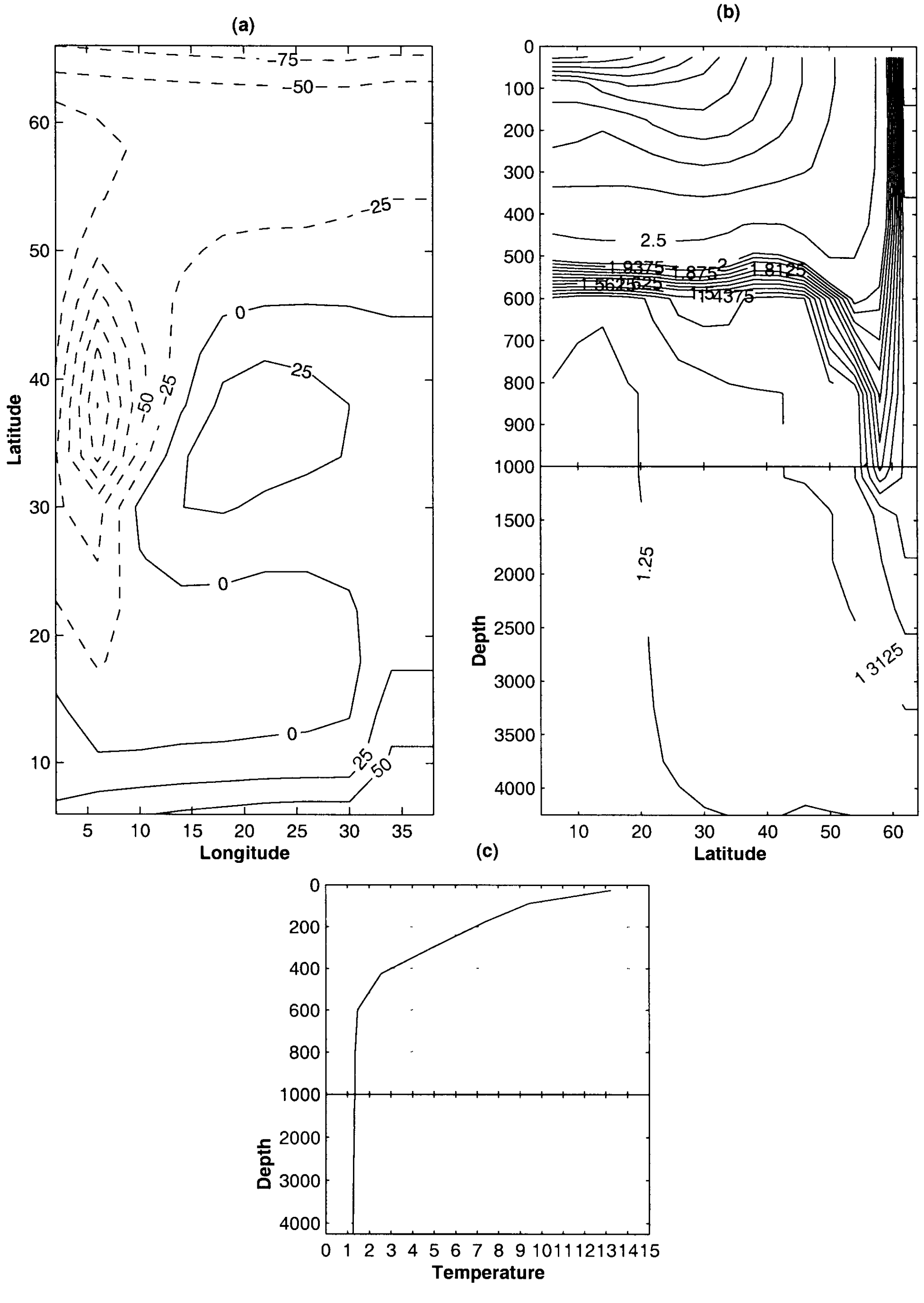

Figure 3-10: Thermal structure of the coarse resolution experiment: (a) surface heat flux, $[W \cdot M^{-2}]$; (b) zonally averaged temperature, $[°C]$, stretched upper $1000M$, variable contour intervals of $0.0625°C$ between $1°C$ and $2°C$, $0.25°C$ between $2°C$ and $3°C$, $2.5°C$ between $3°C$ and $25°C$; (c) horizontally averaged temperature, $[°C]$, as a function of depth, stretched upper $1000M$.

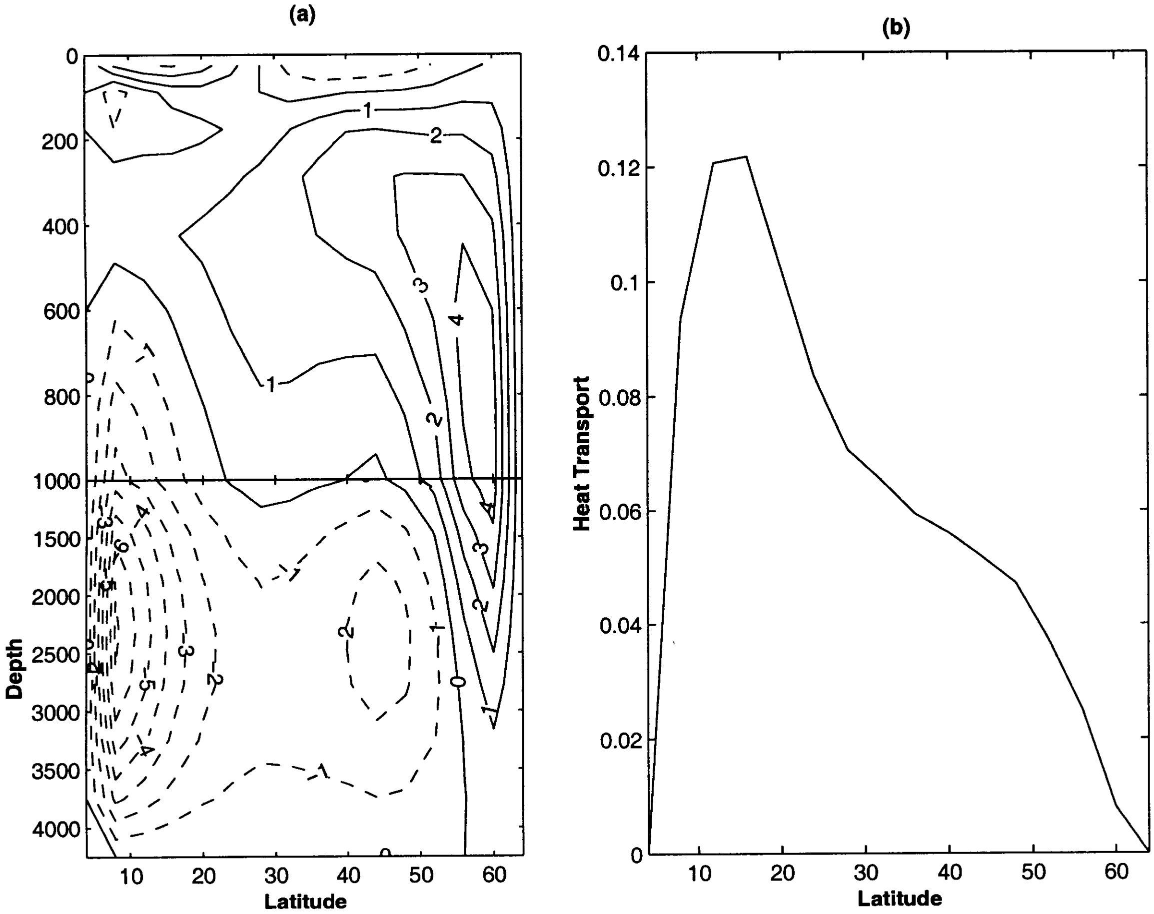

Figure 3-11: Transport properties of the coarse resolution experiment: (a) meridional overturning transport, $[Sv]$, stretched upper $1000M$; (b) total northward heat flux, $[PW]$.

Zonally Averaged Temperature

Figures 3-1(b), 3-8(b) and 3-10(b) present the zonally averaged temperature for the annual mean, the initial state and the coarse resolution experiment respectively. The smoothed climatology of the fine resolution simulation exhibits a more complex structure (variable contour intervals are the same for all Figures). The major qualitative difference is that the main thermocline layer is rather sharper ($700M$–$900M$) in the fine mean than in the initial state. The difference can be assessed quantitatively by considering the difference in quantities between the fine mean and the initial state (Figure 3-12) and the fine mean and the coarse resolution experiment (Figure 3-13).

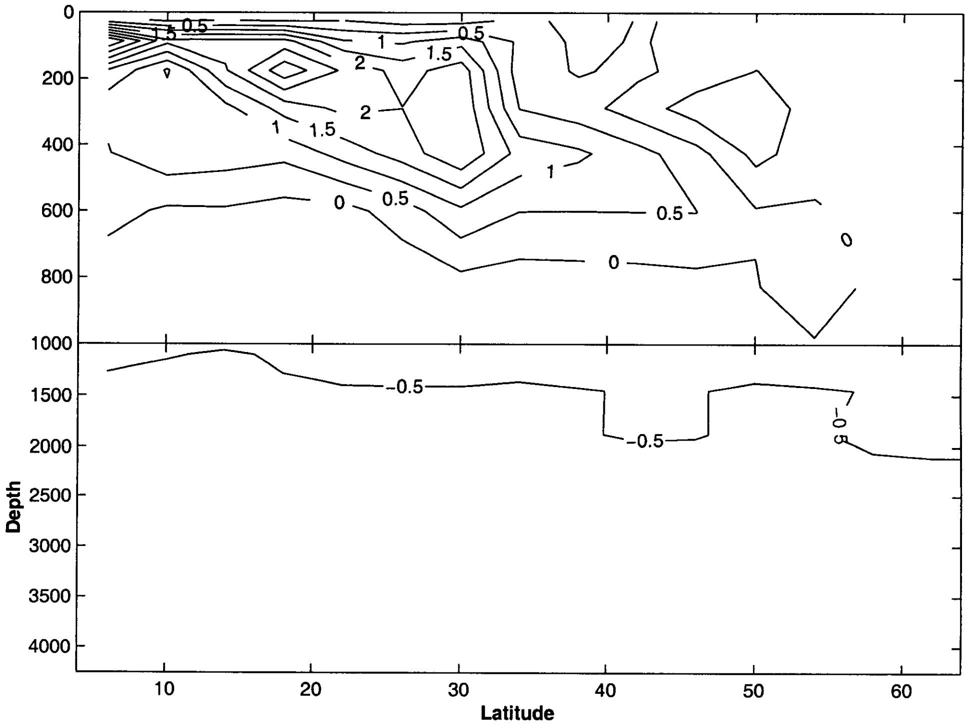

Figure 3-12: Zonally averaged temperature difference, [°C], between the reference experiment and the initial state of the reference fine resolution experiment, stretched upper $1000M$.

In comparison with the initial state, the $0°C$ isoline is located in the middle of the main

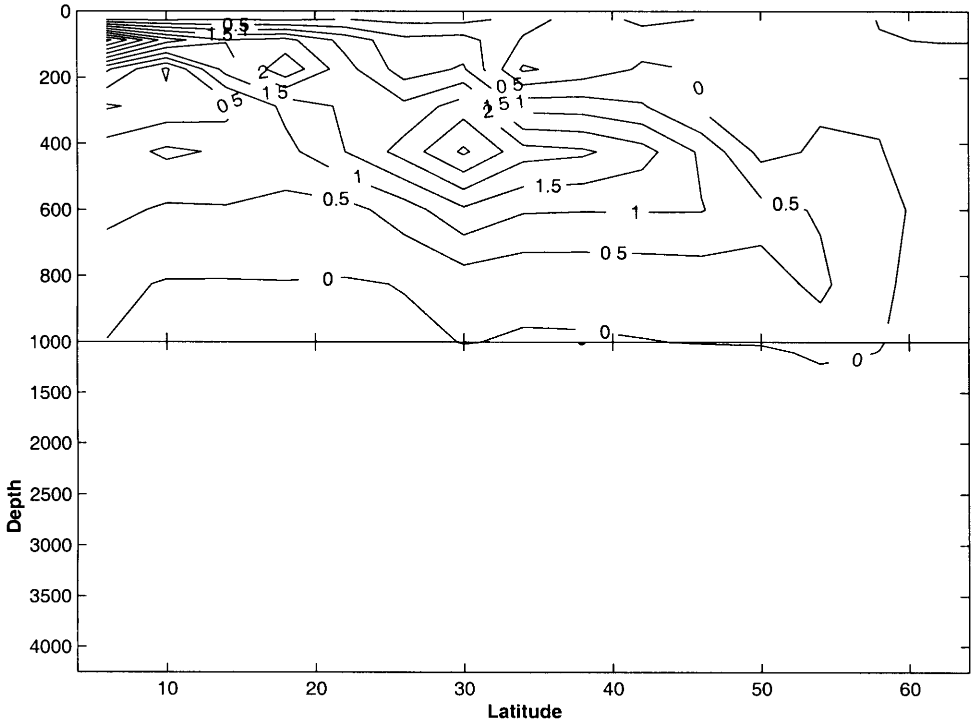

Figure 3-13: Zonally averaged temperature difference, [°C], between the reference experiment and the coarse resolution experiment, stretched upper 1000M.

thermocline. Its depth varies between $600M$ near the southern boundary to $800M$ for the mid-latitude region. It deepens to almost $1000M$ to the South of the deep convection area. The reference experiment produces warmer water everywhere above the isoline. Below the depth of the $0°C$ isotherm, the time average temperature of the reference experiment is more than $0.5°C$ cooler than the initial state. The isotherms of the reference experiment located above the main thermocline are deeper for the Subtropical ocean. The maximum increase in temperature for this areas occurs at the depth of $200M$. The thermal state is more stable in the reference simulation at all latitudes because the deep ocean is always cooler and the upper ocean is warmer then in the initial state. The northern area experiences moderate changes in temperature distribution.

One of the possible explanation of the differences in the simulation of the zonally averaged temperature is in the smaller value of the vertical diffusivity used in the reference simulation. The smaller the value the weaker are the process of the vertical mixing; thus, the temperature contrast between the upper and the abyssal ocean becomes larger. This explanation does not hold as a similar patterns arise in the comparison with the coarse resolution experiment that uses the same value of the vertical diffusivity. The upper ocean is warmer everywhere above $800M$ and cooler below the isoline of $0°C$ in Figure 3-13. This isoline is located deeper than in the previous comparison. Below $1000M$ the ocean in the coarse resolution experiment is warmer, although less than $0.5°C$.

Horizontally Averaged Temperature

The difference in horizontally averaged temperature (Figure 3-14) proves the point made in the previous subsection that the static stability increases in the reference experiment. There are two distinct parts in the profiles: the upper, with warmer ocean, and the lower with cooler. In the initial state the depth of $700M$ divides the profile. It is deeper at $1000M$ in the coarse resolution experiment.

Figure 3-4 from *Robitaille and Weaver, 1995*[48] shows the horizontally averaged temperature for the Levitus climatology (*Levitus and Boyer, 1994* [37]) and coarse resolution

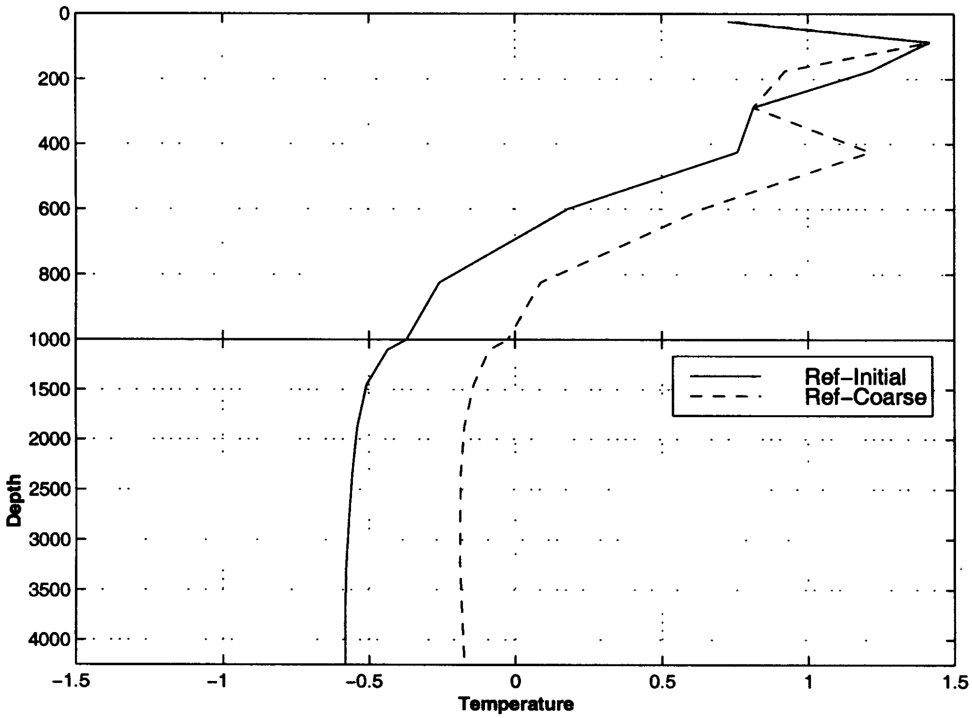

Figure 3-14: Horizontally averaged temperature difference, $[^{\circ}C]$, as a function of depth between the climatology and the initial state of the reference fine resolution simulation and the coarse resolution experiments, upper $1000M$ is stretched.

experiments using different eddy heat flux parameterization schemes. In this study they identified the deficiency of the Laplacian mixing experiment in producing the deep ocean that is warmer than it is suggested from the observations.

The horizontally averaged temperature profiles of the coarse resolution experiments exhibits a similar tendency with respect to the profile of time mean of the reference simulation. It suggests that the reference solution, using a small higher order horizontal diffusivity, with a cooler deep ocean is a better representation of the climatological state than the one produced as in a coarse resolution experiment with significant Laplacian horizontal diffusivity.

3.3.2 Transport

Overturning Transport

The meridional overturning transport (Figures 3-5(a), 3-9(a) and 3-11(a)) shows some important modifications. All three experiments exhibit different patterns in the distribution of the cells.

The amplitude of the main cell is constant at $7Sv$ in the reference experiment and the initial state. The geographic location of the maximum overturning is the same: depth $1500M$ and around $60°N$. The main difference is reflected in the shape of the cell.

The common problems of coarse resolution simulations using the Laplacian mixing are the insufficient spread of the cell into the Equatorward direction and the very deep penetration of convection in the northern region. Both of these deficiencies can be identified in the initial state (Figure 3-9(c)): about $2Sv$ reaches $30°N$, and the cell is $4000M$ deep. The time mean of the reference simulation however shows a significant improvement: the cell is shallower in the northern part, quickly decreasing in magnitude below $2000M$, and about twice as strong at $30°N$.

The critical parameter that is responsible for the shape and the magnitude of the main overturning cell in a coarse resolution experiment is the vertical diffusion. The smaller value of the diffusivity decreases the strength of the main thermohaline cell. In addition due to the corresponding weaker vertical mixing there is a decrease in the exchange processes between the upper and the deeper parts of the ocean resulting in a shallower main overturning cell.

In the coarse resolution experiment the value of the vertical diffusivity, $0.3 \cdot 10^{-4}$ $[M^2 \cdot \sec^{-1}]$ is the same that was used in the reference experiment. The shape of the main cell is similar between the two experiments: shallower penetration in the northern part and larger southward extent. Although the significant drawback of the coarse resolution experiment lies in the decrease of its magnitude by more than 40%.

Both upper ocean cells of the reference solution are stronger as well than in the initial state and the coarse resolution experiment: $3Sv$ vs. $1Sv$ and $2Sv$ for the southern and -$2Sv$ vs. -$1Sv$ and -$1Sv$ for the northern Ekman cell. The stronger southern cell indicates the increase in the upwelling near the boundary. The increase in the upwelling for the coarse resolution experiment is compensated by the subsurface downwelling with the magnitude of $1Sv$; thus, the overall mass transport of the southern cell does not change in the coarse resolution experiments. The midlatitudinal Ekman cell is stronger to compensate an increase in the strength of the main overturning cell.

The deep southern cell is absent in the initial state. This fact indicates that the formation of the cell in the reference and coarse resolution experiments is due to internal parameters. The weaker vertical diffusion, $0.3 \cdot 10^{-4}$ $[M^2 \cdot \sec^{-1}]$, is a possible candidate that is responsible for the formation of this strong local cell. The high sensitivity to the vertical diffusivity had been demonstrated before (*Bryan, 1987* [7], *Weaver and Sarachik, 1990* [60]). The impact of this cell on the climatological properties is weak. In the previous section, it was demonstrated that it does not have a signature in the averaged temperature distributions. It does not change positive tendencies in the development of the main overturning cell in the reference simulation.

Heat Transport

Until about 1997 the prevalent view on the role of the horizontal resolution in the simulation of the total heat transport in the climatological experiments was that the total integrated northward heat transport is not sensitive to the changes in the horizontal resolution of the numerical simulation. Experiments using varying horizontal resolution from 4° to 1/3° and 1/6° with a primitive equation model by Semtner (*Semtner and Mintz 1977* [52]), different versions of GFDL model (*Cox 1985* [13], *Böning and Budich 1992* [4]) and the Miami isopycnal model (*Drijfhout 1994* [16]) show in fact that the total northward heat flux is independent of the resolution. For example, Figure 3-7 presents this quantity computed in 1/3° (*Cox 1985*[13]) and 1/6° (*Böning and Budich 1992* [4]) horizontal resolution simulations. The total meridional heat flux distribution is practically the same in both experiments. In addition, *Böning and Budich 1992* [4] point out that the total heat transport in the Cox solution with even lower resolution (1° × 1.2°) remains the same as in much finer resolution simulations. *Bryan, 1986*[11] suggested that due to the weak diabatic forcing in the experiments, the non–acceleration theorem can be applied (*Andrews and McIntyre 1976*[1]) such that there is a cancellation between the heat transport by eddies and the modifications that eddies introduce to the heat transport by the mean circulation.

The recent results of the climatological simulations negate the non–dependence property. *Fanning and Weaver, 1997* [21] performed a set of experiments using the GFDL MOM with varying horizontal resolution in the configuration close to *Cox, 1985* [13]. They demonstrated a significant, about 30%, increase in the total heat transport in the midlatitude area of the domain when increasing the horizontal resolution from 4° to 0.25°.

Figures 3-5(b), 3-9(b) and 3-11(b) show the total meridional heat transport computed in the climatological mean, in the initial state of the reference simulation and in the coarse resolution experiment. The magnitude of the heat flux in the time mean of the reference simulation and its initial state is about the same at $0.16PW$. It is 25% smaller in the coarse resolution experiment. The decrease in the vertical diffusivity coefficient in the coarse resolution experiment compare to the initial state experiment is responsible for the smaller total heat transport.

The profile of the total heat flux in the reference experiment has a different shape as compared to either coarse resolution experiments. It was previously discussed that in addition to the observed maximum around $20°N$ in the southern part of the domain, there is a second mid–latitude maximum with overall increase in heat transport to the North. This part of the domain corresponds to the area of the thermocline deepening of (Figure 3-1(a)) and increase in the spread of the overturning cell at the depth of the thermocline (Figure 3-8(a)).

In order to understand which processes are responsible for the increase in the total heat transport in the midlatitude and the northern regions I perform the decomposition of (3.1) into time variant and steady components according to *Fanning and Weaver, 1997* [21].

Define the following operators for a variable μ

- The time average

$$\bar{\mu} = \frac{1}{P}\int_0^P \mu dt, \tag{3.2}$$

  where P is the length of the data period,

- The deviation from the time average

$$\mu^{'} = \mu - \bar{\mu},$$

- The vertical average

$$\hat{\mu} = \frac{1}{H}\int_{-H}^{\circ} \mu dz, \tag{3.3}$$

  where H is the depth of the model ocean,

- The deviation from the vertical average

$$\mu'' = \mu - \hat{\mu},$$

- The zonal average

$$[\mu] = \frac{1}{L_x} \int_W^E \mu dx, \tag{3.4}$$

  where L_x is the zonal dimension of the model ocean and the integration is from the western to the eastern boundaries,

- The deviation from the zonal average

$$\mu^* = \mu - [\mu] .$$

The decomposition the total heat flux, H_{Total}, into time–dependent and state components is

$$H_{Total} = H_{Eddy} + H_{Mean} = H_{Eddy} + H_{BrtGr} + H_{BrcOv} + H_{BrcGr}, \tag{3.5}$$

where the components are the following: H_{Eddy}, the time–dependent heat transport or the eddy heat transport is computed as the difference between the total heat transport and the heat transport by the mean circulation

$$H_{Eddy} = H_{Total} - H_{Mean} = \widehat{\left[\overline{v'T'}\right]} = \widehat{\left[\overline{vT}\right]} - \widehat{\left[\bar{v}\bar{T}\right]},$$

where $\overline{v'} = \overline{T'} = 0$; H_{BrtGr}, the barotropic gyre heat transport is the zonally integrated heat transport of the vertically averaged temperature by the barotropic velocity

$$H_{BrtGr} = \left[\widehat{\overline{v^*}}\,\widehat{\overline{T^*}}\right] = \left[\widehat{\overline{v}}\,\widehat{\overline{T}}\right],$$

where the mass conservation property was used, $\left[\widehat{\overline{v}}\right] = 0$; H_{BrcOv}, the baroclinic overturning heat transport is the vertically integrated transport of the zonally averaged temperature by the overturning circulation

$$H_{BrcOv} = \widehat{\left[\overline{v''}\right]\left[\overline{T''}\right]} = \widehat{[\overline{v}]\,[\overline{T}]}\,.$$

The baroclinic gyre component is computed as the residual value

$$H_{BrcGr} = \widehat{\left[\overline{v''^{*}T''^{*}}\right]} = \widehat{[\bar{v}\bar{T}]} - \left[\widehat{\overline{v}}\widehat{\overline{T}}\right] - \widehat{[\overline{v}]\,[\overline{T}]}\,.$$

Due to 9600 years of the integration of the coarse resolution experiments, there is no time dependence in the final state of those simulations; thus, the eddy component in (3.5) is equal to zero. Time mean heat transport is equal to the total.

$$H_{Total} = H_{Mean} = H_{BrtGr} + H_{BrcOv} + H_{BrcGr}, \tag{3.6}$$

Figure 3-15 shows the decomposition of the heat transport of the reference experiment into the components (3.5). The total transport is determined mainly by the balance between baroclinic components the overturning, H_{BrcOv}, and the gyre, H_{BrcGr}. The eddy heat transport and the transport by the barotropic gyre modify the balance. The time–dependent transport is about 10% of the total to the South in the latitudinal band between 4°N and 40°N. In the rest of the domain the time–varying transport is weak and has a northward direction.

The same two baroclinic terms form the total heat transport in the coarse resolution experiments. The barotropic gyre transport is insignificant for both experiments. Figures 3-16 and 3-17 show the decomposition of the transport in the initial state and the coarse resolution experiments respectively.

The comparisons of the decompositions of the total heat flux for the fine resolution and coarse resolution experiments reveals that the steady components are responsible for the modifications of the total heat flux in the reference simulation. The time–dependent or eddy component being less than 10% of the maximum can not explain the difference.

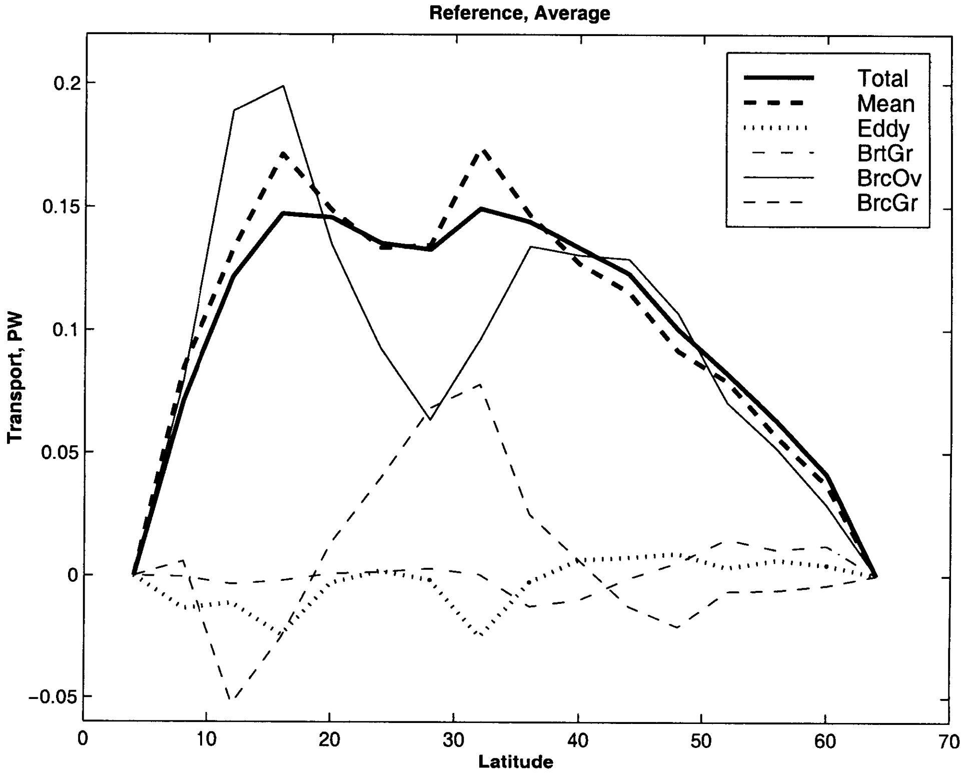

Figure 3-15: The decomposition of the total integrated northward heat transport (*Total*) of the reference experiment into time mean transport (*Mean*), time dependent transport (*Eddy*) and heat transport by the barotropic gyre (*BrtGr*), baroclinic overturning (*BrcOv*) and baroclinic gyre (*BrcGr*) components, [*PW*].

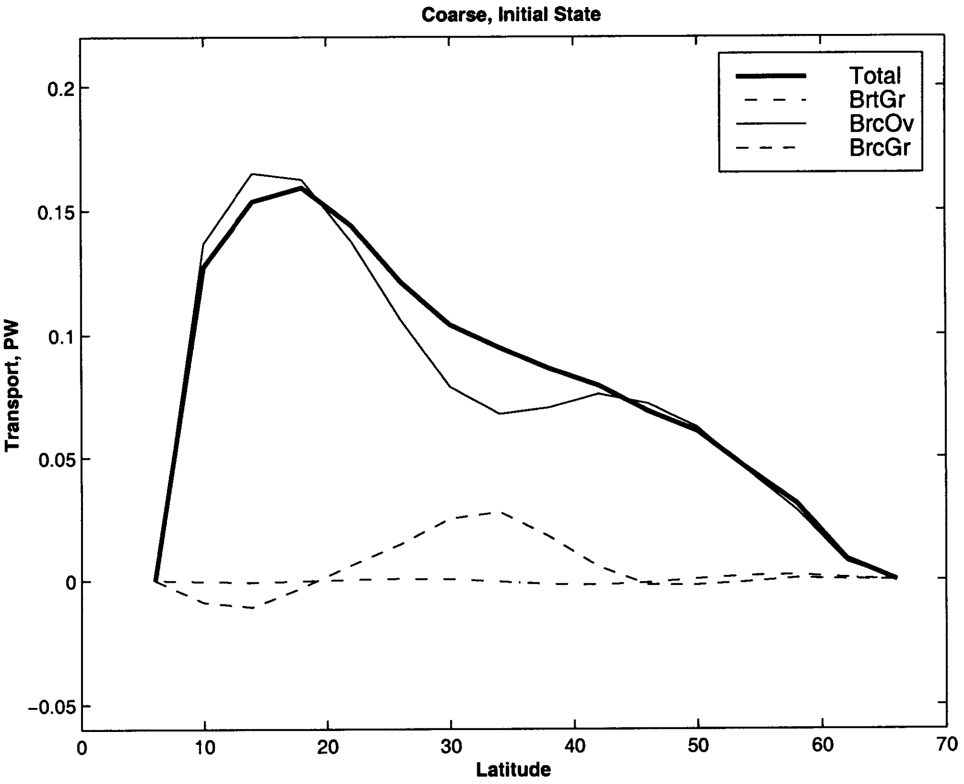

Figure 3-16: The decomposition of the total integrated northward heat transport (*Total*) of the initial state into heat transport by the barotropic gyre (*BrtGr*), baroclinic overturning (*BrcOv*) and baroclinic gyre (*BrcGr*) components, [*PW*].

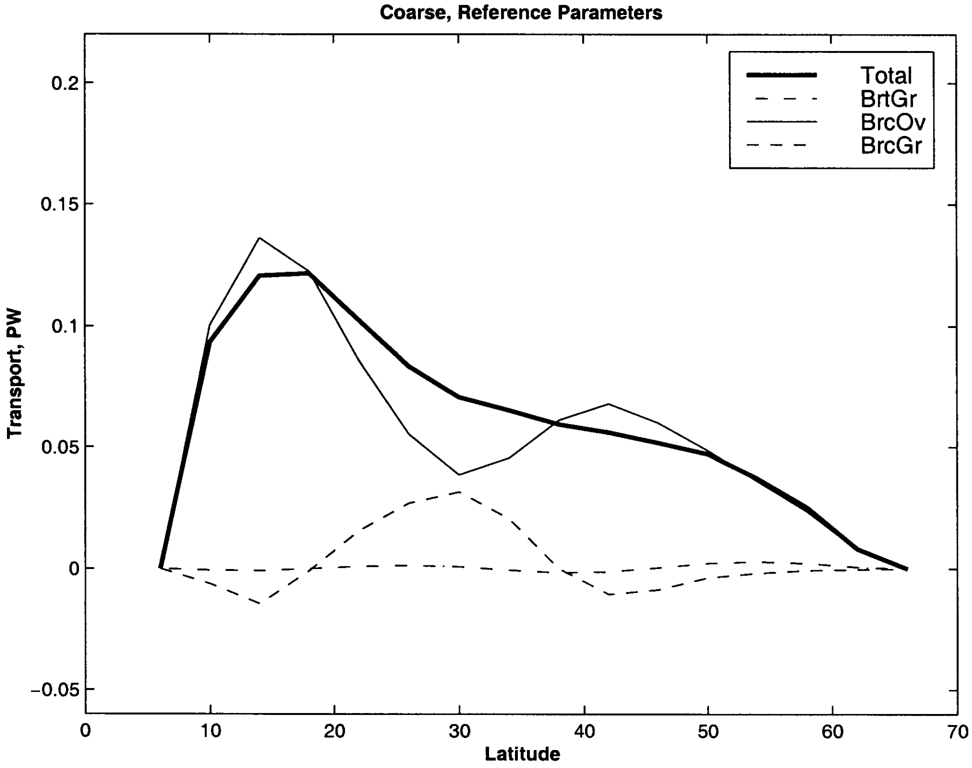

Figure 3-17: The decomposition of the total integrated northward heat transport (*Total*) of the coarse resolution experiment into heat transport by the barotropic gyre (*BrtGr*), baroclinic overturning (*BrcOv*) and baroclinic gyre (*BrcGr*) components, [*PW*].

The barotropic gyre component in the eddy resolving simulation is even weaker. The largest modifications are in the baroclinic components.

In the analysis of the reference (Figure 3-15) and the initial state (Figure 3-16) experiments consider three regions of the profile that are divided by the $20°N$ and $35°N$ latitudes. The southern part shows increase in the magnitude of both baroclinic components such that the total sum of H_{BrcOv} and H_{BrcGr} is nearly equal to the total heat flux in the initial state. The southward transport by the eddy component decreases the total heat flux by $0.02PW$ for this region. Thus, for this area the time–dependent component of the heat flux is responsible for the weak modification. In the region between $20°N$ and $35°N$ the baroclinic gyre component, H_{BrcGr}, increases the total heat transport in the reference simulation. The baroclinic overturning component, H_{BrcOv}, has similar magnitude to the initial state. The weak southward eddy heat flux is not sufficiently strong to cancel an additional contribution of the H_{BrcGr}. The strong increase in the baroclinic overturning component in the northern region causes the additional northward heat transport of about 50% in the reference simulation compared to the initial state. All other three components are weak such that to the North of 45° latitude the total heat flux is equal to the heat transport by H_{BrcOv} within less than 5% of the magnitude.

The magnitude of the total heat transport in the coarse resolution experiment (Figure 3-17) is about 30% smaller than in the other two simulations. The structure of the decomposition is similar to the analysis of the initial state while taking into account the weaker magnitude.

The results of the comparison differ from the observations made by *Fanning and Weaver, 1997* [21]. While the overall increase in the total heat transport in the midlatitudinal region with an increase in the resolution is consistent between the two analyses the reasons behind the increase are different. Fanning and Weaver calculated that the baroclinic gyre component increases the total northward heat flux, while in our estimation the increase is attributed to the baroclinic overturning component. The apparent difference is attributed to the difference in formulation of the experiments resulting in different solutions. While the forcing, the overall length of the experiments and the external parameters are the same, there are differences in the representation of the horizontal mixing: Laplacian in Fanning and Weaver's experiment and biharmonic in the reference simulation.

In addition, the reference experiment differs from the cited above simulations in the formulation. The external parameters of all experiments are similar. The most significant difference lies in the initialization and the execution of the experiment. The time mean of the reference experiment is compared to its initial state, obtained from a coarse resolution simulation with a typical 4° horizontal resolution for a climate experiment. The other simulations quoted use instead a much finer horizontal resolution of the order of 1°. The length of our reference integration is moreover longer than any of the other experiments. *Cox 1985*[13] performed a simulation 24 years long after initialization. *Böning and Budich 1992*[4] simulation is about 9 years long. The length of each individual experiment in *Drijfhout 1994*[16] was about 10 years. Finally, the fine horizontal resolution of about $20KM$ has been used previously only during short periods of time. The reference experiment of the thesis had horizontal resolutions between $9.8KM$ and $22KM$. The total length of the integration after the initialization was more than a 100 years.

3.4 Conclusions

The climatological analysis of the reference fine resolution experiment shows the significant improvements in simulating the climate of the model ocean based on the overcoming the deficiencies of the coarse resolution climate simulations. The thermocline in the fine resolution simulation is sharper and has more complex structure. The thermal structure of the ocean develops more stable temperature distribution in the reference simulation with warmer upper layers and cooler deeper ones. The main overturning cell has more realistic structure. Although the strength of the cell does not increase, the southward penetration is larger and the deep part of the cell is shallower. The ocean in the reference experiment transports more heat in the midlatitudinal and the northern areas where there is almost 50% increase compare to the coarse resolution experiments. The better representation of the main overturning cell leads to the improvements in the total heat transport.

The explanation of the improvements in the reference simulation within the framework of the climatological analysis lies in the specifications of the experiment. The finer horizontal resolution as the major difference between the experiments allowed the development of mesoscale processes and the explicit representation of the role of eddies in the establishment of the climatological thermal state. In addition, the longer overall integration allowed a better adjustment of the thermal structure of the thermocline compare to the short length eddy resolving experiments published so far.

Chapter 4

Eddy Heat Flux and the Thermal Balance

4.1 Introduction

Mesoscale motions or eddies provide the largest contribution to the kinetic energy (Figure 1-2) of the oceanic flows. The atmospheric counterpart of the oceanic mesoscale motions, the cyclones, play an important role in the establishment of the climate and requires an explicit resolution in the climatological experiments. The question whether the oceanic eddies and the associated with them heat flux are important in the establishment of the oceanic climatological state is still open. The lack of observations and small number of eddy resolving oceanic experiments are the main explanations. In this chapter I explicitly calculate the contribution of eddies in the establishment of the time mean state or climatological state, and therefore help to understand some aspects of the problem.

Eddies act on the temperature field through the three–dimensional divergent component of eddy heat flux vector. Due to the non–uniform distribution of the forcing and the spherical and bounded geometry of the basin, I expect that time–dependent processes possess different properties in various regions of the basin. For some areas the eddy contribution is important, while for the rest, the time mean terms singularly dominate the balance. I test the eddy parameterization schemes; therefore, it is necessary to identify the areas of the domain where eddy contribution is strong. The criteria for such identification is the relative magnitude of the three–dimensional divergence of eddy heat flux compared to other terms in the thermal balances. The areas characterized by the strong eddy forcing are the parts of the model domain where eddies need accurate representation in coarse resolution ocean climate models.

I start this chapter with the specifications of the time mean thermal balance. Then, I present the procedures for the estimation of terms in the balance. After that, I compute and describe different terms in the balance. In the summary, I identify the areas of the domain where the magnitude of the three–dimensional divergence of eddy heat flux is comparable to leading terms in the balance and what is the overall eddies contribution to the establishment of the thermal state.

4.2 Prognostic Equation for Temperature

The equation that governs the evolution of temperature T is the following

$$\frac{\partial T}{\partial t} + \nabla\left(\overrightarrow{U}T\right) = Q|_{z=0} + F_T + C, \tag{4.1}$$

where the left hand side represents the sum of the evolution of temperature and three–dimensional (3D) divergence of heat flux, and the right hand side is the sum of the diabatic forcing (heating) at the surface, diffusion terms and the generalized term C, representing convection. This equation is one of the prognostic equations as formulated in the MIT General Circulation Model (MIT GCM).

In order to assess the role of eddies in thermal balance, I perform the decomposition of variables in (4.1) into their respective time mean and deviation from the time mean, or the eddy, components

$$\overrightarrow{U} = \left(\overline{\overrightarrow{u}} + \overrightarrow{u}', \overline{w} + w'\right), T = \overline{T} + T', \tag{4.2}$$

where $\overrightarrow{u} = (u, v)$, is the horizontal components of velocity, the time mean operator is defined as $\overline{T} = \frac{1}{P}\int_0^P T dt$, where P is the length of the integration.

Substituting the decomposition (4.2) into (4.1), I obtain the following equation

$$\begin{aligned}\frac{\partial\left(\overline{T} + T'\right)}{\partial t} + \quad & \nabla_H \left(\left(\overline{\overrightarrow{u}} + \overrightarrow{u}'\right)\left(\overline{T} + T'\right)\right) + \frac{\partial}{\partial z}\left(\left(\overline{w} + w'\right)\left(\overline{T} + T'\right)\right) = \\ & \left(\overline{Q} + Q'\right)\Big|_{z=0} + \left(\overline{F_T} + F_T'\right) + C,\end{aligned} \tag{4.3}$$

here given the definition of time mean: $\frac{\partial}{\partial t}\overline{T} = 0$ and ∇_H is horizontal ∇ operator.

Decompose (4.3) into four parts: time mean terms, eddy terms, convection and the remaining terms

$$\nabla_H \left(\overline{\overrightarrow{u}}\,\overline{T}\right) + \frac{\partial}{\partial z}\left(\overline{w}\,\overline{T}\right) - \overline{Q}\Big|_{z=0} - \overline{F_T} + \tag{4.4a}$$

$$\nabla_H \left(\overrightarrow{u}'T'\right) + \frac{\partial}{\partial z}\left(w'T'\right) - \tag{4.4b}$$

$$C + \tag{4.4c}$$

$$\left[\frac{\partial T'}{\partial t} - Q'\Big|_{z=0} - F_T' + \nabla_H\left(\overline{\overrightarrow{u}}T' + \overrightarrow{u}'\overline{T}\right) + \frac{\partial}{\partial z}\left(\overline{w}T' + w'\overline{T}\right)\right] = 0. \tag{4.4d}$$

4.3 Time–Averaged Temperature Balance

If I perform time–averaging of (4.4) over the total length of the time interval P that defines the data collection time, I obtain the following time–averaged temperature equation or the *thermal balance*,

$$\underbrace{\left[\nabla_H \left(\overline{\overrightarrow{u}\,T}\right)\right]}_{\text{MH}} + \underbrace{\left[\frac{\partial}{\partial z}\left(\overline{wT}\right)\right]}_{\text{MV}} + \underbrace{\left[-\overline{Q}\big|_{z=0}\right]}_{\text{DF}} + \underbrace{\left[-\overline{F_T}\right]}_{\text{VD+HD}} + \tag{4.5a}$$

$$\underbrace{\left[\nabla_H\left(\overline{\vec{u}'T'}\right)\right]}_{\text{EH}}+\underbrace{\left[\frac{\partial}{\partial z}\left(\overline{w'T'}\right)\right]}_{\text{EV}}+ \tag{4.5b}$$

$$\underbrace{\left[\frac{1}{P}\left(\Delta T'\right)\right]}_{\text{TD}}+ \tag{4.5c}$$

$$\underbrace{[-C]}_{\text{RC}}=0. \tag{4.5d}$$

where the forcing terms are

$$\overline{Q}\big|_{z=0} = \lambda\left(T_a-\overline{T}\big|_{z=0}\right), \tag{4.6a}$$

$$\overline{F_T} = k_V\overline{T}_{zz}-k_{bH}\Delta^2\overline{T}, \tag{4.6b}$$

for all variables the definition of the time mean is $\overline{v}=\frac{1}{P}\int_0^P v dt$, for all eddy terms $\overline{v'}=0$, $\overline{T'}=0$ and for the forcing terms $\overline{F_T'}=0$ and $\overline{Q'|_{z=0}}=0$. The label below each term stands for the physical interpretation, which I use in analyzing the thermal balance in following sections. In deriving (4.5c), I use the following integral

$$\overline{\left(\frac{\partial T'}{\partial t}\right)}=\frac{1}{P}\int_0^P\frac{\partial T'}{\partial t}dt=\frac{1}{P}\left[T'\Big|_{t=0}^{t=P}\right]=\frac{1}{P}\Delta T'.$$

The physical interpretation of terms in the balance (4.5) is the following: (4.5a) - time mean balance consisting of 3D divergence of the time mean heat flux: MH - horizontal and MV - vertical, DF - diabatic forcing at the surface (4.6a), VD - vertical Laplacian and HD - horizontal biharmonic diffusivities (4.6b); (4.5b) - 3D divergence of the eddy heat flux: EH - horizontal, EV - vertical; (4.5c) - terms representing the non-stationarity of T or time drift (TD); (4.5d) - convection (RC).

The positive sign of terms in (4.5) signifies a decrease of local temperature in time. The negative sign is the opposite. In the case of small relative magnitude of an individual term, its effect on the tendency in the local value of temperature is small.

4.4 Estimation of Terms in the Time–Averaged Temperature Balance

The identification of the role of eddies in transporting heat requires the estimation of magnitude and geographical distribution of members in (4.5). Some of the terms I can compute directly from the data. This set includes time mean and eddy terms, the forcing of the time mean circulation: diabatic and diffusive, and time drift term. The convective contribution is infeasible to compute exactly from the available data, as it requires the direct estimation from time series of variables at each grid point due to the unknown distribution in time of the convective events.

In order to assess the non-stationarity of temperature state (4.5c), or the *time drift*, I provide the estimation at 40 moorings throughout the basin. I interpolate the estimations on the model grid between nearby stations. For the geographic location of the moorings refer to Figure 2-7. The same time series can help to identify the distribution of possible convection. Unfortunately, this data does not allow the estimation of its magnitude. The sparse moorings time series do not cover all potential convective events.

4.4.1 Time Mean and Eddy Terms

The data required in the computations of (4.5a) and (4.5b) consists of two sets: the time–averaged values of the state variables (u, v, w and T) and time–averaged products of the state variables (uT, vT and wT). The time–averaging of both data sets is defined over the total length of the data run P. I use time–averaged values directly in the evaluation of (4.5a) and (4.5b). In order to estimate the eddy components (4.5c), I apply the definitions of time mean and eddy decomposition (4.2) combining with the properties $\overline{\vec{U}'} = 0$ and $\overline{T'} = 0$. The eddy heat flux is

$$\overline{\vec{U}'T'} = \overline{\vec{U}T} - \overline{\vec{U}}\,\overline{T}, \tag{4.7}$$

where the first term is the time–averaged product of state variables. This term had been accumulated during the model run. The computation of the product term, the second in (4.7), in the model took into account the staggered nature of the model grid. The numerical procedures for the calculations of all terms in (4.5) is presented in the Appendix B.

4.4.2 Non-Equilibrium in Thermal State

Sources of the Non-Equilibrium: *Time Drift*

There is significant intrinsic difference in the time scales required to reach a statistical equilibrium in the dynamical and over-all thermodynamical states. While the former becomes usually equilibrated within a few years in response to a change in external condition, such as the initialization, the latter reaches an equilibrium state on the order of hundreds of years.

The process of the thermal adjustment is not uniform throughout the vertical column (e.g. *Fanning and Weaver, 1997* [21]). The time scale for the upper 500-700M is determined by the propagation of the first baroclinic Rossby wave. For the deeper ocean this time scale is much longer. It is determined by the advection, which is very slow for the deep ocean.

The length of my experiment is 55 years starting after about 50 years of spin-up. Given the length of this period, I can assert that the dynamical state is in near statistical equilibrium with the density structure. The thermal structure at the same time is in a transitional state.

The memory of the thermal state in the areas that are not directly forced has a time scale much longer than the length of the integration. The main processes that control the redistribution of temperature are advection, diffusion and vertical mixing due to convection. The density structure itself controls these processes. Their magnitudes are small in the interior of the ocean and especially for deeper layers partially due to the very small horizontal and vertical variations in the temperature. For example, for two locations with coordinates $(15°E, 10°N)$ and $(15°E, 50°N)$, the difference in temperature between the end and beginning of the simulation at the depth of $3250M$ (layer 13) is $\sim 0.05°C$, while at the depth of $87.5M$ (layer 2) it is $\sim 10°C$ for the same two station.

The adjustment processes have the largest strength in the western boundary and southern areas, where the horizontal advection is the strongest, in the upper layer that is directly forced by the relaxation to the apparent atmospheric temperature and in the northern areas supporting deep convection. Due to the above reasons I can expect a presence of the temperature drift in the local temperature for parts of the domain.

The structure of time series of temperature helps to identify the areas of the domain where the time drift is significant. The upper plot of Figure 4-1 shows the temperature for the upper layer at Station 27 near the western boundary. The time series at this location does not show a drift, only oscillations around some constant value. This area is directly forced by the relaxation to the apparent atmospheric temperature on the short time scale of 30 days. The thermal structure in the quiescent interior (middle plot) contains a clear trend. The magnitude of change is about $1°C$. For the northern part of the domain the typical profile is on the lower panel, and it is similar for other layers. Thus, it demonstrates an efficient vertical exchange in this area of the domain.

The three examples show some of the possible scenarios in the establishment of the thermal structure. The contribution to the thermal balance (4.5) involves the difference in the local temperature between the end and the beginning of the time series. In the following Table 4.1 I am presenting the maximum and minimum differences in temperature for each of the 15 layers.

Given the sign convention in the balance (4.5), the positive difference means warming of the local temperature (positive slope) and the negative - cooling (negative slope). The observations of the ranges from the table 4.1 show the predominant warming in the upper layers (2 to 8), cooling in the deeper layers (12 to 15) and some mixed events for other

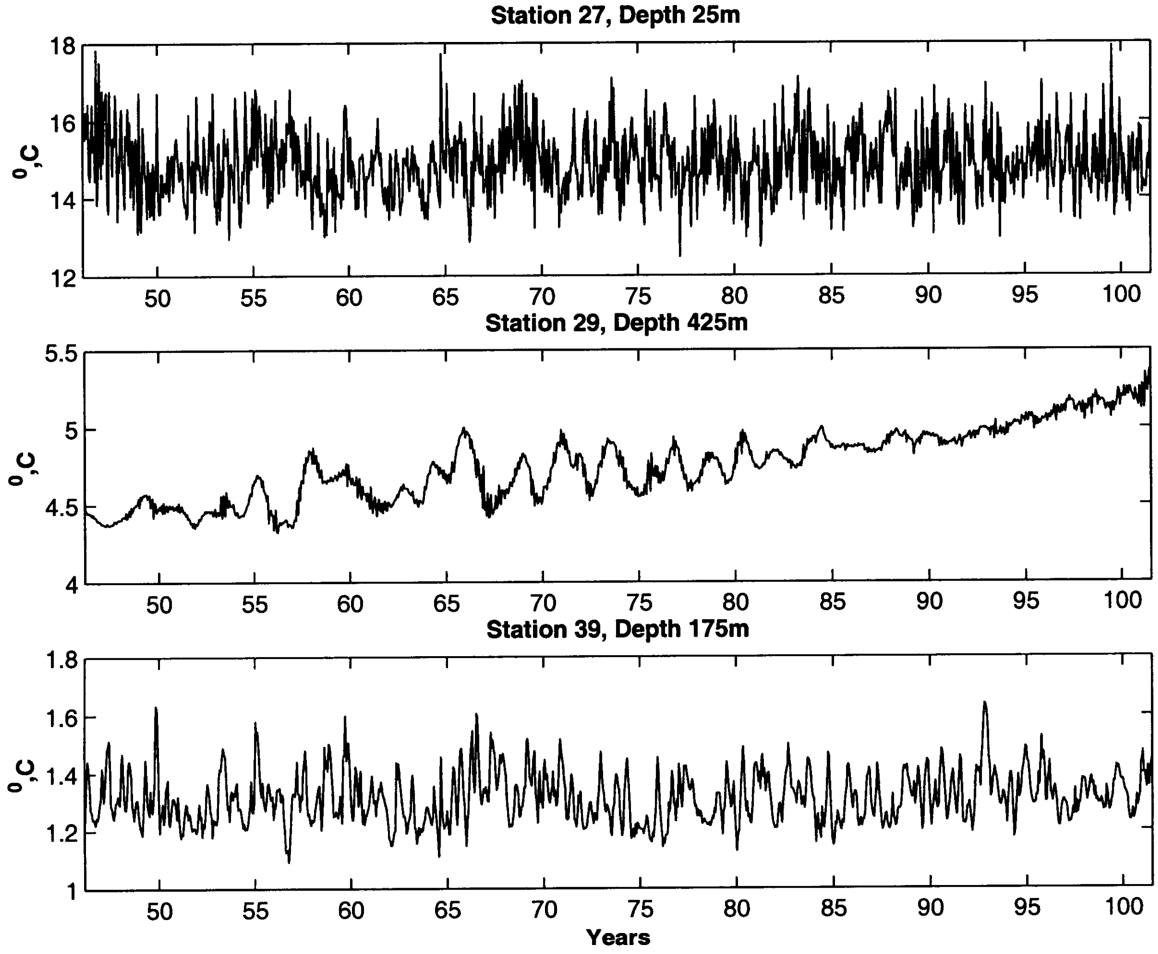

Figure 4-1: Time series of temperature, $[^\circ C]$, for three selected locations and depths. Upper layer in the western boundary area (upper panel). Thermocline in the interior (middle panel). Northern station (lower panel).

Layer	min $\left(\Delta T'\right), ^\circ C$	max $\left(\Delta T'\right), ^\circ C$
1	-1.17 (22)	1.15 (26)
2	-1.12 (28)	1.83 (29)
3	-1.25 (21)	2.03 (26)
4	-1.24 (17)	2.23 (26)
5	-0.853 (17)	1.55 (26)
6	-0.431 (22)	1.10 (12)
7	-0.142 (17)	0.609 (34)
8	-0.0576 (8)	0.445 (35)
9	-0.0575 (9)	0.140 (40)
10	-0.0710 (5)	0.0902 (40)
11	-0.0774 (5)	0.0364 (40)
12	-0.0845 (5)	-0.0135 (25)
13	-0.0958 (35)	-0.0174 (15)
14	-0.101 (35)	-0.0202 (15)
15	-0.102 (35)	-0.0198 (15)

Table 4.1: Range of difference in temperature for 40 stations for each layer

layers. In order to identify the geographical distribution of time drift I look at horizontal distribution of $\Delta T'$ for each layer. This analysis allows to quantify the contribution of the non-equilibrium in thermal state to the time mean and eddy balance.

Contribution to the Thermal Balance The evaluation of thermal time drift contribution to the balance (4.5) requires the identification of difference in temperature at the end and beginning of the data run, for each grid point. The exact calculation of this term requires the data about the instantaneous temperature field at the iterations 1572672 and 3529536. They are the first and the last iterations of the period during which the data were averaged. The data from these iterations is not available due to the technical reasons; therefore, the only possible solution is an approximate estimation of this term from available data. There are two ways for the calculation: from spatially sparse time series of temperature and from the closest to the above in time available temperature fields. The benefit of the first method lies in the exact spanning of the time period, while for the second method it is in the coverage at each model grid point. Although due to the variability on short time scales (Figure 4-1), the drift can be determined if it is larger than this variability. Below I estimate the non-stationarity term using both methods and compare the results.

Estimation from the Time Series The available data consists of time series of temperature for each of the 40 stations. I linearly interpolate the estimations from these selected locations to the grid of the model. For the boundary conditions, I assume the constant from a boundary point to its nearest station. As an example demonstrating this procedure, I present the calculations for the thermocline layer 5. First, Figure 4-2 shows the time drift for each station at this layer. The values are mostly positive,

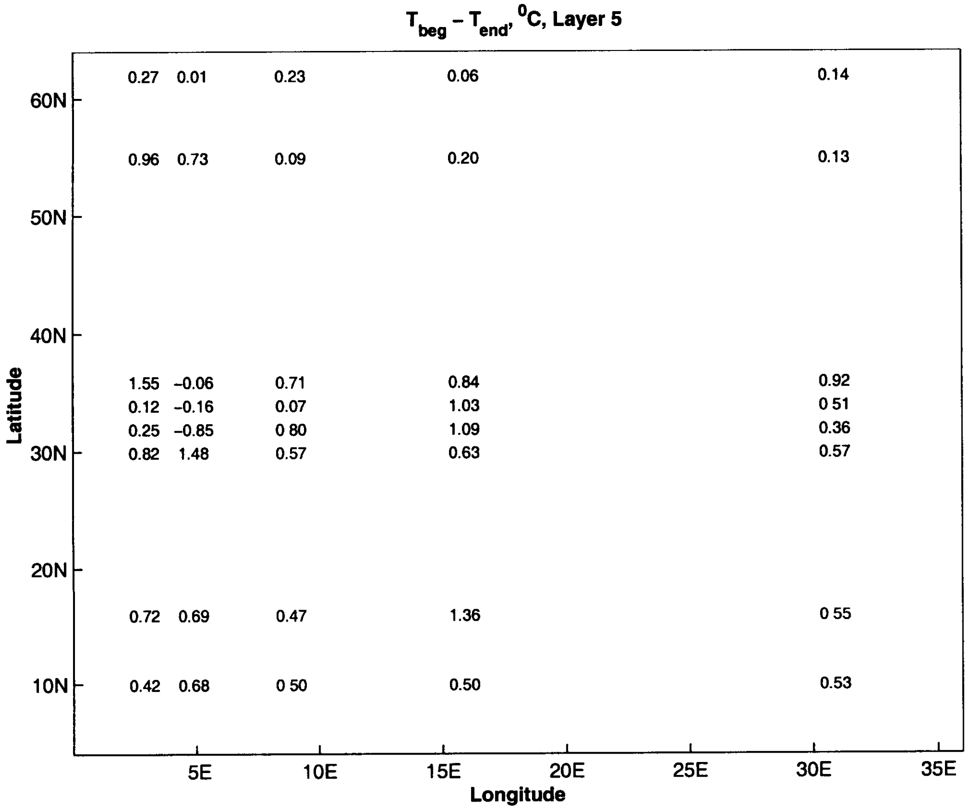

Figure 4-2: Difference in temperature between the end and the beginning of the simulation, $[°C]$. Layer 5. Each number represent a value for the respective station.

except around 5°E near the western boundary, where there is a local cooling. The contribution to (4.5) involves dividing the values above by the length of the interval in seconds ($\sim 1.5 \cdot 10^9$ sec). The contour plot in Figure 4-3, interpolated to the model grid, shows the role of non-equilibrium in temperature in the thermal balance. The same analysis has been performed for each of the fifteen layers.

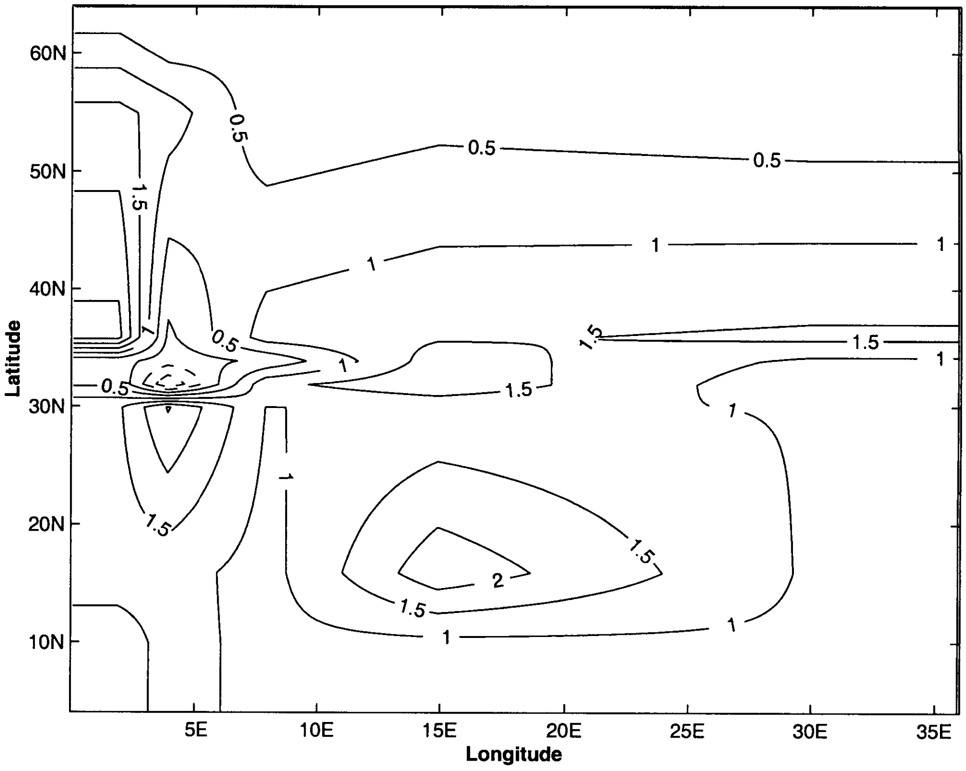

Figure 4-3: Contribution to the temperature balance of the local time–drift. Estimation from the time series, $10^{-9}\,[°C \cdot \text{sec}^{-1}]$ for layer 5.

The magnitude of the time drift for the thermocline layer has an order of $2 \cdot 10^{-9}$ $[°C \cdot \text{sec}^{-1}]$. It has similar value for all of the upper layers, as the amplitude of the temperature difference, see Table 4.1, varies between $-1.25°C$ for the third layer at the station 21 to $2.23°C$ for the fourth layer at the station 26, similar to the layer 5.

Estimation from the Temperature Field The nearest saved fields to the required iterations are the iterations 1304580 and 3491712, which is about one year ahead of the beginning and end of the data period. Figure 4-4 shows the direct estimation of the non–stationarity as the difference between the end and beginning temperature divided by the total length of the time period for each grid point for the 5th layer.

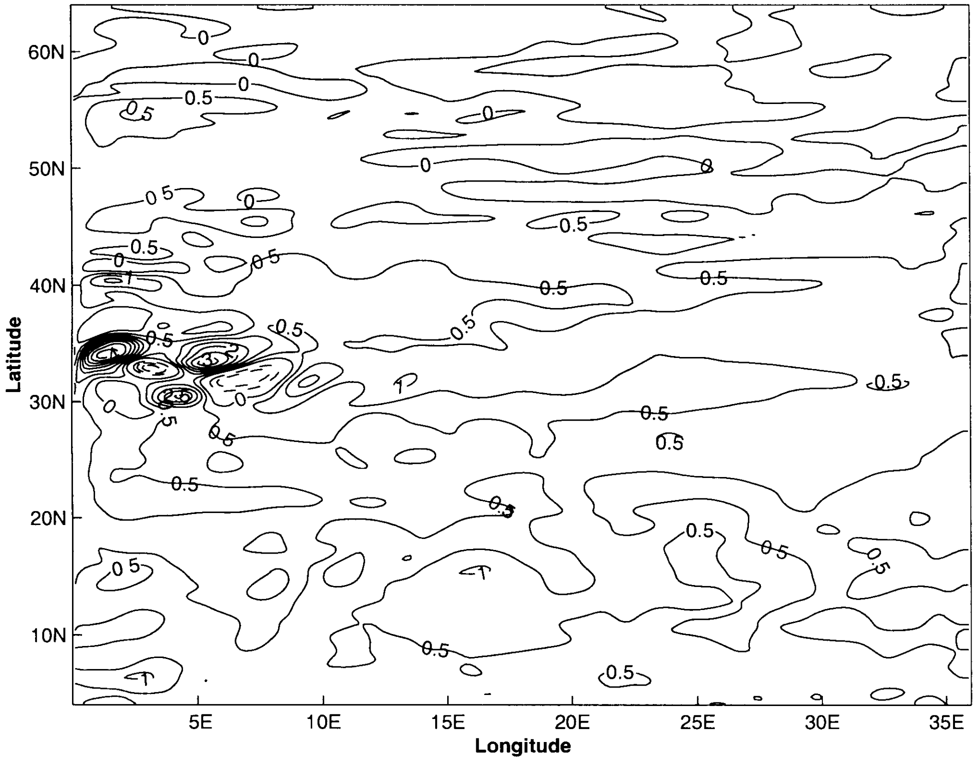

Figure 4-4: Contribution to the temperature balance of the local time–drift. Estimation from the temperature fields at iterations 1304580 and 3491712, 10^{-9} $[°C \cdot \text{sec}^{-1}]$ for layer 5.

The maximum values of the magnitude of the term is less than $5 \cdot 10^{-9}$ $[°C \cdot \text{sec}^{-1}]$. Overall, the magnitude and the location of the strongest time drift is similar. The largest values are in the vicinity of the western boundary current, where the meandering of the thermal front causes the biggest local variations in temperature. The difference from the estimation with the time series is due to the short time scale variability. Figure 4-1 shows the variability that can be of the order of few degrees on a time scale less than a year, that is about $2 \cdot 10^{-9}$ $[{}^{\circ}C \cdot \sec^{-1}]$.

Magnitude of the Time Drift The magnitude of the non–stationarity is less than $5 \cdot 10^{-9}$ $[{}^{\circ}C \cdot \sec^{-1}]$ for the fifth layer and is of the similar values for the upper layers. It is an order of magnitude smaller for deeper layers due to smaller variations in temperature. In the following sections, I demonstrate that the time drift contribution to the thermal balance is 2 to 3 orders of magnitude smaller than other terms in (4.5).

4.4.3 Convection

The numerical algorithm that is involved in the time–stepping of the model equations occasionally creates areas with unstable vertical stratification. These events occur when the temperature of the volume above a current one is cooler. Given the linear equation of state, the stratification of the water column becomes unstable. In nature, this situation causes a continuous convective vertical exchange until the water column reaches neutral stratification. In the model, the convective adjustment mechanism is responsible for maintaining the stability. It periodically searches the domain for these events and vertically mixes volumes of fluid.

There are two connected phenomena which can cause the stratification to become unstable. The first one is the strong diabatic surface cooling. Naturally, this process occurs in the areas where the upper layer exchanges properties with the significantly cooler atmosphere. It takes place in the northern part of the domain. Right from the beginning of the integration the stratification was marginally stable through most of the vertical column. This tendency continues in the model run, causing deep ocean convection. The second cause can be connected with the different time scales in the temperature exchange between the upper layer and atmosphere and between underlining layers. While the former is fixed to be equal 30 days, the latter can be significantly longer, being established by much slower processes such as vertical diffusion and vertical divergence of heat flux. I anticipate this disparity can cause upper layer convection in the areas of fast horizontal currents, such as the vicinity of the western boundary in the midlatitude region. Suppose water from the South is being brought with the fast western boundary current in the upper two layers to midlatitudes. As the difference in temperature between the first and second layers initially is small, fast cooling at the surface can cause convection.

The exact contribution of convection to the balance (4.5) is impossible to compute from the data collected, as it requires the exact location of the convective events, and the amount of heat that being redistributed. In the case of deep convection, this process works by continuously taking the heat out of the whole vertical column, thus affecting time–dependent balances, while in the areas of the shallow upper layer convection just redistributes heat locally between thin upper layers. In the following analysis I demonstrate different types of convective events. I plot the temperature difference between two layers during a 5 years interval from 20.5 to 25.5 years. If the difference is zero, it means the column between the two layers is neutrally stratified at that particular time, or a convective event occurred. The positive difference means stability.

Deep Ocean Convection

The upper panel of Figure 4-5 shows the temperature differences between layers 1 ($25M$) and 5 ($425M$), the lower panel between layers 5 and 10 ($1885M$) for the station 37 located in the northern part of the domain.

During most of the 5 year period the vertical column was neutrally stable between layers 1 and 5. The stratification is stable between layers 5 and 10. There is only one very strong convective event in the vicinity of year 25, when the column was well mixed from the surface to a deeper layer ($1885M$). The stratification during the whole length of the integration exhibits similar behavior: the presence of convective events, which span at least the upper $500M$, during the significant portion of the integration with

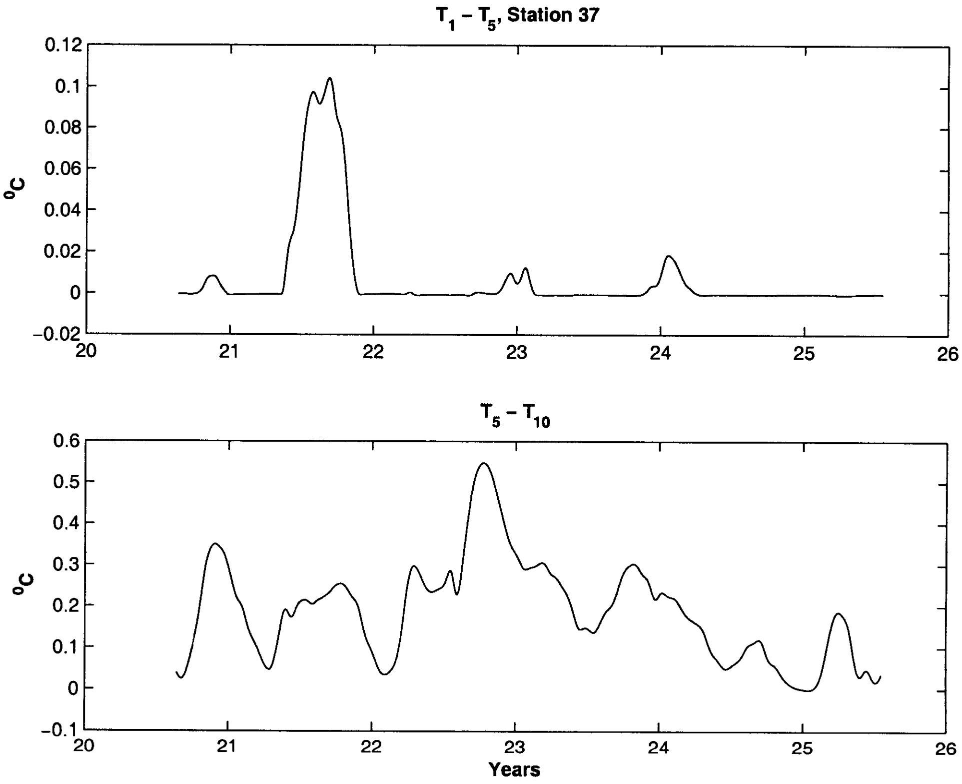

Figure 4-5: Convective events. Station 37. Northern part of the domain. Difference in temperature [$^\circ C$] for layers 1-5 ($25M$-$425M$) upper panel, 5-10 ($425M$-$1885M$) lower panel.

occasional deep convection from the surface to at least as deep as 2000M. Even though the data I have does not allow an exact computation of the role of convective adjustment in the balance (4.5), these arguments suggest an important role of the convection for the northern part of the domain.

Upper Ocean Convection

The following Figure 4-6 presents the temperature differences for the layers 1-2 (25M-87.5M) and 2-3 (87.5M-175M), respectively, for the midlatitude Station 27 in the vicinity of the western boundary.

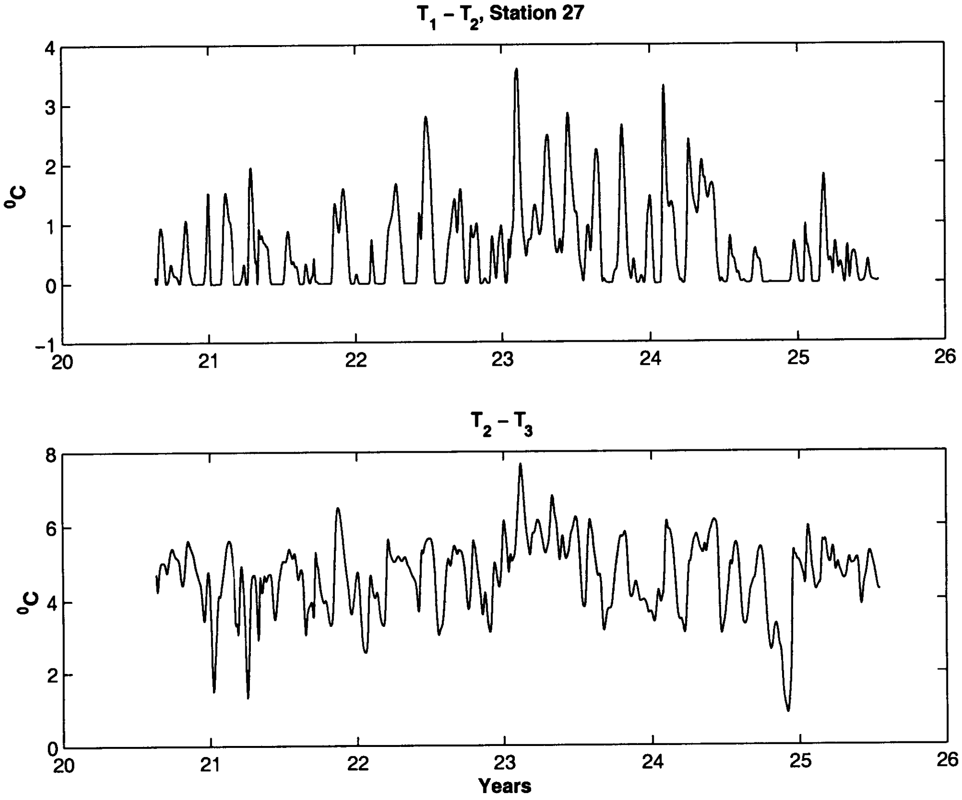

Figure 4-6: Upper layers convection. Station 27. Difference in temperature [°C] for layers 1-2 (25M-87.5M) upper panel, 2-3 (87.5M-175M) lower panel.

For the upper two layers the difference periodically drops to 0°C showing episodes of convection. These events span the two upper layers, while at the same time the stratification between the second and third layers is always stable. This process shows the redistribution of temperature between the directly forced upper layer and the indirectly forced subsurface layer. I anticipate that the upper ocean convection plays an important role in the balance of the upper two layers in the midlatitude areas of strong diabatic forcing.

Stable Stratification

Going further to the South, Station 7, Figure 4-7, I expect the stratification to be stable at all times; therefore, the convective events are absent. Indeed, the difference is always significant and equal about $5°C - 7°C$.

This observation demonstrates that there are no convective events in the Southern part of the domain. Subsequently, there is no convective contribution to the balance (4.5).

4.5 Horizontal Averaging

There are two issues which might require horizontal averaging. The first is the presence of a numerical noise due to the application of a ∇ operator. The second has a deeper meaning and is connected with the ultimate question I am addressing: do the proposed eddy heat flux parameterization work? This question is posed in the frame of coarse resolution climate models. The spatial grid of such models is of the order $2°$ to $4°$. This size determines the horizontal dimensions of features that it is possible to reproduce in coarse resolution climate models.

The first term that I compute is the horizontal divergence of the heat flux by the mean flow. I anticipate that this term has the largest magnitude. Figure 4-8 shows the cross-section at $5°E$ for layer 2. The presence of fine–scale oscillations is most obvious in the southern part of the domain. What is the nature of this oscillations?

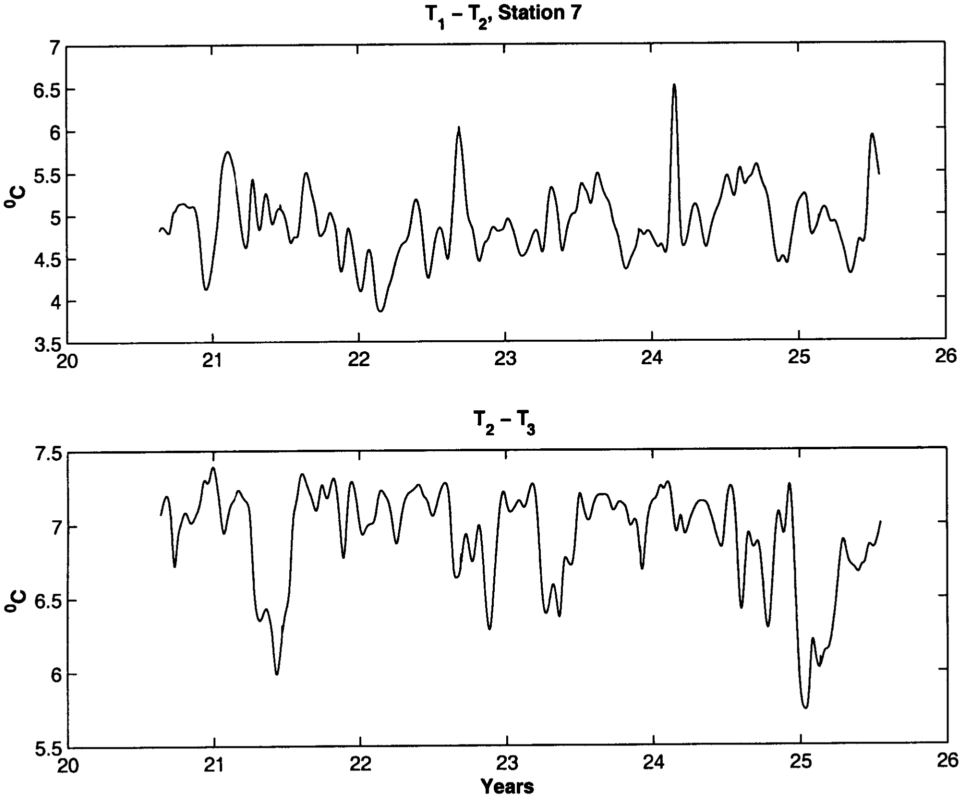

Figure 4-7: Stable stratification during the whole length of the simulation. Station 7. Temperature difference, [°C], for layers 1-2 (25M-87.5M) upper panel, 2-3 (87.5M-175M) lower panel.

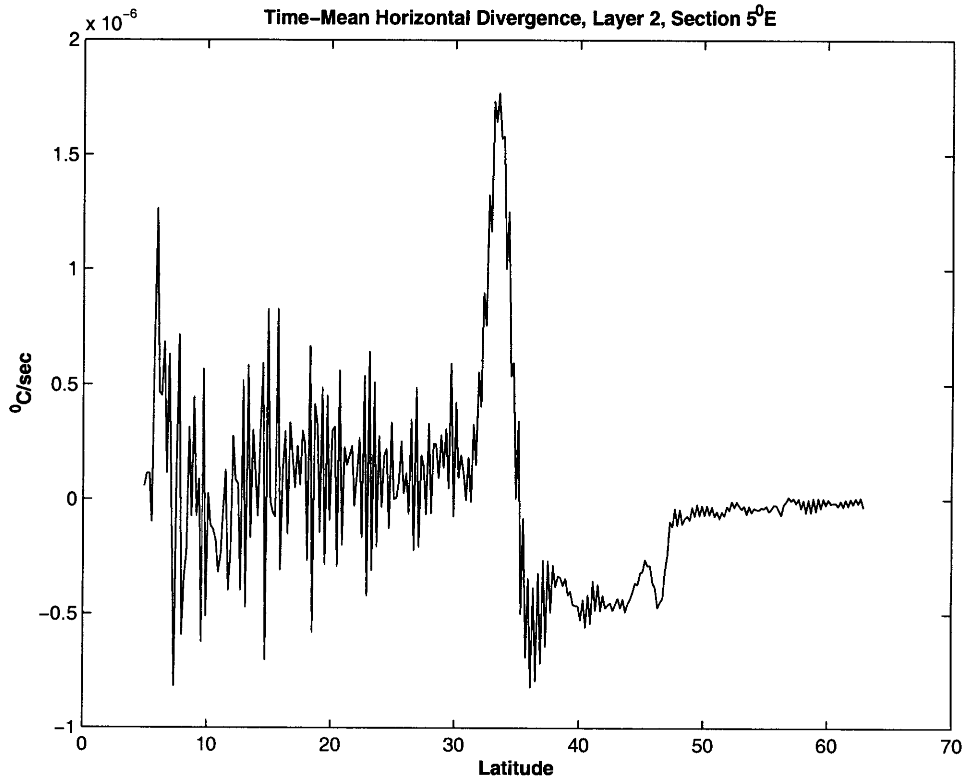

Figure 4-8: Cross-section at 5°E of horizontal divergence of the time mean heat flux for layer 2.

If I zoom on a smaller area of the section Figure 4-9 it is possible to identify the 2-grid period in the noise structure. This observation suggests the numerical nature of the noise due to the application of the ∇ operator. To remove the artificial oscillations I perform some form of a local spatial averaging, that preserves the important large–scale structures.

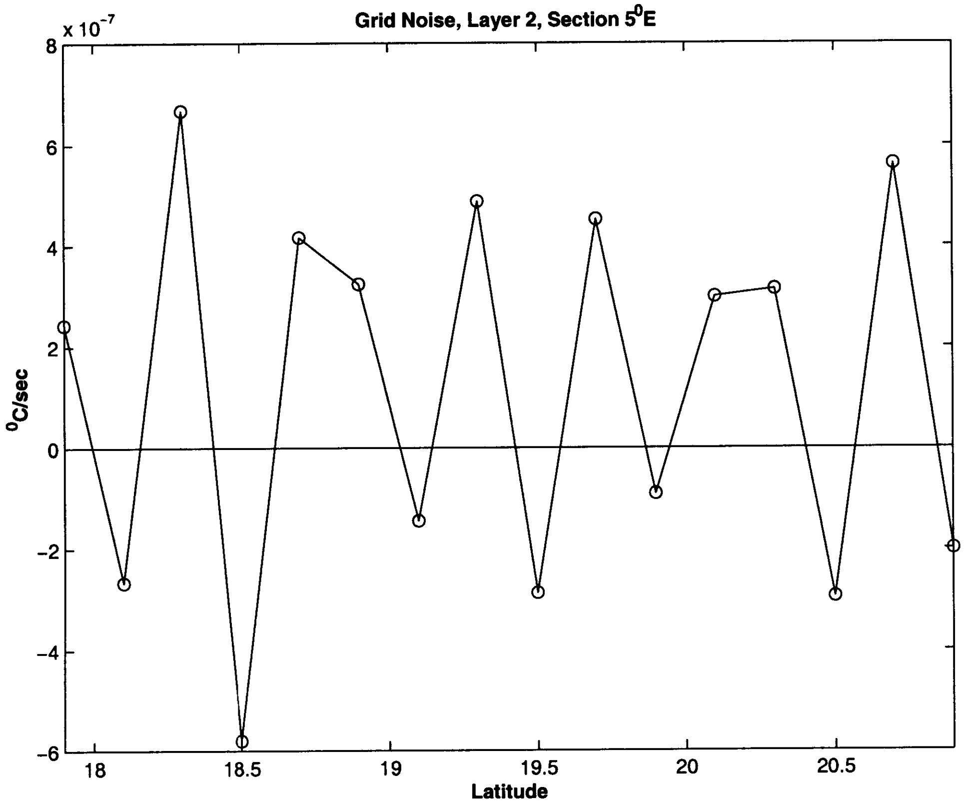

Figure 4-9: Noise in the computations of the time mean horizontal divergence. Part of the 5°E cross-section for layer 2.

The natural way of implementing the spatial averaging is to perform a moving average over a square with the size $M \times M$ according to the following formula

$$v_M(i,j) = \frac{1}{M^2} \sum_{i'=i-M/2}^{i+M/2} \sum_{j'=j-M/2}^{j+M/2} v(i',j').$$

In order to identify the required dimension M, I perform a series of moving averages ranging from 1° to 4°. This range spans a typical resolution of a climate model. The larger size is more efficient to remove fine scales oscillations, but it can significantly smooth out the physical features. Figure 4-10 demonstrates the use of moving averaging on the horizontal divergence of the time mean heat flux for an area in the vicinity of the western boundary current for the second layer.

The 1° averaging significantly smooths out the grid noise while preserving the larger–scale structures. The positive anomaly is centered at the same location around $(5°E, 33°N)$. There is a decrease in magnitude from $2.3 \cdot 10^{-6}\,[°C \cdot \mathrm{sec}^{-1}]$ to $1.8 \cdot 10^{-6}\,[°C \cdot \mathrm{sec}^{-1}]$ The situation is similar for the negative anomalies. As expected the 2° operator decreases the magnitude of larger peaks by almost a half while preserving the general geographical distribution of anomalies. When I increase the averaging box to even larger size 4°, a qualitative change occurs. The local positive anomaly completely disappears from its original location. There is a new weak positive anomaly to the south–east of the old one due to the contribution from the meridional band between $[0°E, 2°E]$ which is not shown on the plots. The negative anomaly in the immediate vicinity of the western boundary, although still present, is much weaker: $-0.8 \cdot 10^{-6}\,[°C \cdot \mathrm{sec}^{-1}]$ from the original $-4.8 \cdot 10^{-6}\,[°C \cdot \mathrm{sec}^{-1}]$. This result is important as it shows that 4° resolution of the majority of ocean climate models is too crude for the simulation and actually changes dramatically the distribution of properties. The above analysis suggests that the resolution of between 1° and 2° is required to reproduce the gross features of the horizontal divergence of the time mean heat flux. Below I perform the analysis using 1° moving average.

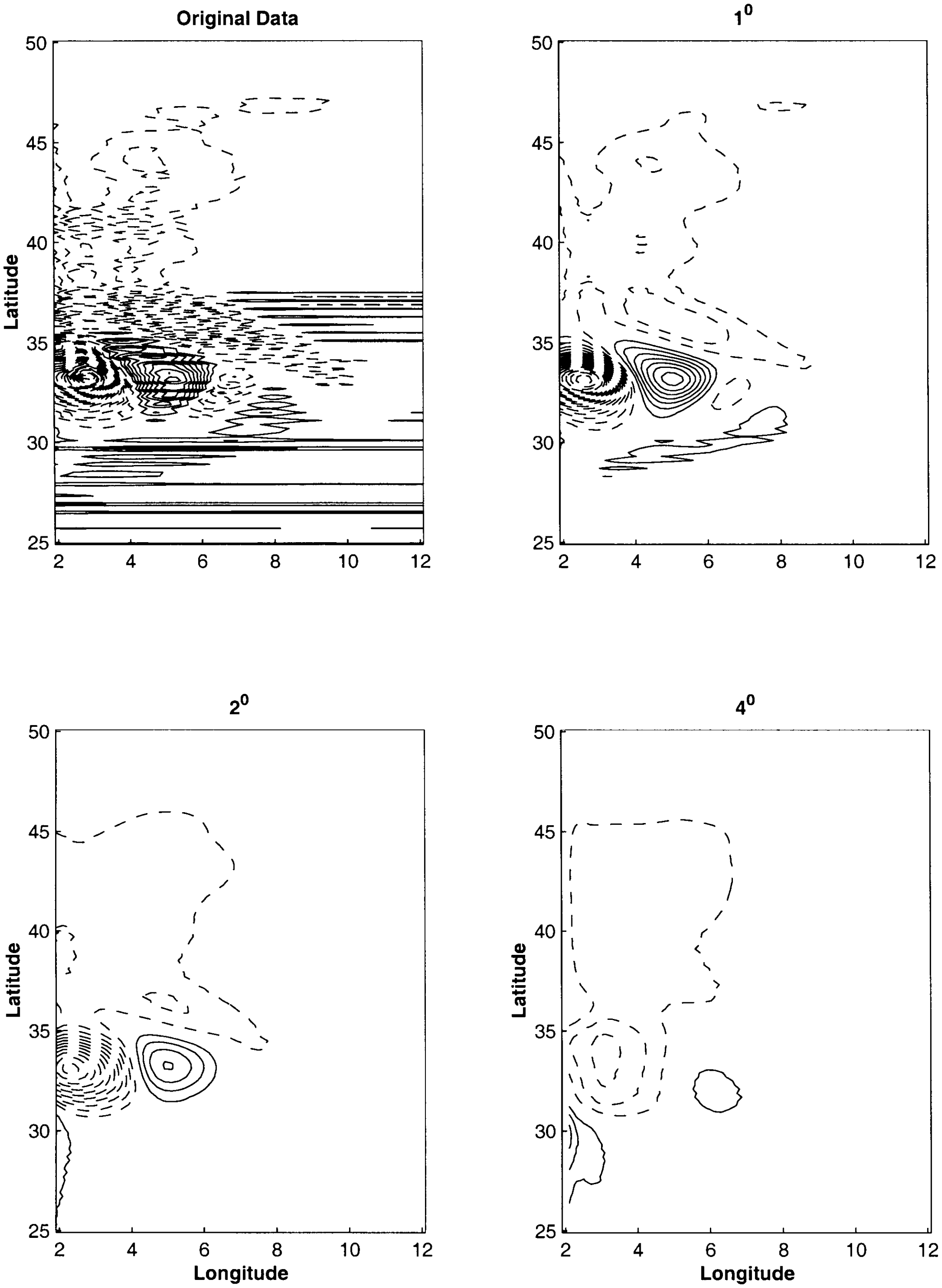

Figure 4-10: Effects of moving averaging. Horizontal divergence of time mean heat flux for an area in the layer 2. Original data (upper left) and averaged data with the box size of 1°(upper right), 2°(lower left) and 4°(lower right). Dashed contours are negative. C.I. $2.5{\cdot}10^{-7}\,[°C \cdot \mathrm{sec}^{-1}]$.

4.6 Balances in the Time–Averaged Temperature Equation

The large number of terms in the balance (4.5) complicates the analysis of the equation. In order to identify the role of eddy heat flux in the balance I compute the individual contribution of each term. Then I isolate areas of the domain where eddies provide a significant contribution to (4.5). The analogy with ocean observations suggests the different role of the divergence of eddy heat flux in various areas of the simulated domain. In the western boundary area in the midlatitude of the basin I anticipate the strongest eddy signal. For the quiescent interior regions the eddy activity is weaker. Deep ocean convection dominates the northern areas. I analyze these areas through a series of South-North cross-sections through the basin for 3 vertical layers: 1, 2 and 5 with their centers at $25M$, $87.5M$ and $425M$ respectively. The sections examine the western and interior regions of the basin. Below, I describe the balances for these sections with the goal of identifying the major patterns of distributions.

The magnitudes of horizontal diffusion (HD) in (4.6b): $10^{-8} - 10^{-9}\,[{}^{\circ}C \cdot \mathrm{sec}^{-1}]$ and the time drift (TD) in (4.5c): $10^{-9} - 10^{-10}\,[{}^{\circ}C \cdot \mathrm{sec}^{-1}]$, are much small than other terms throughout the cross-section. I exclude them from the graphs because if I plot them on the same scale as the larger magnitude terms they are indistinguishable from zero.

4.6.1 Layer 2

The $75M$ thick second layer is not directly forced, although it exchanges properties with the upper layer through the divergent components of the time mean and eddy heat fluxes, vertical diffusion and convective mixing.

Western Section at $5°E$

From Figure 4-11 I observe that the major terms in the balance are 3D divergence of the time mean and eddy heat fluxes[1] and convection. The vertical mixing with a magnitude less than $10^{-7}\,[°C \cdot \mathrm{sec}^{-1}]$ is much smaller throughout the basin. The diabatic forcing is absent. I can identify five areas with the different relative contribution of terms: $4°N - 12°N$ - balance between 3D time mean divergence and horizontal eddy divergence; $12°N - 32°N$ - balance between horizontal and vertical divergences of time mean flow, i.e. almost non-divergent heat flux; $32°N - 36°N$ - 3D time mean and eddy divergencies, $36°N - 50°N$ - 3D time mean and horizontal eddy divergence and convection; $50°N - 64°N$ - weak horizontal time mean divergence and convection. The most important features are the relatively strong contribution of eddy heat flux in the midlatitude and strong convective forcing (cooling) to the North of this area.

Interior Section at $15°E$

The balance in Figure 4-12 is maintained predominantly by 3D time mean divergence, convection and horizontal eddy divergence. There are three distinctive areas: $4°N - 20°N$ - 3D time mean and horizontal eddy divergencies; $20°N - 42°N$ - balance between horizontal and vertical divergences of time mean flow, i.e. almost non-divergent heat flux; $42°N - 64°N$ - time mean horizontal divergence and convection. Eddies play a role in the balance mostly in the southern part. The vertical derivative of the eddy heat flux is small throughout the section.

4.6.2 Upper Layer

The model ocean is directly forced through this layer. Both the wind and the relaxation to the apparent atmospheric temperature act on this layer. This is the most dynamically

---

[1] From this point forward, I call 3D divergences of time-mean heat flux and eddy heat flux as 3D time-mean and eddy divergences respectively.

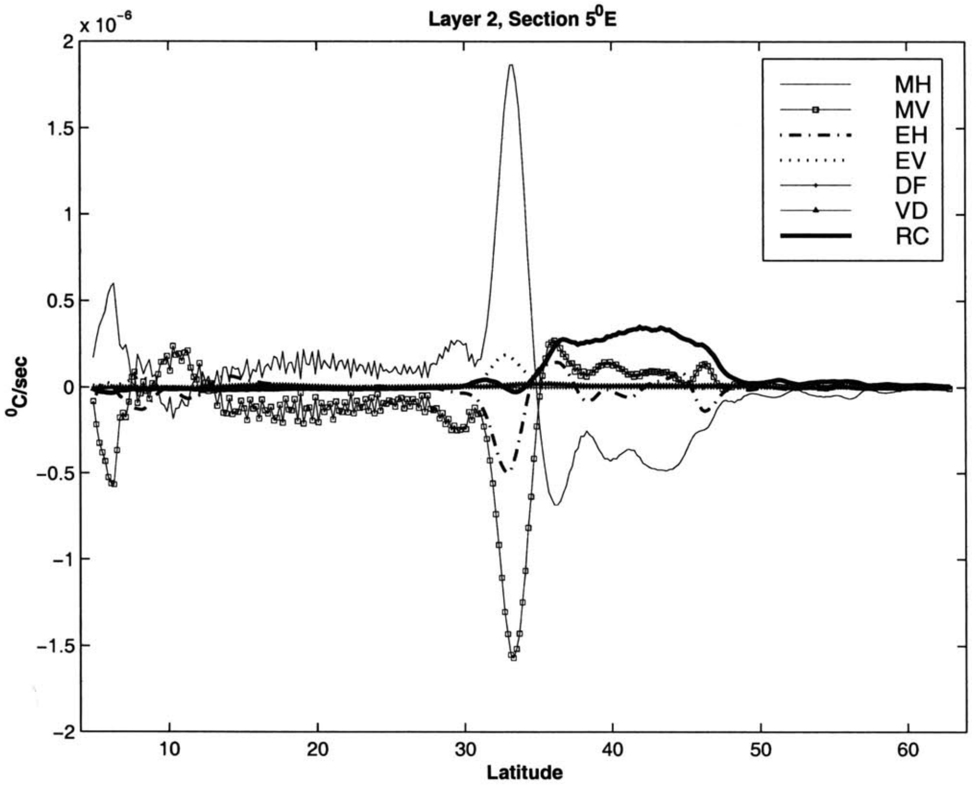

Figure 4-11: Balances in the temperature equation. Layer 2. Section at 5°E. MH - horizontal divergence of time-mean heat flux, MV - vertical derivative of time-mean flux, EH - horizontal divergence of eddy heat flux, EV - vertical derivative of eddy heat flux, DF - restoring diabatic forcing, VD - vertical diffusion, RC - residual implied convection.

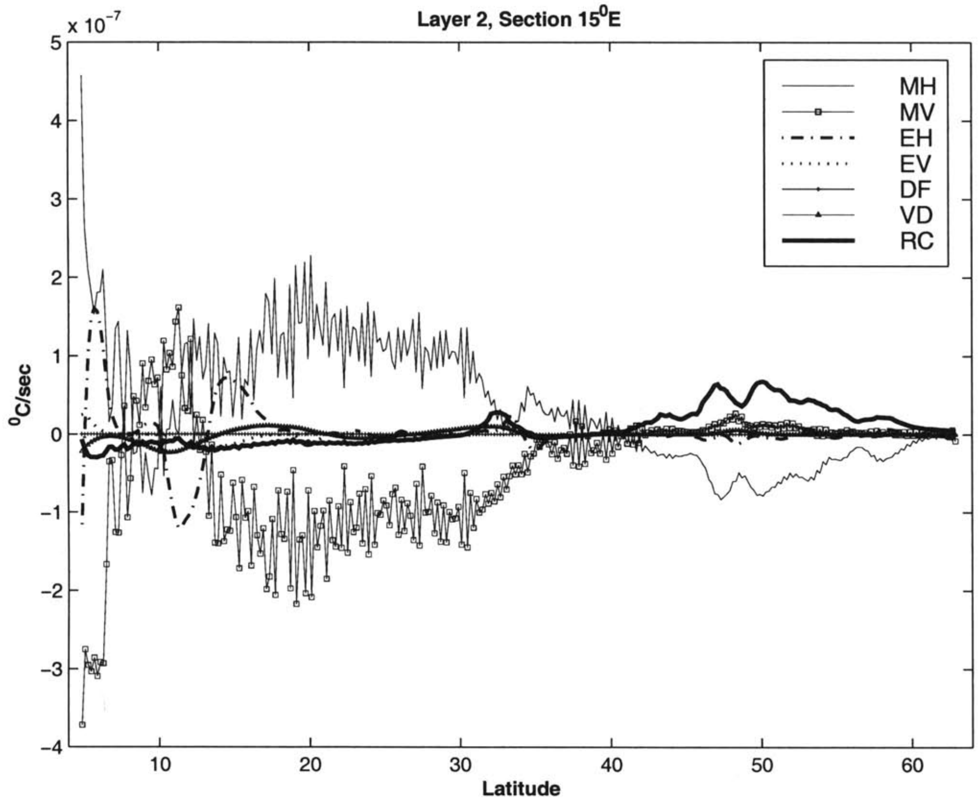

Figure 4-12: Balances in the temperature equation. Layer 2. Section at 15°E. MH - horizontal divergence of time-mean heat flux, MV - vertical derivative of time-mean flux, EH - horizontal divergence of eddy heat flux, EV - vertical derivative of eddy heat flux, DF - restoring diabatic forcing, VD - vertical diffusion, RC - residual implied convection.

active layer. Given the constant-in-time wind forcing and the relatively short relaxation time scale of 30 days for the diabatic forcing, I can expect that this layer is in near equilibrium with both the apparent atmosphere and the underlining ocean layer.

Western Section at $5°E$

The contribution to the balance (Figure 4-13) is very similar to the second layer, except that the diabatic forcing provides the strongest contribution in the sub-section between $32°N$ to $50°N$. The other prominent feature is strong convective signal in the same band, which suggests the connection between the diabatic forcing and convection. Its magnitude and distribution is similar to the second layer convection. The sign is opposite. The total sum of convective signal from the layers 1 and 2 is small suggesting the redistribution of heat between the two layers. The other specific feature is the moderate contribution from vertical diffusivity in the southern part of the domain.

Interior Section at $15°E$

The balance in (Figure 4-14) is similar to the corresponding section from the second layer: major contribution from 3D time mean divergence. In addition there is a moderate cooling due to vertical diffusion in the lower half of the section. The presence of the diabatic forcing changes the picture for the northern part of the domain where it causes convection for the northern part. The other interesting feature is the balance between diabatic cooling and 3D time mean divergence between $32°N$ to $42°N$. Eddy heat flux does not contribute a significant amount to the balance except a small local contribution around $5°N$ and $25°N$.

4.6.3 Layer 5

This layer, that spans depths from $350M$ to $500M$, is located within the main thermocline. It is not directly forced. The temperature slowly evolves, driven by divergent components

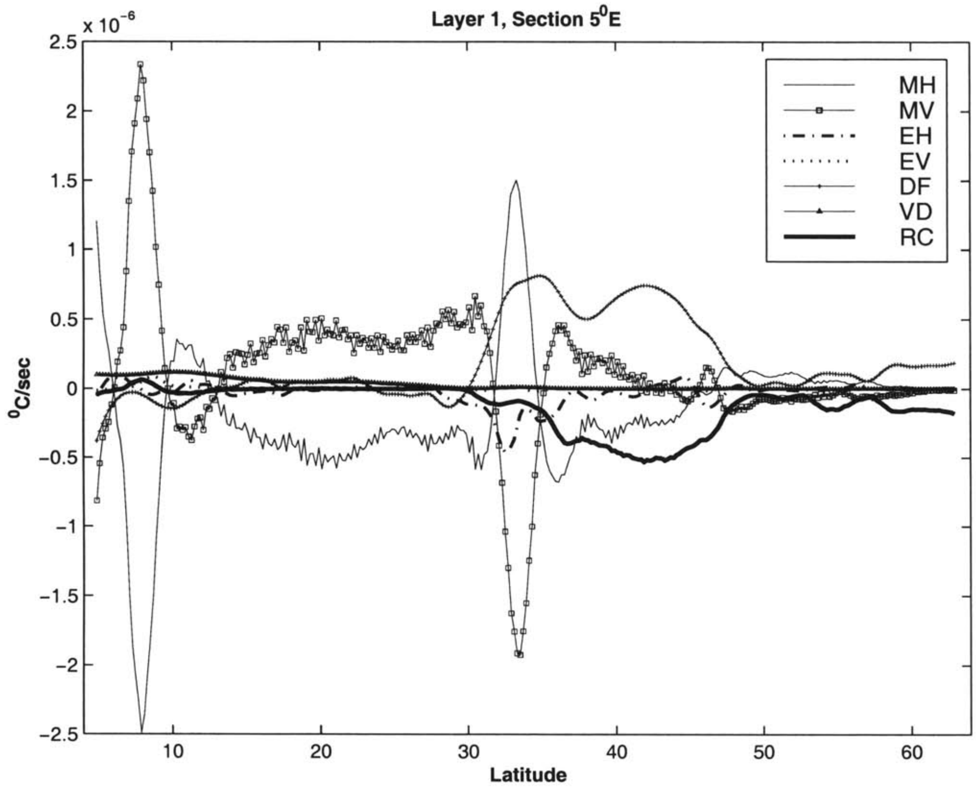

Figure 4-13: Balances in the temperature equation. Layer 1. Section at $5°E$. MH - horizontal divergence of time-mean heat flux, MV - vertical derivative of time-mean flux, EH - horizontal divergence of eddy heat flux, EV - vertical derivative of eddy heat flux, DF - restoring diabatic forcing, VD - vertical diffusion, RC - residual implied convection.

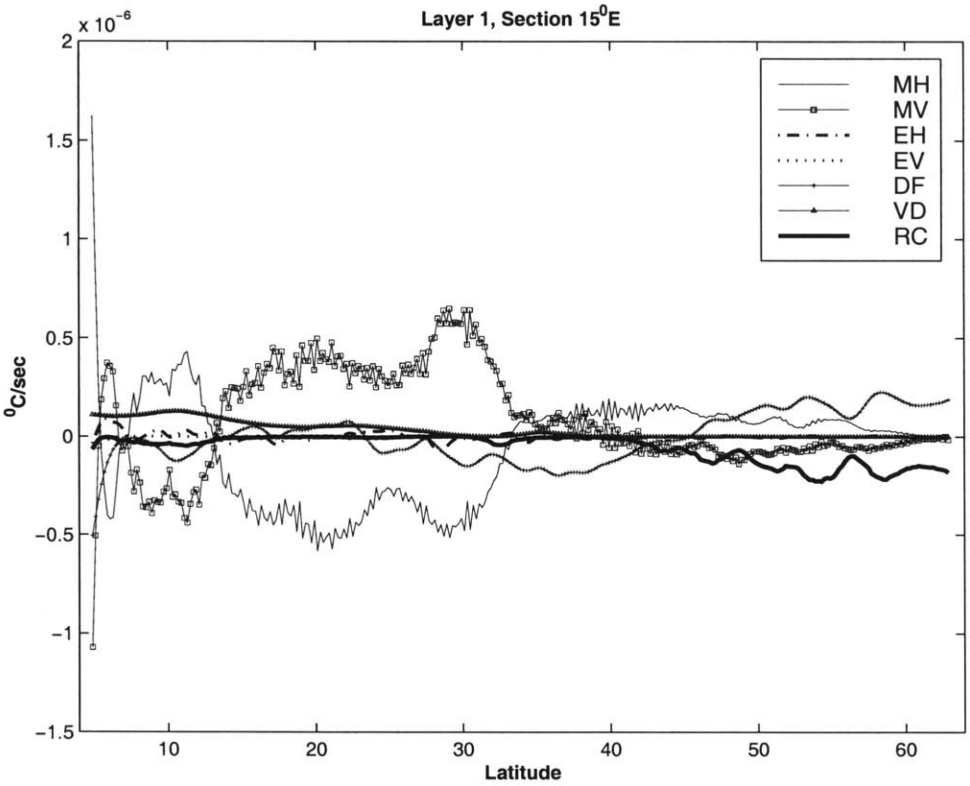

Figure 4-14: Balances in the temperature equation. Layer 1. Section at $15°E$. MH - horizontal divergence of time-mean heat flux, MV - vertical derivative of time-mean flux, EH - horizontal divergence of the eddy heat flux, EV - vertical derivative of the eddy heat flux, DF - restoring diabatic forcing, VD - vertical diffusion, RC - residual implied convection.

of heat fluxes, diffusion and convection.

Western Section at $5°E$

I identify 4 distinctive sub-sections in (Figure 4-15). The area between $4°N$ and $10°N$ can be characterized by the balance between 3D time mean divergence and horizontal eddy divergence. The bands $10°N - 27°N$ and $48°N - 53°N$ have much weaker contributions from all terms, resulting in small values. The most active subsection is between $27°N$ and $48°N$, where there is a balance between 3D time mean and eddy divergencies, with the magnitude of horizontal divergence of the eddy heat flux almost 50% of local values of the horizontal divergence of time mean heat flux. This is the area where the contribution of eddies is the most important. The last band is between $53°N$ and $64°N$, where the horizontal divergencies of time mean and eddy fluxes are in balance. The convection is present in the northernmost part of the section.

Interior Section at $15°E$

The largest terms in the balance (Figure 4-16) are the components of the 3D time mean divergence and convection. Eddies provide a moderate contribution throughout the section. Eddy horizontal divergence as well as convection are most pronounced in the norther part of the section. Convection slightly decreases the temperature of the deeper layers to the North of $55°N$. Overall, the magnitude of terms is about 10 times smaller compared to the cross-section at $5°E$ in the vicinity of the western boundary.

4.7 Horizontal and Vertical Distribution of Balances

The cross-sections presented in Figures 4-11 through 4-16 reveal a complex nature in the distribution of terms in (4.5). In this section I identify the geographical areas where the balances have similar nature. The following Tables 4.2 and 4.3 summarize observa-

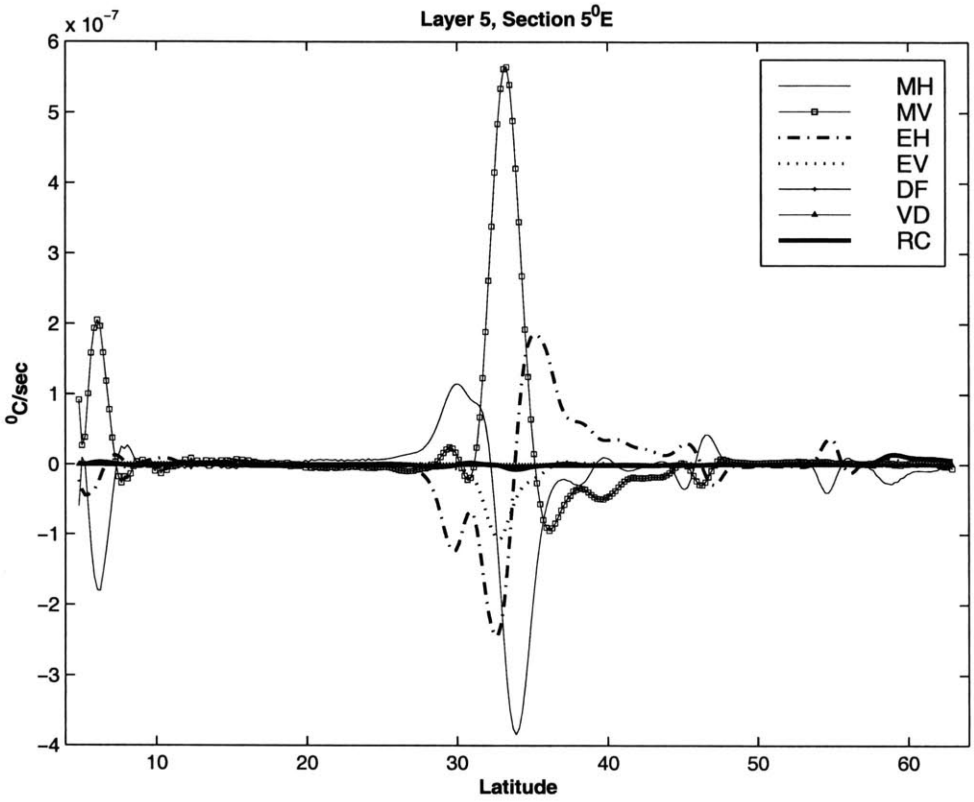

Figure 4-15: Balances in the temperature equation. Layer 5. Section at 5°E. MH - horizontal divergence of time-mean heat flux, MV - vertical derivative of time-mean flux, EH - horizontal divergence of the eddy heat flux, EV - vertical derivative of the eddy heat flux, DF - restoring diabatic forcing, VD - vertical diffusion, RC - residual implied convection.

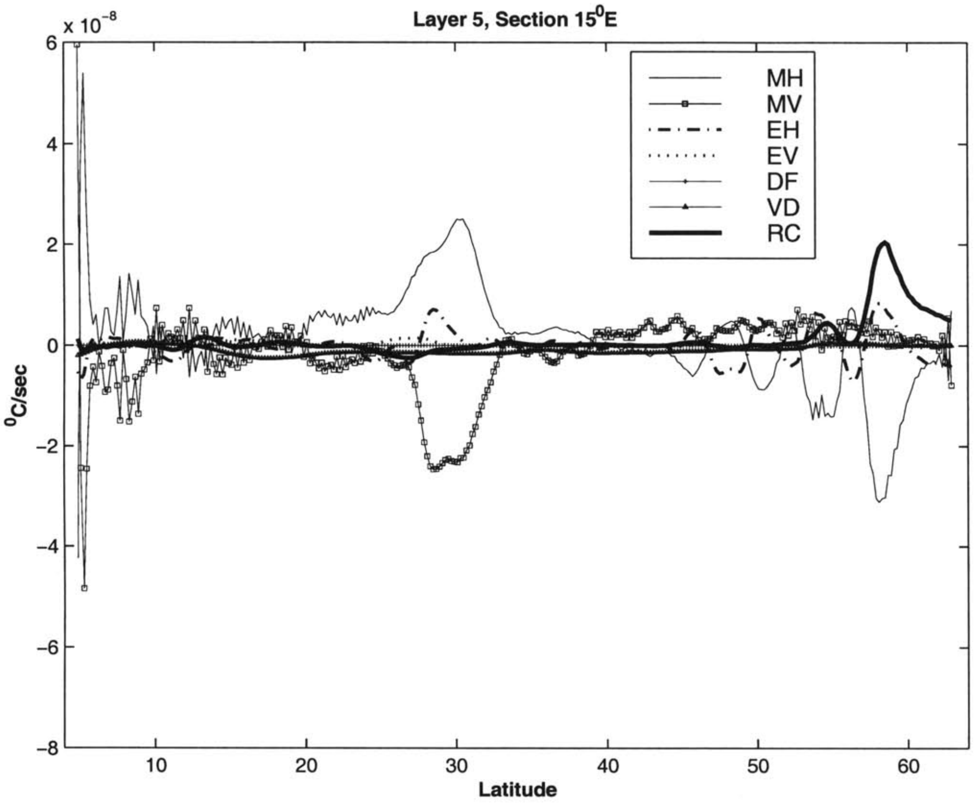

Figure 4-16: Balances in the temperature equation. Layer 5. Section at $15°E$. MH - horizontal divergence of time-mean heat flux, MV - vertical derivative of time-mean flux, EH - horizontal divergence of the eddy heat flux, EV - vertical derivative of the eddy heat flux, DF - restoring diabatic forcing, VD - vertical diffusion, RC - residual implied convection.

Layer	Sub-section	Terms
1	$4^\circ N - 12^\circ N$	MH, MV, DF
	$12^\circ N - 32^\circ N$	MH, MV
	$32^\circ N - 50^\circ N$	**MH, MV, EH, DF, RC**
	$50^\circ N - 64^\circ N$	DF, RC
2	$4^\circ N - 12^\circ N$	**MH, MV, EH**
	$12^\circ N - 32^\circ N$	MH, MV
	$32^\circ N - 36^\circ N$	**MH, MV, EH, EV**
	$36^\circ N - 50^\circ N$	**MH, EH, RC**
	$50^\circ N - 64^\circ N$	not significant
5	$4^\circ N - 10^\circ N$	**MH, MV, EH**
	$10^\circ N - 27^\circ N$ $48^\circ N - 53^\circ N$	not significant
	$27^\circ N - 48^\circ N$	**MH, MV, EH, EV**
	$48^\circ N - 64^\circ N$	**MH, EH, RC**

Table 4.2: Local contribution to the thermal balance. Section 5°E

tions from the previous sections. I highlight the sub-sections where the eddy heat flux divergence is significant.

The dominant terms throughout the basin are the components of the 3D divergence of the time mean heat flux. It is important to point out the three-dimensional nature of the time mean heat flux, as both the horizontal divergence and vertical derivative provide comparable contribution to the total balance. The analysis of the local thermal balance is performed for selected vertical levels. In the following chapter some of the diapycnal and isopycnal properties of the eddy heat flux will be evaluated.

The contribution of eddies varies throughout the domain both in horizontal and vertical dimensions. According to the distributions of horizontal divergence and vertical derivatives of the eddy heat flux I identify the following areas.

The *Southern area* spans a latitudinal band from $4^\circ N$ to $12^\circ N$. Its zonal dimension from the western boundary almost to the eastern. This is a shallow layer with the depth of about $200M$. The horizontal component of the eddy divergence (EH) is larger than the vertical (EV) suggesting the 2D nature of variability in the eddy heat flux. Given

Layer	Sub-section	Terms
1	$4^{\circ}N - 12^{\circ}N$	**MH, MV, EH, VD**
	$12^{\circ}N - 32^{\circ}N$	MH, MV, VD, DF
	$32^{\circ}N - 42^{\circ}N$	MH, MV, DF
	$42^{\circ}N - 64^{\circ}N$	MH, MV, DF, RC
2	$4^{\circ}N - 20^{\circ}N$	**MH, MV, EH**
	$20^{\circ}N - 42^{\circ}N$	MH, MV
	$42^{\circ}N - 64^{\circ}N$	MH, RC
5	$4^{\circ}N - 25^{\circ}N$	MH, MV, VD
	$25^{\circ}N - 32^{\circ}N$	**MH, MV, EH, EV, VD**
	$32^{\circ}N - 43^{\circ}N$	MH, MV, VD
	$43^{\circ}N - 64^{\circ}N$	**MH, MV, EH, RC**

Table 4.3: Local contribution to the thermal balance. Section 15°E

the relative magnitude of the eddy forcing compare to the time mean, I expect the main forcing to be the divergence of time mean circulation.

The *Western Midlatitude area* is the part of the domain with the strongest eddy forcing. It roughly occupies the area from western boundary to about $10^{\circ}E$ and from $25^{\circ}N$ to $50^{\circ}N$. The magnitude of the eddy heat forcing is about 50% of the time mean divergency. Both of the components are large, demonstrating that the eddy heat flux varies in horizontal as well as vertical planes. The magnitude of the eddy forcing is of the order $5 \cdot 10^{-7}\,[^{\circ}C \cdot \sec^{-1}]$, that is about an order of magnitude larger than in the interior. This is the area where eddies are strong and correspondingly require the accurate representation in coarse resolution climate models.

The bowl shape of this area has a slight southward tilt. Its meridional span decreases with depth and centers more to the south for deeper layers. In the next section I address the distribution of 3D divergence of the eddy heat flux with regard to the isotherms of the time mean temperature. That diagnostic will help in identification of the vertical penetration of the eddy forcing and its relationship with the established density structure.

The *Northern area* is located to the North of $50^{\circ}N$ from the western to the Eastern boundaries. The major components of the balance are time mean divergence, convection and for the upper layer - the diabatic forcing. In this region the observations of the eddy heat flux are the least reliable. First, the absence of a quantitative diagnostic for the deep convection complicates the exact calculation of the eddy forcing. Second, performing a statistical analysis of temperature time series for this location I identified the presence of low-frequency variability. The total time of the integration is insufficient to resolve this longer time scale. It makes the diagnostics of the eddy heat flux unreliable.

The *Interior area* occupies the rest of the domain. It includes the eastern part of the domain, deep areas which lay below $1000M$, small band between Southern and western areas. The major characteristics of this region is the predominant balance between the components of the time mean divergence and external diabatic forcing. All other terms are much smaller in magnitude.

4.8 Geographical Distribution of the Eddy Forcing

To better visualize the geographical areas where eddies exhibit strong influence on the thermal structure, I present contour plots of 3D eddy divergence superimposed on the isotherms of time mean temperature. The two sets of plots show horizontal and vertical distributions at the depths of $87.5M$ and $425M$ and for the sections $5°E$ and $15°E$ respectively.

In the second layer, Figure 4-17 there are two distinctive areas with strong eddy activity corresponding to the western and Southern areas. They consist of the positive an negative patterns ranging in size from $20° \times 2°$ (zonal×meridional) in the Southern area to $2° \times 12°$ in the Western. The maximum amplitude is $\sim 10^{-6}\,[°C \cdot \sec^{-1}]$ near the western boundary in the Southern $(1°E, 7°N)$ and Western $(2°E, 32°N)$ areas. The locations of the maximums correspond to the fast and narrow western boundary currents and the areas with the strongest deflection of the isotherms.

In the fifth layer, Figure 4-18, the area with the strong eddy forcing is situated only in the western boundary region from $30°N$ to $40°N$ and from the western boundary to

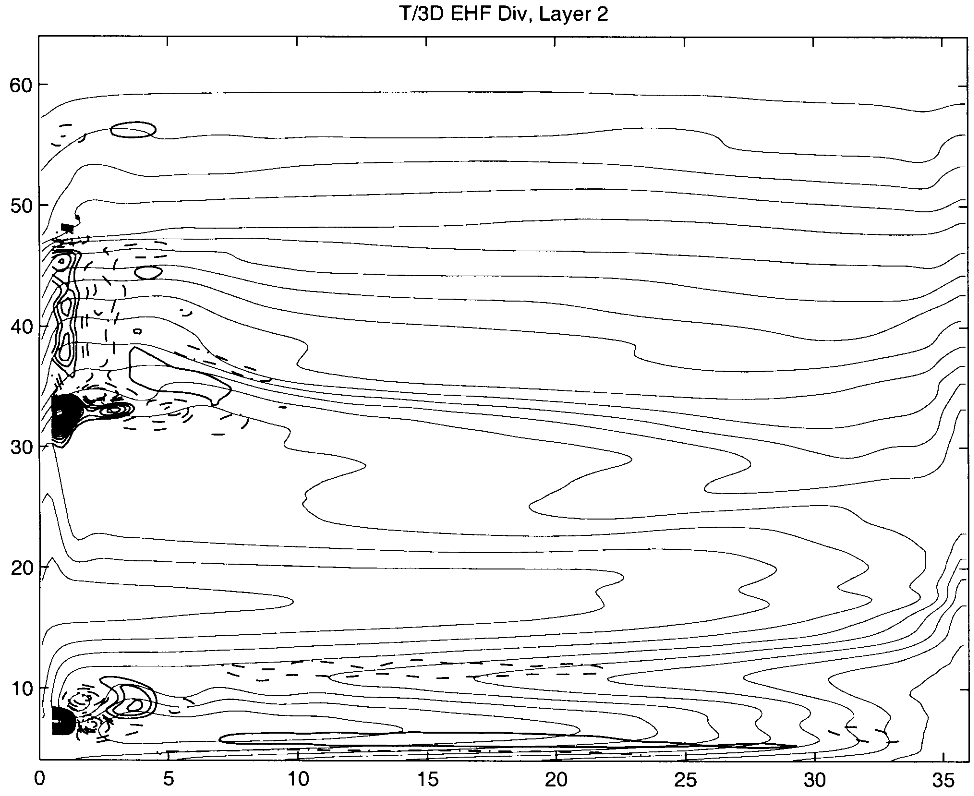

Figure 4-17: 3D divergence of the eddy heat flux, C.I. $10^{-7}\,[°C \cdot \mathrm{sec}^{-1}]$, and isotherms of time-mean temperature, C.I. $1\,[°C]$. Layer 2.

$10°E$. Its magnitude is still strong of the order $10^{-6}\,[°C \cdot \sec^{-1}]$. The location is strongly correlated with the convergence of the isotherms.

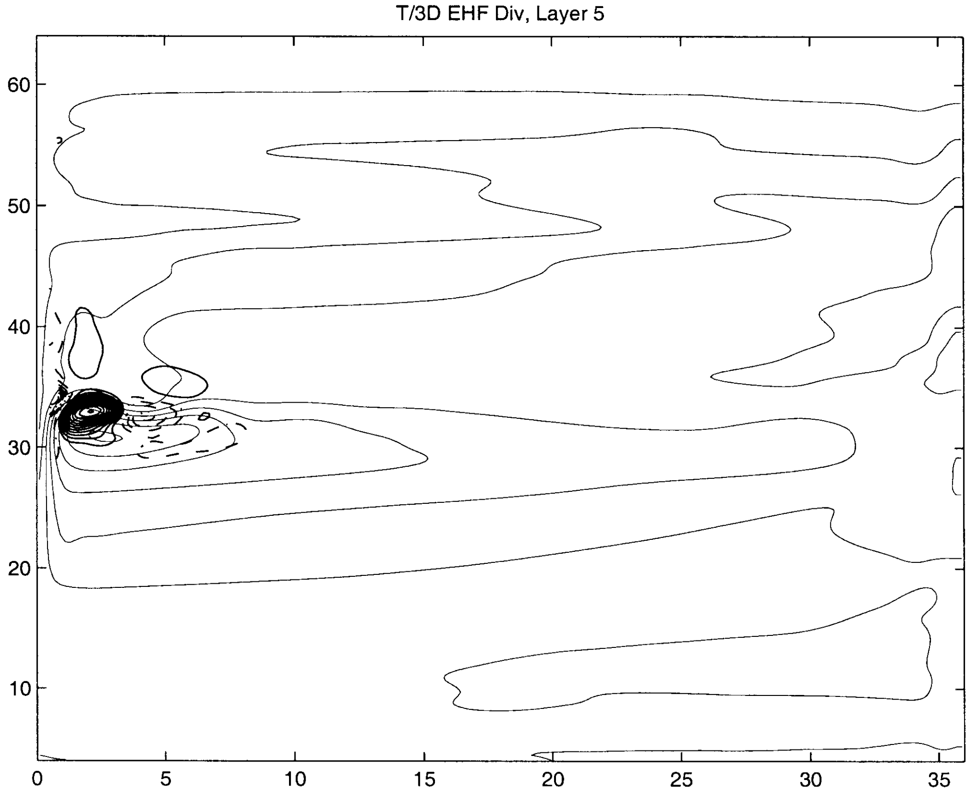

Figure 4-18: 3D divergence of the eddy heat flux, C.I. $10^{-7}\,[°C \cdot \sec^{-1}]$, and isotherms of time-mean temperature, C.I. $1\,[°C]$. Layer 5.

In the vertical cross-section at $5°E$, Figure 4-19, the meridional distribution of eddy activities corresponds to the horizontal distribution. There are two areas with large eddy divergencies: Western and Southern. In the vertical dimension, eddies act on the thermal structure in the upper $700M$ for the Western area, reaching maximum of $0.4{\cdot}10^{-6}\,[°C \cdot \sec^{-1}]$ around $250M$, and only in the upper $300M$ in the Southern part of the domain. According to the balance (4.5), an overall negative balance corresponds to the increase in time of the local value of temperature. The deepening of the isotherms in the band between $26°N$ and $34°N$, that implies local warming, corresponds to the negative values of the 3D eddy heat flux divergence. It changes to the local cooling, the rising of the isotherms, in the area between 34°N and 40°N with the positive eddy divergence. It is important to point out the connection between the strong deflection of the isotherms and the corresponding values of the divergence of the eddy heat flux. The variations in temperature for the depths below 1000M is less than the 1°C and the magnitude of the eddy heat flux divergence is smaller than $10^{-7}\,[°C \cdot \mathrm{sec}^{-1}]$. Subsequently, there are no contours in the deep ocean with the magnitude equals to the contour interval (C.I.).

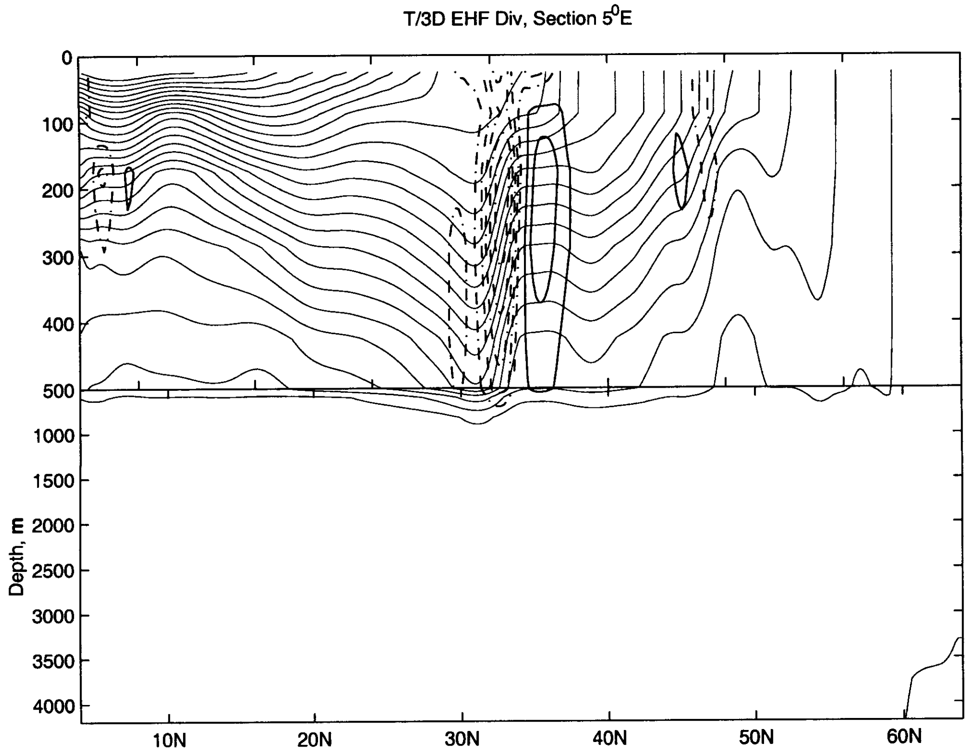

Figure 4-19: 3D divergence of the eddy heat flux, C.I. $10^{-7}\,[°C \cdot \mathrm{sec}^{-1}]$, and isotherms of time-mean temperature, C.I. $1\,[°C]$. Section at 5°E.

Further in the interior, Figure 4-20 the magnitude of the eddy forcing becomes smaller of about $10^{-7}\,[°C \cdot \mathrm{sec}^{-1}]$. The location of the patterns is still connected to deflection of the isotherms, although there is no clear correlation between deepening or rising of the isotherms and the sign of the eddy divergence. The magnitude of the eddy divergence suggests that the eddy forcing in the interior is weak except in the Southern area.

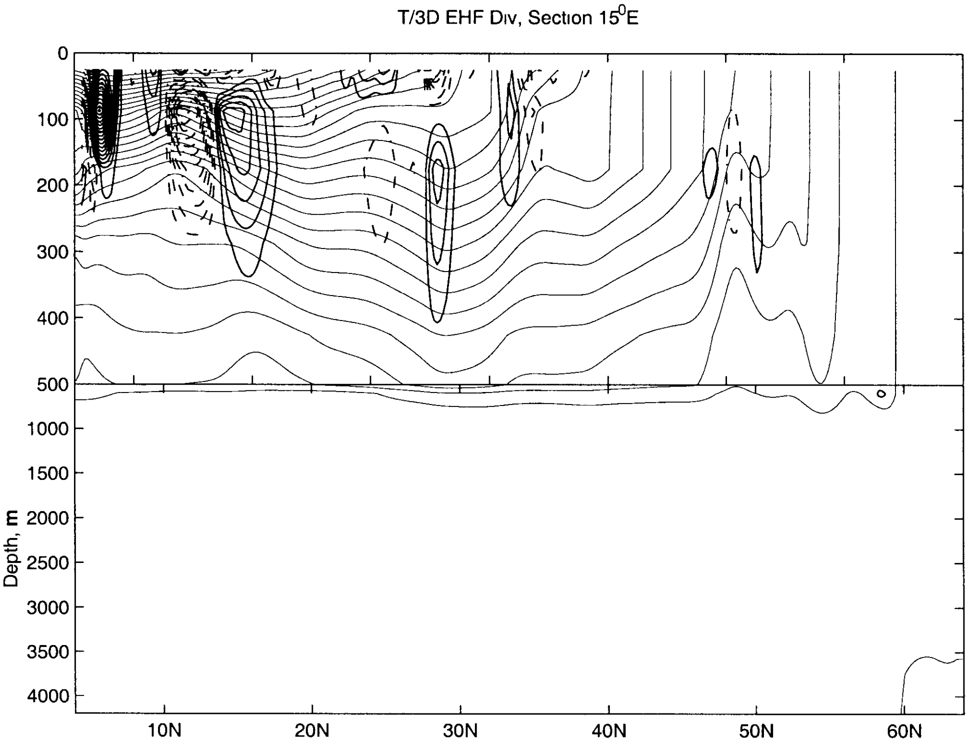

Figure 4-20: 3D divergence of the eddy heat flux, C.I. 10^{-8} $[°C \cdot \text{sec}^{-1}]$, and isotherms of time-mean temperature, C.I. 1 $[°C]$. Section at $15°E$.

The above distributions identify the areas where the eddy forcing on the time mean thermal structure is strong. The first area is the Western area located in the midlatitude western boundary current region with the horizontal dimensions in the upper layers of about 20° × 10°: from $30°N$ to $50°N$ and from the western boundary to $10°E$. It shrinks to about $10° \times 10°$: from $30°N$ to $40°N$ and the same zonal span, at $425M$ depths. It does not penetrate deeper than $700M$. The sign of the eddy heat flux divergence corresponds to the changes in the local tendencies in temperature. The region has a bowl shape tilted southward with depth. The second area is the Southern area, with the meridional width of about 5° and a depth to about $300M$. It spreads through most of the domain decreasing in magnitude progressing away from the western boundary.

4.9 Divergences of the Time Mean and Eddy Heat Fluxes

It was shown in the previous section that the eddy forcing on temperature distribution in the form of the three–dimensional divergence of the eddy heat flux is important only in three separate geographical regions: Southern, Western Midlatitude and Northern areas. In the rest of the basin the magnitude of the divergence is small compare to the dominant terms in the thermal balance (4.5). The eddy forcing is the largest in the Western Midlatitude area.

Even though the magnitude of the eddy heat flux divergence can be large, it does not necessarily mean that eddies provide significant contribution to the climatological properties of the model ocean, such as northward integrated heat flux. If the increase in the eddy activity is reflected in the decrease of the divergence by the time mean flux, or vice versa, than the changes in the overall contribution can be small, and eddies does not transport heat to the North. Indeed, Figure 4-21 presents the evaluation of three–dimensional divergencies of the time mean and eddy heat fluxes in the Western Midlatitudinal area for the same three layers.

There is a clear tendency for the cancellation between the divergencies where the additional terms in the balance are small. If in the upper layer (subplots (a) and (d)) the magnitude of difference between the divergencies is the largest, due to the presence of the diabatic forcing, it is small for the fifth layer (subplots (c) and (f)). This fact suggests that the diabatic forcing is weak for the deeper layers and the non–acceleration theorem (*Andrews and McIntyre, 1976* [1]) is valid. The consequences for the eddy heat flux is in the non–transport properties of eddies.

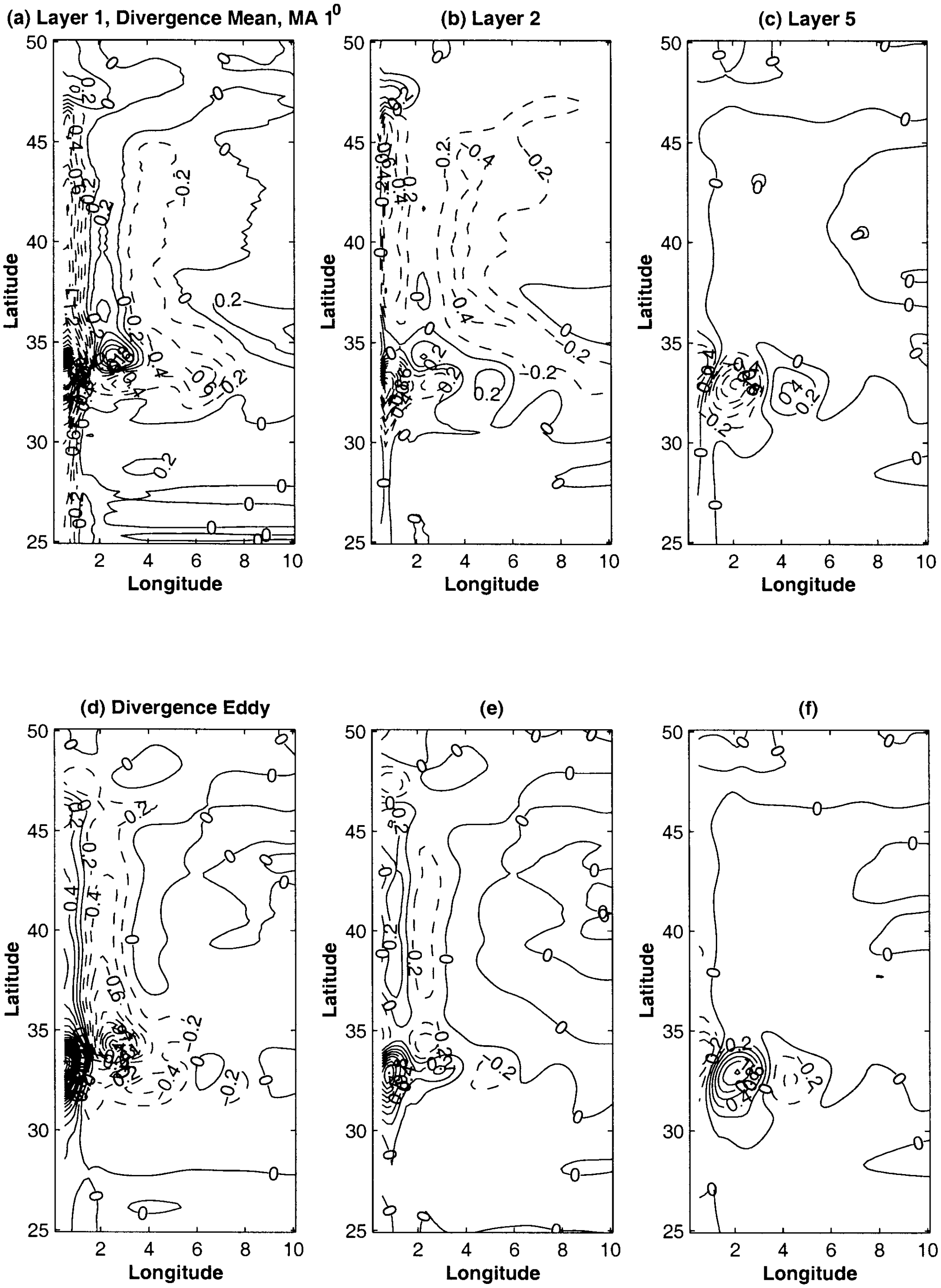

Figure 4-21: Three dimensional divergencies of the time mean (upper row) and eddy (lower row) heat fluxes. C.I. $0.2 \cdot 10^{-6}$ $[°C \cdot \sec^{-1}]$. Layer 1 (a,d), Layer 2 (b,e), Layer 5 (c,f).

4.10 Conclusions

The direct calculation of the contribution of eddies to the thermal balance of the reference experiment identified the areas where the divergence to the eddy heat flux is one of the leading terms in the balance. They are the Western Midlatitudinal area with the strongest forcing located from the western boundary to approximately $10°E$ and between latitudes $25°N$ and $50°N$ for the upper layer and smaller area, tilted to the South the deeper layers, the Northern area: to the North of $50°N$ and the Southern that spans a latitudinal band from $4°N$ to $12°N$. The areas are filled with anomalies of the opposite signs and overall cover a smaller part of the whole basin.

The analysis performed in this chapter evaluates the magnitude of the eddy heat flux divergence for selected vertical levels. The important properties of the along– and cross–isopycnal components of the eddy heat flux will be presented in a series of diagnostic tests of the next chapter.

Even in the areas where the magnitude of the eddy heat flux divergence is large, there is a cancellation with the divergence of the time mean heat flux, such that the sum of two is a small value, especially in the deeper layers. This cancellation property suggests that the overall contribution of eddies to the northward integrated heat transport is small.

The identification of the importance of the eddy heat flux is important for the testing of different parameterization schemes that will be presented in the next chapters. The local schemes should reproduce the larger magnitudes where the eddy heat flux divergence is large and at the same time do not introduce some artificial forcing where the eddy heat flux divergence is small. The Western Midlatitudinal areas where the eddy contribution is the strongest is chosen for the testing of the schemes.

Chapter 5

Diagnostic Tests of Eddy Heat Flux Parameterization Schemes

5.1 Introduction

The orientation of the isopycnal surfaces defines the three–dimensional distribution of density. By definition if one moves a particle along one of these surfaces its density remains constant. Such processes which conserves the density of an incompressible fluid element are called *adiabatic.* On the other hand if an element crosses an isopycnal surface its density is automatically changed. The processes which are responsible for such movements are called diabatic processes.

The time–dependent motions or eddies are one of the potential candidates which can cause such transfers. If eddy characteristic horizontal scale is small compare to the horizontal resolution of the climatological ocean models and these small–scale processes influence the large–scale distribution of properties, then they require a representation through an eddy heat flux parameterization scheme or an eddy parameterization scheme[1].

---

[1] In the thesis I address only temperature transfers so when an eddy parameterization scheme is mentioned it means an eddy heat flux parameterization scheme.

The local underlying nature of the process is the central idea behind its proposed parameterization schemes. If the direction of the transfer is along isopycnal then the adiabatic schemes were proposed. Among them are the isopycnal parameterization (*Solomon, 1971* [53]) and the adiabatic parameterization scheme proposed by *Gent and McWilliams, 1990* [23]. The former is automatically employed in the isopycnal general circulation models (*Bleck and Boudra, 1986* [2]) and can be implemented in pressure or Z-coordinate models (*Redi, 1982* [46]). The latter is a modern eddy parameterization scheme that can be used in the majority of ocean GCMs. In the case of the diabatic mechanism of eddy transfer, the proposed schemes are the horizontal Laplacian mixing and the scheme based on the eddy transfer theory originally developed for the atmospheric flows by *Green, 1970* [26] and *Stone, 1972* [55]. The first scheme is the most widely used eddy parameterization scheme representing the eddy heat flux as the downgradient transfer, so–called Fickian diffusion. The second relies on the assumption that transfer of heat by eddies occurs during the growth phase of the baroclinic eddies and represents the process in terms of the structure of the growing mode.

The proposed parametrization schemes were designed through the observations of the release or consumption of energy while redistributing the potential density. Due to the linear equation of state, fixed salinity and hydrostatic approximation of the reference experiment, the temperature in the simulation is the equivalent of the potential density.

The distribution of temperature is a three–dimensional field. If exposed only to the gravitational force, the three–dimensional distribution evolves into a one–dimensional structure. Temperature becomes the function of a vertical coordinate only and eventually uniformly distributed through the action of molecular processes. In the presence of external forcing it is possible to obtain a steady state with a 3D distribution of temperature. The state is characterized by a complex balance of local and remote processes of release and input of energy. The authors of the eddy parametrization schemes assumed that eddies are responsible for the local maintenance of the statistically steady balance, and thus their role can be represented as a function of a local statistically steady temperature distribution.

In this chapter I test these assumptions by observing the validity of the conditions behind the proposed eddy heat flux parameterization schemes in the direct evaluation from the reference experiment.

5.2 Vector Decomposition

This section defines a geometrical framework related to the orientation of the isopycnal surfaces that is used to derive and perform tests of the proposed eddy heat flux parameterization schemes.

5.2.1 Flux Vectors and Gradients

The MIT GCM is formulated in the finite volume framework. For each elementary volume (i, j, k) the variables are defined in different locations. The dynamical variables u, v and w are defined on the surfaces of a volume, while the thermodynamical variables S and T are specified in the center of a volume (Figure B-1). The benefit of this staggered formulation of the numerical grid is in the simplicity and accuracy in performing the computations of integrated fluxes into and out of an elementary volume. This is the most fundamental operation of the model numerical algorithm. On the other hand due to the fact that the variables are specified in different locations, it complicates analysis of the model in Eulerian framework, in which it is necessary to specify the flux vector of properties and the local isopycnal slope at specified locations in the domain. This framework is important for the visualization of physical mechanisms which are proposed to represent the eddy heat flux.

The transformation from an integrated over each individual volume (i, j, k) flux to vector flux property involves some averaging, in order for the components, that define the flux, to be specified at one geographical location. There is some freedom in deciding where this place should be.

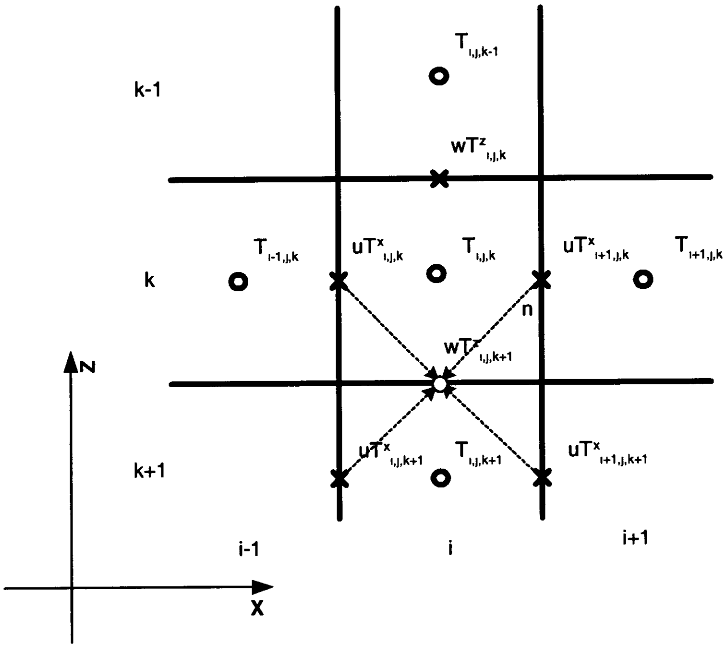

Figure 5-1: Definition of the reference point for a flux vector for an individual volume (i, j, k) in (X, Z) plane.

The most sensitive variables of the model as it was demonstrated in the previous chapter are related to the vertical direction: vertical velocity $w_{i,j,k}$ and the vertical temperature flux into or out of the volume $wT|_{i,j,k}$. In order to represent these quantities as they are specified in the model I choose the reference point, where I define the flux vector for each individual volume, at the w point (Figure B-1(b)). Due to the rigid lid boundary condition at the surface, the vertical velocity w_{ij1} at the surface is zero for all (i, j). On the other hand, the effective vertical flux of temperature is not zero because of the vertical flux at the lower boundary from the neighbouring volume $(i, j, 2)$. This interface value is assigned to represent a vertical flux for a volume $(i, j, 1)$. This rule is applied for all layers; thus, the reference point for a volume (i, j, k) is at the location where $w_{i,j,k+1}$ is defined that is at the center of the lower side of the volume (i, j, k).

All other components of the flux vector are averaged from their respective model locations. For example, consider the heat flux vector $\vec{v}T|_{i,j,k}$. The model evaluates two of its components $uT|_{i,j,k}$ and $wT|_{i,j,k}$ at the locations shown in Figure 5-1.

In the model's finite volume formulation the components are

$$\begin{aligned} uT|_{i,j,k}^{vol} &= u_{i,j,k}\overline{T}^{x}_{i,j,k}, \\ wT|_{i,j,k}^{vol} &= w_{i,j,k}\overline{T}^{z}_{i,j,k}, \end{aligned}$$

where $\overline{T}^{x}_{i,j,k} = \frac{T_{i-1,j,k}+T_{i,j,k}}{2}$ and $\overline{T}^{z}_{i,j,k} = \frac{T_{i,j,k-1}+T_{i,j,k}}{2}$ and the superscript *vol* indicates the model's finite volume framework. In the vector formulation, the horizontal component of the flux is defined to be an average of the values for the four volumes nearest to the reference point. The vertical component is equal to the model's value at this point.

$$\begin{aligned} uT|_{i,j,k} &= \frac{1}{4}\left(uT|_{i,j,k}^{vol} + uT|_{i+1,j,k}^{vol} + uT|_{i,j,k+1}^{vol} + uT|_{i+1,j,k+1}^{vol}\right), \\ wT|_{i,j,k} &= wT|_{i,j,k+1}^{vol}. \end{aligned}$$

The computations of meridional components are performed in a similar manner.

The slope of the isopycnal is evaluated at the same grid point corresponding to the w point on the lower volume's side. Within the reference formulation the evaluation of the slope involves the computation of the three–dimensional temperature gradient at this point. For the horizontal components the temperature is interpolated to the reference point by averaging between the two neighbouring layers. Then, the horizontal derivatives are evaluated as a central difference. The vertical component of the temperature gradient is evaluated directly from the volume data as $\frac{\partial}{\partial z} T|_{i,j,k} = \frac{T_{i,j,k}-T_{i,j,k+1}}{\Delta z}$, where Δz is a distance between the centers of volumes.

5.2.2 Isopycnal basis

A local orthonormal basis is formed by the isopycnal surface (Figure 5-2) and its normal vector. Two orthogonal unit vectors span every vector that lies on the isopycnal surface plane. The third unit vector is parallel to the temperature gradient.

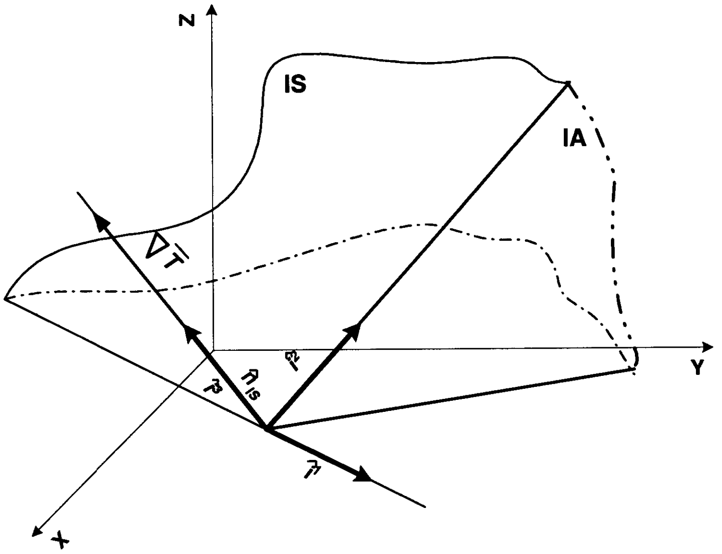

Figure 5-2: Local orthonormal isopycnal basis $(\hat{\imath}^1, \hat{\imath}^2, \hat{\imath}^3)$. IS - isopycnal surface plane, IA - isopycnal angle surface.

The vector of temperature gradient $\nabla\bar{T}$ is colinear to the unit normal vector $\hat{n}_{IS}$ to the isopycnal surface. This unit vector uniquely defines a plane that is tangental to the isopycnal surface at this location. I call this plane as the *Isopycnal Surface Plane* (IS). The density stays constant in a limit of small movements in this plane. The plane formes an angle with the horizontal plane that I call the *isopycnal angle.* The *Isopycnal Angle plane* (IA) is a plane that contains the isopycnal angle. It can be viewed as being perpendicular to the horizontal plane and containing $\nabla\bar{T}$ or the unit normal vector $\hat{n}_{IS}$ to the isopycnal surface.

Form an orthogonal basis $\hat{\imath} = (\hat{\imath}^1, \hat{\imath}^2, \hat{\imath}^3)$ consisting of two orthogonal vectors spanning the isopycnal angle plane $(\hat{\imath}^2, \hat{\imath}^3)$ and a vector normal to the plane $\hat{\imath}^1$, that belongs to the horizontal plane (X, Y).

The orthonormal basis $\hat{\imath}$ in the local Cartesian coordinate system $(\hat{x}, \hat{y}, \hat{z})$ is chosen to have the following structure

$$\begin{aligned}
\hat{\imath}^1 &\subset (\hat{x}, \hat{y}) \text{ and } \hat{\imath}^1 \perp (\text{IA}) \rightarrowtail \hat{\imath}^1 = \frac{(1, i^1_2, 0)}{|\hat{\imath}^1|}, \\
\hat{\imath}^2 &\subset (\text{IS}) \rightarrowtail \hat{\imath}^2 = \frac{(i^2_1, 1, i^2_3)}{|\hat{\imath}^2|}, \\
\hat{\imath}^3 &= \frac{(\bar{T}_x, \bar{T}_y, \bar{T}_z)}{|\nabla \bar{T}|},
\end{aligned} \tag{5.1}$$

where the superscript for $\hat{\imath}$ indicates the index of a basis vector and the subscript is the component of the vector in the Cartesian coordinate system $(\hat{x}, \hat{y}, \hat{z})$ and the operator $|\cdot|$ means the length of a vector.

The orthonormality property is used in order to identify the unknown components.

$$\begin{aligned}
\hat{\imath}^1 &\perp \hat{\imath}^2 \Longrightarrow i^2_1 + i^1_2 = 0, \\
\hat{\imath}^2 &\perp \hat{\imath}^3 \Longrightarrow \bar{T}_x \cdot i^2_1 + \bar{T}_y + \bar{T}_z \cdot i^2_3 = 0, \\
\hat{\imath}^1 &\perp \hat{\imath}^3 \Longrightarrow \bar{T}_x + \bar{T}_y \cdot i^1_2 = 0.
\end{aligned} \tag{5.2}$$

The solution of the linear system of equations (5.2) allows the construction of the orthonormal basis

$$\begin{aligned}
\hat{\imath}^1 &= \left(\frac{\bar{T}_y}{|\nabla_h \bar{T}|}, -\frac{\bar{T}_x}{|\nabla_h \bar{T}|}, 0 \right), \\
\hat{\imath}^2 &= \left(-\frac{\bar{T}_x \bar{T}_z}{|\nabla_h \bar{T}|\,|\nabla \bar{T}|}, -\frac{\bar{T}_y \bar{T}_z}{|\nabla_h \bar{T}|\,|\nabla \bar{T}|}, \frac{|\nabla_h \bar{T}|}{|\nabla \bar{T}|} \right), \\
\hat{\imath}^3 &= \left(\frac{\bar{T}_x}{|\nabla \bar{T}|}, \frac{\bar{T}_y}{|\nabla \bar{T}|}, \frac{\bar{T}_z}{|\nabla \bar{T}|} \right),
\end{aligned} \tag{5.3}$$

where $|\nabla_h \bar{T}| = \sqrt{\bar{T}_x^2 + \bar{T}_y^2}$ is the modulus of the horizontal component of the time mean temperature gradient and $|\nabla \bar{T}| = \sqrt{\bar{T}_x^2 + \bar{T}_y^2 + \bar{T}_z^2}$ is the modulus of the three–dimensional gradient.

Every vector that belongs to the IA plane can be expanded by $(\hat{\imath}^2, \hat{\imath}^3)$.

5.2.3 Projections of Vectors on the Isopycnal Basis

In order to derive the tests of eddy heat flux parameterization schemes I need to specify the coordinates of the following vectors (Figure 5-3) in the original local Cartesian basis $(\hat{x}, \hat{y}, \hat{z})$.

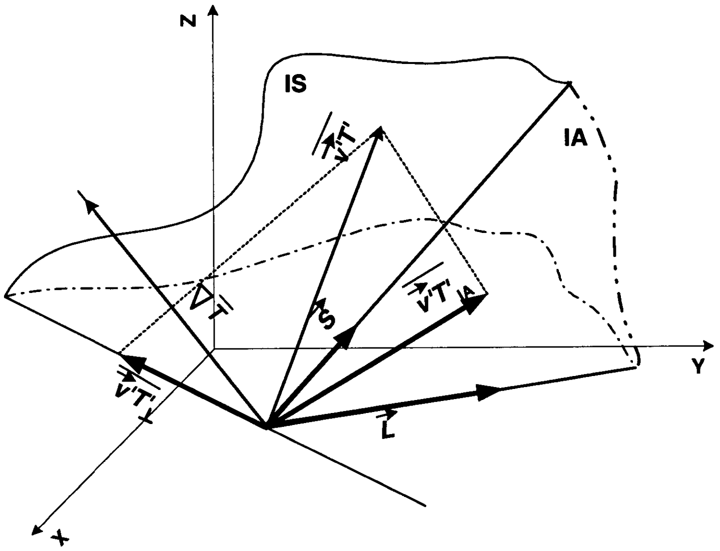

Figure 5-3: Projections of vectors on the IA plane.

The three–dimensional *temperature gradient* is computed as

$$\nabla \bar{T} = \left(\bar{T}_x, \bar{T}_y, \bar{T}_z\right).$$

The *isopycnal vector* $\vec{S}$ corresponds to the isopycnal basis vector $\hat{\imath}^2$.

$$\vec{S} = \hat{\imath}^2 = \left(-\frac{\bar{T}_x \bar{T}_z}{|\nabla_h \bar{T}|\,|\nabla \bar{T}|}, -\frac{\bar{T}_y \bar{T}_z}{|\nabla_h \bar{T}|\,|\nabla \bar{T}|}, \frac{|\nabla_h \bar{T}|}{|\nabla \bar{T}|} \right). \tag{5.4}$$

The horizontal *slope vector* $\vec{L}$ is a vector that is collinear with the projection of $\vec{S}$ on the horizontal. The magnitude of $\vec{L}$ is defined by the *slope of the isopycnal surface* $\hat{s}_{IS}$. The value of the isopycnal angle is small everywhere in the domain, except in the northern convective region, where the slope is not well defined; thus,

$$\vec{L} = \left(-\frac{\bar{T}_x}{\bar{T}_z}, -\frac{\bar{T}_y}{\bar{T}_z}, 0 \right), \tag{5.5}$$

and the magnitude of the slope

$$\hat{s}_{IS} = \frac{|\nabla_h \bar{T}|}{\bar{T}_z}.$$

The decomposition of the eddy heat flux vector $\vec{v}'T' = \left(\overline{u'T'}, \overline{v'T'}, \overline{w'T'}\right)$ in the isopycnal basis $\hat{\imath}$ is the following

$$\overline{\vec{v}'T'} = \left(\left(\overline{\vec{v}'T'} \cdot \hat{\imath}^1\right), \left(\overline{\vec{v}'T'} \cdot \hat{\imath}^2\right), \left(\overline{\vec{v}'T'} \cdot \hat{\imath}^3\right) \right)\Big|_{\hat{\imath}}, \tag{5.6}$$

where $(\cdot)$ is the scalar product of two vectors and subindex $\hat{\imath}$ indicates the coordinates evaluated in the isopycnal basis. The first component define the projection of the eddy heat flux on $\hat{\imath}^1$ or the direction that is normal to the IA plane $\overline{\vec{v}'T'}\Big|_{\perp}$. The last two components in (5.6) define the projection of the eddy heat flux vector on the IA plane $\overline{\vec{v}'T'}\Big|_{\mathrm{IA}}$. The component of $\overline{\vec{v}'T'}\Big|_{\perp}$ and $\overline{\vec{v}'T'}\Big|_{\mathrm{IA}}$ in the isopycnal basis $\hat{\imath}$ are

$$\begin{aligned} \overline{\vec{v}'T'}\Big|_{\perp} &= \left(\left(\overline{\vec{v}'T'} \cdot \hat{\imath}^1\right), 0, 0 \right)\Big|_{\hat{\imath}}, \\ \overline{\vec{v}'T'}\Big|_{\mathrm{IA}} &= \left(0, \left(\overline{\vec{v}'T'} \cdot \hat{\imath}^2\right), \left(\overline{\vec{v}'T'} \cdot \hat{\imath}^3\right) \right)\Big|_{\hat{\imath}}. \end{aligned}$$

The components in the original Cartesian system $(\hat{x}, \hat{y}, \hat{z})$ are

$$\left.\overline{\vec{v}'T'}\right|_{\perp} = \left(\begin{array}{c} \frac{\bar{T}_y}{\left|\nabla_h \bar{T}\right|^2} \left(\bar{T}_y \cdot \overline{u'T'} - \bar{T}_x \cdot \overline{v'T'} \right) \\ -\frac{\bar{T}x}{\left|\nabla_h \bar{T}\right|^2} \left(\bar{T}_y \cdot \overline{u'T'} - \bar{T}_x \cdot \overline{v'T'} \right) \\ 0 \end{array} \right),$$

$$\left.\overline{\vec{v}'T'}\right|_{\mathrm{IA}} = \left(\begin{array}{c} \frac{\bar{T}_x}{\left|\nabla_h \bar{T}\right|^2} \left(\bar{T}_x \cdot \overline{u'T'} + \bar{T}_y \cdot \overline{v'T'} \right) \\ \frac{\bar{T}y}{\left|\nabla_h \bar{T}\right|^2} \left(\bar{T}_x \cdot \overline{u'T'} + \bar{T}_y \cdot \overline{v'T'} \right) \\ \overline{w'T'} \end{array} \right).$$

In the following sections I demonstrate how the vectors $\nabla\bar{T}$, $\vec{S}$, $\vec{L}$ define the eddy parameterization schemes. The eddy heat flux $\overline{\vec{v}'T'}$ and its projection on the isopycnal angle plane $\left.\overline{\vec{v}'T'}\right|_{\mathrm{IA}}$ will be compared with the values that are predicted with the eddy heat flux parameterization schemes.

5.3 Tests of Eddy Heat Flux Parameterization Schemes

5.3.1 Diabatic Schemes

Fickian Diffusion

The Fickian diffusion is the simplest and the most widely used in the coarse resolution models scheme. The eddy heat flux is parameterized in terms of the downgradient transport of time mean temperature with a constant scalar diffusivity coefficient. For the horizontal transport it is

$$\overline{\vec{v}_h'T'} = -K_{Th}\nabla_h\bar{T},$$

where $\overline{\vec{v}_h' T'} = \left(\overline{u'T'}, \overline{v'T'}\right)$ is the horizontal eddy heat flux, K_{Th} is a diffusivity coefficient and $\nabla_h = \left(\frac{\partial}{\partial x}, \frac{\partial}{\partial y}\right)$. For the vertical component it is

$$\overline{w'T'} = -K_{Tw}\frac{\partial \bar{T}}{\partial z},$$

where K_{Tw} is a vertical diffusivity coefficient. The diffusion coefficients must be positive. In its simplest form the mixing coefficients are constant in space and time; therefore, the isotropy of the horizontal and vertical mixing is assumed. In the majority of the coarse resolution experiments the horizontal component of the eddy heat flux were assumed to be much larger than the vertical component (e.g. *Sarmiento, 1982* [49]), resulting in the parameterization scheme to be quasi–horizontal.

The physical mechanism that is the basis of the Fickian parameterization scheme together with the constraints on the values of the diffusivity coefficients suggests the way how to test the parameterization scheme. It involves a comparison between the time mean eddy heat flux $\overline{\vec{v}'T'}$ diagnosed from the data run part of the reference experiment and the transfer vector with a direction defined by $(K_{Th}\bar{T}_x,\ K_{Th}\bar{T}_y,\ K_{Tw}\bar{T}_z)$. The direction of the eddy heat flux has to be downgradient with respect to the time mean temperature field, that is the positive coefficients K_{Th} and K_{Tw} must exist such that

$$\overline{\vec{v}'T'} = -K_{Th}\frac{\partial \bar{T}}{\partial x}\hat{\imath} - K_{Th}\frac{\partial \bar{T}}{\partial y}\hat{\jmath} - K_{Tw}\frac{\partial \bar{T}}{\partial z}\hat{k}, \tag{5.7}$$

where $(\hat{\imath},\ \hat{\jmath},\ \hat{k})$ is a Cartesian basis.

The test in its strong form requires (5.7) to be satisfied for positive K_{Th} and K_{Tw} that are constant everywhere in the domain. In addition I derive a weaker form of the test

$$\overline{\vec{v}'T'} = -K_{Tu}\frac{\partial \bar{T}}{\partial x}\hat{\imath} - K_{Tv}\frac{\partial \bar{T}}{\partial y}\hat{\jmath} - K_{Tw}\frac{\partial \bar{T}}{\partial z}\hat{k}, \tag{5.8}$$

where the diffusivity coefficients are allowed to be functions of space. By observing the distribution and the magnitude of the coefficients I can identify the strength of the local downgradient mixing throughout the model domain. Unless the vectors $\overline{\vec{v}'T'}$ and $\nabla\bar{T}$ are orthogonal, the diffusion coefficients in (5.8) can be found. The downgradient condition can be examined by observing the angle between the two vectors. If $\angle\left(\overline{\vec{v}'T'}, \nabla\bar{T}\right) > 90°$, then the eddy heat flux is downgradient and the condition (5.8) is satisfied with the proper choice of the diffusivity coefficients K_{Tu}, K_{Tv} and K_{Tw}.

The divergence of the flux $\vec{F}_{FD}$ associated with the Fickian diffusive parameterization scheme (5.7) is evaluated for constant coefficients of horizontal mixing K_{Th} and vertical K_{Tw} :

$$\nabla \cdot \vec{F}_{FD} = -K_{Th}\bar{T}_{xx} - K_{Th}\bar{T}_{yy} - K_{Tw}\bar{T}_{zz}. \tag{5.9}$$

This quantity will be compared with the divergence of the eddy heat flux.

Isopycnal Mixing

The isopycnal mixing scheme can be considered as a modification of the Fickian diffusion. This parameterization scheme represents mixing as occurring in the normal direction to the isopycnal surfaces or the diapycnal direction. In the reference experiment the density is a linear function of the temperature alone; thus, the temperature gradient $\nabla\bar{T}$ defines the direction of normal vector $\hat{n}_{IS}$ to the isopycnal surface and specifies the direction of the diapycnal flux. The along isopycnal mixing is absent because by the definition temperature is constant in this direction. The form of the parameterization scheme is similar to (5.7) with the constant diffusivity coefficient K_{IS}:

$$\overline{\vec{v}'T'} = -K_{IS}\frac{\partial\bar{T}}{\partial n}\hat{n}_{IS} = -K_{IS}\nabla\bar{T} = -K_{IS}\left(\frac{\partial\bar{T}}{\partial x}\hat{\imath} + \frac{\partial\bar{T}}{\partial y}\hat{\jmath} + \frac{\partial\bar{T}}{\partial z}\hat{k}\right). \tag{5.10}$$

Given the downgradient nature of the diapycnal diffusivity, the test of the scheme is similar to the Fickian diffusivity. The vectors $\overline{\vec{v}'T'}$ and $\nabla\bar{T}$ must be oriented in the opposite directions. In the stronger form of the test K_{IS} is a constant throughout the basin. In the weaker form I identify positive K_{IS} as a function of space.

Green, 1970 [26] and *Stone, 1972* [55] Parameterization Scheme (GS)

The GS parameterization scheme was proposed originally for the modelling of atmospheric flows, where it relates the meridional and vertical components of eddy flux in zonal flows. It is based on the linear baroclinic instability theory that explains mechanisms underlying the processes of eddy formation and interaction with the time mean density structure. The baroclinically unstable process extracts the potential energy of the time mean density field. The necessary energy is then supplied by diabatic processes, thus maintaining the steady eddy heat flux across isentropic surfaces. Bellow, I explain the parameterization scheme based on the original publications and a review of the scheme in *Visbeck et al., 1997* [58].

The formulation of the GS parameterization scheme for the zonally averaged flows is

$$\begin{aligned} \overline{v'T'} &= -K_{vy}\frac{\partial \bar{T}}{\partial y} - K_{vz}\frac{\partial \bar{T}}{\partial z}, \\ \overline{w'T'} &= -K_{wy}\frac{\partial \bar{T}}{\partial y} - K_{wz}\frac{\partial \bar{T}}{\partial z}. \end{aligned} \tag{5.11}$$

The diffusivity coefficient K_{vy} was proposed in the following form

$$K_{vy} = \alpha\frac{f}{\sqrt{\mathrm{Ri}}}l^2, \tag{5.12}$$

where f is the Coriolis parameter, Ri$= \frac{N^2}{\left(\frac{\partial v}{\partial z}\right)}$ is the Richardson number, $N^2 = -\frac{g}{\rho_0}\frac{\partial \bar{\rho}}{\partial z}$ is the buoyancy frequency, l is a characteristic length scale or a mixing length scale, α is a parameter reflecting the efficiency of eddies in transforming the energy. The other way of describing the relation (5.12) is by using scaling arguments. The dimension of K_{vy} suggests to present (5.12) as a product of a characteristic eddy velocity $U_{eddy} = \frac{f}{\sqrt{\mathrm{Ri}}}l$ and characteristic length scale l. The characteristic eddy velocity can be estimated through the thermal wind relation. There are different proposals for the underlying nature of the mixing length scale. *Green, 1970* [26] suggested that the width of the baroclinic zone is a good representation of the length scale. *Stone, 1972* [55] proposed to use the first baroclinic radius of deformation $l = \frac{NH_B}{f}$, where H_B is the vertical scale of the baroclinic zone. While both of these scales are of a similar magnitude for atmospheric flows, they are different in the ocean circulation. The typical value of the oceanic radius of deformation for the midlatitudinal regions is about 30-40KM, while the width of the baroclinic zone is much larger and can be of the order of few hundred kilometers.

The second important part of the scheme lies in the connection with the vertical diffusivity. The underlying assumption of the scheme is that the mechanism of the eddy transfer is similar to the Eady model of the baroclinic instability. It specifies the direction of the fastest growing wave that corresponds to the half slope of the isopycnal, s_{IS}. The slope of the isopycnal in the case of the reference experiment can be computed as

$$\hat{s}_{IS} = \tan^{-1}\left(\frac{M^2}{N^2}\right),$$

where $M^2 = g\alpha\left|\nabla_h\bar{T}\right|$ and $N^2 = g\alpha\bar{T}_z$ are the measures of the horizontal and vertical stratifications. In deriving this relation the linear form of the equation of state had been used. The vertical temperature gradients usually are much larger then horizontal resulting in a relatively flat orientation of the isotherms in the interior of the ocean. Because for small angles $\tan\varphi \approx \varphi$, the slope of the isopycnal can be evaluated as

$$\hat{s}_{IS} = \frac{\left|\nabla_h\bar{T}\right|}{\bar{T}_z}. \tag{5.13}$$

This value equals to the magnitude of the slope vector $\vec{L}$ (Figure 5-2).

The baroclinic nature of the eddy transfer relates vertical components of the diffusive tensor as follows

$$K_{vz} = K_{wy} = \frac{1}{2}\hat{s}_{IS}K_{vy}, \tag{5.14}$$

and for the last component

$$K_{wz} = \frac{1}{2}\hat{s}_{IS}K_{vz} = \frac{1}{4}\hat{s}_{IS}^2 K_{vy}. \tag{5.15}$$

The original derivation of the parameterization scheme was developed for the zonally averaged flows in the atmosphere, where due to the absence of meridional boundaries the concept of zonal average (3.3) across the basin is well defined. In the case of oceanic flows, the presence of meridional coastal boundaries has a complex impact on the distribution of properties, thus breaking the homogeneity in the zonal direction. Instead I consider a local transfer in the IA plane. First, the eddy heat flux vector is decomposed into two components

$$\overline{\vec{v}'T'} = \overline{\vec{v}'T'}\Big|_{\mathrm{IA}} + \overline{\vec{v}'T'}\Big|_{\perp}, \tag{5.16}$$

where the first component belongs to the Isopycnal Angle plane (IA) (Figure 5-3) and the second is normal to that plane. The GS parameterization scheme can not be applied to the $\overline{\vec{v}'T'}\Big|_{\perp}$ because this component is orthogonal to the plane where the baroclinic transfer is predicted. Thus, the local GS scheme is used to diagnose only the component of the eddy heat flux $\overline{\vec{v}'T'}\Big|_{\mathrm{IA}} = \left(\overline{v'T'}\Big|_{\mathrm{IA}}, \overline{w'T'}\Big|_{\mathrm{IA}}\right)$ in a fashion analogous to zonally averaged representation (5.11)

$$\begin{aligned} \overline{v'T'}\Big|_{\mathrm{IA}} &= -K_{vs}\frac{\partial \bar{T}}{\partial s} - K_{vz}\frac{\partial \bar{T}}{\partial z}, \\ \overline{w'T'}\Big|_{\mathrm{IA}} &= -K_{ws}\frac{\partial \bar{T}}{\partial s} - K_{wz}\frac{\partial \bar{T}}{\partial z}, \end{aligned} \tag{5.17}$$

where s defines the direction of a slope vector (5.5) and the mixing coefficients are determined according to the rules (5.12)–(5.15):

$$K_{vs} = \alpha\frac{f}{\sqrt{\mathrm{Ri}}}l^2, \tag{5.18}$$

and

$$
\begin{aligned}
K_{vz} &= K_{ws} = \frac{1}{2}\hat{s}_{IS}K_{vs}, && (5.19)\\
K_{wz} &= \frac{1}{4}\hat{s}_{IS}^{2}K_{vs}. && (5.20)
\end{aligned}
$$

The test of the parameterization scheme involves the observation of the direction of the eddy heat flux with respect to the isopycnal surface. Consider the cross-section through IA (Figure 5-4). The shaded area defines the wedge of instability. If a fluid particle starting from the point A moves within the wedge to the point B or in the opposite direction, the baroclinic instability process extracts the potential energy from the time mean density structure. The mathematical formulation of the test involves the evaluation of the $ratio_{GS}$ of two angles (Figure 5-4): the fluid particle trajectory with the horizontal plane $\angle\left(\overline{\mathrm{AB}}, \vec{L}\right)$ and the isopycnal angle $\angle\left(\vec{S}, \vec{L}\right)$. The angles are computed by calculating the scalar product of two vectors. For two arbitrary vectors $\vec{a}$ and $\vec{b}$, the

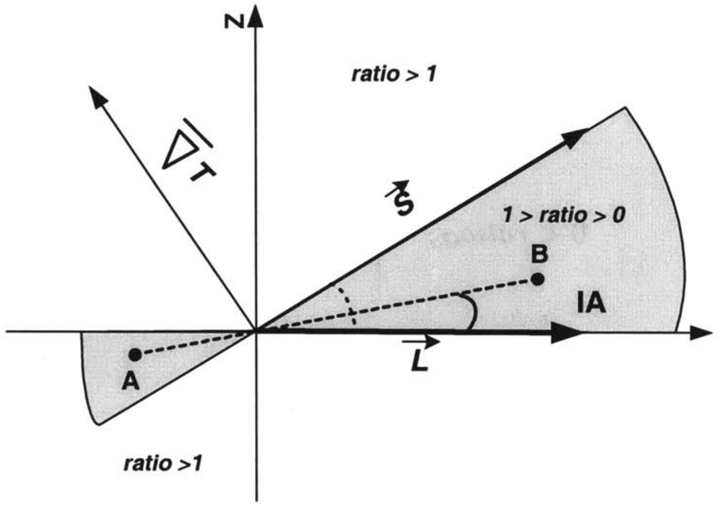

Figure 5-4: Wedge of intstability.

angle α between the vectors is

$$\alpha = \angle\left(\vec{a}, \vec{b}\right) = \cos^{-1}\left(\frac{\left(\vec{a} \cdot \vec{b}\right)}{|\vec{a}|\left|\vec{b}\right|}\right). \tag{5.21}$$

The local version of the parameterization scheme that is presented in this section proposes that the direction of the particle transfer is equivalent to the direction defined by the eddy heat flux in the IA plane. Thus, the evaluation of the angle of the particle trajectory is performed by evaluating the angle between the projection of the eddy heat flux on the IA plane and horizontal $\angle\left(\overline{\vec{v}'T'}\Big|_{\mathrm{IA}}, \vec{L}\right)$.

The test of the GS parameterization scheme identifies whether the direction of the eddy heat flux vector points into the wedge of instabilities. In this case the $ratio_{GS}$ is

$$0 < ratio_{GS} = \left|\frac{\angle\left(\overline{\vec{v}'T'}\Big|_{\mathrm{IA}}, \vec{L}\right)}{\angle\left(\vec{S}, \vec{L}\right)}\right| < 1. \tag{5.22}$$

If

$$ratio_{GS} = \left|\frac{\angle\left(\overline{\vec{v}'T'}\Big|_{\mathrm{IA}}, \vec{L}\right)}{\angle\left(\vec{S}, \vec{L}\right)}\right| = \frac{1}{2},$$

then within these areas the Green–Stone parameterization scheme provides a consistent representation of the component of the eddy heat flux $\overline{\vec{v}'T'}\Big|_{\mathrm{IA}}$.

The divergence of the flux $\vec{F}_{GS}$ associated with the transfer in the IA plane according to GS parameterization scheme (5.17) can be computed provided the estimate of the variable mixing coefficient K_{vs} (5.18). The derivative of $\bar{T}$ in the direction defined by the isopycnal slope $\vec{L}$ can be calculated as

$$\frac{\partial \bar{T}}{\partial s} = \left(\nabla_h \bar{T} \cdot \frac{\vec{L}}{\left|\vec{L}\right|}\right) = -\left|\nabla_h \bar{T}\right|. \tag{5.23}$$

The components of the flux in the IA plane are

$$\vec{F}_{GS} = \left(F^L_{GS}, F^w_{GS}\right)\big|_{\mathrm{IA}} = \left(\overline{v'T'}\Big|_{\mathrm{IA}}, \overline{w'T'}\Big|_{\mathrm{IA}}\right), \tag{5.24}$$

where the first component belongs to the horizontal plane with the direction defined by $\vec{L}$ and the second component is in the vertical direction. The model evaluates divergence of a flux vector in the original geodetic coordinate system; thus, (5.24) requires projection on the basis $(\hat{x}, \hat{y}, \hat{z})$ according to formula

$$\vec{F}_{GS} = \left(F^x_{GS}, F^y_{GS}, F^z_{GS}\right) = \left(-\left|F^L_{GS}\right| \frac{\bar{T}_x}{\left|\nabla_h \bar{T}\right|}, -\left|F^L_{GS}\right| \frac{\bar{T}_y}{\left|\nabla_h \bar{T}\right|}, F^w_{GS}\right).$$

The evaluation of the mixing coefficient K_{vs} is performed according to *Visbeck et. al, 1997* [58] as a two–dimensional field:

$$K_{vs} = \alpha \overline{\frac{f}{\sqrt{\mathrm{Ri}}}}^{z} l^2, \tag{5.25}$$

where the Eady growth rate is averaged (operator $\overline{\cdot}^{z}$) over the upper 7 layers of the model of the total depth $950M$. All other mixing coefficients in (5.17) are computed according to (5.19) and (5.20).

The computed divergence of $\vec{F}_{GS}$ is compared with the total divergence of the eddy heat flux evaluated from the reference simulation.

5.3.2 Adiabatic Parameterization Schemes

Gent and McWilliams, 1990 [23] Parameterization Scheme (GM90)

The Gent–McWilliams eddy heat flux parameterization scheme assumes that the role of eddies in the establishment of the time mean density structure can be represented by an adiabatic process. An additional component of velocity, so called *residual velocity,* is added to the time mean Eulerian velocity $\overline{\vec{v}}$, so that the effective advective velocity in the time mean temperature balance becomes a transformed Eulerian velocity.

The temperature balance equation in the Eulerian sense is

$$\overline{\vec{v}_h} \cdot \nabla_h \bar{T} + \bar{w}\frac{\partial}{\partial z}\bar{T} = -\nabla\left(\overline{\vec{v}'T'}\right) + \overline{Q} + \overline{D}, \qquad (5.26)$$

where $\overline{Q}$ is the diabatic forcing, $\overline{D}$ is internal mixing due to processes other than mesoscale eddies and the divergence of the time mean heat flux $\nabla\left(\overline{\vec{v}'T'}\right)$ was simplified using a non–divergence condition $\nabla \cdot \overline{\vec{v}} = 0$. GM90 reformulates the balance (5.26) in the transformed Eulerian mean formulation as

$$\overline{\vec{V}_h} \cdot \nabla_h \bar{T} + \bar{W}\frac{\partial}{\partial z}\bar{T} = \overline{Q} + \overline{D} - \bar{R}, \qquad (5.27)$$

where

$$\begin{aligned} \overline{\vec{V}_h} &= \overline{\vec{v}_h} + \vec{v}_h^*, \\ \overline{W} &= \bar{w} + w^*, \end{aligned}$$

a right hand side term $\bar{R}$ is the along isopycnal mixing and $(\vec{v}_h^*, w^*)$ is the residual velocity.

The proposed form of the residual circulation in the case of a linear equation of state with constant salinity can be obtained as

$$\begin{aligned} \vec{v}_h^* &= -\frac{\partial}{\partial z}\left(K_{GM}\,\vec{L}\right), \\ w^* &= \nabla_h \cdot \left(K_{GM}\vec{L}\right), \end{aligned} \qquad (5.28)$$

where the magnitude of the horizontal vector $\vec{L}$ (5.5) defines the isopycnal slope. By construction the flow of the residual circulation is non–divergent, i.e.

$$\nabla_h \cdot \vec{v}_h^* + \frac{\partial}{\partial z}w^* = 0.$$

In addition with the simplified equation of state the isopycnal diffusion is absent; thus, $\bar{R} = 0$. The external diabatic forcing $\overline{Q} = 0$ for all layers excluding the upper one.

Substituting the components of the residual velocity (5.28) into (5.27) I obtain the following temperature balance equation in the transformed Eulerian mean formulation within the framework of the reference simulation. It can be directly compared to the Eulerian mean formulation of the equations (5.26)

$$\begin{aligned} \overline{\vec{v}_h} \cdot \nabla_h \bar{T} + \bar{w}\frac{\partial}{\partial z}\bar{T} &= \overline{Q} + \overline{D} + \frac{\partial}{\partial z}\left(K_{GM}\vec{L}\right) \cdot \nabla_h \bar{T} - \nabla_h \cdot \left(K_{GM}\vec{L}\right)\frac{\partial}{\partial z}\bar{T} && (5.29)\\ &= \overline{Q} + \overline{D} - \nabla \cdot \vec{F}_{GM}, && (5.30) \end{aligned}$$

where $\vec{F}_{GM}$ is flux vector that can be associated with the GM mixing.

The comparison between right hand sides of (5.26) and (5.29) forms the test of the parameterization scheme. GM90 parameterization scheme used a constant coefficient $K_{GM} = const$. Thus, by evaluating the sign of ratio

$$ratio_{GM} = \frac{\nabla \cdot \overline{\vec{v}'T'}}{-\frac{\partial}{\partial z}\vec{L} \cdot \nabla_h \bar{T} + \nabla_h \cdot \vec{L}\frac{\partial}{\partial z}\bar{T}}$$

I can identify the areas where the $ratio_{GM} > 0$, that is the positive coefficient K_{GM} exists and the divergence of the eddy heat flux can be represented with the Gent-McWilliams parameterization scheme. The distribution of the mixing coefficient shows the strength of mixing due to the Gent–McWilliams parameterization scheme. The smaller the $ratio_{GM}$ the larger is the implied mixing.

Expanding the formula for $\nabla \cdot \vec{F}_{GM}$ in the case of constant K_{GM} I obtain

$$\nabla \cdot \vec{F}_{GM} = -K_{GM}\left(\frac{\partial}{\partial z}\vec{L} \cdot \nabla_h \bar{T} - \nabla_h \cdot \vec{L}\frac{\partial}{\partial z}\bar{T}\right). \qquad (5.31)$$

After substituting $\vec{L} = (L^x, L^y, 0) = \left(-\frac{\bar{T}_x}{\bar{T}_z}, -\frac{\bar{T}_y}{\bar{T}_z}, 0\right)$, where superscript indicates the component in the local Cartesian basis and subscript — partial derivative, the divergence of GM flux can be evaluated as

$$\begin{aligned}\nabla \cdot \vec{F}_{GM} &= -K_{GM}\left(\bar{T}_{xx} + \bar{T}_{yy} + \frac{\bar{T}_x^2 + \bar{T}_y^2}{\bar{T}_z^2}\bar{T}_{zz} - 2\frac{\bar{T}_x}{\bar{T}_z}T_{xz} - 2\frac{\bar{T}_y}{\bar{T}_z}T_{yz}\right) \\ &= -K_{GM}\left(\bar{T}_{xx} + \bar{T}_{yy} + \hat{s}_{IS}^2\bar{T}_{zz} + 2L^xT_{xz} + 2L^yT_{yz}\right).\end{aligned} \tag{5.32}$$

If the slope of the isopycnal is small $\hat{s}_{IS} \ll 1$, then the dominant terms in the balance are the horizontal Fickian diffusion. This simplifications shows the correspondence between the diabatic Fickian diffusion and Gent–McWilliams eddy parameterization scheme in a simplified formulation of a reference simulation.

5.4 Evaluation of the Tests

This section evaluates the tests of the eddy heat flux parameterization schemes as outlined in previous sections. In Chapter 4 it was demonstrated by calculating the contribution of eddies to the establishment of the thermal state of the reference experiment that time–dependent motions are important only in limited parts of the model domain, predominantly in the upper $1000M$ of the western boundary area in the mid–latitudinal region. Figure 5-5 presents the three–dimensional divergence of the eddy heat flux for the second layer. The areas where the eddy heat flux divergence is strong are located in this region for the other thermocline layers as well. The western area from $25°N$ to $50°N$ and from the western boundary to about $10°E$ is chosen for the evaluation of the schemes (larger rectangular area in Figure 5-5. The three layers that span the vertical range of the main thermocline are considered: the upper layer $0M$—$50M$, the subsurface layer $50M$—125M and a thermocline layer $350M$—$500M$ (fifth layer). Some parts of the region possess a large divergence of the eddy heat flux; for others this quantity is relatively weak. I test how well the parameterization schemes reproduce the eddy heat flux and its three–dimensional divergence for the areas where it is a leading member of the balance and where it is weak.

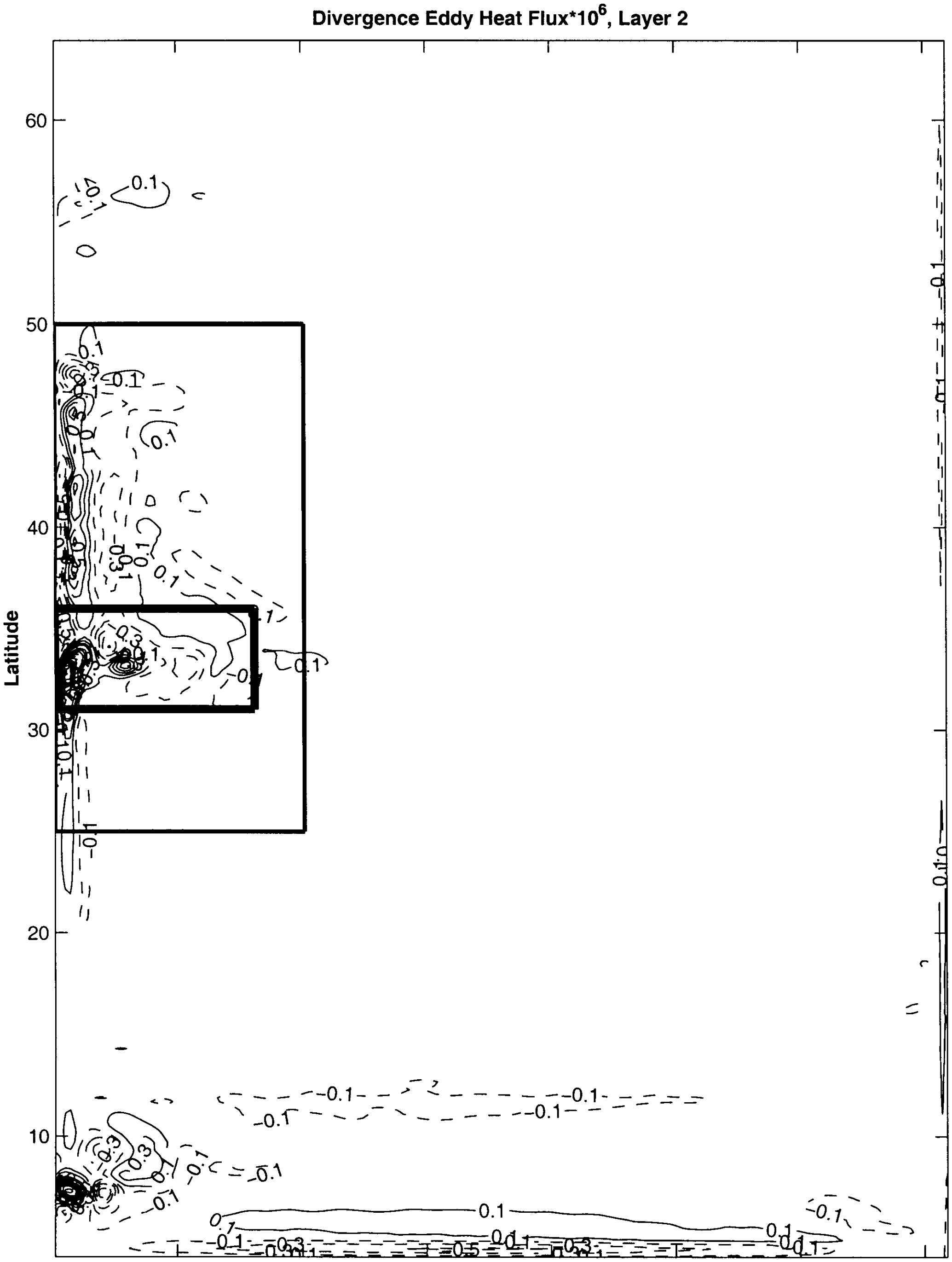

Figure 5-5: Divergence of the eddy heat flux. Layer 2. C.I. $0.2 \cdot 10^{-6}$ $[°C \cdot \text{sec}^{-1}]$.

The evaluation of the tests is performed on the fine grid of the reference experiment as well as averaged over boxes with 1° × 1° and 2° × 2° in the horizontal dimension. The time mean temperature field and the components of the eddy heat flux were averaged according to the procedure outlined in the Appendix A. before the evaluation of the tests.

The evaluation of the tests based on the physical mechanism of the parameterization scheme allows the estimation of respective mixing coefficients. The three–dimensional divergence of implied flux using the estimated coefficients is presented for the parameterization schemes and compared with the divergence of the eddy heat flux calculated from the data. This set of diagnostic quantities is computed in the smaller subdomain of the western area (smaller rectangular area in Figure 5-5) where eddies are the most active for all three considered layers. Figure 5-6 shows the three–dimensional divergence of the eddy heat flux in this subdomain for layers 1, 2 and 5 (subplots (a), (b) and (c) respectively).

5.4.1 Test of Fickian Diffusion

Figures 5-7, 5-8 and 5-9 present the evaluation of the test of the Fickian diffusion on the fine grid 0.2° × 0.2° for the layers 1, 2 and 5 respectively.

The most important observation about the direction of the eddy heat flux with respect to the isotherms is the eddy heat flux in general is not downgradient to the time mean temperature distribution. For each component the areas of the downgradient flux, represented as white on the figures, neighbour the areas where the eddy heat flux is upgradient, shaded in gray. For the individual coefficients the area corresponding to the positive sign, or white areas, varies as well (Table 5.1). It ranges from 42% for K_{Tw} in the thermocline layer (Figure 5-9(c)) to 78% for K_{Tv} in the upper layer (Figure 5-7(b)). In general the area representing the positive mixing coefficients decreases with the depth for all three components.

The magnitude of the implied downgradient mixing also varies. In general, it is

(a) Divergence Eddy Heat Flux*10^6, Layer 1

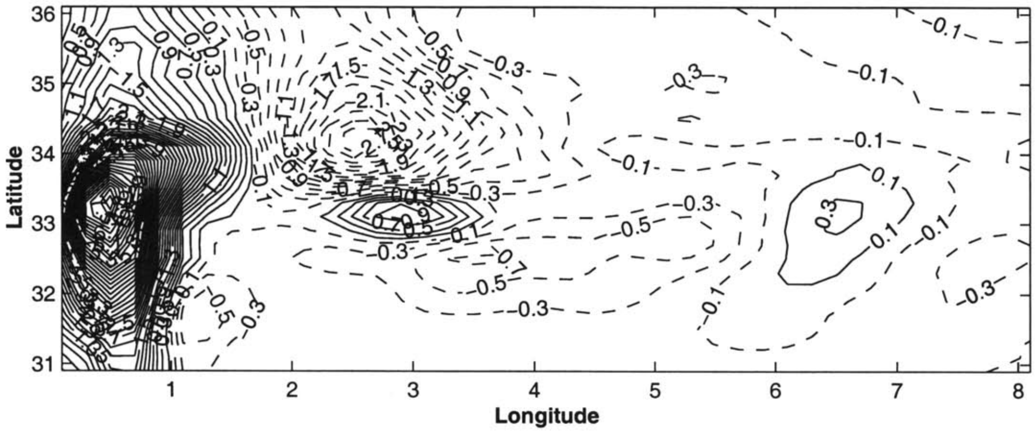

(b) Layer 2

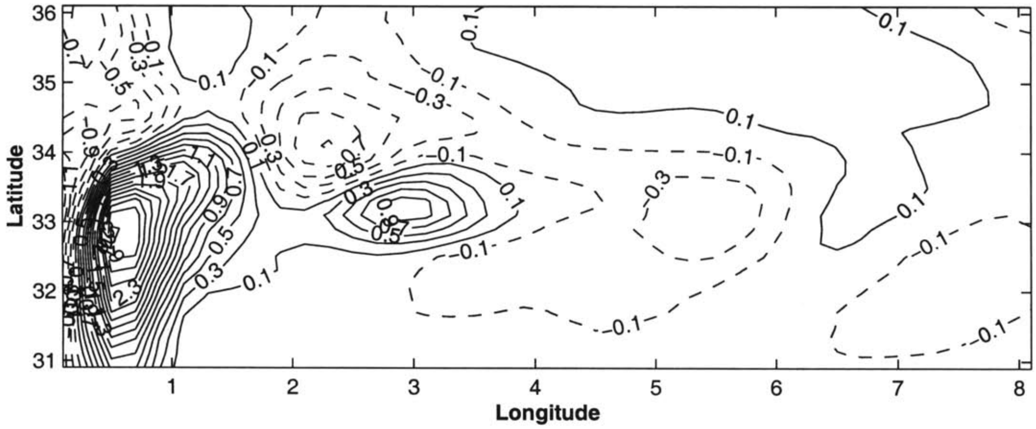

(c) Layer 5

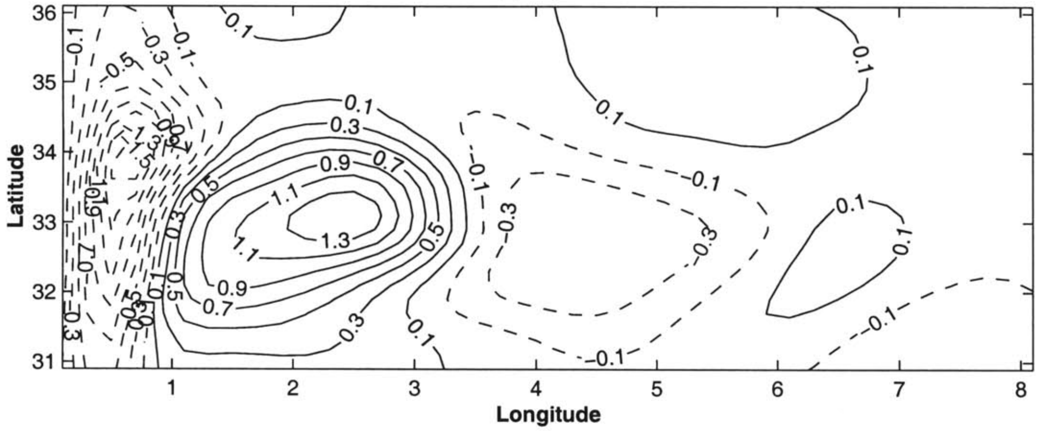

Figure 5-6: Divergence of the eddy heat flux. (a) Layer 1. (b) Layer 2. (c) Layer 5. C.I. $0.2{\cdot}10^{-6}\ [^{\circ}C \cdot \sec^{-1}]$

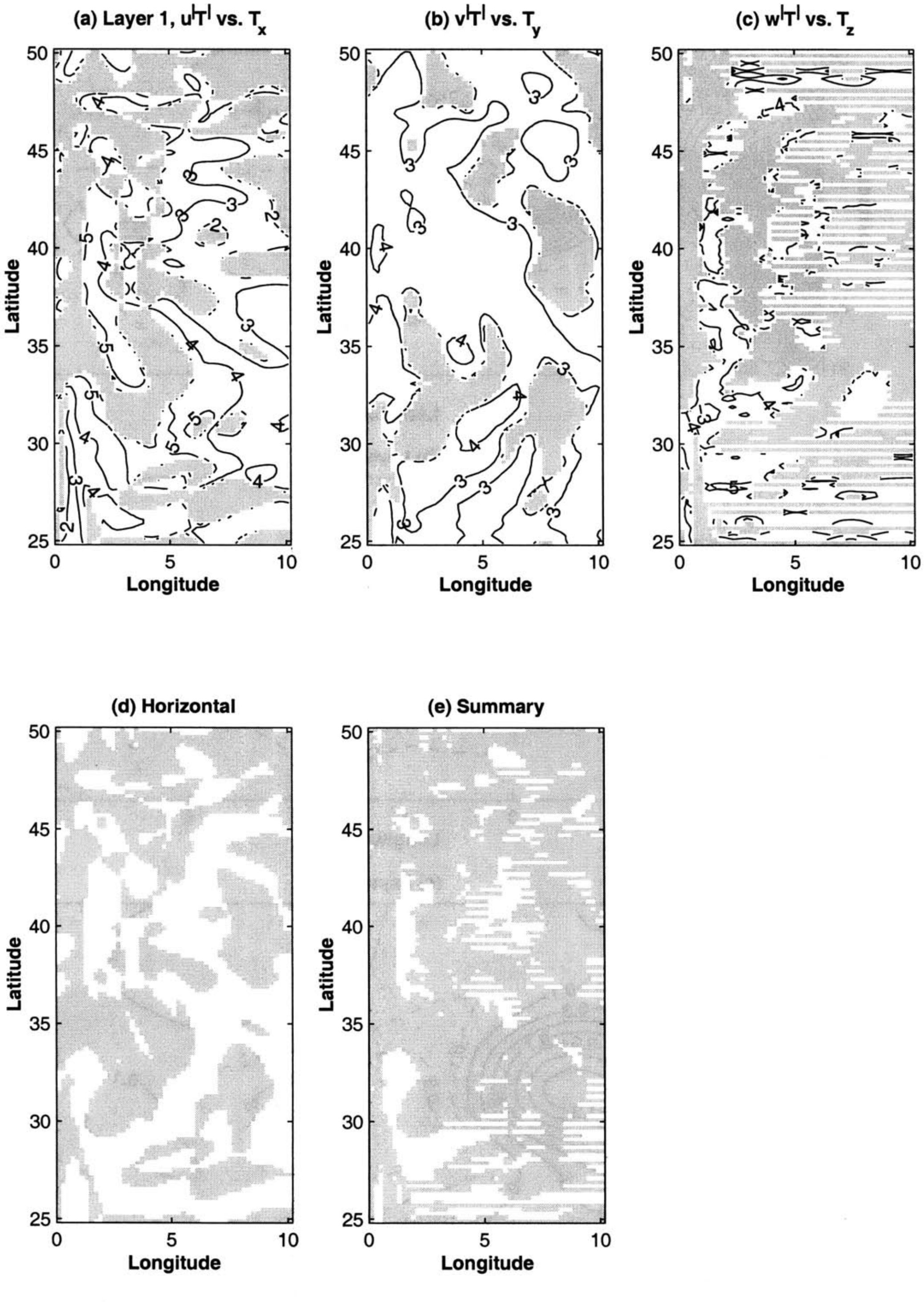

Figure 5-7: Test of the Fickian diffusivity on the fine grid. Layer 1. (a) K_{Tu}, (b) K_{Tv}, (c) K_{Tw}, (d) horizontal test, (e) summary of the test. White areas identify the positive diffusivity coefficients. Contour values are $\log_{10}$ of the coefficients, $[M^2 \cdot \sec^{-1}]$.

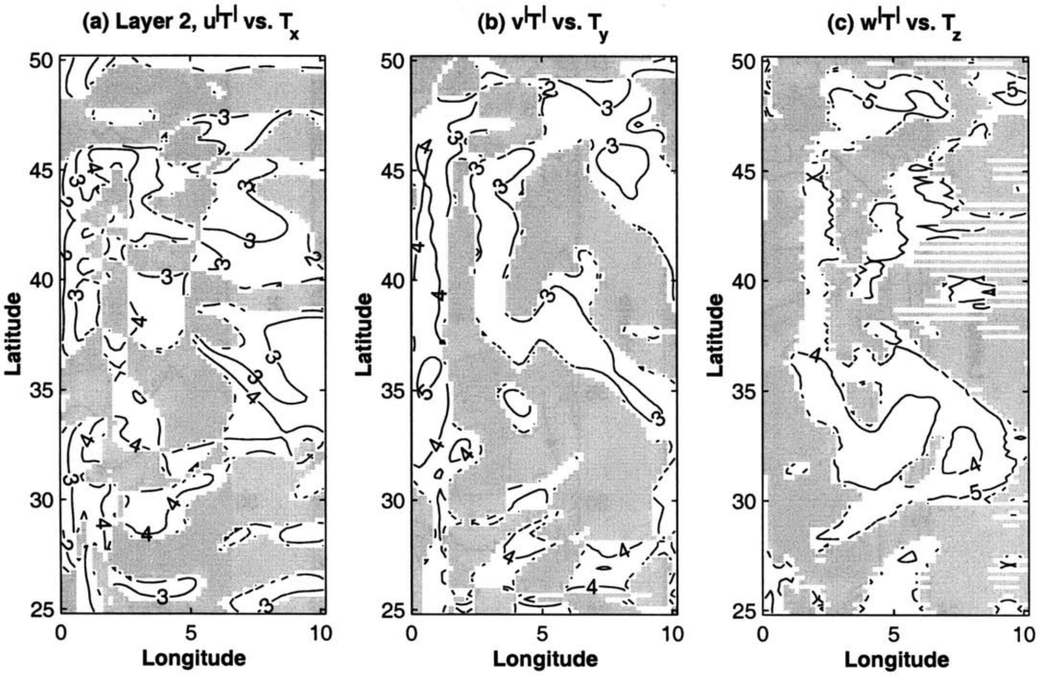
(a) Layer 2, u'T' vs. T_x (b) v'T' vs. T_y (c) w'T' vs. T_z

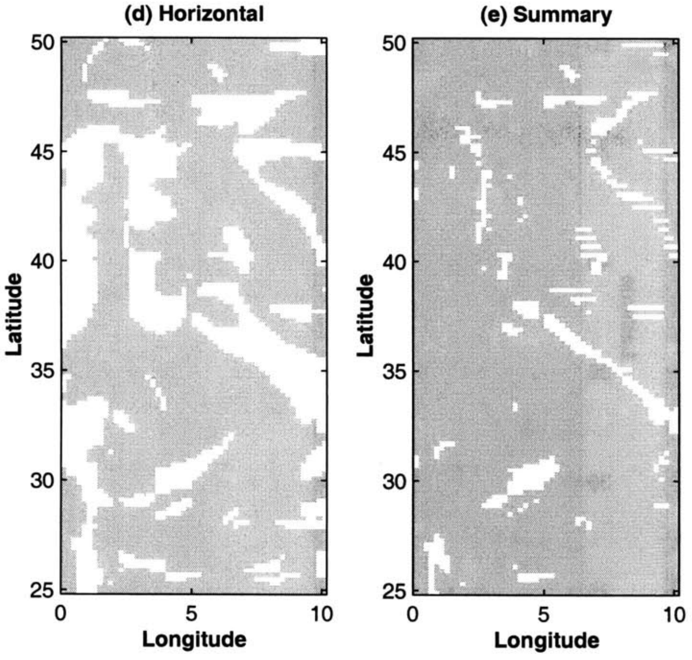
(d) Horizontal (e) Summary

Figure 5-8: Test of the Fickian diffusivity on the fine grid. Layer 2. (a) K_{Tu}, (b) K_{Tv}, (c) K_{Tw}, (d) horizontal test, (e) summary of the test. White areas identify the positive diffusivity coefficients. Contour values are $\log_{10}$ of the coefficients, $[M^2 \cdot \sec^{-1}]$.

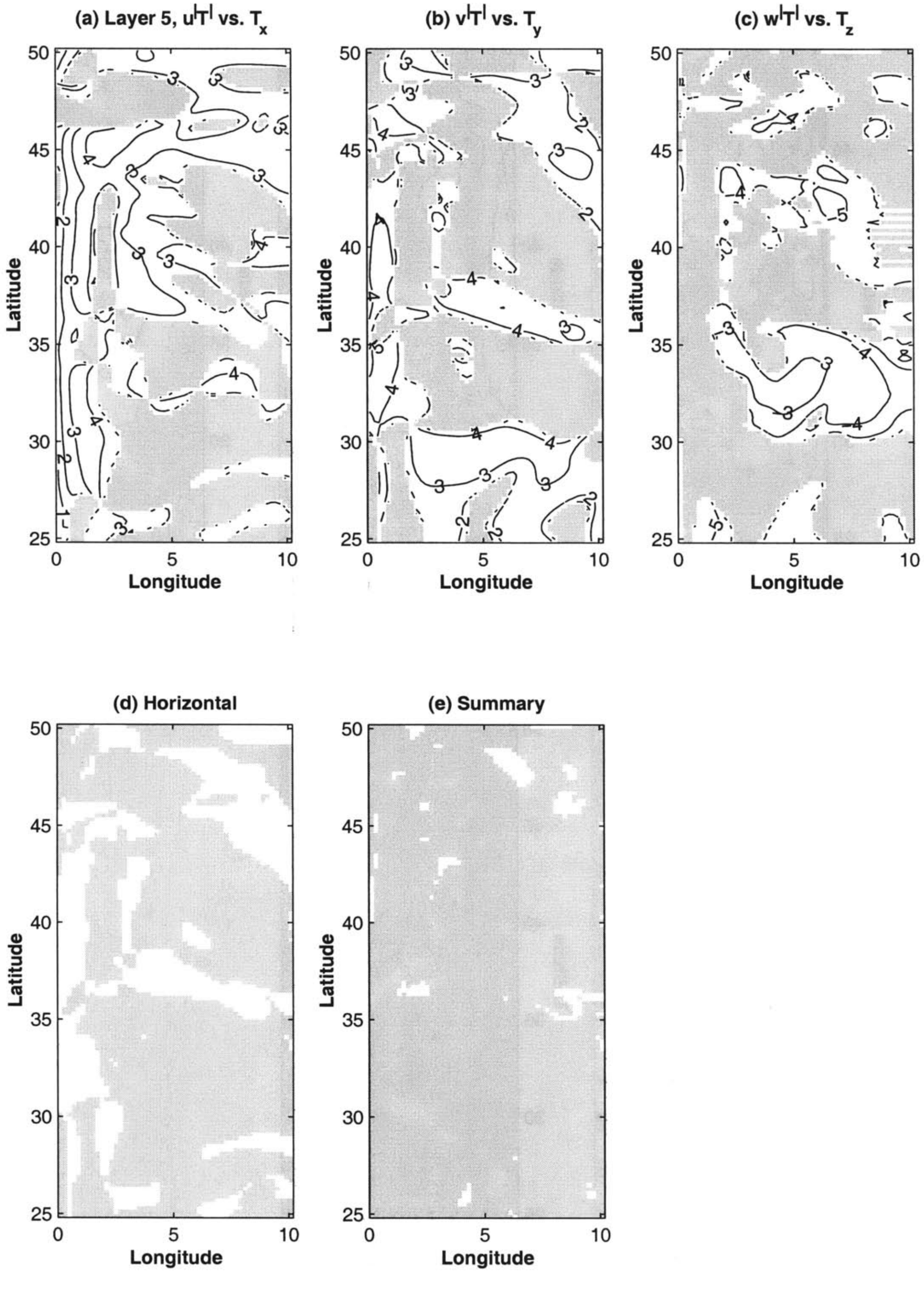

Figure 5-9: Test of the Fickian diffusivity on the fine grid. Layer 5. (a) K_{Tu}, (b) K_{Tv}, (c) K_{Tw}, (d) horizontal test, (e) summary of the test. White areas identify the positive diffusivity coefficients. Contour values are $\log_{10}$ of the coefficients, $[M^2 \cdot \sec^{-1}]$.

Layer	$\frac{\text{area}(K_{Tu}>0)}{\text{total area}}$	$\frac{\text{area}(K_{Tv}>0)}{\text{total area}}$	$\frac{\text{area}(K_{Tw}>0)}{\text{total area}}$	Horizontal	Summary
1	63%	78%	51%	47%	23%
2	56%	52%	49%	29%	8%
5	57%	50%	42%	30%	4%

Table 5.1: Percent of total area of the Western region with positive diffusivity coefficients. Fine grid

consistent with the magnitude of the coefficients used in coarse resolution climate models: about $10^3 - 10^4$ $[M^2 \cdot \text{sec}^{-1}]$ for the horizontal components and $10^{-4} - 10^{-5}$ $[M^2 \cdot \text{sec}^{-1}]$ for the vertical component. The qualitative analysis of the areas reveals the strengthening of horizontal mixing in the upper layers and closer to the western boundary where the strength of eddies is the largest.

The overall test of the parameterization scheme indicates that the Fickian diffusion fails in reproducing the eddy heat flux as the three–dimensional downgradient transport of temperature. The summary plots (Figures 5-7(e), 5-8(e) and 5-9(e)) show that only small area of the domain where all three coefficients are positive simultaneously. The coverage of these areas decreases from 23% for the upper layer to 8% for the second and only 4% for the fifth. The small correlation between all three coefficients for each layer can be explained by general anticorrelation in the distribution of the vertical mixing coefficient K_{Tw} with either horizontal coefficients. The evaluation of downgradient horizontal diffusivity alone (Figures 5-7(d), 5-8(d) and 5-9(d)) reveals a significant decrease in the areas simultaneously occupied by the positive coefficients when introducing the vertical mixing coefficient K_{Tw}.

The noisy patterns of the K_{Tw} field for the upper layer are due to the distribution of $\overline{w'T'}$ for this area (Figure 5-10). As described in a previous section this value estimated at the interface with the subsurface layer was assigned to represent the vertical eddy heat flux for the upper layer. The magnitude of the vertical eddy heat flux is small in this area and oscillates around 0. In addition the vertical component of temperature gradient $\bar{T}_z$ (Figure 5-11) due to strong convective mixing between the upper and the second layer in this region is small. Thus, the resulting estimate of the vertical mixing coefficient is not stable.

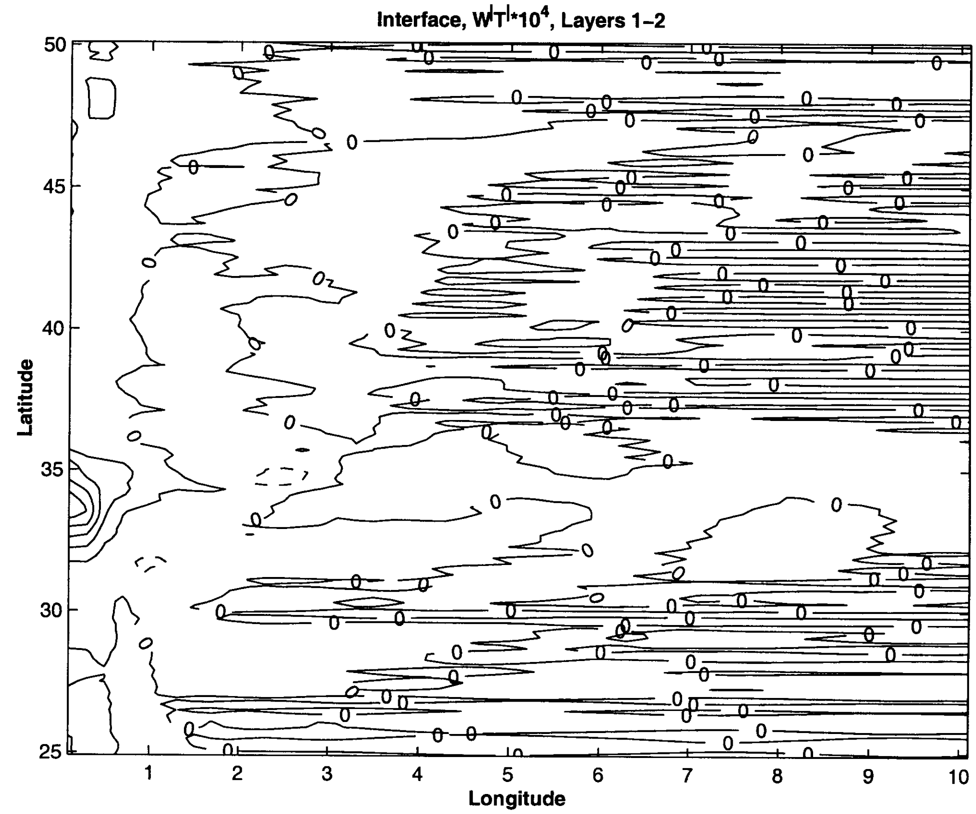

Figure 5-10: Vertical component of the eddy heat flux, evaluated at the interface between the first and second layers, $[10^{-4} {}^{\circ}C \cdot M \cdot \sec^{-1}]$.

The evaluation of the test on the averaged fields over boxes with 1° × 1° (Figures 5-12, 5-13 and 5-14 for layers 1,2 and 5 respectively) and 2° × 2° (Figures 5-15, 5-16 and 5-17 for layers 1,2 and 5 respectively) does not change the overall balances.

Tables 5.2 and 5.3 show the areas where the individual diffusivity coefficients and their superimposition are positive as a percent of total area of the region.

The vertical component again is generally anticorrelated with the horizontal components especially in deeper layers in the western boundary region. The estimation is more

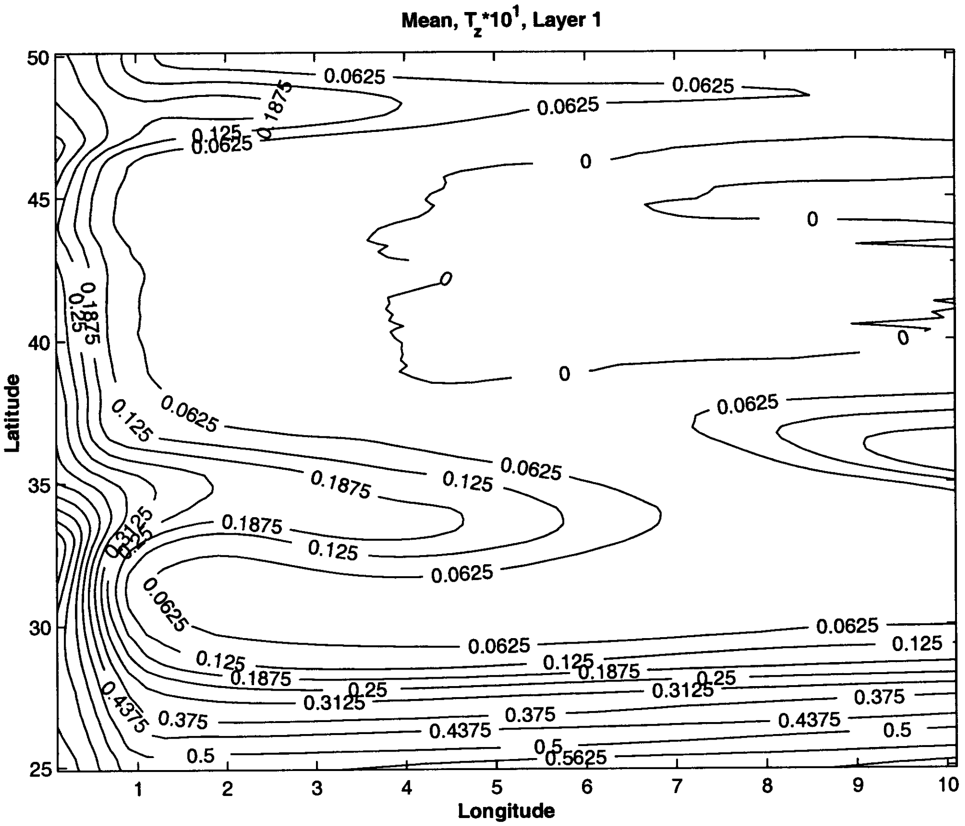

Figure 5-11: Distribution of $\bar{T}_z$, evaluated at the interface between the first and second layers, $[10^{-1}{}^\circ C \cdot M^{-1}]$.

Layer	$\frac{\text{area}(K_{Tu}>0)}{\text{total area}}$	$\frac{\text{area}(K_{Tv}>0)}{\text{total area}}$	$\frac{\text{area}(K_{Tw}>0)}{\text{total area}}$	Horizontal	Summary
1	62%	81%	53%	49%	22%
2	55%	53%	47%	30%	8%
5	57%	50%	40%	27%	4%

Table 5.2: Percent of total area of the Western region with positive diffusivity coefficients. Averaged over a 1° × 1° box

Layer	$\frac{\text{area}(K_{Tu}>0)}{\text{total area}}$	$\frac{\text{area}(K_{Tv}>0)}{\text{total area}}$	$\frac{\text{area}(K_{Tw}>0)}{\text{total area}}$	Horizontal	Summary
1	42%	85%	51%	33%	15%
2	74%	56%	42%	45%	10%
5	60%	44%	34%	21%	5%

Table 5.3: Percent of total area of the Western region with positive diffusivity coefficients. Averaged over a 2° × 2° box

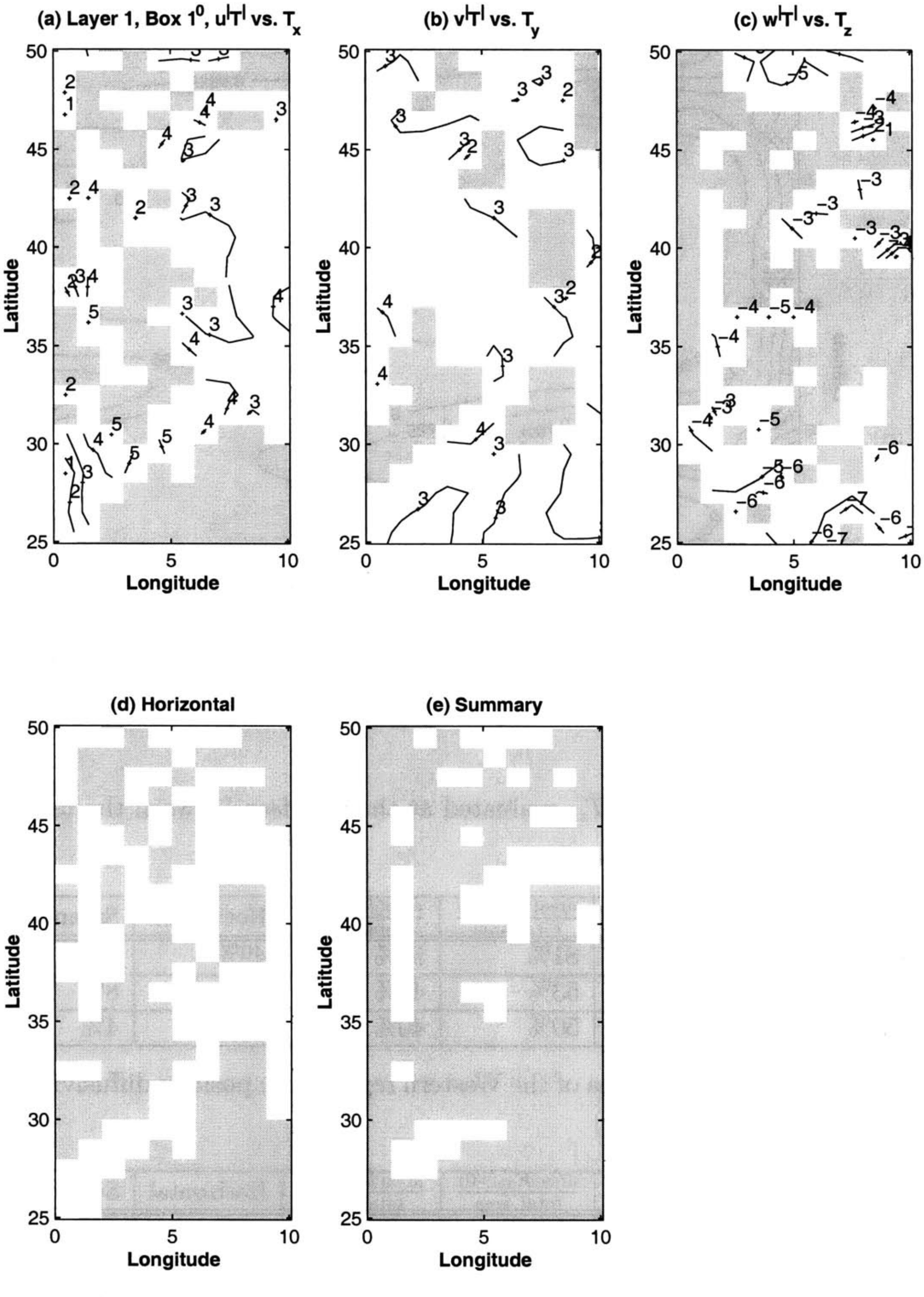

Figure 5-12: Test of the Fickian diffusivity on the 1° × 1° grid. Layer 1. (a) K_{Tu}, (b) K_{Tv}, (c) K_{Tw}, (d) horizontal test, (e) summary of the test. White areas identify the positive diffusivity coefficients. Contour values are $\log_{10}$ of the coefficients, $[M^2 \cdot \mathrm{sec}^{-1}]$.

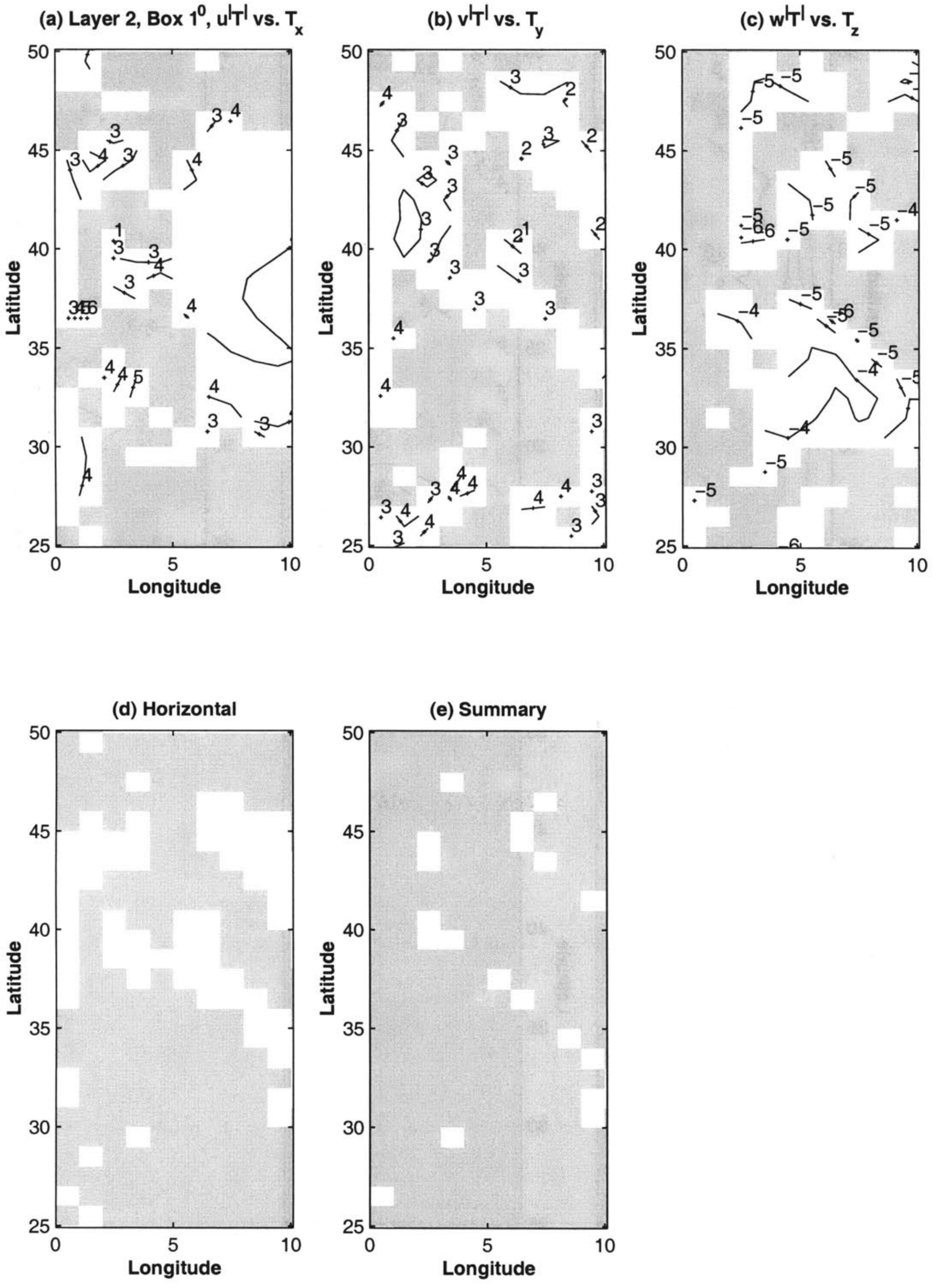

Figure 5-13: Test of the Fickian diffusivity on the 1° × 1° grid. Layer 2. (a) K_{Tu}, (b) K_{Tv}, (c) K_{Tw}, (d) horizontal test, (e) summary of the test. White areas identify the positive diffusivity coefficients. Contour values are $\log_{10}$ of the coefficients, $[M^2 \cdot \sec^{-1}]$.

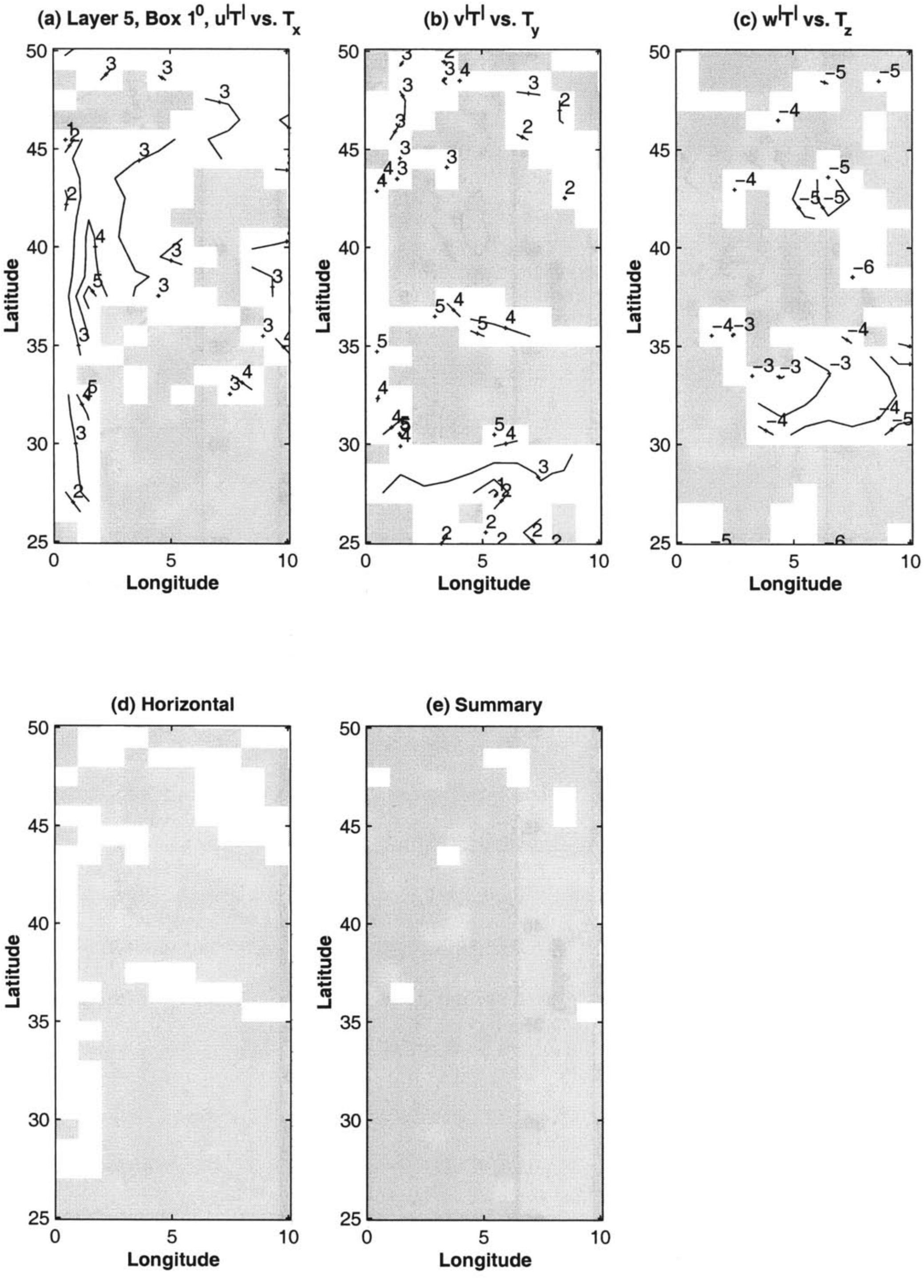

Figure 5-14: Test of the Fickian diffusivity on the 1° × 1° grid. Layer 5. (a) K_{Tu}, (b) K_{Tv}, (c) K_{Tw}, (d) horizontal test, (e) summary of the test. White areas identify the positive diffusivity coefficients. Contour values are $\log_{10}$ of the coefficients, $[M^2 \cdot \text{sec}^{-1}]$.

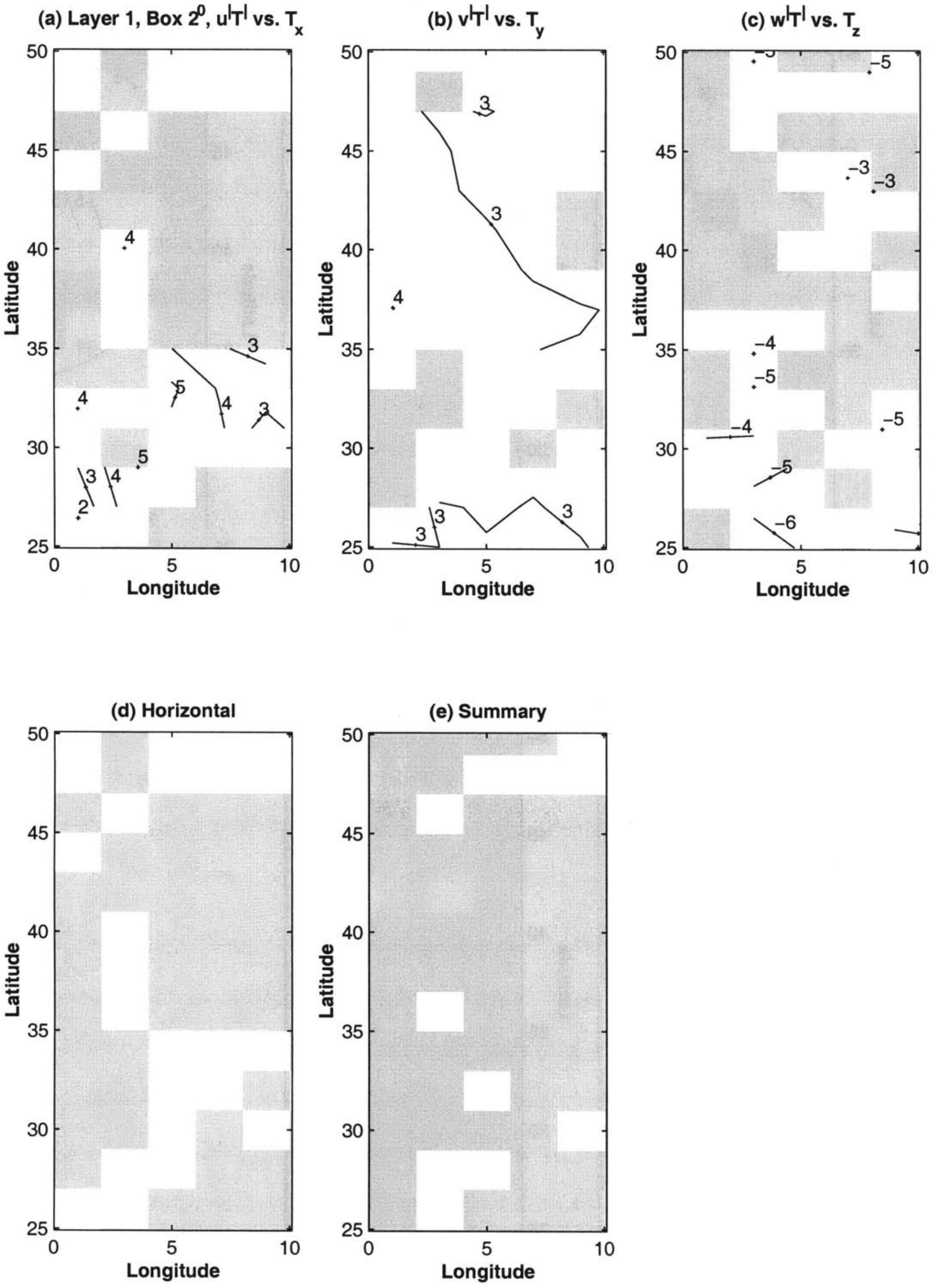

Figure 5-15: Test of the Fickian diffusivity on the 2° × 2° grid. Layer 1. (a) K_{Tu}, (b) K_{Tv}, (c) K_{Tw}, (d) horizontal test, (e) summary of the test. White areas identify the positive diffusivity coefficients. Contour values are $\log_{10}$ of the coefficients, $[M^2 \cdot \sec^{-1}]$.

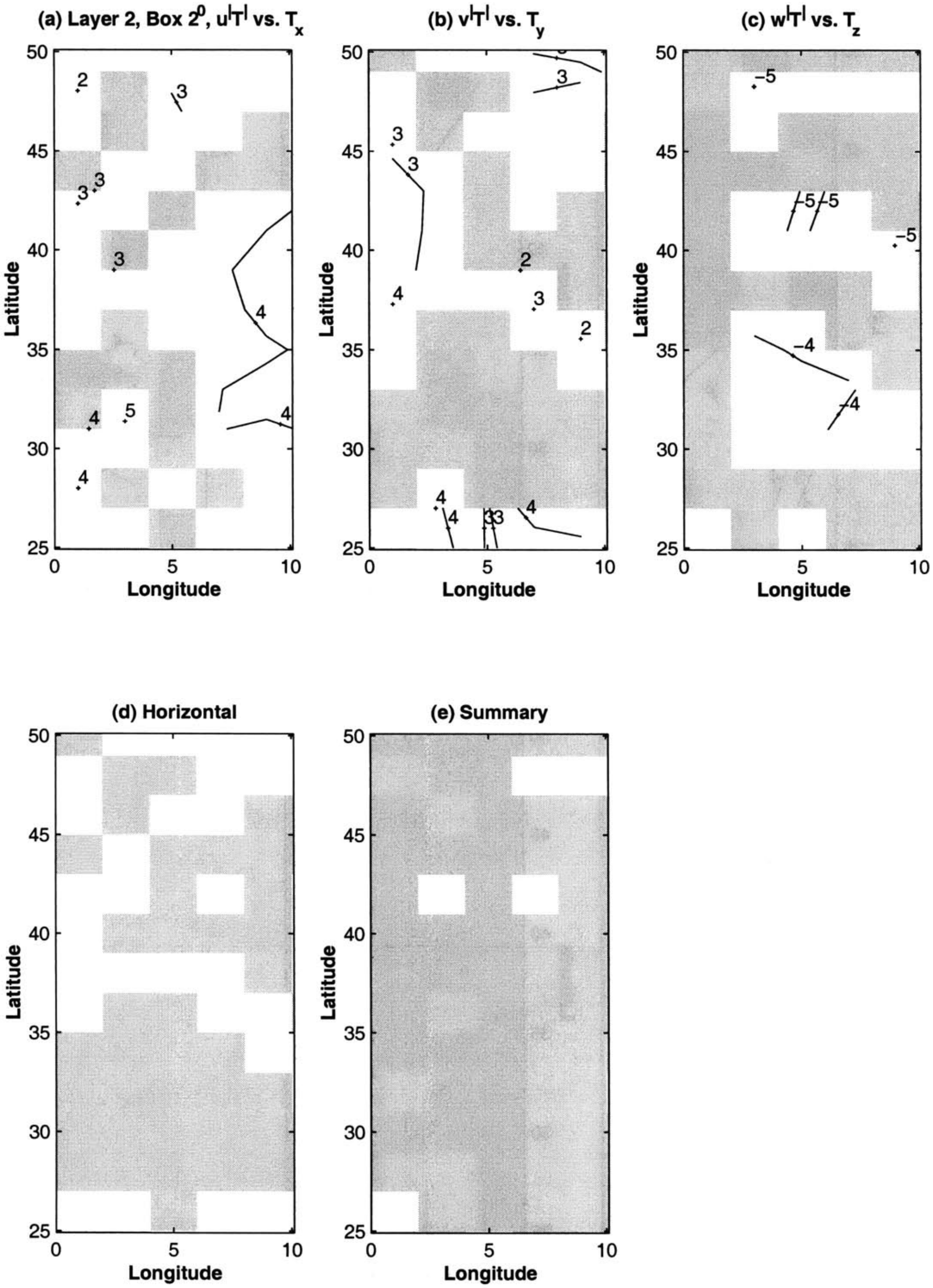

Figure 5-16: Test of the Fickian diffusivity on the 2° × 2° grid. Layer 2. (a) K_{Tu}, (b) K_{Tv}, (c) K_{Tw}, (d) horizontal test, (e) summary of the test. White areas identify the positive diffusivity coefficients. Contour values are $\log_{10}$ of the coefficients, $[M^2 \cdot \sec^{-1}]$.

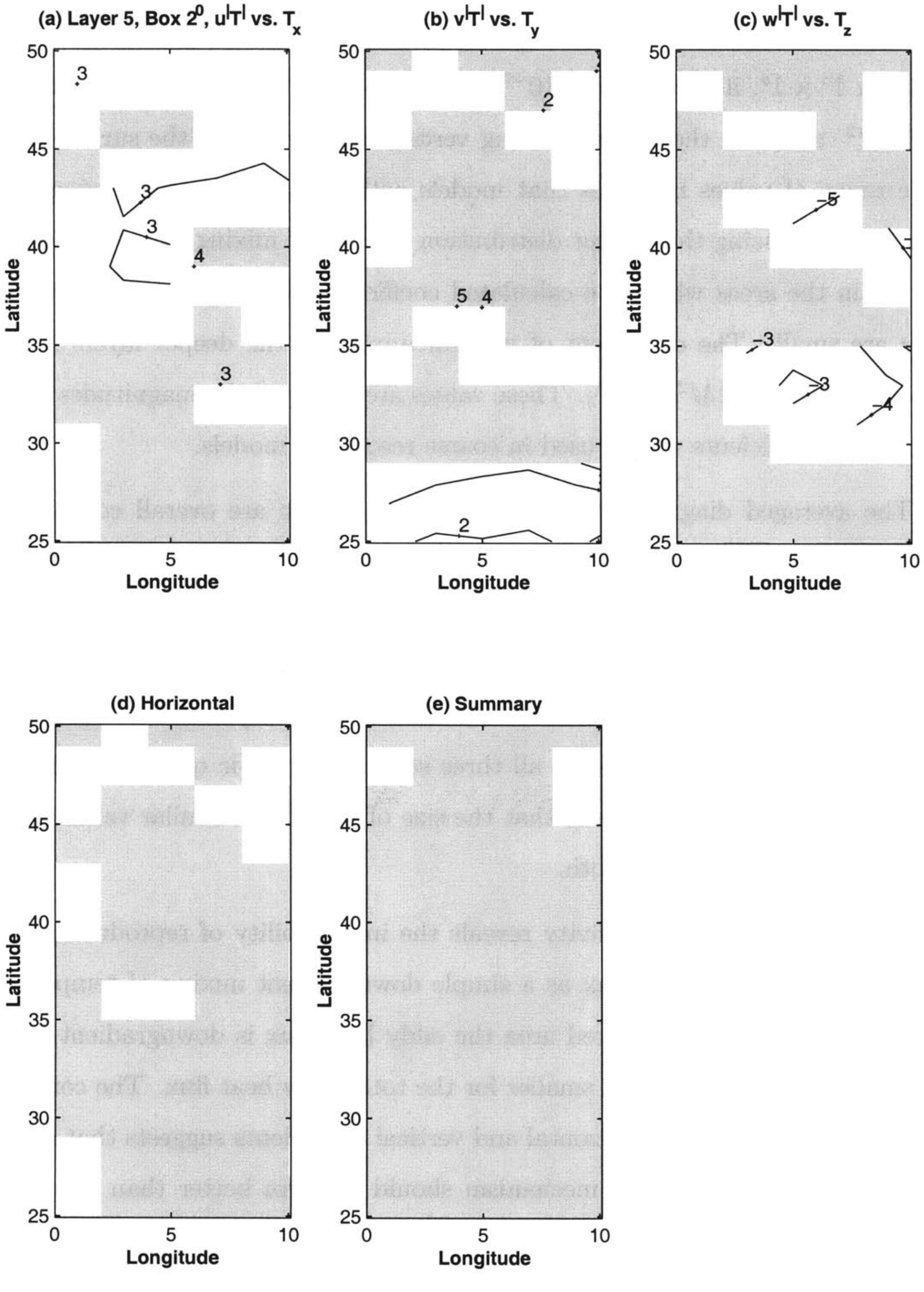

Figure 5-17: Test of the Fickian diffusivity on the $2^\circ \times 2^\circ$ grid. Layer 5. (a) K_{Tu}, (b) K_{Tv}, (c) K_{Tw}, (d) horizontal test, (e) summary of the test. White areas identify the positive diffusivity coefficients. Contour values are $\log_{10}$ of the coefficients, $[M^2 \cdot \text{sec}^{-1}]$.

stable, thus, allowing the evaluation of the vertical mixing coefficient. The magnitude of vertical mixing has a wide range. In the upper layer (Figure 5-12(c)), when averaged on 1° × 1°, it ranges from $10^{-7}\,[M^2 \cdot \mathrm{sec}^{-1}]$ for the southern part of the region to $10^{-1}\,[M^2 \cdot \mathrm{sec}^{-1}]$ in the areas of strong vertical mixing due to the surface cooling. This wide range of values indicates that models with uniform vertical mixing will not succeed in reproducing the correct distribution of vertical mixing. They underestimate the mixing in the areas where the calculated coefficients are large, and overestimate where they are small. The coefficient of vertical mixing in the deeper layers 2 and 5 is between $10^{-5} - 10^{-3}\ [M^2 \cdot \mathrm{sec}^{-1}]$. These values are closer to the magnitudes of the vertical diffusivity coefficients widely used in coarse resolution models.

The averaged diagnostics on the box with 1° side are overall consistent with the fine resolution diagnostics (Tables 5.1(a) and 5.2(b)), thus, indicating that the gross features of the correlations between the eddy heat flux and temperature distribution can be reproduced from the 1° averaged fields. The larger averaging of 2° smooths out structures in the western boundary area of the upper layer. In the deeper layers the distributions are similar between all three sets of diagnostic quantities. The sensitivity to horizontal averaging suggests that the size of areas with similar values of the mixing coefficients increases with depth.

The test of Fickian diffusivity reveals the impossibility of reproducing the complex patterns of the eddy heat flux as a simple downgradient mixing of temperature. Only at about 50% of the considered area the eddy heat flux is downgradient for individual components and significantly smaller for the total eddy heat flux. The complementarity in the distribution of the horizontal and vertical coefficients suggests that schemes based on the baroclinic instability mechanism should perform better than the downgradient mixing.

Figure 5-18 shows the divergence of $\vec{F}_{FD}$ (5.9), the heat flux diagnosed with the Fickian diffusive scheme, evaluated for the subdomain for the values of mixing coefficients

$K_{Th} = 10^3\,[M^2 \cdot \text{sec}^{-1}]$ and $K_{Tw} = 5 \cdot 10^{-5}\,[M^2 \cdot \text{sec}^{-1}]$. These coefficients were used in the coarse resolution initialization experiments and belong to the range of values estimated in the test. In general, the correspondence between patterns in divergence with the data (Figure 5-6) is better in the deeper layers. Fickian diffusion for the chosen coefficients correctly diagnoses strong negative divergence in the western current area followed by a strong positive anomaly around $2°E$ and again negative at $4°E$. Both calculated divergencies are weaker in the interior. For the two upper layers while relatively successfully identifying strong positive divergencies in the area near the western boundary and the patterns to the East of $4°E$, the scheme misses strong negative anomaly around $(34°N, 2.5°E)$ predicting moderate positive values.

5.4.2 Test of Isopycnal Diffusion

In the special formulation of the reference experiment the isopycnal diffusion is a stronger version of the Fickian diffusivity. It requires that the eddy heat flux has direction opposite to the local temperature gradient or the mixing coefficients must be equal for all three components. The test of the Fickian parameterization scheme in the previous section clearly identified that the implied horizontal mixing coefficients are about eight orders of magnitude larger then the vertical; thus, the diapycnal diffusion alone will overestimate or underestimate the horizontal or vertical components if it is the single mixing scheme used in a model.

5.4.3 Test of the Green–Stone Parameterization Scheme

The diagnostic test of the GS eddy heat flux parameterization scheme is applied only to the component of the eddy heat flux $\left.\overline{\vec{v}'T'}\right|_{\text{IA}}$ (5.16) that belongs to the isopycnal angle plane. Figure 5-19 (white area) shows where the magnitude of $\left.\overline{\vec{v}'T'}\right|_{\text{IA}}$ is larger than the orthogonal component $\left.\overline{\vec{v}'T'}\right|_{\perp}$. Overall this area occupies the larger portion of total region especially for deeper layers, indicating that the eddy heat flux is mainly in the

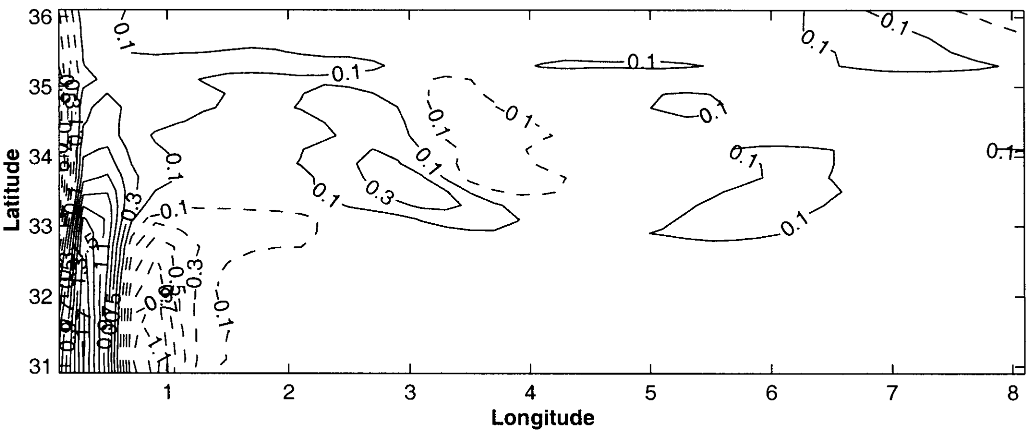

(a) Fickian*10^6, K_{Th}=10^3, K_{Tw}=5*10^{-5}, Layer 1

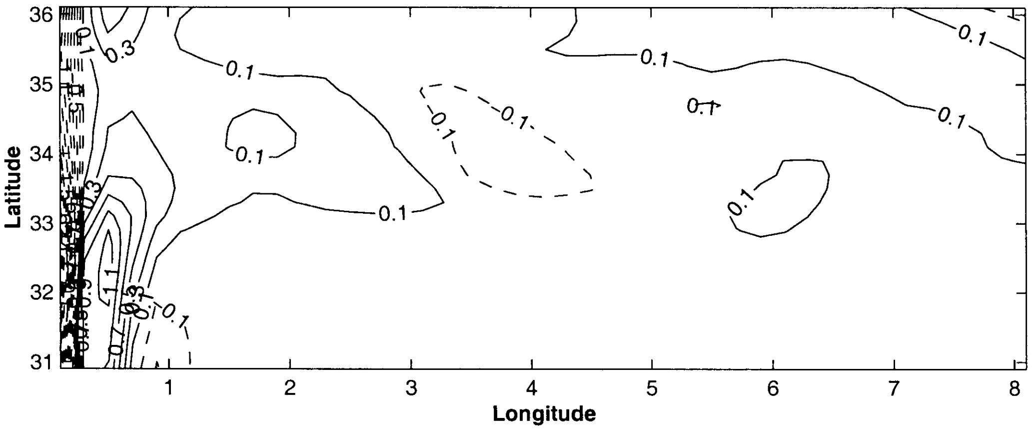

(b) Layer 2

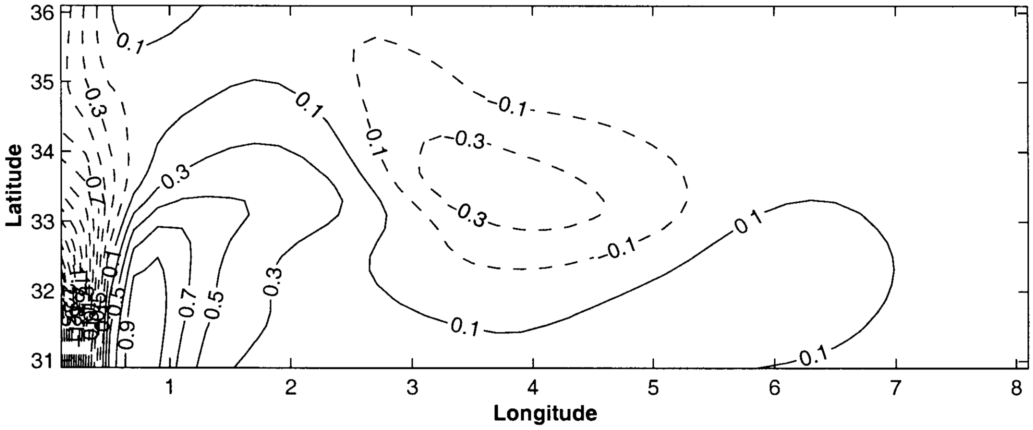

(c) Layer 5

Figure 5-18: Divergence of the heat flux associated with Fickian diffusion. $K_{Th} = 10^3\,[M^2 \cdot \sec^{-1}]$, $K_{Tw} = 5 \cdot 10^{-5}\,[M^2 \cdot \sec^{-1}]$. (a) Layer 1. (b) Layer 2. (c) Layer 5.

isopycnal angle plane.

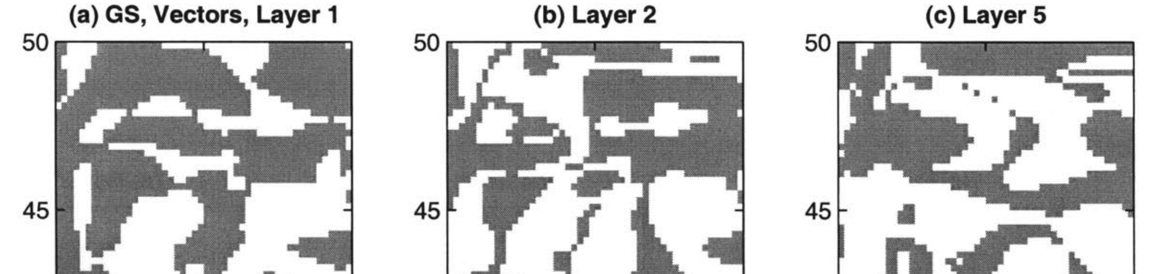

Figure 5-19: Projections of $\overline{\vec{v}'T'}$ on the isopycnal basis. White areas indicate the magnitude of the IA projection is larger compared to the orthogona projection. (a) Layer 1. (b) Layer 2. (c) Layer 5.

The local evaluation of $ratio_{GS}$ (5.22) is presented in Figures 5-20, 5-21 and 5-22 for the upper layer, subsurface layer and the fifth layer respectively. Each of the figures shows the value of $ratio_{GS}$ on the fine grid and averaged over 1° and 2° horizontal boxes.

The GS parameterization approximates the $ratio_{GS}$ as 0.5. Table 5.4 shows areas of the region where the $ratio_{GS}$ is within $[0,1]$ interval. The interval is divided into two parts: $[0,0.5]$ and $[0.5,1]$. If the ratio belongs to the first interval, the corresponding flux

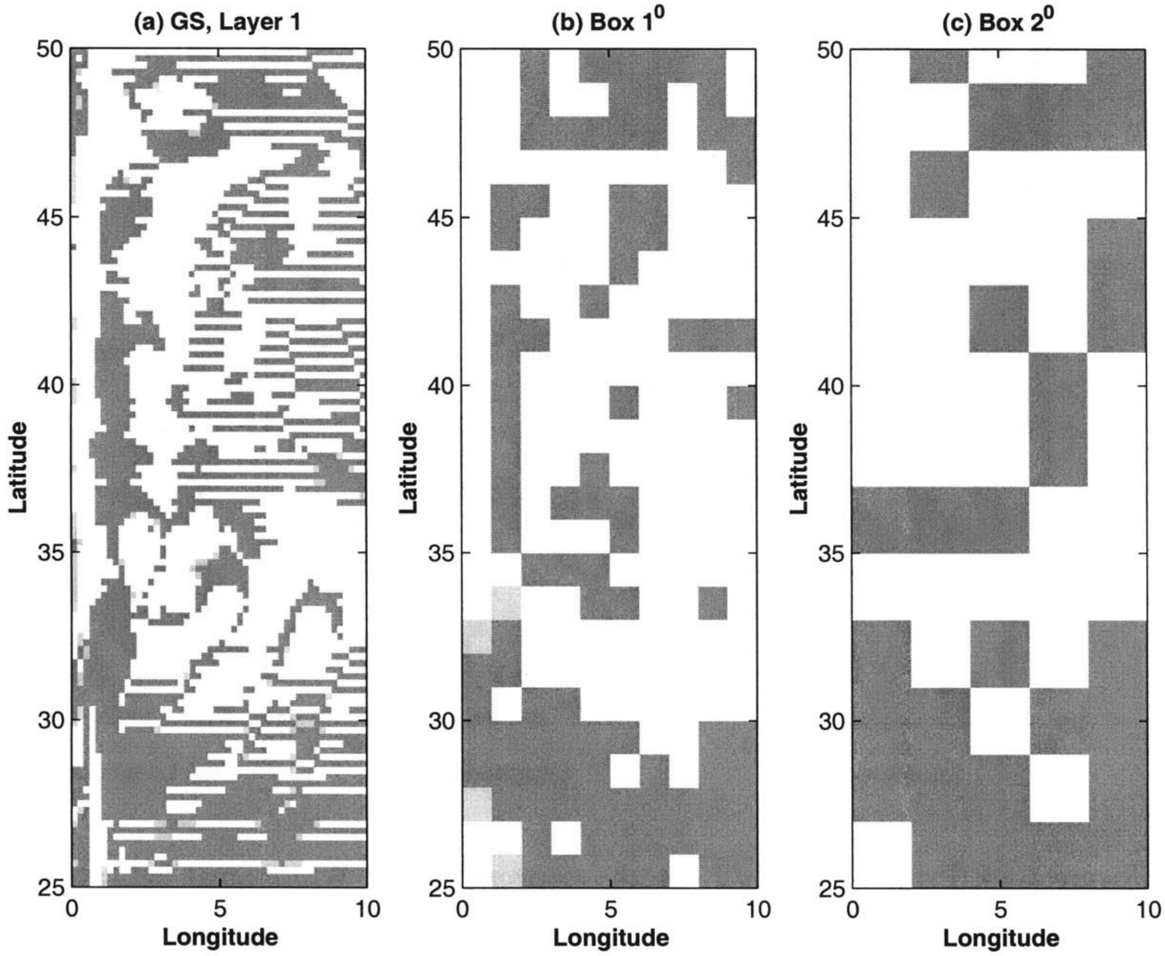

Figure 5-20: Test of the GS parameterization scheme. Layer 1. White areas: $0 < ratio_{GS} < 1/2$. Light gray areas: $1/2 \leqslant ratio_{GS} < 1$. Dark gray areas: the angle outside the wedge. (a) Fine resolution. Averaged over (b) $1^\circ \times 1^\circ$ and (c) $2^\circ \times 2^\circ$.

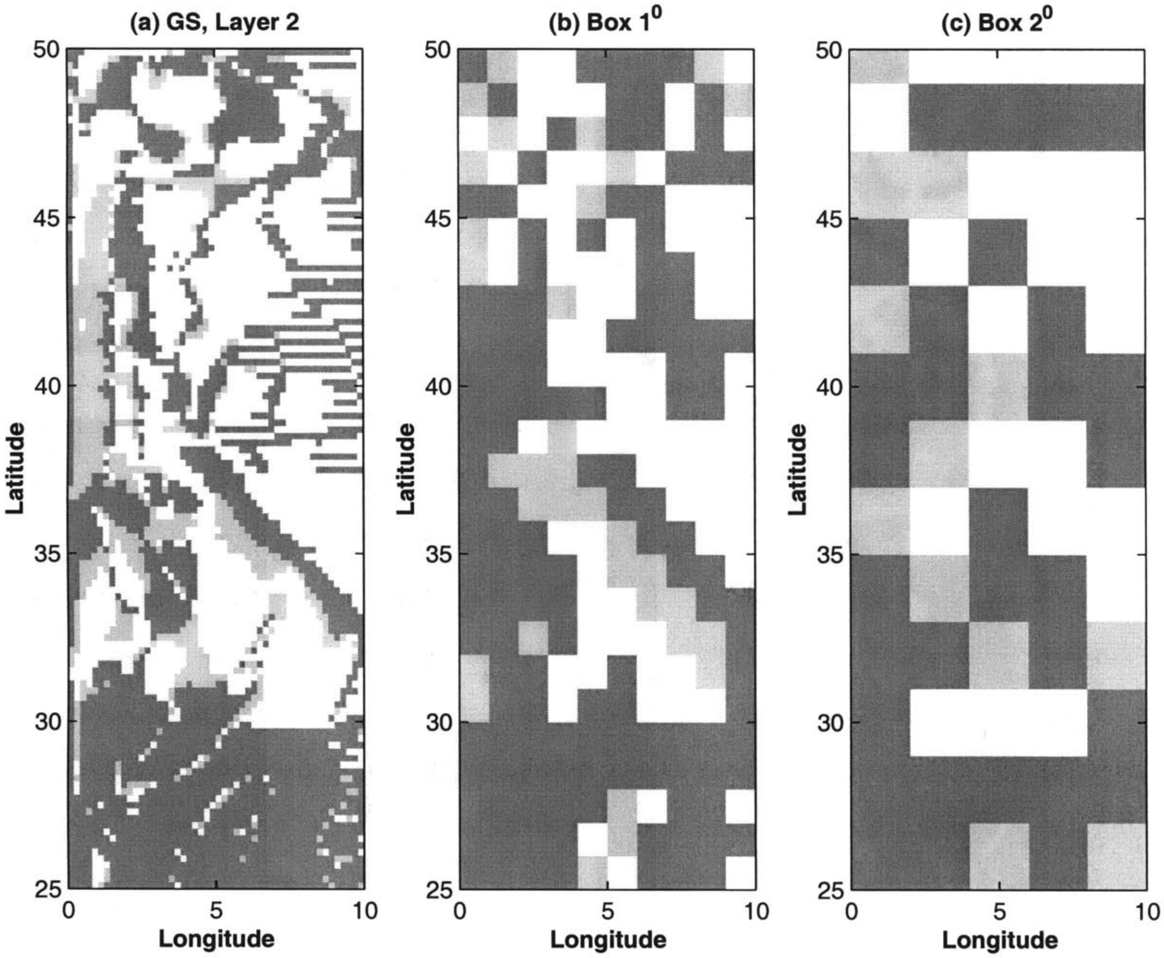

Figure 5-21: Test of the GS parameterization scheme. Layer 2. White areas: $0 < ratio_{GS} < 1/2$. Light gray areas: $1/2 < ratio_{GS} \leqslant 1$. Dark gray areas: the angle outside the wedge. (a) Fine resolution. Averaged over (b) $1^\circ \times 1^\circ$ and (c) $2^\circ \times 2^\circ$.

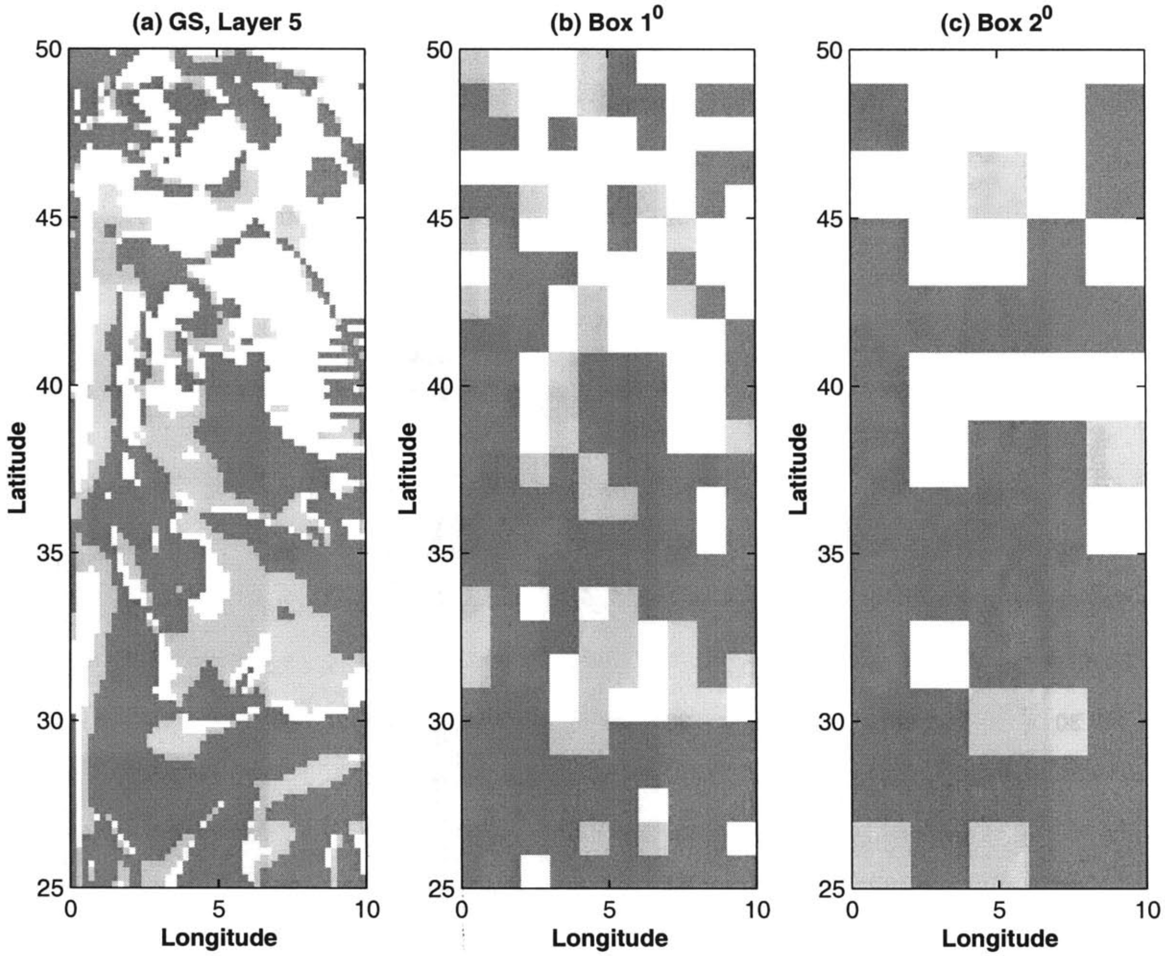

Figure 5-22: Test of the GS parameterization scheme. Layer 5. White areas: $0 < ratio_{GS} < 1/2$. Light gray areas: $1/2 \leqslant ratio_{GS} < 1$. Dark gray areas: the angle outside the wedge. (a) Fine resolution. Averaged over (b) 1° × 1° and (c) 2° × 2°.

Layer	1			2			5		
$ratio_{GS}$	fine	1°×1°	2°×2°	fine	1°×1°	2°×2°	fine	1°×1°	2°×2°
0.0 to 0.5	54%	57%	51%	43%	37%	35%	31%	30%	30%
0.5 to 1	2%	2%	1%	12%	12%	15%	21%	14%	12%
<0 or >1	44%	41%	48%	45%	51%	50%	48%	56%	58%

Table 5.4: Percent of total area for $ratio_{GS}$

vector has larger component in the horizontal direction. The vector is predominantly in the direction of the slope if the ratio is within the interval $[0.5, 1]$.

For the upper layer in the areas where the projection of the eddy heat flux is within the wedge of instabilities, the area with the $ratio_{GS}$ between 0.5 and 1 is a small value covering 2% of the total area. It shows that the flux vector forms a small angle with the horizontal plane. In about 54% of the area, the ration belongs to the interval between 0 and 0.5. The overall noisy patterns, similar to observed when testing the Fickian diffusivity in a previous section, are due to high sensitivities of $ratio_{GS}$ to the vertical components of $\nabla\bar{T}$ and $\overline{\vec{v}'T'}\Big|_{\text{IA}}$ which are used in the evaluation of the $ratio_{GS}$.

In parts where the distribution of $ratio_{GS}$ as computed on the fine grid is more stable (about 3° to the East from the boundary), the baroclinic parameterization scheme explains the Isopycnal angle projection of the eddy heat flux in about 50% of the area with a value of $ratio_{GS}$ equal to 1/2 only in a few small regions to the South of $35°N$. The estimates are more stable for the averaged fields showing that to the North of 30° latitude the transfer due to the eddies extracts the potential energy in a baroclinically unstable process.

The analysis of the second layer on the fine grid (Figure 5-21(a)) revealed a similar tendency in producing an unstable estimate if the vertical component of the eddy heat flux oscillates around 0. The resulting diagnostic of the $ratio_{GS}$ does not posses a meaningful explanation. Some subregions such as the western boundary current area to the North of 37° and the area around $32°N$ spreading into the interior demonstrate higher success in the local evaluation of the $ratio_{GS}$. Similar to the upper layer the range of $0 < ratio_{GS} < 1$

covers a larger area of 43% of the region to the North of 30° latitude. The range of $1/2 \leqslant ratio_{GS} < 1$ occupies a larger area of 12% compare to the upper layer, thus showing that the eddy heat flux is becoming more aligned with the isopycnal vector $\vec{S}$ (5.4). When evaluating $ratio_{GS}$ from the averaged fields there is a 5% reduction of the area with $0 < ratio_{GS} < 1$ to 50% .

The fifth layer of the model is not directly forced; thus, the adiabatic nature of the transfer is expected. In the formulation of the test, it should demonstrate itself in the slope of the eddy heat flux to be close to the isopycnal slope, or the $ratio_{GS} \approx 1$. Indeed, the plot of $ratio_{GS}$ (Figure 5-22) demonstrates a larger coverage of the $ratio_{GS}$ between 0.5 and 1 (the light gray area) of 21% compare with 12% for the second layer. They are located in the areas where the divergence of the eddy heat flux is the largest.

In order to evaluate the divergence of heat flux predicted with the GS scheme, it is necessary to specify the coefficients which determine K_{vs} (5.18). The efficiency parameter α is assign to be equal to 0.02. This value is in the range of possible values estimated by *Visbeck et. al, 1997* [58] in the configuration of a wind–driven channel. For the mixing length scale I have a choice between the radius of deformation as suggested by *Stone, 1972* [55] and the larger value representing the width of the baroclinic zone *Green, 1970* [26]. Figure 5-23 shows the radius of deformation for the subdomain, where the divergence is evaluated. For this area this quantity is computed as

$$R_D = \frac{\overline{N}^z H}{f},$$

where $N = \sqrt{\alpha g \bar{T}_z}$ is evaluated as an average value over the upper $950M$ (upper 7 layers). The radius of deformation is between $47.5KM$ and $58.75KM$.

It was recommended for the oceanographic studies (*Larichev and Held, 1995* [34], *Visbeck et. al, 1997* [58]) that the width of a baroclinic zone is more suitable as an estimate of a mixing length scale. In the present calculation the mixing length scale is set to a larger, compare to the radius of deformation, value of $200KM$ and is a constant

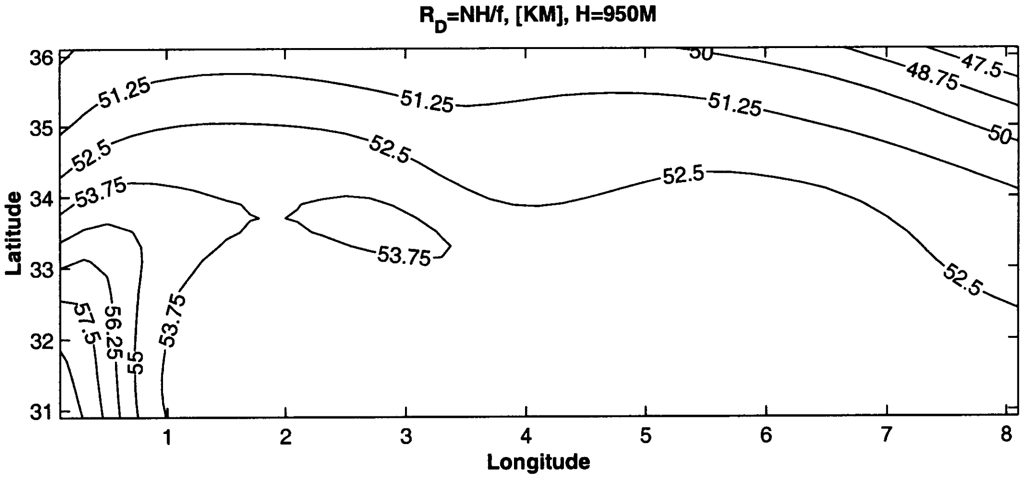

Figure 5-23: Radius of deformation, $[KM]$, averaged over $950M$ (upper 7 layers).

value for the subdomain.

For the choice of efficiency coefficient $\alpha = 0.02$ and mixing length scale $l = 200KM$, the distribution of the mixing coefficient K_{vs} is shown in Figure 5-24. The distribution of patterns generally follows the areas with the largest eddy divergence. The magnitude of the mixing is the largest in the western boundary current area.

Figure 5-25 shows the divergence of the GS heat flux $\vec{F}_{GS}$ (5.24). For the chosen parameters the GS scheme demonstrates mixed skills in representing the divergence of the eddy heat flux. The choice of parameters guarantees a reasonable correspondence in magnitude of the divergencies. The similarity in the patterns of distribution is weak. The parameterization is least successful in the western boundary area where it predicts strong divergence of the opposite sign to the eddy heat flux divergence and in the North–East corner of the subdomain for the upper layer, where it predicts strong positive divergence due to the increasing isopycnal slope. The failure of the scheme in the identified areas suggests that an additional tapering of the scheme needs to be implemented in the boundary regions of the domain.

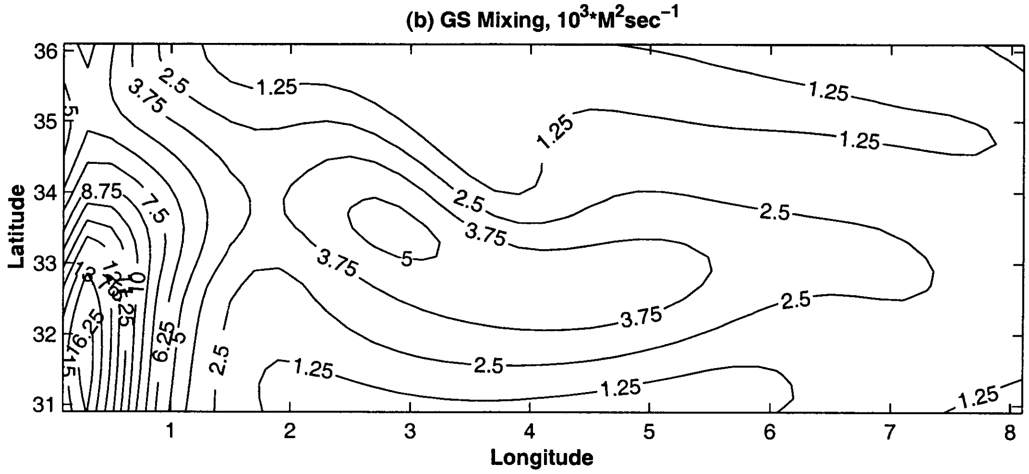
(b) GS Mixing, $10^3{*}M^2sec^{-1}$

Figure 5-24: Mixing coefficient in the GS parameterization scheme. $[M^2 \cdot \sec^{-1}]$ for the choice of $\alpha = 0.02$ and $l = 200\,[KM]$ averaged over $950M$ (upper 7 layers).

Layer	1			2			5		
Test	fine	1°×1°	2°×2°	fine	1°×1°	2°×2°	fine	1°×1°	2°×2°
Success	42%	37%	39%	54%	42%	31%	59%	57%	60%
Failure	58%	63%	61%	46%	58%	69%	41%	43%	40%

Table 5.5: Percent of total area for the GM scheme

5.4.4 Test of the Gent–McWilliams Parameterization Scheme

The test of the GM eddy heat flux parameterization scheme involves the comparison between the total divergencies of the eddy heat flux diagnosed from the reference experiment and the computed three–dimensional divergence of the heat flux by the residual circulation. Figures 5-26, 5-27 and 5-28 present the evaluation of $ratio_{GM}$ for the upper, the subsurface and the fifth layer. The evaluation of divergencies is a well defined operation in the MIT GCM and is performed for each individual volume. Compared to the analysis in the previous sections evaluations of all quantities are performed at the middle of the volume where tracer variables are defined.

Table 5.5 presents the areas of the domain where the GM parameterization scheme can represent the divergence of the eddy heat flux.

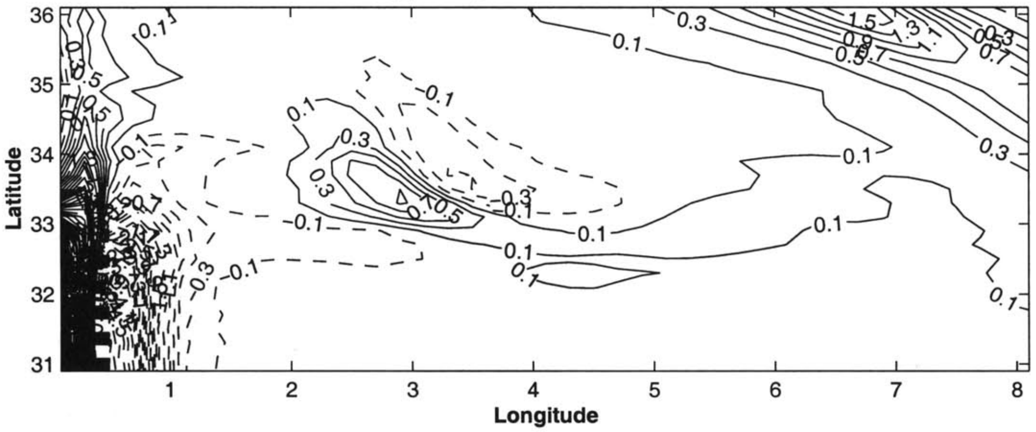
(a) Divergence GS*10^6, Layer 1

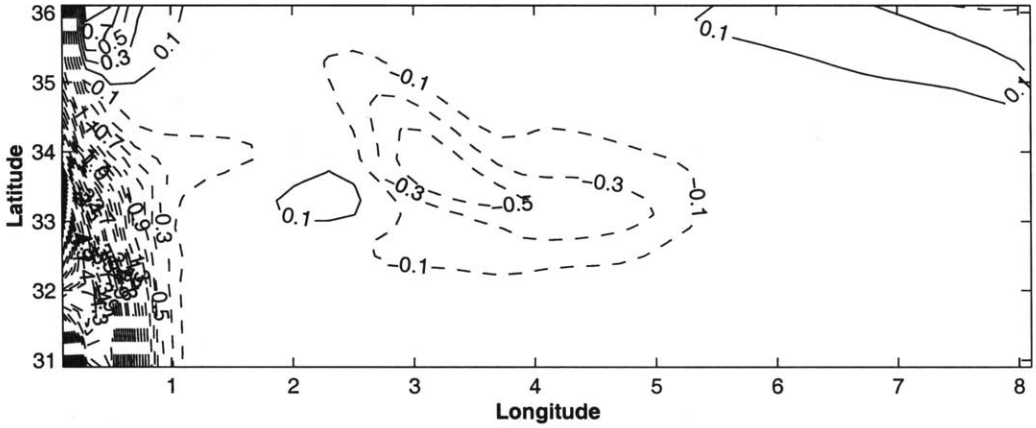
(b) Layer 2

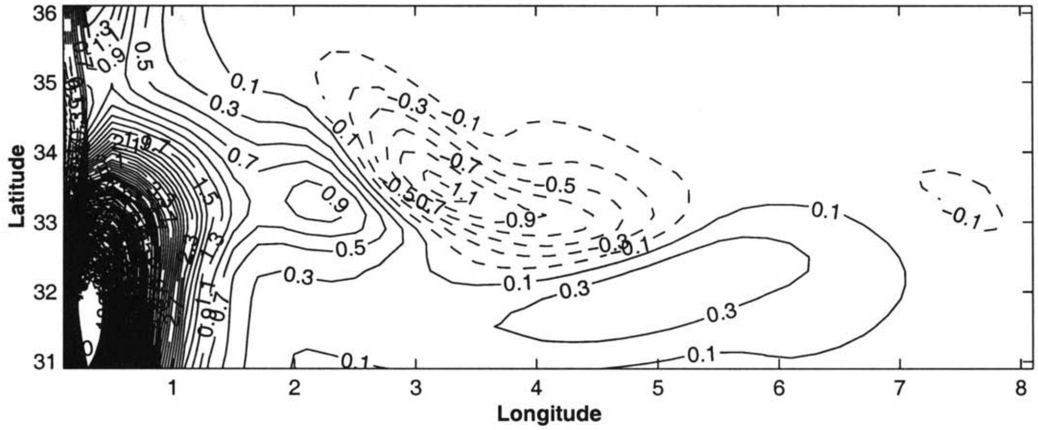
(c) Layer 5

Figure 5-25: Divergence of the heat flux estimated with the GS parameterization scheme. C.I. $0.2 \cdot 10^{-6}\,[{}^{\circ}C \cdot \mathrm{sec}^{-1}]$. (a) Layer 1, (b) Layer 2, (c) Layer 5.

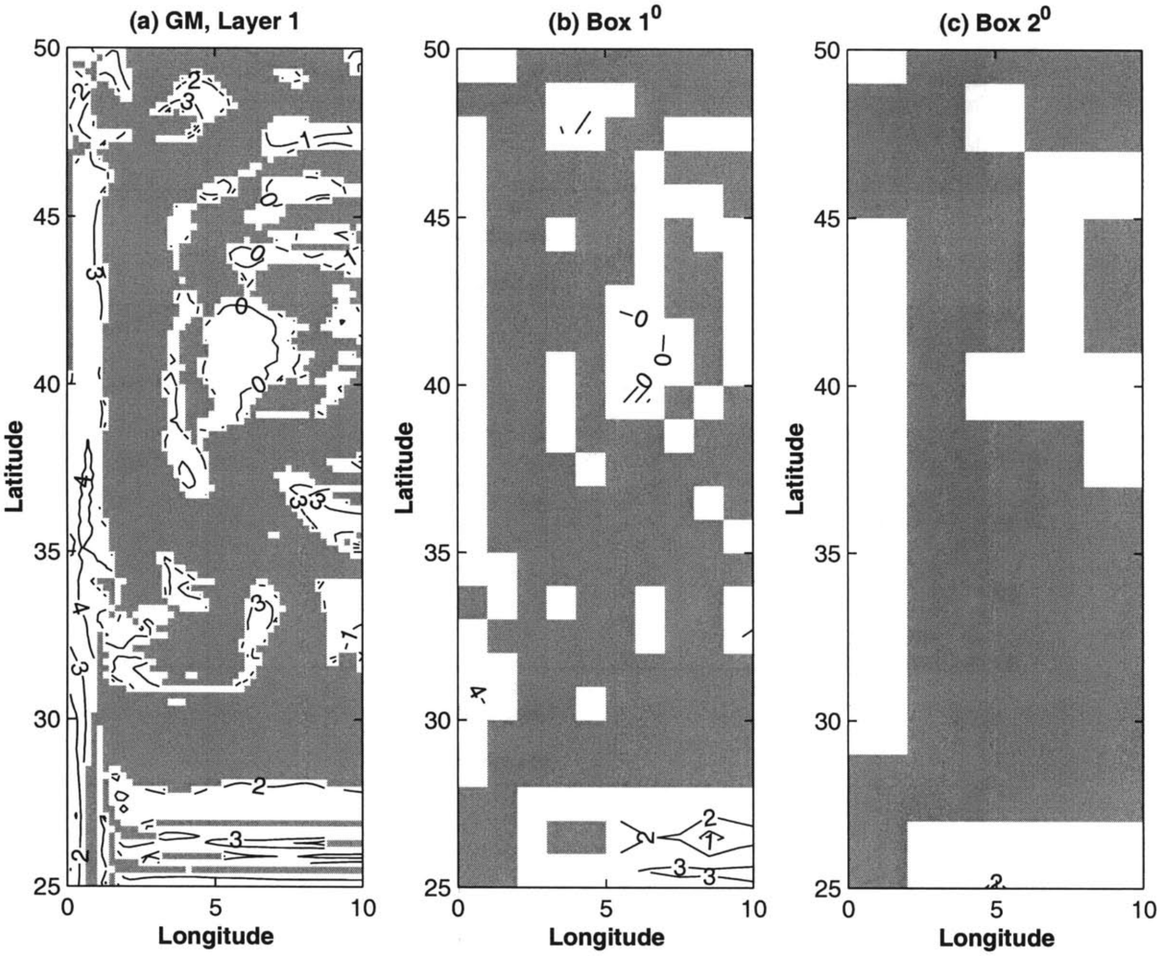

Figure 5-26: Test of the GM parameterization scheme. Layer 1. White areas: $ratio_{GM} > 0$. Gray areas: $ratio_{GM} \leqslant 0$. Contours value is $\log_{10}$ of $ratio_{GM}$, $[M^2 \cdot \sec^{-1}]$. (a) Fine resolution. Averaged over (b) $1^\circ \times 1^\circ$ and (c) $2^\circ \times 2^\circ$.

The coverage of areas where the GM parameterization scheme can reproduce the eddy heat flux divergence increases with depth from about 40% for the upper layer to almost 60% in the deeper. This is consistent with the adiabatic nature of the scheme as the diabatic forcing is the strongest in the upper layers. In addition the estimate is becoming more stable and does not vary when averaged over larger boxes, thus even more demonstrating the predictive skill for deeper layers.

Considering the test on the fine grid for the first layer (Figure 5-26(a)) there is a limited area in the immediate vicinity of the western boundary where the divergence of the heat flux by the residual circulation represents the divergence of the eddy heat flux with reasonable values of diffusion coefficient of the order of $10^3 - 10^4$ $[M^2 \cdot \sec^{-1}]$. I believe some diffusive aspects of the scheme (5.32) are responsible for it. For the area in the eastern part around $45°N$ the required K_{GM} is computed to be about $10^\circ - 10^1$ $[M^2 \cdot \sec^{-1}]$. This area corresponds to the region where the mixed layer deepens into the second layer as it was identified when analyzing the thermal balance in Chapter 4. The Gent–McWilliams scheme forces the levelling of the isopycnals with corresponding a large local parameterized flux. Overall in the upper layer the application of the GM parameterization scheme overestimates mixing due to time–dependent motions. This conclusion is valid for the averaged fields as well (Figure 5-26(b) and (c)): the parameterization succeeds only in the western boundary current area and overestimates mixing in the interior. In addition there is a decrease in area coverage.

The contours of $ratio_{GM}$ for the second layer (Figure 5-27) show that the area to the North of $30°N$ where the residual divergence implies K_{GM} to be $10^3 - 10^4$ $[M^2 \cdot \sec^{-1}]$ is significantly larger than in the upper layer. In the rest of the region the parameterization does not work or significantly overestimates the eddy heat flux divergence. The parameterization succeeds in a larger area of the region compare to the surface layer. The overestimation of the divergence in the North–East corner of the region is due to the presence of strong diabatic forcing due to the deepening mixed layer.

As expected due to the adiabatic nature of the scheme, the area in the deeper fifth

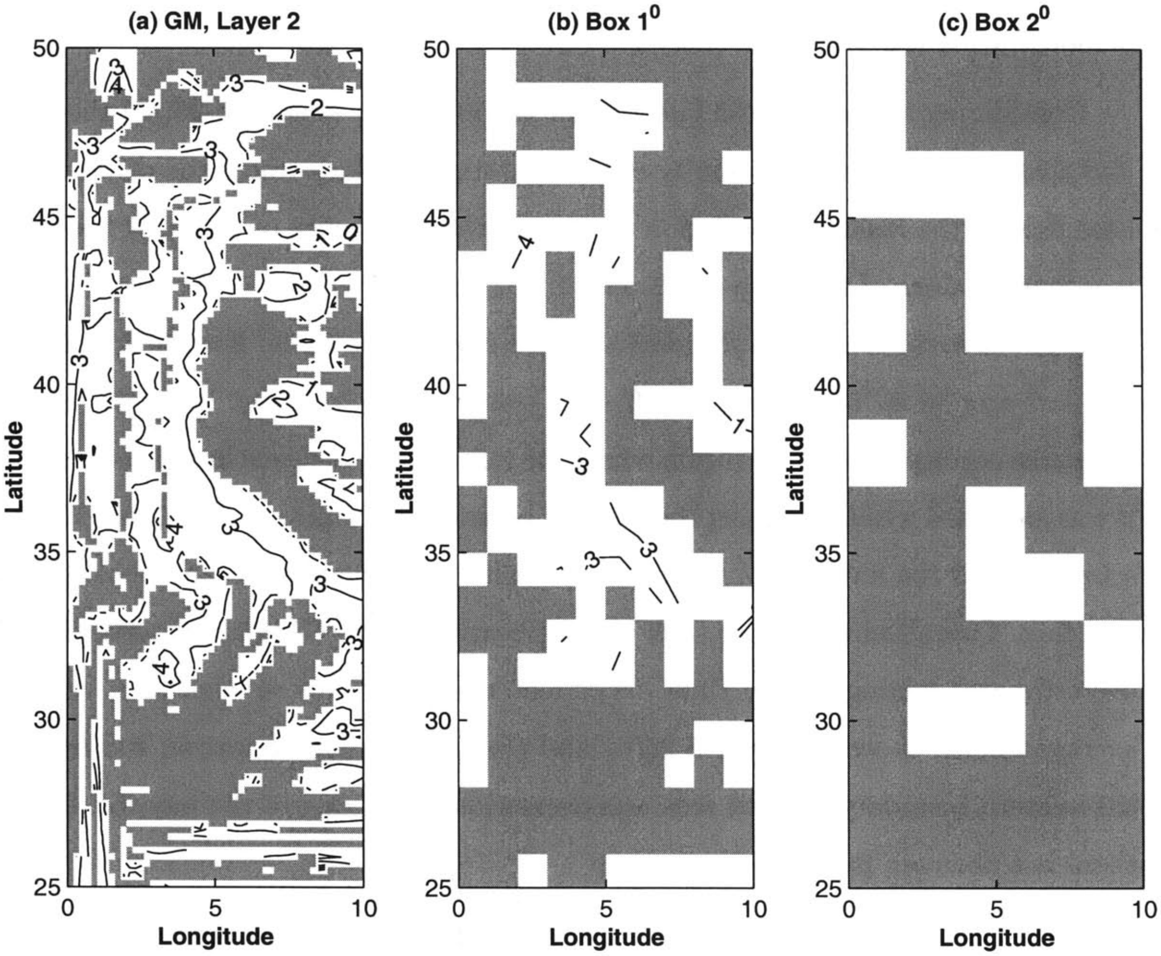

Figure 5-27: Test of the GM parameterization scheme. Layer 2. White areas: $ratio_{GM} > 0$. Gray areas: $ratio_{GM} \leqslant 0$. Contours value is $\log_{10}$ of $ratio_{GM}$, $[M^2 \cdot \sec^{-1}]$. (a) Fine resolution. Averaged over (b) 1° × 1° and (c) 2° × 2°.

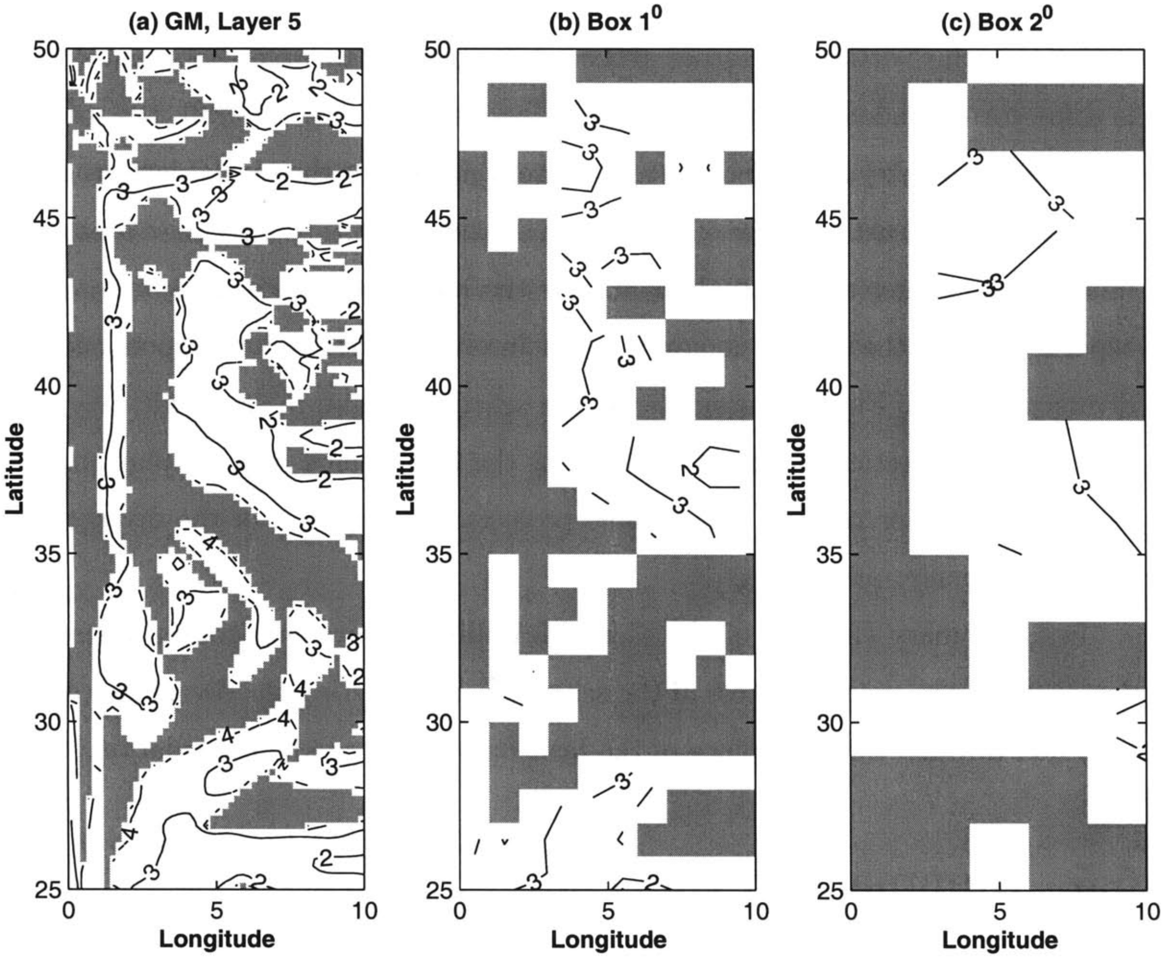

Figure 5-28: Test of the GM parameterization scheme. Layer 5. White areas: $ratio_{GM} > 0$. Gray areas: $ratio_{GM} \leqslant 0$. Contours value is $\log_{10}$ of $ratio_{GM}$, $[M^2 \cdot \sec^{-1}]$. (a) Fine resolution. Averaged over (b) $1^\circ \times 1^\circ$ and (c) $2^\circ \times 2^\circ$.

layer where the GM scheme succeeds is much larger than in the upper layers. The K_{GM} is estimated to be of the order $10^3\,[M^2 \cdot \sec^{-1}]$ in most of the Central and eastern parts of the region. The estimate is stable for both averaging sizes.

Figure 5-29 presents divergence of heat flux associated with the residual circulation for a constant $K_{GM} = 10^3\,[M^2 \cdot \sec^{-1}]$. In the upper layer the scheme overestimate divergence in the North–East corner of the subdomain due to larger isopycnal slope. There is some correspondence in distribution for the interior areas. Overall, the magnitude of divergence is weaker in the interior and western parts. For the second layer the predicted divergence is at least an order of magnitude smaller. It fails to reproduce a positive maximum in the center of the subdomain. For the interior of the fifth layer some diffusive aspects (5.32) of the scheme demonstrate themselves in the close correspondence with the divergence of the Fickian parameterization scheme (Figure 5-18(c)) with $K_{Th} = K_{GM}$. The additional vertical mixing introduced by the GM scheme does not play an important role in the interior region. The scheme predicts a wrong sign of the divergence in the western boundary area.

In a summary the test of the Gent–McWilliams parameterization scheme did not demonstrate the overall success of the scheme in representing the divergence of the eddy heat flux through the divergence of the heat flux by the residual circulation.

5.5 Summary of the Tests

The evaluation of the Fickian diffusion scheme demonstrated that the total eddy heat flux is not downgradient to the distribution of temperature in a larger portion of the region. For individual components the horizontal flux is more of a downgradient nature than the vertical. The magnitude of the implied mixing is consistent with the values used in coarse resolution experiments of the order $10^3 - 10^4\,[M^2 \cdot \sec^{-1}]$ for the horizontal coefficients and $10^{-4} - 10^{-5}\,[M^2 \cdot \sec^{-1}]$ for the vertical coefficient. Horizontal mixing is stronger in the upper layers and closer to the western boundary. There is a general anticorrelation

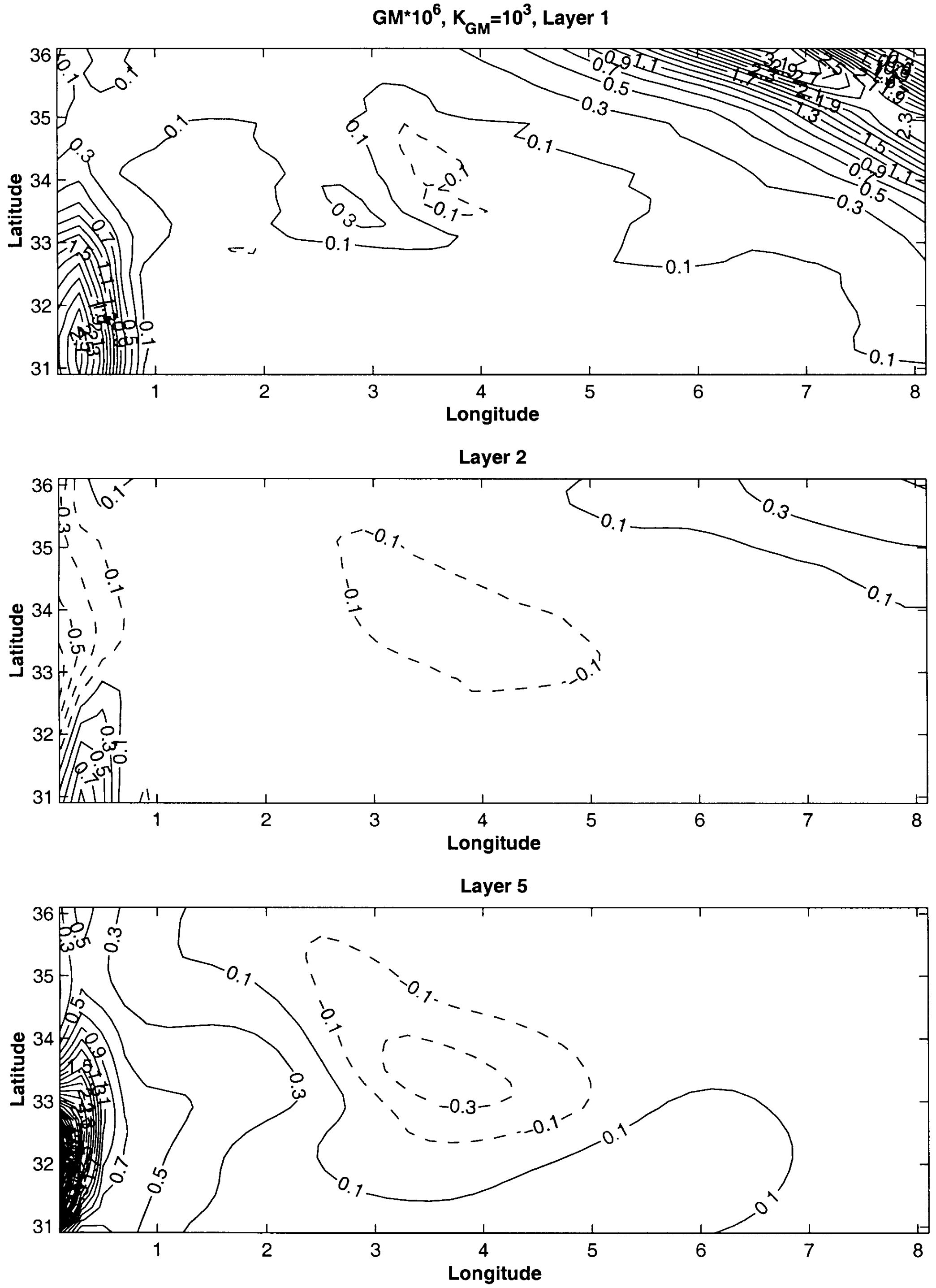

Figure 5-29: Divergence of heat flux estimated with the GM scheme for $K_{GM} = 10^3\,[M^2 \cdot \sec^{-1}]$. (a) Layer 1, (b) Layer 2, (c) Layer 5. C.I. $0.2{\cdot}10^{-6}\,[{}^{\circ}C \cdot \sec^{-1}]$.

between the horizontal and vertical mixing coefficients resulting in a much smaller area where all three components are downgradient than for each individual component. The test of the scheme on averaged fields revealed that 1° × 1° average is sufficiently well reproduces the fine resolution results for all three considered layers. The evaluation of a vertical mixing on 1° × 1° grid showed a large range of coefficients suggesting that the use of a constant coefficient will significantly change the vertical mixing patterns. The vertical mixing coefficient is more uniformly distributed in the lower layers.

Due to a simple linear equation of state and constant salinity of the reference experiment the evaluation of the isopycnal mixing is a rather trivial procedure. The diagnosed vertical mixing coefficient is 7-8 orders of magnitude smaller then the horizontal, thus automatically ruling out the scheme.

The component of the eddy heat flux in the direction of the isopycnal vector was shown to be large compare to the orthogonal component. The test of the Green–Stone parameterization scheme demonstrated some mixed results in its representation. High sensitivity to noisy values of vertical component of the eddy heat flux complicates the analysis. In general it was demonstrated that the eddy heat flux to be closer aligned with the isopycnal surfaces for deeper layers thus suggesting that the associated transfer becomes more adiabatic.

The evaluation of the Gent–McWilliams scheme did not demonstrate the overall success of a scheme in simulation of the divergence of the eddy heat flux everywhere in the region as well. The adiabatic nature of the scheme was demonstrated by observing an increase in area where the GM scheme can diagnose observed divergence of the eddy heat flux with depth. There is some correspondence between the GS and GM tests. First, the areas where GS succeeds decrease with depth. Second, there is some anticorrelation in the distribution of areas of the two tests, that is especially pronounced in the Fifth layer.

The comparison of the divergencies predicting by the schemes for the smaller subdomain could not identify the best performing scheme. For the upper layer distribution of divergency predicted by GS scheme is the most favorable except in the North–East corner. In the interior of the fifth layer all three scheme have some skills generally predicting the correct number of anomalies although with different magnitude. Two of the schemes, GS and GM, fail in the western boundary current area predicting the wrong sign of divergencies.

Overall, the transfer of heat associated with time–dependent motions as diagnosed from the reference experiment is a complicated process that can not be uniquely explained with any one of the proposed local schemes. The tests did not demonstrate that the more sophisticated schemes are better in the representation of the local distribution of the eddy heat flux compare to the simpler Fickian diffusion. The Green–Stone and Gent–McWilliams schemes contain some tunable parameters which can potentially improve the schemes' performance. Some experiments testing the sensitivities to these parameters will be explored in the next Chapter in a series of coarse resolution experiments with the eddy heat flux parameterization schemes. The chapter follows by the general discussion of the performance of the considered eddy parameterization schemes.

Chapter 6

Tests of Parameterization Schemes in Coarse Resolution Experiments

The goal of developing sophisticated parameterization schemes is to improve climatological simulation with coarse resolution models. This chapter addresses the implementation of the three major proposed parameterization schemes in the framework of such experiments with MIT OGCM. The experiments explore sensitivities to changes in specific parameters of the schemes in a controlled set–up by comparing the climatology of solutions with the reference state. In addition, the diagnostic evaluation of the implied flux divergencies is performed for a number of experiments with the proposed parameterization schemes and compared with the eddy heat flux divergence of the reference experiment.

6.1 Experimental Set–Up

6.1.1 Internal and External Parameters

Coarse resolution experiments employing different parameterization schemes are performed in a configuration similar to the reference calculation. All the external parameters, among which are the horizontal and vertical dimensions of the domain (Table 2.2) external forcing (Figure 2-1), are the same as in the reference experiment. The internal parameters are divided into two sets. The first set comprises the internal parameters that are the same in both the fine and coarse resolution calculations, i.e. the boundary conditions, the vertical viscosity and diffusivity. The second set contains values specific for each particular parameterization scheme. The boundary conditions for velocity are no–slip at the side walls, rigid lid at the surface and a linear drag at the bottom. For the temperature, they are insulated walls. The form of vertical subgrid mixing is preserved in both sets of experiments. The value of the vertical viscosity K_{Vw} is $10^{-3}\,[M^2 \cdot \mathrm{sec}^{-1}]$. The vertical diffusivity K_{Tw} is kept constant with the magnitude $0.3 \cdot 10^{-4}\,[M^2 \cdot \mathrm{sec}^{-1}]$ except where it is one of the specific parameters related to the parameterization scheme used. The horizontal viscosity K_{Vh} of $5{\cdot}10^5\,[M^2 \cdot \mathrm{sec}^{-1}]$ is a constant value used in all experiments.

Each of the parameterization schemes contains some tunable internal parameters. The formulations of the schemes was outlined in the previous chapter and will be repeated in a concise form here. The sensitivity to the tunable internal parameters will be explored in the coarse resolution experiments. A number of simulations with each of the parameterization schemes will be analyzed. The experiments will explore the typical values of the specific parameters without trying to perform an inverse study for identifying the best possible combination.

The horizontal resolution of the experiments is $4^\circ \times 4^\circ$. It is equal to the one used in the climatological experiments that was described in Chapters 2 and 3. The vertical resolution is 15 layers as in the reference calculation (Table 2.3).

6.1.2 Initialization

Each of the coarse resolution experiments is initialized with the climatology for the temperature field that was used in the initialization of the reference experiment (Figure

2-3). Salinity is kept constant throughout the whole length of the integrations. The initial condition for the velocity field is a motionless ocean.

6.1.3 Execution

The length of the coarse resolution calculations is chosen to be equal to the total length of the reference simulation. After 50 years of spin–up, the data is averaged over the next 50 years of integration. All climatological quantities and the divergence of parameterized fluxes are computed during this period.

6.2 Evaluation Criteria

The evaluation of parameterization schemes is based on the comparison with the reference experiment. The diagnostic quantities evaluated from the reference calculation in the previous Chapters 3 and 5 are compared with the output of the coarse resolution experiments. First, the coarse resolution climatologies are evaluated and compared with the diagnostics presented in Chapter 3. Second, the divergences of parameterized heat flux are computed and compared with the direct evaluations from the reference experiment discussed in Chapter 5. The skill of a parameterization scheme is judged on the basis of how well it can reproduce the reference data.

6.2.1 Climatological Evaluation

By construction the major goal of coarse resolution experiments is to reproduce the true climatological state of the model ocean in response to external atmospheric forcing. Thus, the evaluation of schemes' skill in the simulation of the ocean climate is of the outmost importance. The climatological state of the model ocean is discussed using the same criteria outlined in Chapter 3. The density distribution defines the major climatological properties such as ocean heat content and the interaction with the atmosphere that in turn determines the poleward heat transport. The thermal state of the experiments is evaluated based on two diagnostics: the vertical profile of horizontally averaged temperature and a cross–section of the zonally averaged temperature on the meridional/vertical plane through the thermocline. The second part of the climatological evaluation includes comparison of transport properties such as the total northward integrated heat transport and the meridional overturning circulation. The comparison between the patterns of overturning transport in the experiments is performed by evaluating the maximum transport in the vicinity of the Northern boundary and the value of transport for a mid–latitudinal location at the thermocline depth of $425M$. The first value indicates the strength of water mass formation while the second shows the southward penetration of the main overturning cell.

The above climatological diagnostics evaluated from the reference experiment are presented in Figures (3-1) and (3-5).

6.2.2 Flux Divergence

The second part of the schemes' assessment includes comparison between the divergence of the eddy heat flux diagnosed from the reference experiment and computed in the coarse resolution experiments. This diagnostic demonstrates the skills of the schemes in reproducing the contribution of parameterized mesoscale eddies to the establishment of the thermal structure.

The divergence of the eddy heat flux is calculated from the reference experiments as it was presented in Chapters 4 and 5. Chapter 5 examined the divergence on the fine grid of the reference experiment in a limited part of the domain $[0°E\text{-}8°E] \times [31°N\text{-}36°N]$ for three thermocline layers. This chapter evaluates the eddy heat flux divergence averaged on a horizontal grid of the coarse resolution experiments for the full basin.

Figure 6-1 shows the three–dimensional divergence of the eddy heat flux from the fine resolution calculation averaged on 4° horizontal grid for the thermocline layers. Note that the horizontal dimensions of the domain shown here are $[2°E\text{-}34°E] \times [6°N\text{-}62°N]$, which are different from the evaluation in Chapters 4 and 5, where figures' coverage starts at the physical boundaries of the domain (0° and 4° respectively). In this chapter each boundary point corresponds to the center of a volume next to its respective boundary.

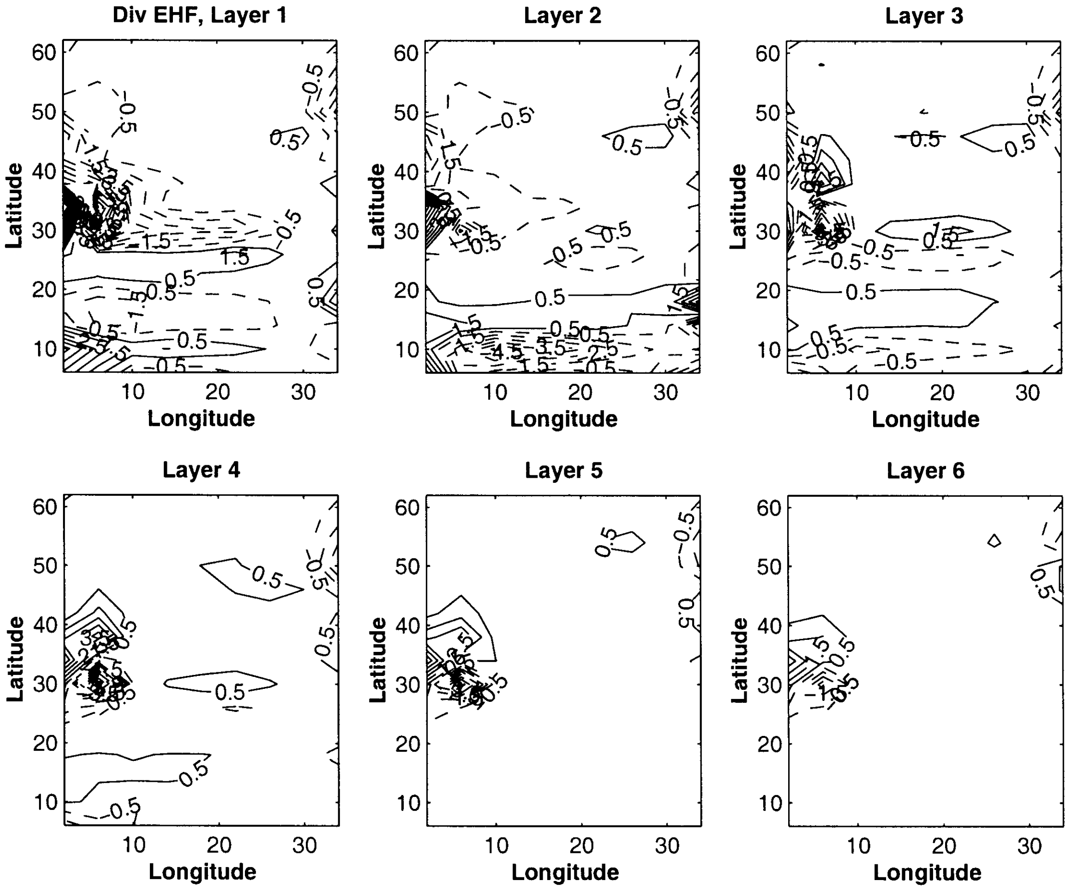

Figure 6-1: Divergence of the eddy heat flux averaged over 4° × 4° horizontal box. Layers 1 to 6. C.I. $2.0 \cdot 10^{-8}\,[°C \cdot \text{sec}^{-1}]$.

The divergence analysis of the previous chapter on a fine grid was concentrated on the midlatitudinal area in the vicinity of the Western boundary current. When averaged over 4° × 4° horizontal box the magnitude of the divergence is about one order of magnitude smaller than shown in Figures 4-17 and 4-18. The patterns of distribution are consistent with the geographical distribution of areas identified in Chapter 4. The Southern and midlatitudinal areas are those with the largest divergence of the eddy heat flux.

The parameterization schemes are evaluated according to their skills in reproducing the divergence diagnosed in the reference experiment. The computations of the time–averaged divergencies in the coarse resolution experiments takes into account a background vertical diffusivity that was used in the reference simulation by substracting $-K_{Tw}^{ref}\bar{T}_{zz}$ from the result with the mixing coefficient K_{Tw}^{ref} equal to $0.3{\cdot}10^{-4}\,[M^2 \cdot \sec^{-1}]$.

6.3 Coarse Resolution Experiments

This section evaluates the skills of different parameterization schemes in simulating the climatological state of the model ocean. The parameter space of each individual scheme that was identified in Chapter 5 will be explored. In addition the patterns of divergence of parameterized heat flux will be compared with those evaluated from the reference experiment.

6.3.1 Fickian Diffusion

The flux $\vec{F}_{FD}$ associated with the Fickian diffusive scheme in its simplest form using constant horizontal and vertical coefficients is

$$\vec{F}_{FD} = -\begin{pmatrix} K_{Th} & 0 & 0 \\ 0 & K_{Th} & 0 \\ 0 & 0 & K_{Tw} \end{pmatrix} \nabla T. \tag{6.1}$$

It is the divergence of this flux that forces the thermal balance (4.5).

There are two specific parameters entering (6.1): horizontal K_{Th} and vertical K_{Tw} diffusivities. The former coefficient represents the strength of the horizontal mixing by unresolved mesoscale processes. In Chapter 4, while performing the evaluation of

		K_{Th}	$[M^2 \cdot \sec^{-1}]$
		10^2	10^3
K_{Tw}	$0.1 \cdot 10^{-4}$	FFH5V1	FFH1V1
	$0.3 \cdot 10^{-4}$	FFH5V2	FFH1V2
	$1.0 \cdot 10^{-4}$	FFH5V3	FFH1V2

Table 6.1: Experiments with Fickian diffusive parameterization

different terms in the thermal balance, it was demonstrated that the horizontal mixing due to biharmonic diffusivity is weak compared to the horizontal divergence of the eddy heat flux; thus, it is assumed that the horizontal mixing due to a parameterization scheme should represent the horizontal mixing due to mesoscale eddies only. The magnitude of K_{Th} was estimated in the diagnostic tests of the previous chapter. It varies between 10^2 and 10^4 $[M^2 \cdot \sec^{-1}]$. The vertical diffusivity K_{Tw} of $0.3 \cdot 10^{-4}$ $[M^2 \cdot \sec^{-1}]$ was explicitly presented in the reference experiment. Changes in the magnitude of vertical diffusivity of the coarse resolution experiments represent an additional vertical mixing due to the mesoscale eddies. Thus, the range of values being explored in the coarse resolution experiments of this section is centered at the above value.

A number of coarse resolution experiments were performed. The specific parameters identifying each individual experiment are presented in Table 6.1. The names in the Table are the reference labels of different experiments and will be used in the Figures for the identification purposes.

Values of the viscosities are kept constant. The horizontal viscosity K_{Vh} is $5 \cdot 10^5$ $[M^2 \cdot \sec^{-1}]$. The vertical viscosity K_{Vw} is set to 10^{-3} $[M^2 \cdot \sec^{-1}]$. The second value was used in the reference experiment. The coarse resolution experiments demonstrate much stronger sensitivities to variation in the diffusivities (*Bryan,.1987* [7]) than in viscosity. Therefore the values of viscosity are kept constant.

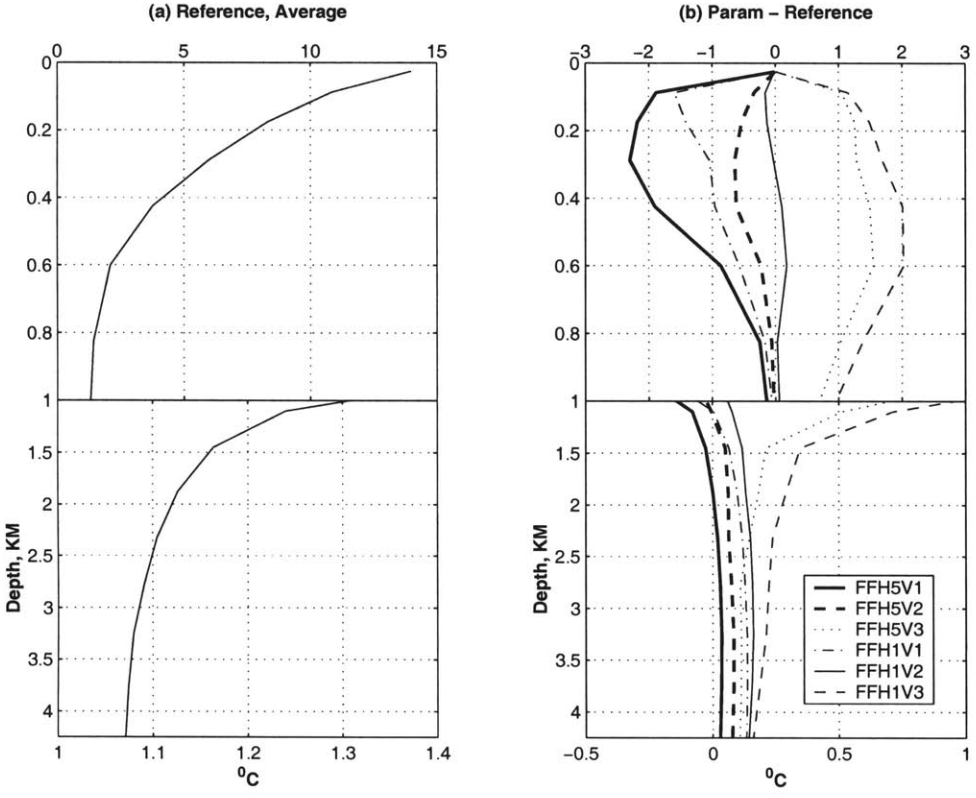

Figure 6-2: Horizontally averaged temperature, $[{}^\circ C]$. Fickian Diffusivity. (a) Reference experiment. (b) Parameterization experiments minus Reference. Stretched upper $1000M$. Labels identify experiments.

Climatological Analysis

Horizontally Averaged Temperature Figure 6-2 shows the evaluation of this diagnostic property for coarse resolution experiments employing Fickian diffusion.

Profiles of temperature differ for the upper $1000M$, the thermocline layers, and the deep ocean. Consider the experiments with the smaller values of vertical diffusivity of $0.1 \cdot 10^{-4}$ and $0.3 \cdot 10^{-4}\,[M^2 \cdot \mathrm{sec}^{-1}]$ (labels ending in V1 and V2). The simulated thermocline is warmer while the deeper ocean is cooler than in the reference experiment resulting in a decreased temperature contrast between the upper and deeper ocean compared to the reference simulation. The decreased contrast in turn leads to less sharp thermocline. In the case of higher K_{Tw} (labels ending in V3) with the magnitude of $1.0 \cdot 10^{-4}\,[M^2 \cdot \sec^{-1}]$ the upper ocean becomes warmer than in the reference case, thus increasing the overall temperature contrast, although it will be demonstrated that a large vertical diffusivity leads to significant modifications of transport diagnostics compared with the reference values. An increase in the horizontal diffusivity K_{Th} leads to a uniform shift of the whole profile to the warmer, which can be explained by enhanced horizontal mixing of temperature. The deep convection in the Northern part of the domain could be strongly affected by this process resulting in a lateral mixing of the convective vertical column with warmer surroundings so that the deeper water becomes warmer.

The best correspondence is observed in the experiments FFH5V2 and FFH1V2 which use vertical mixing of the same value as in the reference experiment, thus indicating that the overall vertical mixing due to time–dependent motions has small contribution to the establishment of horizontally averaged temperature.

Zonally Averaged Temperature The zonally averaged temperature is analyzed by estimating the deviations from the reference profile for the 5^{th} thermocline layer at $425M$ (Figure 6-3).

Overall patterns similar to the previous section occur for most of the domain: the layer is generally cooler than in the reference state when moderate vertical mixing is used and warmer for larger mixing coefficients. The closest to the reference state temperature profile occurs for experiment FFH1V2. The temperature deviates in both directions from the reference profile for this thermocline level, again showing that the best reproduction is obtained with the same value of vertical mixing that was used in the reference experiment and larger value of the horizontal mixing.

Total Heat Transport The total heat transport for the analyzed experiments is presented in Figure 6-4. A number of publications (e.g. *Bryan, 1987* [7]; *Fanning and Weaver, 1997* [21]) demonstrated high dependence of this property on the value of verti-

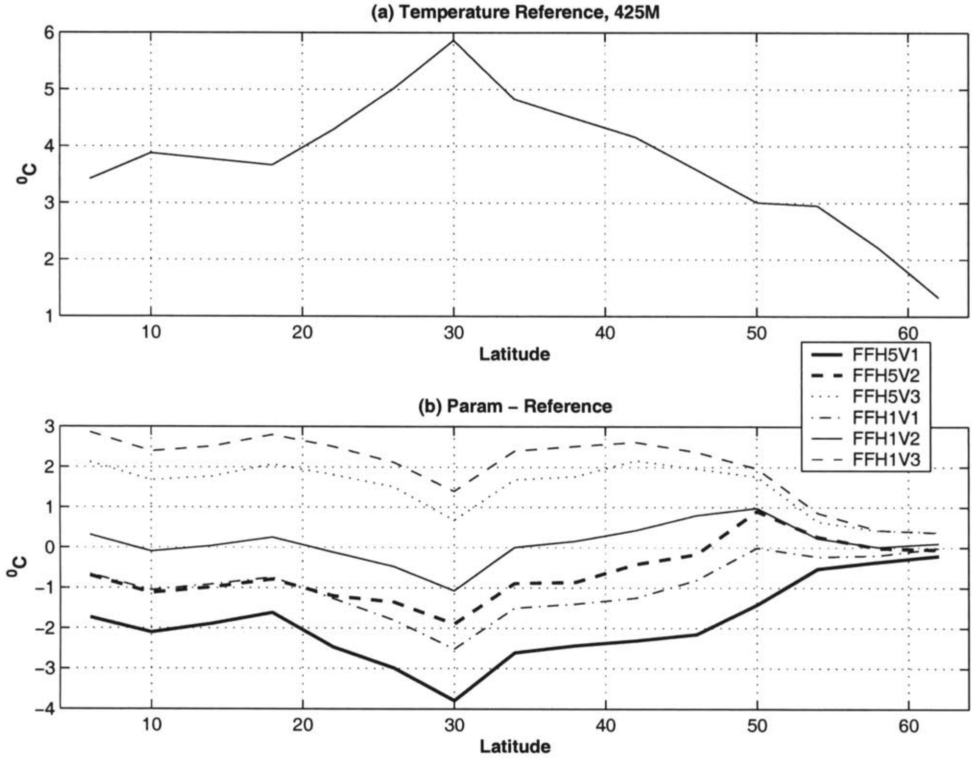

Figure 6-3: Zonally averaged temperature, section at $425M$, $[°C]$. Fickian Diffusivity. (a) Reference experiment. (b) Parameterization experiments minus Reference. Labels identify experiments.

cal diffusivity. The analysis of the previous sections shows that the best representation of the thermal structure is achieved with the same value of vertical diffusivity that was used in the control experiment. Thus, it is not surprising that the closest magnitude of total heat transport is obtained in the experiments FFH5V2 and FFH1V2 with K_{Tw} equals to $0.3 \cdot 10^{-4}\,[M^2 \cdot \sec^{-1}]$. The experiments with smaller diffusivity can only achieve about 60% of the reference magnitude, and on the other hand larger diffusivity causes strong, about 60%, increase in magnitude.

None of the experiments are able to reproduce the reference heat flux for latitudes North of $30°N$. There is an increase in the heat transport for this region when the horizontal diffusivity decreases, although it quickly reaches the level of experiments with

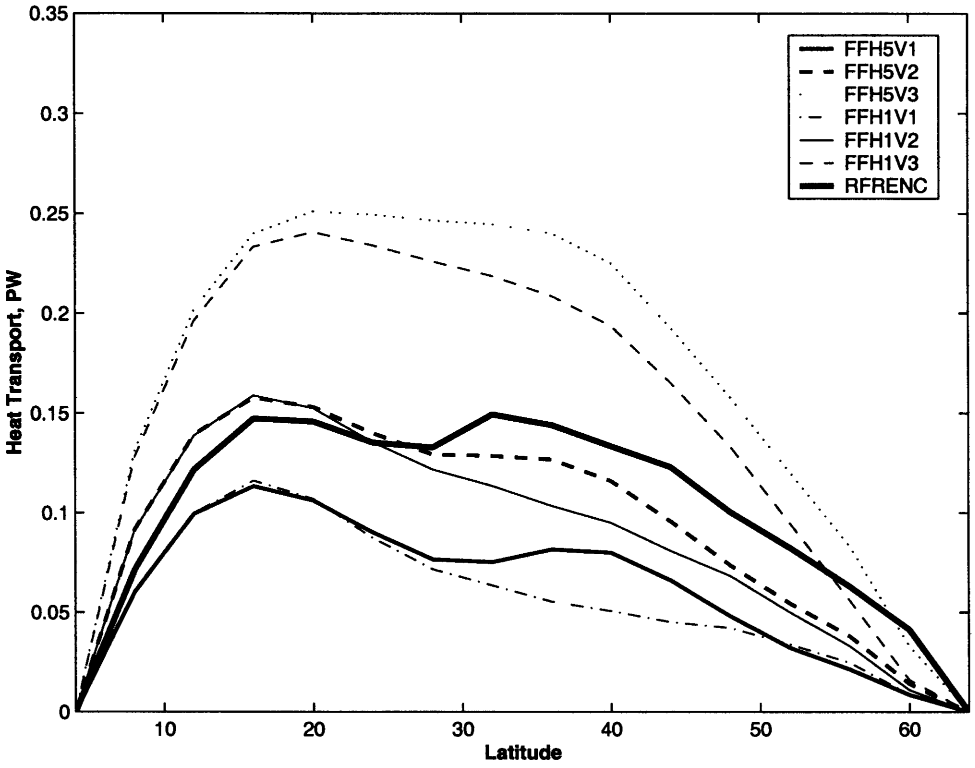

Figure 6-4: Total heat transport, $[PW]$. Fickian Diffusivity. Labels identify experiments. RFRENC is the reference experiment.

higher horizontal diffusivities by 50°N.

Meridional Overturning Transport Figure 6-5 presents the evaluation of the overturning circulation. Only experiments with high vertical diffusivity create overturning circulation larger than in the reference state and with a strong penetration to the South. Other experiments underestimate both values.

Divergence of Parameterized Flux

The divergence of flux represented with the Fickian diffusion is analyzed for three experiments: FFH5V2, FFH1V1 and FFH5V3. The experiments were chosen according to their performance when comparing the climatologies of the solutions. The first experiment has

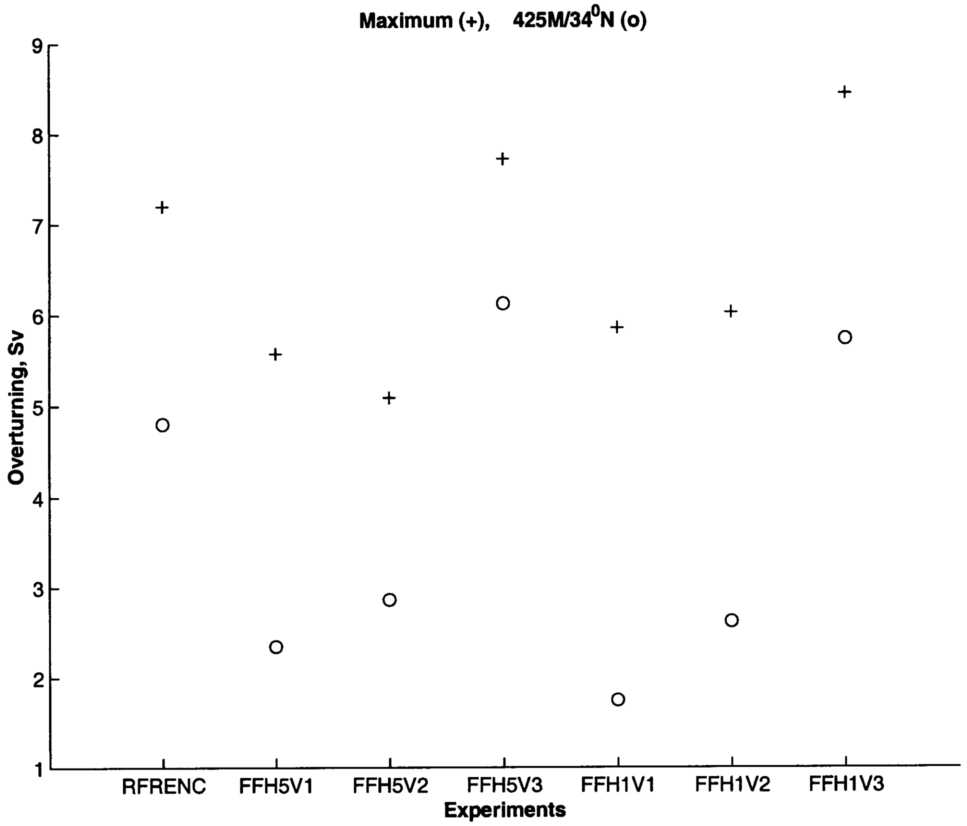

Figure 6-5: Overturning stream function, $[Sv]$. (+) Maximum. (o) at $(34^\circ N, 425M)$. Fickian Diffusivity. Labels identify experiments. RFRENC is the reference experiment.

the best skills in simulating the total northward heat transport. The other two experiments do not perform well with respect to this diagnostic quantity. The higher horizontal and lower vertical diffusivity case (FFH1V1) significantly underestimates transport, while the high vertical diffusivity experiment (FFH5V3) overestimates the reference value.

Figures 6-6, 6-7 and 6-8 show the divergence of implied flux after subtracting the divergence of the background vertical diffusive flux.

In the experiment FFH5V2 the vertical diffusivity equals to the reference value; thus,

$$\overline{\nabla \cdot \vec{F}_{FD}} + K_{Tw}^{ref} \bar{T}_{zz} = -K_{Th} \left(\bar{T}_{xx} + \bar{T}_{yy} \right), \tag{6.2}$$

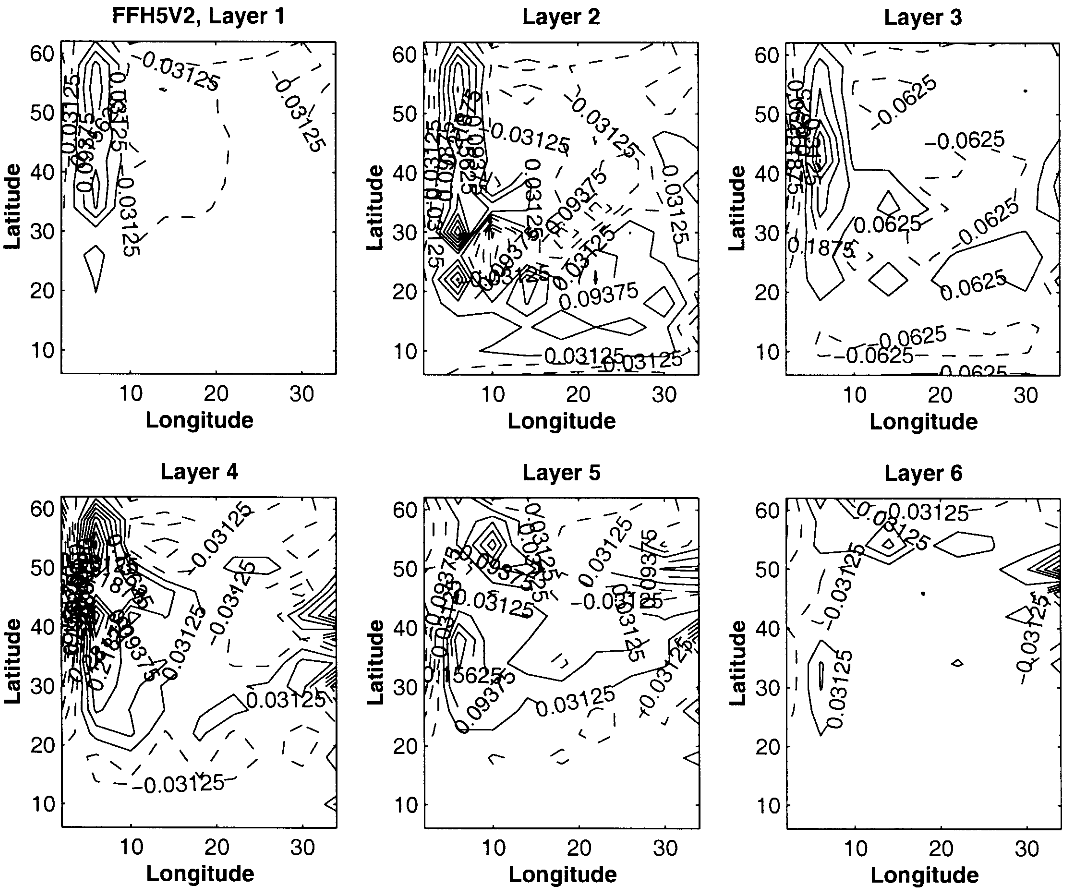

Figure 6-6: 3D flux divergence. Fickian diffusivity. Experiment FFH5V2 (K_{Th} $=10^2\,[M^2 \cdot \mathrm{sec}^{-1}]$, $K_{Tw} = 0.3 \cdot 10^{-4}\,[M^2 \cdot \mathrm{sec}^{-1}]$). Layers 1 to 6. Variable C.I. $10^{-8}\,[^{\circ}C \cdot \mathrm{sec}^{-1}]$.

where over–bar indicates time–averaged quantities.

Even though the patterns of distribution in the experiment tend to be geographically located in the areas corresponding to the boundary regions similar to the reference case (Figure 6-1), they have a much deeper interior penetration. The magnitude for all considered layers is more than ten times smaller than in the reference case. This considerate difference suggests that the Fickian diffusive scheme with the selected parameters can not reproduce the reference eddy heat flux divergence

In other two experiments, FFH1V1 and FFH5V3, the vertical diffusivities differ from

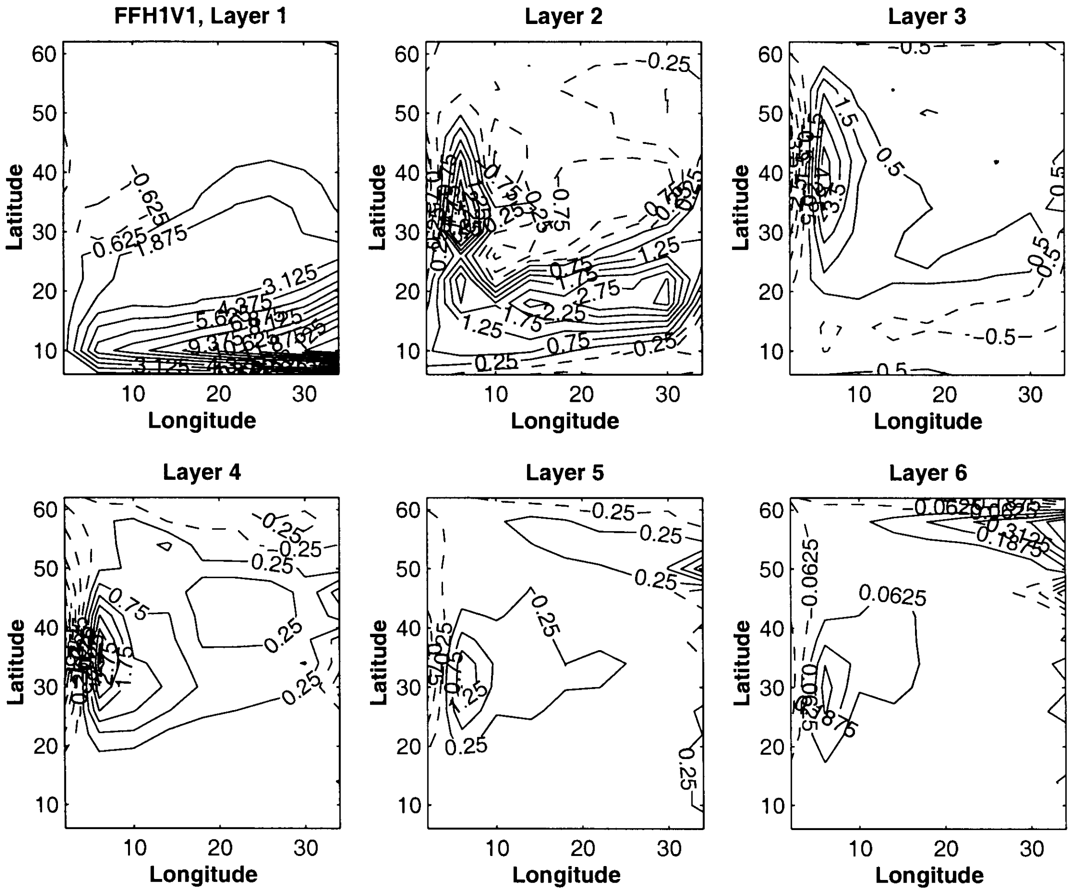

Figure 6-7: 3D flux divergence. Fickian diffusivity. Experiment FFH1V1 (K_{Th} =10^3 [$M^2 \cdot \mathrm{sec}^{-1}$], K_{Tw} = $0.1{\cdot}10^{-4}$ [$M^2 \cdot \mathrm{sec}^{-1}$]). Layers 1 to 6. Variable C.I. 10^{-8} [$°C \cdot \mathrm{sec}^{-1}$].

the reference value; thus,

$$\overline{\nabla \cdot \vec{F}_{FD}} + K_{Tw}^{ref}\bar{T}_{zz} = -K_{Th}\left(\bar{T}_{xx} + \bar{T}_{yy}\right) - \left(K_{Tw} - K_{Tw}^{ref}\right)\bar{T}_{zz}. \tag{6.3}$$

The presence of vertical diffusivity significantly modifies the magnitude of divergencies. In the case of weaker vertical diffusivity $0.1{\cdot}10^{-4}$ [$M^2 \cdot \mathrm{sec}^{-1}$] compared to the reference value, an area of strong positive divergence dominates the Southern part of the domain for the upper layer. A small local minimum is situated around mid–latitudinal

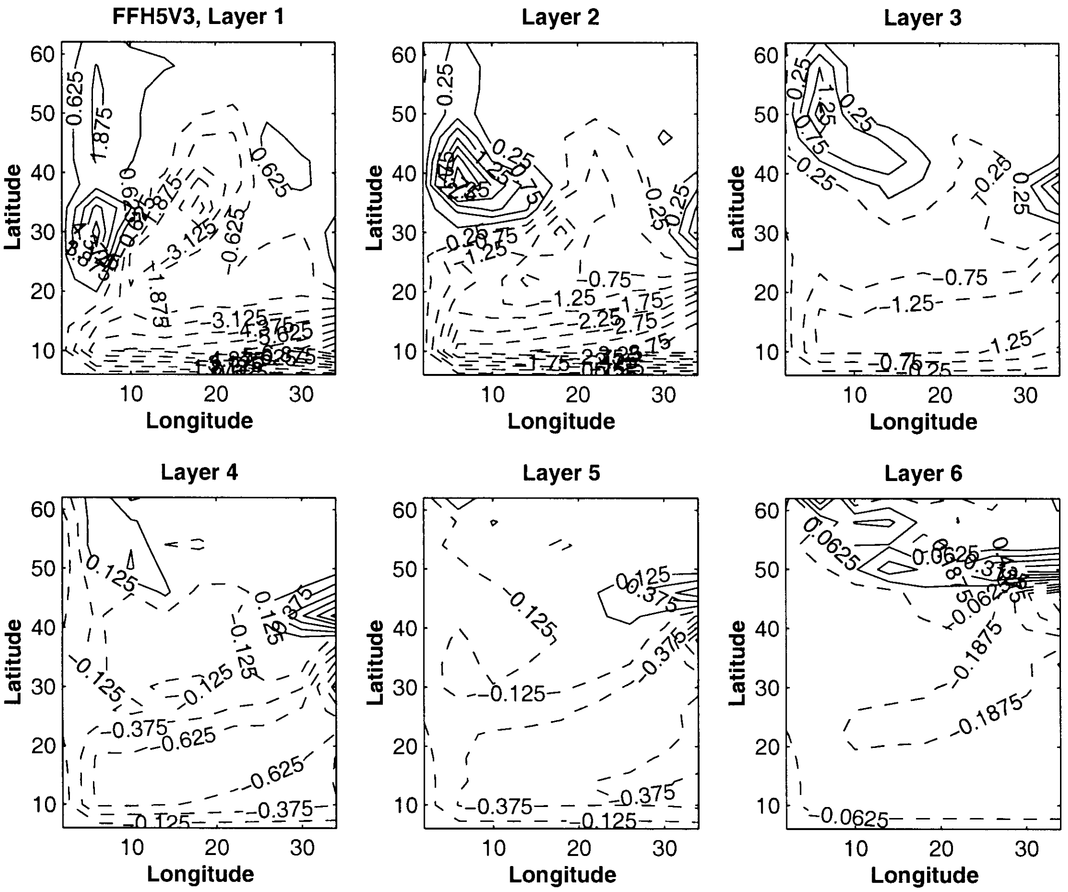
FFH5V3, Layer 1

Layer 2

Layer 3

Layer 4

Layer 5

Layer 6

Figure 6-8: 3D flux divergence. Fickian diffusivity. Experiment FFH5V3 (K_{Th} $=10^2\,[M^2\cdot\mathrm{sec}^{-1}]$, $K_{Tw} = 1{\cdot}10^{-4}\,[M^2\cdot\mathrm{sec}^{-1}]$). Layers 1 to 6. Variable C.I. $10^{-8}\,[^\circ C\cdot\mathrm{sec}^{-1}]$.

region. In the second layer of the same experiment divergence is large everywhere in the domain except in the Northern boundary area where the vertical term in (6.3) is small. The areas with the largest magnitude follows Western and Southern boundaries, similar to the reference case (Figure 6-1) although penetrating much deeper in the interior. In the high vertical diffusivity case FFH5V3 (K_{Tw} equals to $1.0\cdot 10^{-4}\,[M^2\cdot\mathrm{sec}^{-1}]$) an increase in magnitude similar to the previous experiment is identified. In the upper layer there is a strong divergence of temperature flux due to the larger value of vertical diffusivity compared to reference value. In the second layer the larger magnitude of vertical diffusivity produced larger negative divergence which is consistent with the diagnostics of the reference experiment, although it misses the positive anomaly in the mid–latitudinal area off the Western boundary. The fifth layer possesses a weak negative divergence lacking correspondence with the reference eddy heat flux divergence.

Summary

The presented coarse resolution experiments employing Fickian diffusivity were not successful in reproducing the climatological average properties of the reference calculation. The closest results in simulating the thermal structure as well as the total northward heat transport are achieved with the experiments using the exact value of the vertical diffusivity as in the reference simulation. The closest overturning circulation is achieved in the high viscous cases which at the same time overestimate the total northward heat flux by about 60%. The main deficiency of the Fickian scheme as evaluated in the climatological analysis is in simulating a deep ocean that is too warm. It leads to a decrease in the vertical temperature gradients, a less sharp thermocline and a decrease in the total northward heat transport for the interior regions

The analysis of the three–dimensional divergence of the heat flux implied by the Fickian diffusive scheme demonstrated a rather weak correspondence with the divergence of the eddy heat flux evaluated in the reference experiment. The conclusions are similar to the results of the previous chapter. The Fickian diffusivity in its most common form with constant coefficients lacks predictive skills. Climatological analysis showed that the experiments with the vertical diffusivity equal to the one used in simulating the reference state are the closest in reproducing the magnitude of the northward total heat transport. When evaluating divergence of the parameterized flux in those simulations, the magnitude was shown to be smaller; thus, the weaker are the modifications of the thermal balance the better the climatological results of the experiments. This conjecture is valid only if the nature of vertical flux is known, thus making impossible to produce some consistent results with Fickian diffusive scheme in the real ocean where the magnitude and nature of the vertical mixing is still an open question.

6.3.2 Green–Stone Parameterization Scheme

The flux vector that represents the Green–Stone eddy heat flux parameterization scheme has relatively simple form in the framework of the coarse resolution experiments presented in this chapter. The flux vector predicted with the scheme (5.24) can be written in the form of a diagonal tensor

$$\vec{F}_{GS} = -K_{vs} \begin{pmatrix} \frac{1}{2} & 0 & 0 \\ 0 & \frac{1}{2} & 0 \\ 0 & 0 & -\frac{1}{4}\hat{s}_{IS}^2 \end{pmatrix} \nabla T, \tag{6.4}$$

where $K_{vs} = \alpha \overline{\frac{f}{\sqrt{\text{Ri}}}}^{z} l^2$. The mixing coefficient is computed according to the suggestion by *Visbeck et. al, 1997* [58] as an averaged over thermocline layers. The distribution of the coefficient K_{vs} is a two–dimensional function that reflects variability in the Richardson number Ri$= \frac{N^2 f^2}{M^2}$. In the vertical direction, it is necessary to introduce some variability to the parameterization scheme (6.4) due to non–homogenous properties of mesoscale eddies with depth. *Stone, 1972* [54] identified a mid–depth intensification of the correlation between the components of the vertical eddy heat flux. His analytical solution of the baroclinic instability problem of the Eady model (*Eady, 1949* [18]) revealed a parabolic structure of the correlation within the vertical dimension of the baroclinic zone. In the conceptual Eady model the total depth of fluid represents the vertical scale of the baroclinically unstable zone. In the framework of the coarse resolution experiments here carried out, it is necessary to identify the baroclinic zone where the underlying physical assumptions of the Green–Stone scheme are valid.

The thermocline and the upper ocean are the areas of the domain where eddies were demonstrated to be the strongest (Chapters 4 and 5). As a first approximation the depth H_{GS} of the upper 950 meters that corresponds to the first seven layers of the model ocean is chosen to approximate the vertical scale of the baroclinic zone. It is assumed to be constant for the whole numerical domain. A parabolic function $f_w(z)$ consistent with the Stone's analysis is introduced to reflect the vertical structure of mesoscale eddies. It multiples the mixing coefficient K_{vs}. The form of this function is

$$f_w(z) = \begin{cases} \frac{4}{H_{GS}^2} z \left(z - H_{GS}\right), \text{ if } 0 < z \leqslant H_{GS}, \\ 0, \text{ if } z > H_{GS}, \end{cases} \tag{6.5}$$

such that it is equal to zero at the surface and below the depth H_{GS} of the baroclinic zone and reaches mid–depth maximum at approximately the fifth layer of the model. Accordingly, the mixing, both horizontal and vertical, is intensified for the thermocline ocean and is represented only as a background vertical mixing for the deep ocean. Figure 6-9 shows $f_w(z)$ which represents the vertical variability in the mixing coefficients.

Taking into account the vertical dependence of the mixing coefficient the Green–Stone scheme is implemented in the MIT Model as the divergence of the flux

$$\vec{F}_{GS} = -K_{vs}(z) \begin{pmatrix} \frac{1}{2} & 0 & 0 \\ 0 & \frac{1}{2} & 0 \\ 0 & 0 & -\frac{1}{4}\hat{s}_{IS}^2 \end{pmatrix} \nabla T, \tag{6.6}$$

where

$$K_{vs}(z) = \alpha \overline{\frac{f}{\sqrt{\mathrm{Ri}}}}^{z} l^2 \cdot f_w(z).$$

The depth of vertical averaging is equal to the depth of the baroclinic zone H_{GS} used in deriving the vertical profile of f_w.

There are two related parameters which define the scheme. The efficiency parameter α and the mixing length scale l which can be evaluated as one value: multiplying α by 2 is equivalent to increasing the mixing length scale l by $\sqrt{2}$ times while keeping the other constant. The experiments in this chapter will be with variable α.

There is a potential implementational problem with the GS scheme as presented in

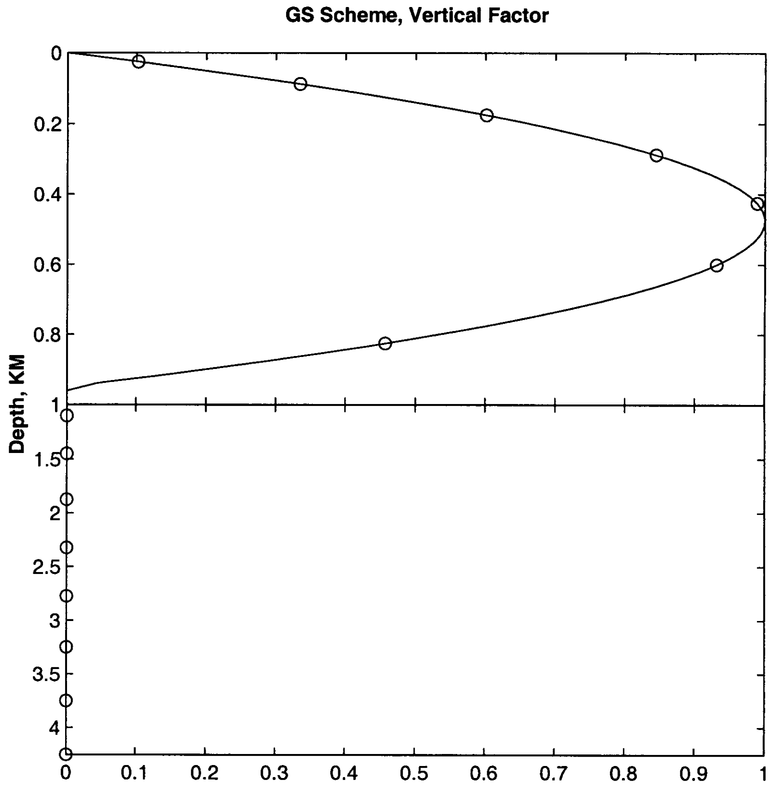

Figure 6-9: Coefficient of the vertical dependence of K_{vs}. Each circle represents the value for its respective layer. Stretched upper $1000M$.

(6.6). It lies in the negative sign of the (3, 3) element of the tensor. Without stabilizing effects as a large background vertical diffusivity there is a potential for numerical instability in areas of large slopes. How large the slope is allowed to be in order to avoid numerical instabilities? Consider the distribution of the coefficient K_{vs} as estimated in the reference experiment and the initial conditions for temperature (Figure 6-10) for α equals 0.02 and mixing length scale $200KM$. These estimations were obtained with additional assumptions that the slope $\hat{s}_{IS}$ is not allowed to be larger than 0.01 and the cut–off for K_{vs} is $2500[M^2 \cdot \sec^{-1}]$. These values are in the range of parameters which were used in *Visbeck et. al, 1997* [58]. The magnitude of K_{vs} is about $10^2 - 10^3\,[M^2 \cdot \sec^{-1}]$. In the Northern area of the domain it reaches the maximum allowed values. In order to perform a stable numerical experiment it is necessary that the vertical diffusivity, the only

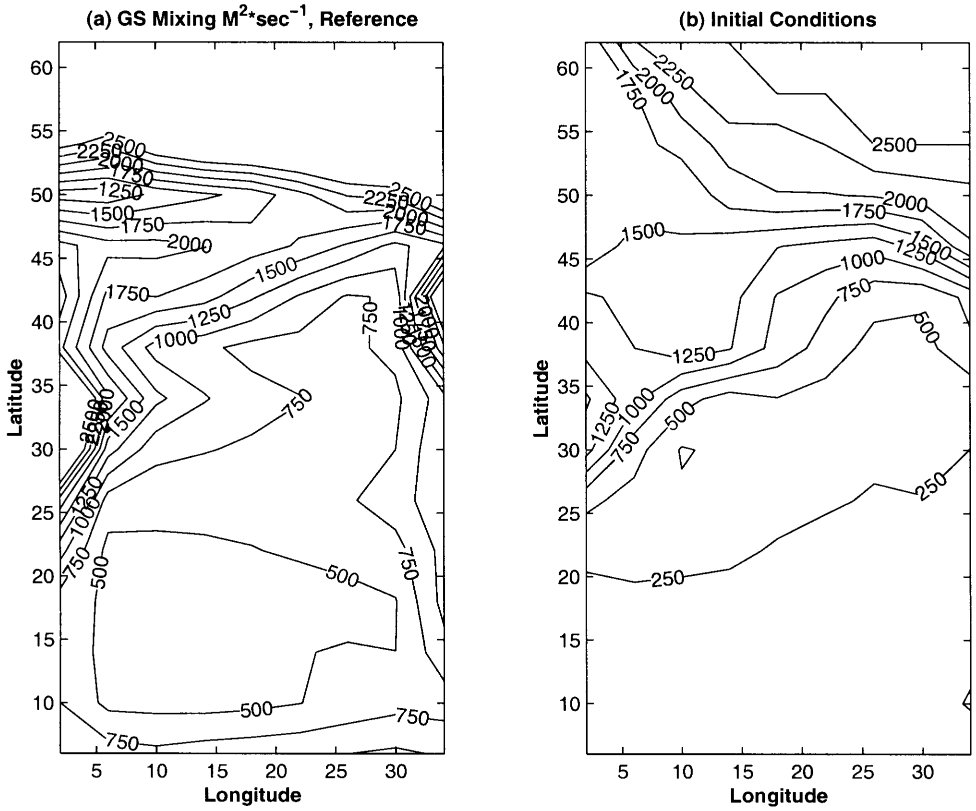

Figure 6-10: Estimation of the GS mixing coefficient K_{vs}, $[M^2 \cdot \sec^{-1}]$ averaged over 950M (upper 7 layers), $\hat{s}_{IS} < 0.01$, $\alpha = 0.02$, $l = 200KM$. (a) Reference experiment smoothed on 1° × 1° box, (b) initial conditions. Contours shown $< 2500\,[M^2 \cdot \sec^{-1}]$.

available counteracting mechanism, balances the upgradient flux of $\vec{F}_{GS}$ in the vertical direction, that is

$$K_{Tw} > K_{vs}\left(\frac{1}{4}\hat{s}_{IS}^2\right),$$

or

$$\hat{s}_{IS} < 2\sqrt{\frac{K_{Tw}}{K_{vs}}}. \tag{6.7}$$

For the reference value of the vertical diffusivity $0.3 \cdot 10^{-4}\,[M^2 \cdot \sec^{-1}]$ and maximum allowed K_{vs} of $2.5 \cdot 10^3\,[M^2 \cdot \sec^{-1}]$ it translates in the condition on the slope to be

$$\hat{s}_{IS} \lesssim 2 \cdot 10^{-4}.$$

		α		
		0.004	0.02	0.1
$\max(\hat{s}_{IS})$	10^{-4}	GSA2S3	GSA1S3	GSA3S3
	10^{-3}	GSA2S1	GSA1S1	GSA3S1
	10^{-2}	GSA2S2	not stable	not stable

Table 6.2: Experiments with the Green–Stone parameterization

Thus, a numerical experiment with the preliminary specified restrictions on the slope will be numerically unstable. In order to be able to execute an experiment it is necessary either to decrease α or to restrict the slope to a smaller upper bound. Both of the assumptions lead to a smaller value of the K_{vs} and result in numerical stability. At the same time with smaller value of K_{vs} the restriction on the slope (6.7) can be relaxed. This relation is non–linear (K_{vs} depends on the slope itself), so it is impossible a priori to set limits on coefficients. The numerical experiments presented in this section which use only the Green–Stone scheme together with the background vertical diffusivity will explore the relations between these parameters.

Table 6.2 presents experiments performed with the Green–Stone scheme. The horizontal and vertical viscosity coefficients are the same as in the Fickian diffusivity experiments.

Climatological Analysis

Horizontally Averaged Temperature Due to the constraints imposed on the mixing coefficient such as the combination of the maximum slope and the efficiency parameter, the resulting mixing coefficients do not significantly vary for different experiments. The solutions, except in the experiment GSA3S3, are close to the reference state. The difference is only within $1°C$ from the reference profile. For the upper $1000M$ (Figure 6-11) five out of six considered experiments are within $0.2°C$ from each other and underestimate horizontally averaged temperature by about 1 degree. The sixth experiment GSA3S3 with the resulting higher horizontal mixing has the closest to the reference profile temperature with difference only $0.1°C$. For the deeper ocean all experiments slightly overestimate the temperature.

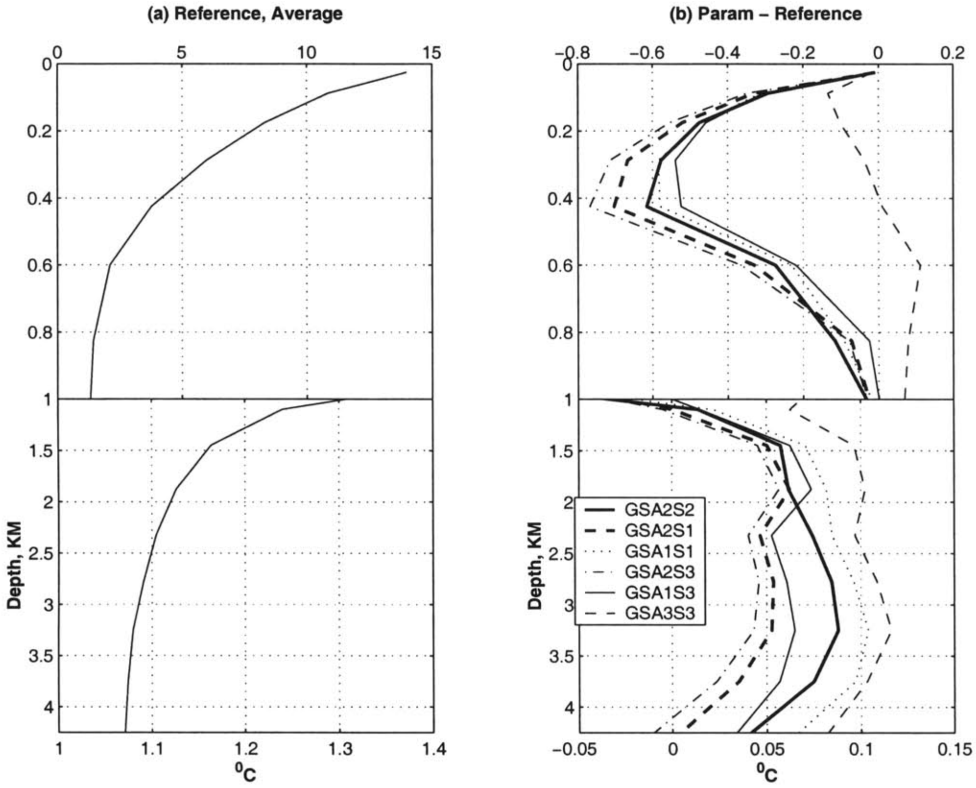

Figure 6-11: Horizontally averaged temperature, $[°C]$. Green–Stone scheme. (a) Reference experiment. (b) Parameterization experiments minus Reference. Stretched upper $1000M$. Labels identify experiments.

Zonally Averaged Temperature The plots presenting the simulation of thermocline temperature (Figure 6-12) also shows the same two groups of experiments. Within the larger group the profiles are close to each other and produce cooler ocean at this depth compared to the reference. The temperature profile of the sixth experiment is about one degree warmer than the rest. All experiments converge for high latitudes, North of $50°N$. The mixing coefficient and the slope reach their respective maximum values such that all experiments have similar mixing properties in this region.

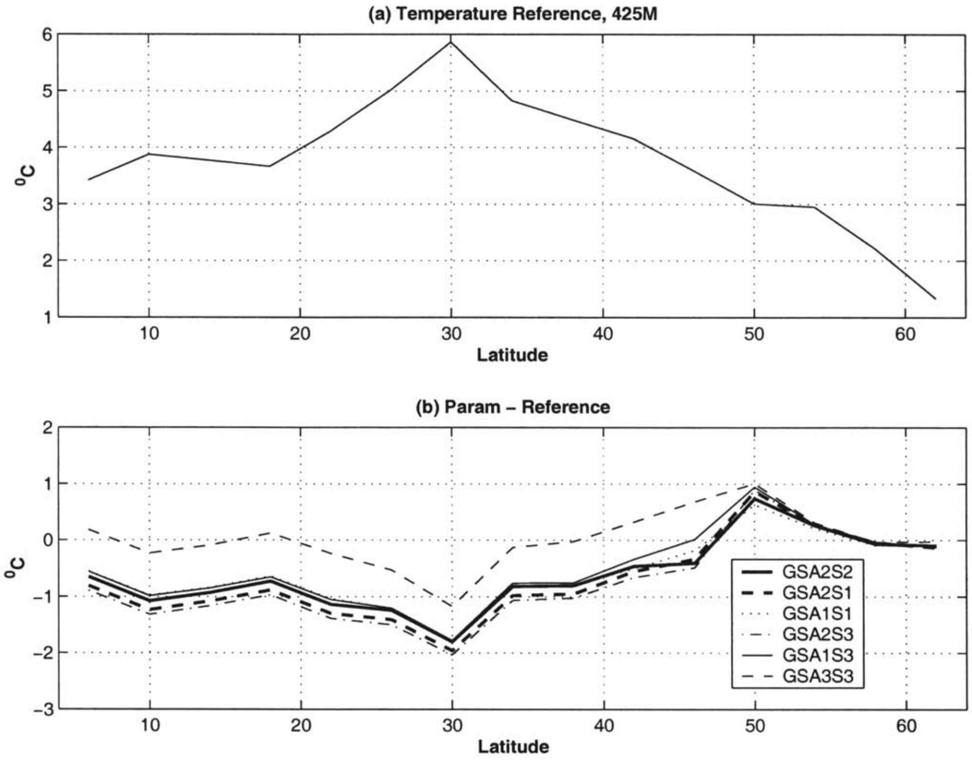

Figure 6-12: Zonally averaged temperature, section at $425M$, $[°C]$. Green–Stone scheme. (a) Reference experiment. (b) Parameterization experiments minus Reference. Labels identify experiments.

Total Heat Transport All experiments show a similar magnitude and distribution of the heat transport (Figure 6-13) due to the same value of background diffusivity used in the experiments. This demonstrates that the correction to the vertical mixing due to upgradient vertical flux have moderate climatological impact. The first five considered experiments with smaller values of K_{vs}, due to smaller α or stricter restrictions on the magnitude of the slope, produce overall stronger heat transport compare to the sixth experiment which shows almost linear decrease in transport with latitude. The difference is due to the effective horizontal mixing which is stronger in the experiment GSA3S3. There is an analogy with the Fickian parameterization experiments where a similar enhancement to the total heat transport was observed in simulations with weaker horizontal mixing. All experiments converge by 50° N.

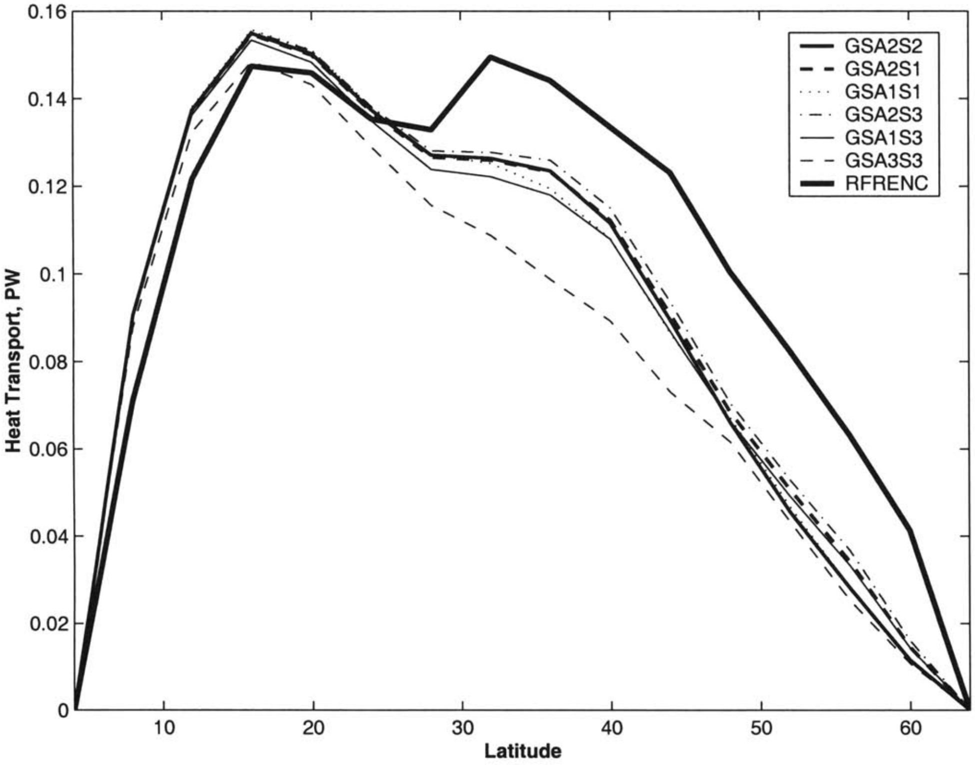

Figure 6-13: Total heat transport, $[PW]$. Green–Stone scheme. Labels identify experiments. RFRENC is the reference experiment.

Meridional Overturning Transport The patterns of the overturning transport are similar for all experiments. Both values are about $2Sv$ smaller than the reference values suggesting that the considered implementation of the Green–Stone parameterization scheme for the range of parameters presented in this chapter leads to a weak compact main overturning cell without significant southward penetration.

Divergence of Parameterized Flux

The divergence of the flux $\vec{F}_{GS}$ computed with the Green–Stone scheme is evaluated for the data averaged over the last 50 years of the coarse resolution experiments. The

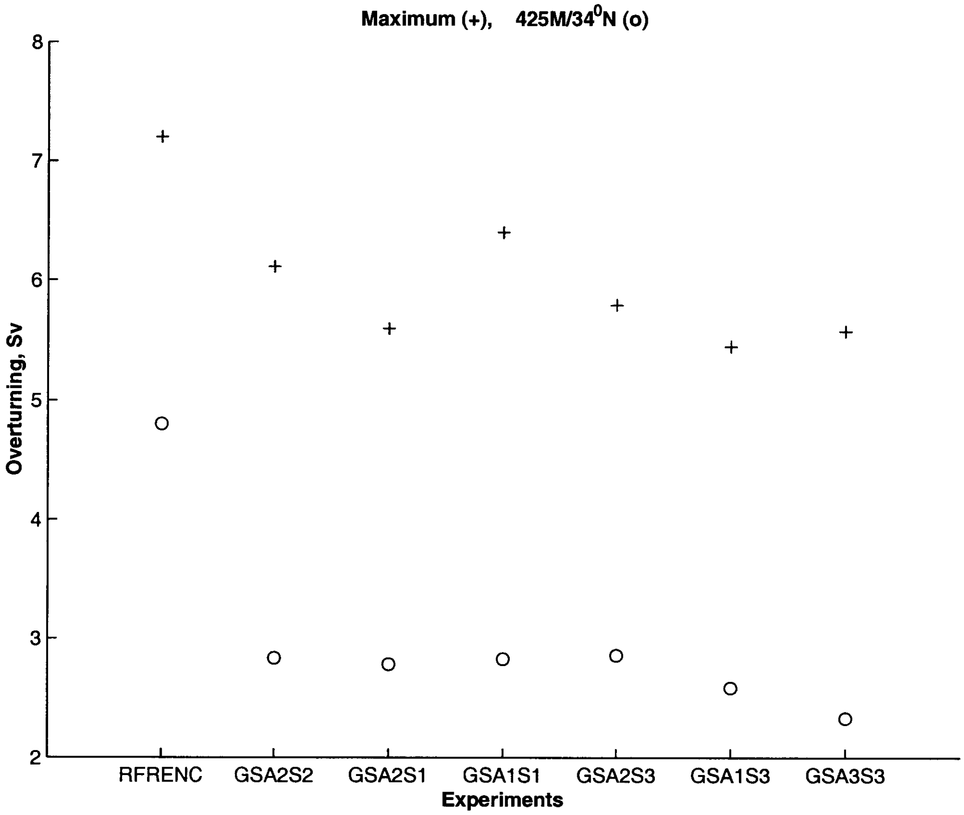

Figure 6-14: Overturning stream function, $[Sv]$. (+) Maximum. (o) at $(34°N, 425M)$. Green–Stone scheme. Labels identify experiments. RFRENC is the reference experiment.

background vertical diffusivity is equal to the reference value; therefore, it does not effect the evaluation

$$\nabla \cdot \overline{\vec{F}_{GS}} = -\nabla \left[\overline{K_{vs}} f_w(z) \begin{pmatrix} \frac{1}{2} & 0 & 0 \\ 0 & \frac{1}{2} & 0 \\ 0 & 0 & -\frac{1}{4}\left(\overline{L^x}^2 + \overline{L^y}^2\right) \end{pmatrix} \nabla \bar{T} \right], \tag{6.8}$$

where all time–varying components are averaged over 50 years of integration and the time–averaged slope is estimated as the sum of its time–averaged zonal and meridional components.

The evaluation of divergencies is performed for two experiments which results demonstrate varying skills in reproducing the climatology of the reference experiment. The first presented experiment GSA1S1 represent a group of five similarly performing experiments. The maximum allowed slope in this experiment is 10^{-3}. The efficiency coefficient α is 0.02. As a first step, I estimate the magnitude of mixing. The GS mixing coefficient $\overline{K_{vs}}$ defines the horizontal downgradient mixing. Figure 6-15 shows its magnitude evaluated in the experiment GSA1S1. Given the vertical dependence according to $f_w(z)$ (6.5) and the diagonal coefficients of the tensor (6.8), the values correspond to twice the magnitude of horizontal mixing for the 5^{th} layer. The right panel of Figure 6-15 shows the actual vertical mixing (including the contribution of the background diffusivity) for the fifth layer.

The patterns of high latitude enhanced mixing are similar to the diagnosed from the reference experiment and the initial conditions (Figure 6-10). The magnitude reaches about $1500[M^2 \cdot \sec^{-1}]$ for the Northernmost areas. This intensification is connected with the larger slope of the isopycnals limited by the maximum allowed value. Even for the moderate horizontal mixing the resulting vertical mixing is strongly upgradient for the Northern area and near the Western boundary area. These are the regions where a numerical instability develope when the restrictions on the slope and efficiency coefficient are relaxed. The GS scheme in the interior and Southern parts of domain do not produce additional vertical fluxes. The small slope and stable stratification leads to small vertical parameterized flux such that the resulting mixing coefficient is nearly equal to the background vertical diffusivity.

Figure 6-16 shows the three–dimensional divergence of the flux (6.8) for the experiment GSA1S1.

The upper layer divergence is weak because of the effective small mixing coefficients. The general position of the patterns similar to the Fickian diffusivity case of moderate horizontal and the reference vertical diffusivity with the same deficiencies in reproducing the eddy heat flux divergence. For the subsurface area the magnitude becomes larger

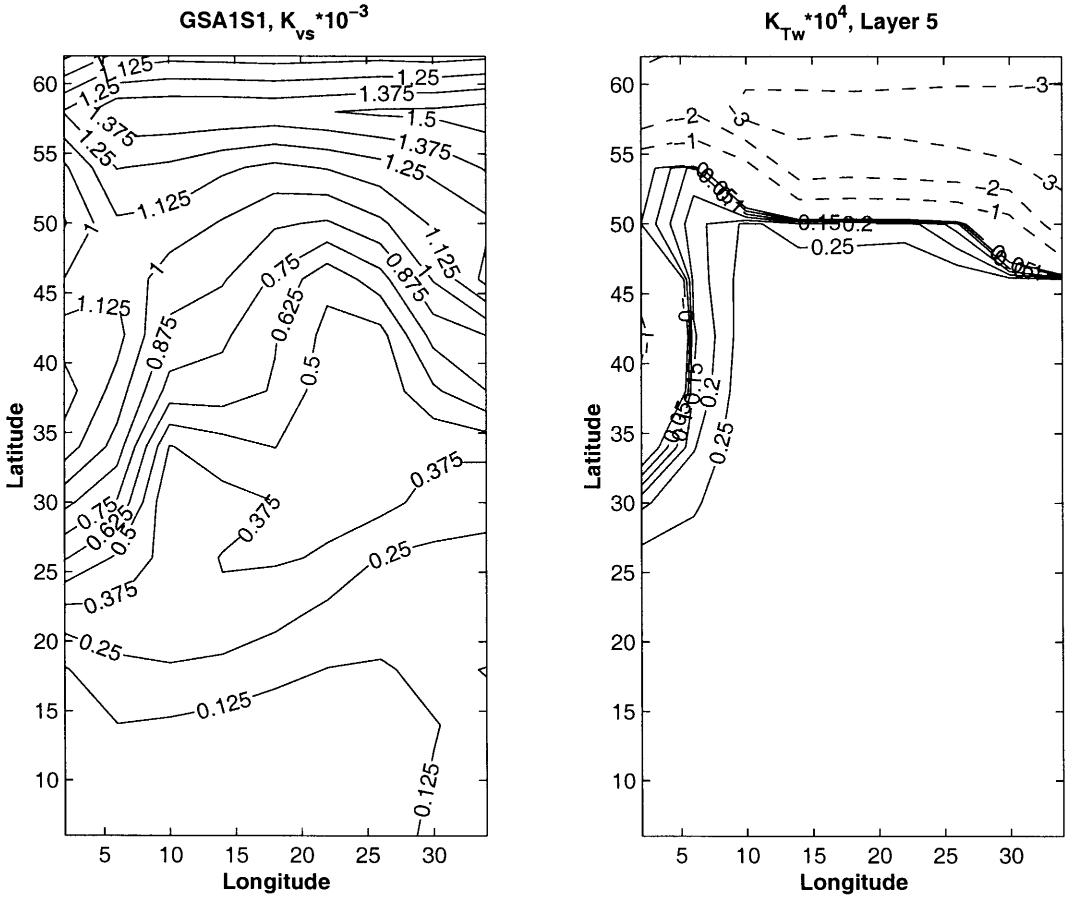

Figure 6-15: Mixing coefficients in experiment GSA1S1 ($\alpha = 0.02$, $\max(\hat{s}_{IS}) = 10^{-3}$). Left: K_{vs}, C.I. $0.125{\cdot}10^3\,[M^2 \cdot \mathrm{sec}^{-1}]$. Right: vertical mixing coefficient, variable C.I. $1{\cdot}10^{-4}\,[M^2 \cdot \mathrm{sec}^{-1}]$ for negative, $0.05{\cdot}10^{-4}\,[M^2 \cdot \mathrm{sec}^{-1}]$ for positive.

being of the same order as diagnosed from the reference experiment. The location of the patterns for the interior mid–latitudinal and Northern areas of the domain have some similarity with the geographical distribution in the reference experiment. The scheme fails in the Western boundary for deeper layers predicting the opposite sign of the divergence. The result consistent with the observations made in the previous chapter when evaluating the scheme's local properties. The Green–Stone parameterization can not identify the patterns in the Southern part of the domain due to weak parameterized flux in addition to the flux due to the background vertical diffusivity.

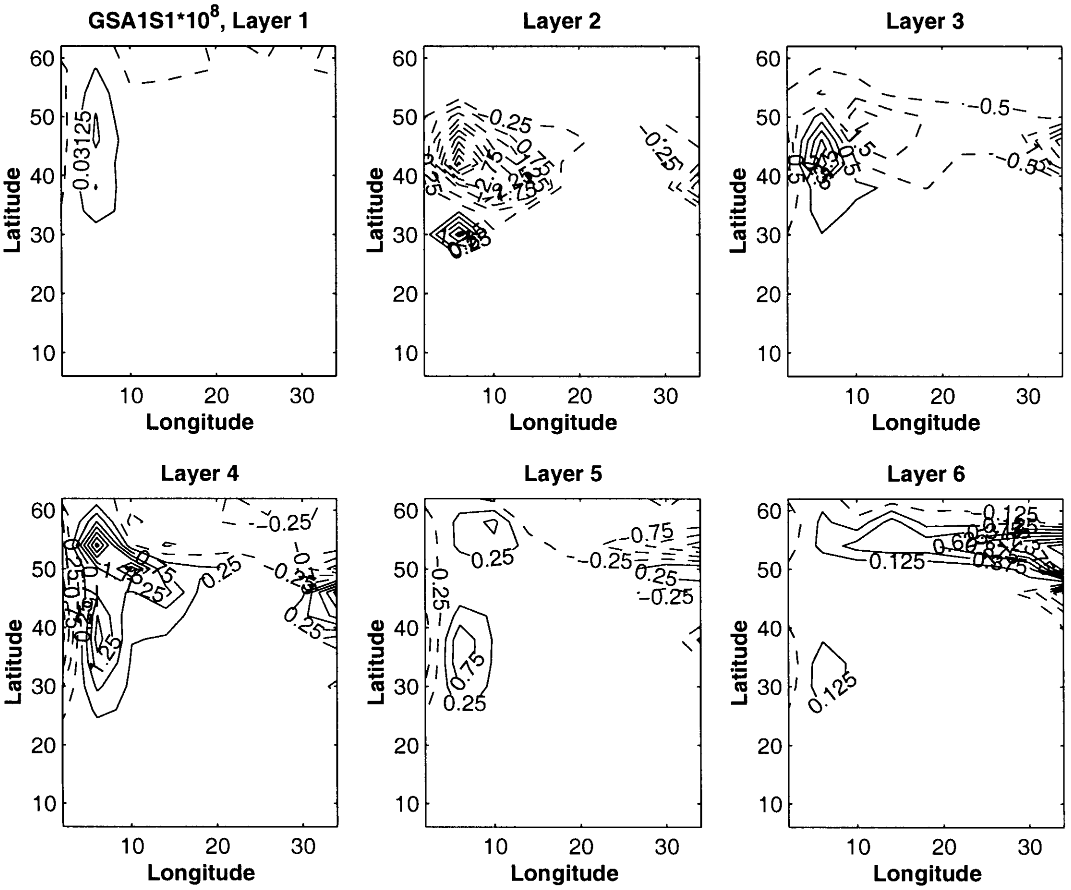

Figure 6-16: Flux divergence. Green–Stone scheme. Experiment GSA1S1 (α = 0.02, $\max(\hat{s}_{IS}) = 10^{-3}$). Layers 1 to 6. Variable C.I. in $10^{-8}\,[^{\circ}C \cdot \sec^{-1}]$ units.

The second experiment considered is GSA3S3 with stricter restrictions on the slope ($<10^{-4}$) and larger efficiency coefficient $\alpha = 0.1$ (or bigger mixing length scale). The resulting horizontal mixing (Figure 6-17, left panel) is significantly enhanced reaching almost a maximum allowed value of $2500[M^2 \sec^{-1}]$. At the same time due to the slope restricted to be small an additional vertical transport (Figure 6-17, right panel) is weak such that it equals to background vertical diffusivity with a small negative correction.

Given the constraints on the coefficients the resulting distribution of the divergencies (Figure 6-18) points on similarities with a Fickian diffusivity experiment FFH5V2 (Figure 6-6) taking into account larger variable horizontal mixing coefficient. This observation

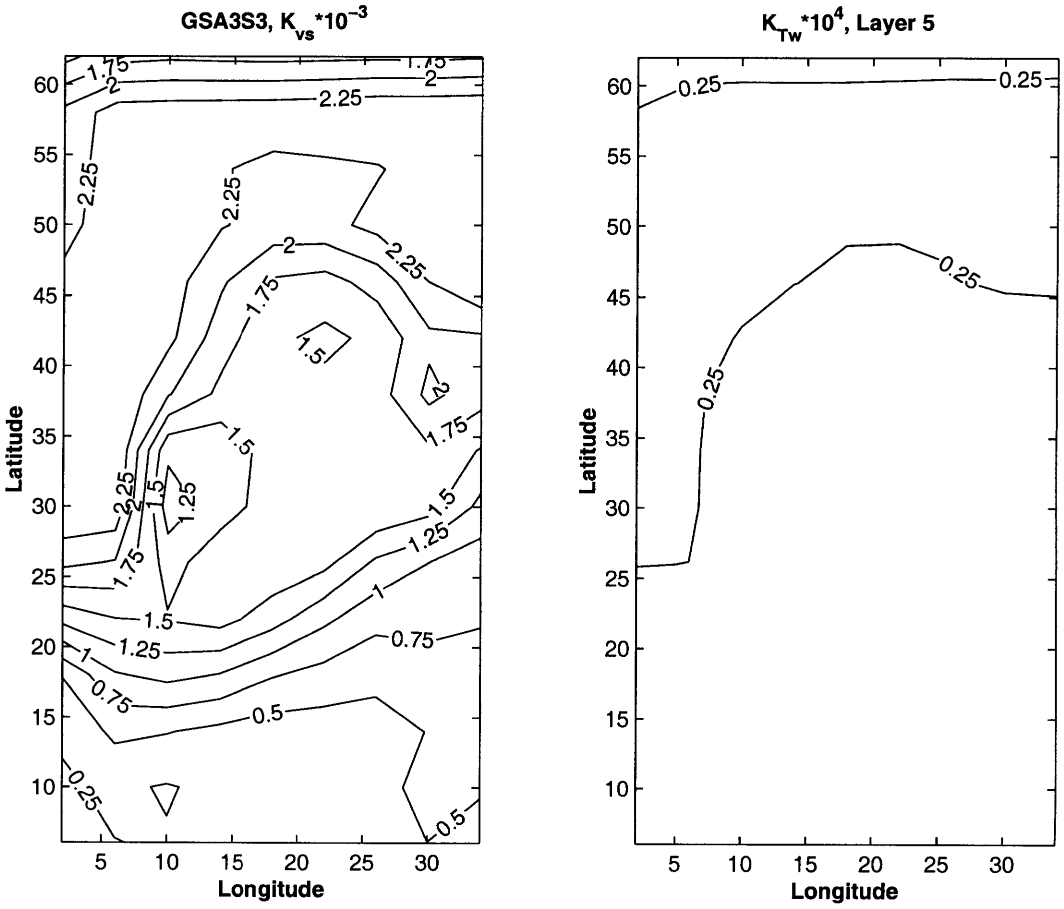

Figure 6-17: Mixing coefficients in experiment GSA3S3 ($\alpha = 0.1$, $\max(\hat{s}_{IS}) = 10^{-4}$). Left: K_{vs}, C.I. $0.25 \cdot 10^3\, [M^2 \cdot \sec^{-1}]$. Right: vertical mixing coefficient $10^{-4}\, [M^2 \cdot \sec^{-1}]$.

holds for all presented six layers.

Summary

The baroclinic instability mechanism underlying Green–Stone parameterization scheme leads to upgradient vertical flux of heat, thus making the scheme numerically unstable in the absence of complementary stabilizing processes, such as vertical diffusion. The implied mixing coefficients exhibit increasing magnitude for high latitude regions as well as in the areas with a convergent isopycnals. Application of the scheme in the form of hori-

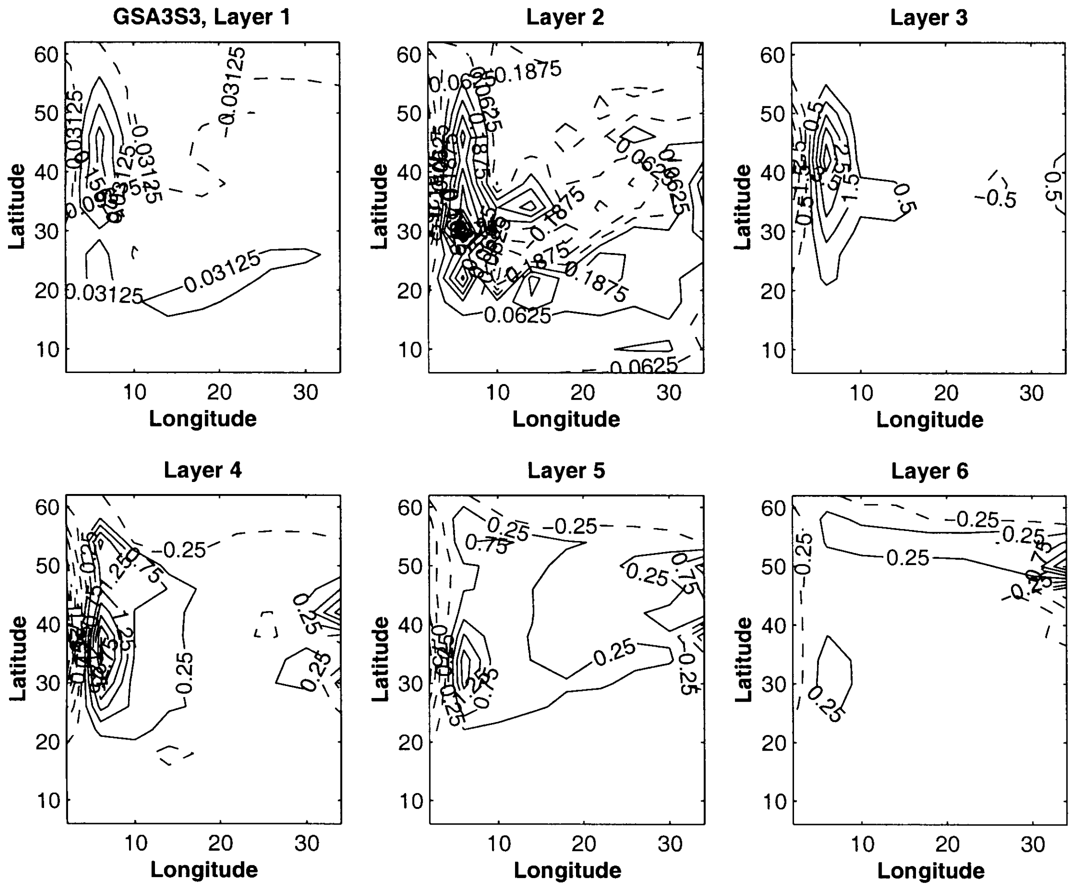

Figure 6-18: Flux divergence. Green–Stone scheme. Experiment GSA3S3 ($\alpha = 0.1$, $\max(\hat{s}_{IS}) = 10^{-4}$). Layers 1 to 6. Variable C.I. in $10^{-8}\,[°C \cdot \mathrm{sec}^{-1}]$ units.

zontally varying coefficient with vertical weight that reflects the approximate correlation between the components of the eddy heat flux leads to a relatively good representation of the upper ocean and with slightly warmer deep ocean compared to the reference simulation. The experiments do not reproduce the total heat transport of the reference simulation, even though they are able to approximate heat transport for higher latitude with a better skill than the Fickian scheme.

The diabatic nature of the scheme suggests some similarities with the distribution of properties with the Fickian diffusivity experiments. Though the Green-Stone scheme reproduces the magnitude better than the Fickian diffusivity. In all cases the magnitude of the evaluated divergence for subsurface layers is closer to the eddy heat flux divergence diagnosed in the reference experiment. The geographical distribution lacks the correspondence with the eddy heat flux divergence.

6.3.3 Gent–McWilliams Parameterization Scheme

The Gent–McWilliams scheme as formulated in the MIT GCM represents the flux due to the unresolved mesoscale motions as

$$\vec{F}_{GM} = -K_{GM} \begin{pmatrix} 1 & 0 & 0 \\ 0 & 1 & 0 \\ 2L^x & 2L^y & \hat{s}_{IS}^2 \end{pmatrix} \nabla T, \tag{6.9}$$

where the magnitude of the slope vector is

$$\hat{s}_{IS} = |(L^x, L^y, 0)| = \left|\left(-\frac{T_x}{T_z}, -\frac{T_y}{T_z}, 0\right)\right|.$$

The scheme as implemented in the model is applied only in the limit of a small slope, where its magnitude can be computed according to the above formula. The model checks the magnitude of the slope and does not allow it to be larger than a specified value. In the experiments presented in this chapter the slope $\hat{s}_{IS}$ is limited to 0.01.

The parameter that solely defines the scheme is the background mixing coefficient K_{GM}. The experiments will address the sensitivity of the climatological state to the magnitude of the mixing coefficient. In all experiments K_{GM} is constant value everywhere in the domain. The parameterization represents only effects of the unresolved mesoscale motions. In addition it requires some extra mixing terms due other unresolved processes, such as internal waves breaking or implicit numerical diffusion. An additional vertical viscosity is introduced in the model to address these issues. The vertical diffusivity coefficient used in the reference experiment is the base value for the coarse resolution experiments with this parameterization. In the coarse resolution experiments performed

		K_{GM}, $[M^2 \cdot \sec^{-1}]$		
		10^1	10^2	10^3
	0		AGM5V0	
K_{Tw}	$0.1 \cdot 10^{-4}$		AGM5V1	
	$0.3 \cdot 10^{-4}$	AGM7V2	AGM5V2	AGM2V2
	$1.0 \cdot 10^{-4}$		AGM5V3	

Table 6.3: Experiments with the Gent–McWilliams parameterization

so far, the background vertical diffusivity is the most important parameter in order to reproduce a correct magnitude of the total heat transport. The Gent–McWilliams parameterization experiments with different values of the background vertical diffusivity will explore the sensitivity of the magnitude of the total heat transport to the value of background vertical diffusivity.

Table 6.3 presents the experiments performed with the GM scheme.

Climatological Analysis

Horizontally Averaged Temperature Figure 6-19 presents the horizontally averaged temperature for the experiments with Gent–McWilliams parameterization scheme. The thermocline layers show cooler temperature compare to the reference experiments when the scheme used together with the moderate vertical diffusivity. The introduction of the background vertical diffusivity of 10^{-4} $[M^2 \cdot \sec^{-1}]$ causes the warming of the thermocline layers (Experiments AGM5V0 to AGM5V3). The larger K_{Tw} causes significant erosion of the thermocline by mixing warmer upper water with the deeper ocean making it warmer than in the reference experiment. The increase in the GM mixing coefficient (Experiments AGM7V2, AGM5V3, AGM2V2) on the other hand cause cooling of the upper layers.

The sensitivity to the values of mixing coefficients for deeper layers show similar patterns. The three experiments with the vertical diffusivity used in the reference experiment demonstrate good skills in reproducing temperature profile. All of them are within $0.1°C$ of the reference values.

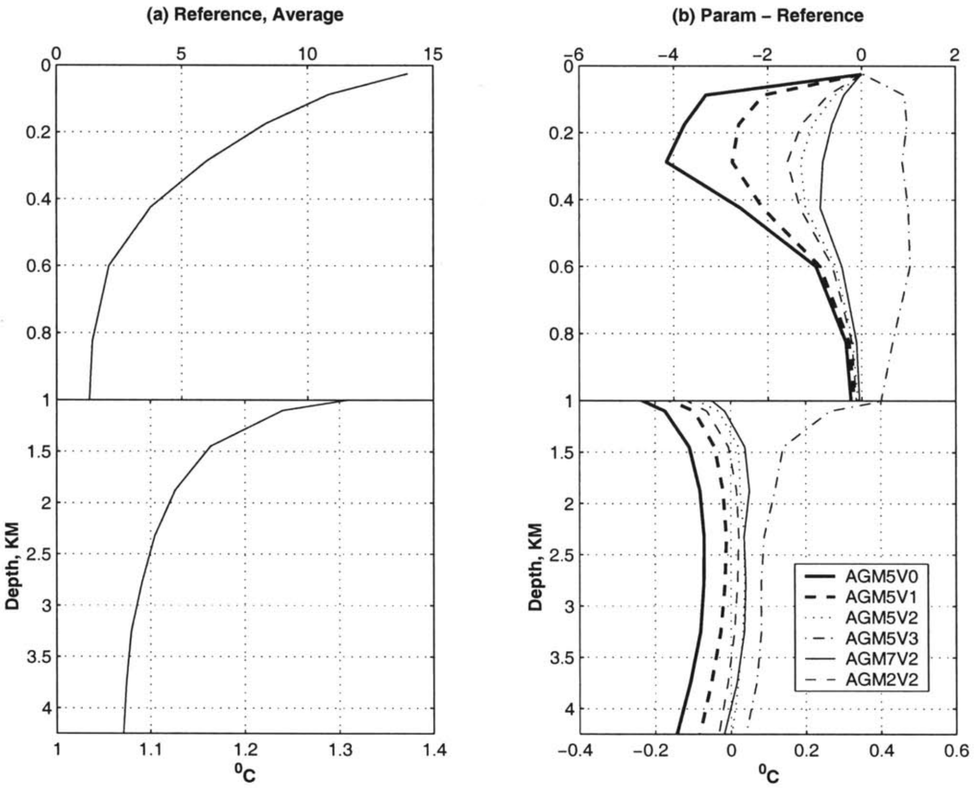

Figure 6-19: Horizontally averaged temperature, [$^\circ C$]. Gent–McWilliams scheme. (a) Reference experiment. (b) Parameterization experiments minus Reference. Stretched upper $1000M$. Labels identify experiments.

Zonally Averaged Temperature The temperature profile for the thermocline layer (Figure 6-20) shows that only high viscous case overestimates the temperature of the thermocline. Other experiments produces cooler thermocline to the South of $47N$. The non–diffusive (AGM5V0) and low–diffusive (AGM5V1) cases underestimate the temperature everywhere by as much as $4^\circ C$ for midlatitudinal areas. Increase in the coefficient of the background vertical diffusivity warms the thermocline layers. On the other hand increase in K_{GM} decreases the temperature. The experiments with smaller values of the GM mixing coefficient demonstrate better skills.

(a) Temperature Reference, 425M

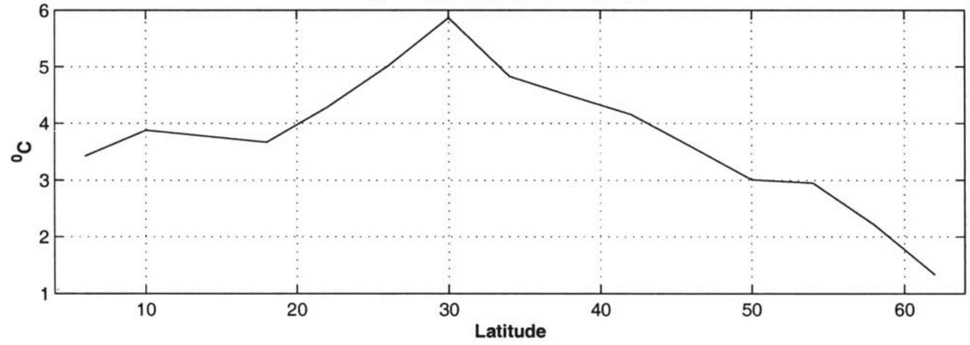

(b) Param – Reference

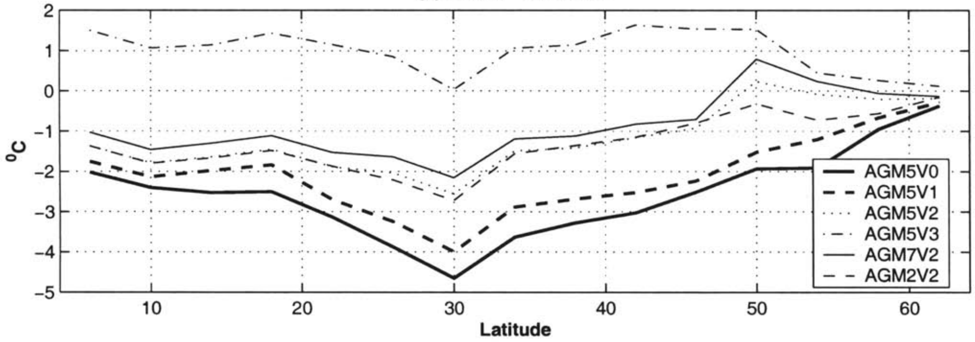

Figure 6-20: Zonally averaged temperature, section at $425M$, $[{}^{\circ}C]$. Gent–McWilliams Scheme. (a) Reference experiment. (b) Parameterization experiments minus Reference. Labels identify experiments.

Total Heat Transport The evaluation of total heat transport for the experiments is shown in Figure 6-21. The background vertical diffusivity defines the magnitude of the total heat transport. The changes in magnitude are of the same order as in the Fickian diffusivity experiments. The Gent–McWilliams parameterization scheme modifies the profile. Three experiments with varying K_{GM} with the reference value for the vertical diffusivity as expected produce the closest fit for the total heat transport. In the Southern part of the basin, increase in the coefficient leads to continuous increase in the heat transport. At the same time for mid–latitudinal area there is a convergence of all three curves. In addition by increasing K_{GM} from $10\,[M^2 \cdot \mathrm{sec}^{-1}]$ (AGM7V2) to $100\,[M^2 \cdot \mathrm{sec}^{-1}]$ (AGM5V2) the heat transport at $40N$ is increased, but for the subsequent increase to

1000 $[M^2 \cdot \sec^{-1}]$ (AGM2V2) the heat transport is decreased. This sensitivity is different from the experiments with Fickian diffusion where the changes were monotonous.

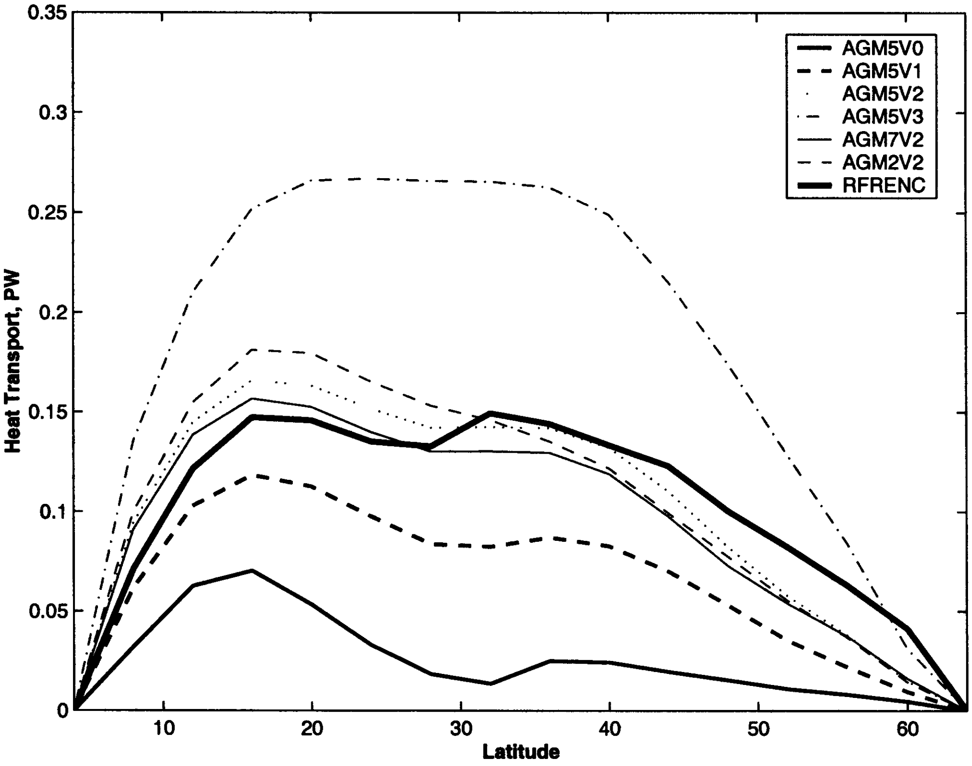

Figure 6-21: Total heat transport, $[PW]$. Gent–McWilliams scheme. Labels identify experiments. RFRENC is the reference experiment.

Overturning Circulation Figure 6-22 shows the strength of water formation and the southward penetration of the main overturning cell at $(34N{,}425M)$. The increase in K_{GM} (AGM7V2, AGM5V2 and AGM2V2) leads to increase in the magnitude of the water formation from less than $6Sv$ to more than $9Sv$. At the same time the corresponding southward penetration is about the same at about $3Sv$. Increase in background vertical diffusivity for a moderate value of K_{GM} of 100 $[M^2 \cdot \sec^{-1}]$ from $0.1{\cdot}10^{-4}$ $[M^2 \cdot \sec^{-1}]$ (AGM5V1) to $0.3{\cdot}10^{-4}$ $[M^2 \cdot \sec^{-1}]$ (AGM5V2) does not develop difference in the experiments' values maintaining about $8Sv$ for the maximum and $3Sv$ for the midlatitudinal thermocline location.

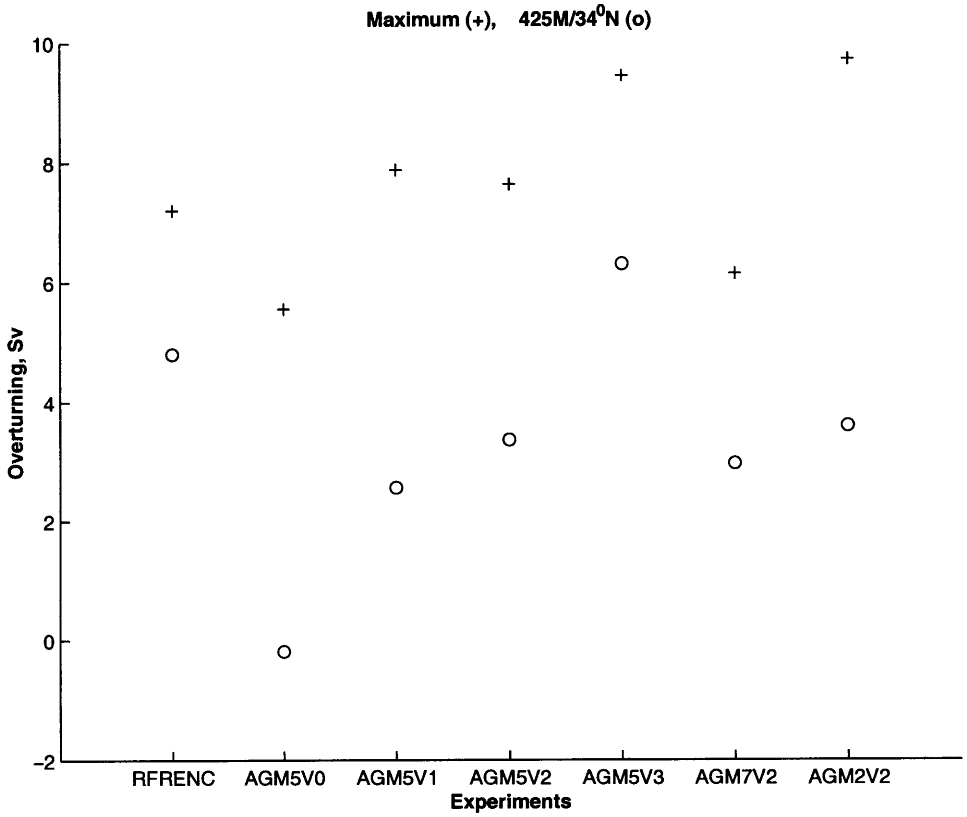

Figure 6-22: Overturning stream function, $[Sv]$. (+) Maximum. (o) at $(34°N, 425M)$. Gent–McWilliams scheme. Labels identify experiments. RFRENC is the reference experiment.

Divergence of Parameterized Flux

Three experiments are considered for the evaluation of the divergence of the parameterized heat flux. They are AGM5V2 and AGM5V3 ($K_{GM} = 10^2\,[M^2 \cdot \text{sec}^{-1}]$) and AGM7V2 ($K_{GM} = 10^2\,[M^2 \cdot \text{sec}^{-1}]$). The first and third experiments have a background vertical diffusivity equal to the reference value. The second experiment is performed with a larger diffusivity of $1.0 \cdot 10^{-4}\,[M^2 \cdot \text{sec}^{-1}]$. The evaluation of the divergence of $\vec{F}_{GM}$ (6.9) is performed on the data averaged over the last 50 years of integration as

$$\nabla \cdot \overline{\vec{F}_{GM}} + \left(K_{Tw}^{ref} - K_{Tw}\right) \bar{T}_{zz} =$$
$$-K_{GM} \nabla \cdot \begin{pmatrix} 1 & 0 & 0 \\ 0 & 1 & 0 \\ 2\overline{L^x} & 2\overline{L^y} & \left(\overline{L^y}^2 + \overline{L^x}^2\right) \end{pmatrix} \nabla \bar{T} + \left(K_{Tw}^{ref} - K_{Tw}\right) \bar{T}_{zz}$$

where $\overline{(\cdot)}$ indicates time–averaging. The slope is evaluated by through the time–averaged horizontal components.

Figure 6-23 shows the divergence of parameterized flux for the upper six layers in experiment AGM5V2.

The implementation of the GM scheme in MIT Model imposes a zero slope for the upper layer; thus, for the surface layer the vertical mixing is provided only by the background vertical diffusivity. This leads to a close correspondence with the divergence of parameterized flux of the experiment FFH5V2 with Fickian diffusivity. The surface temperature is strongly forced by the interaction with the atmosphere. The distribution strongly differs for the subsurface layers. The second, third and fourth layers are dominated by a strong positive divergence in the Western area located North of $40^\circ N$. The implied magnitude is about one to two orders of magnitude larger than the largest domain value of the eddy heat flux divergence. The reason for such high magnitude is a combination of a large slope in this area, that is limited by the largest allowed magnitude of 10^{-2} and non–zero vertical temperature gradient. It leads to the magnitude of the $(3,3)$ coefficient of the tensor in (6.9) to be about $10^{-2}\,[M^2 \cdot \sec^{-1}]$ that is at least two order of magnitude larger than the background vertical diffusivity of $\backsim 10^{-4}\,[M^2 \cdot \sec^{-1}]$. The location of these local maxima corresponds to the area which was identified in Chapter 5 when performing the diagnostic tests of the scheme (Figures 5-26 to 5-29). The patterns become weaker with depth and their location is shifted to the area of water mass production in the North–Western corner of the basin.

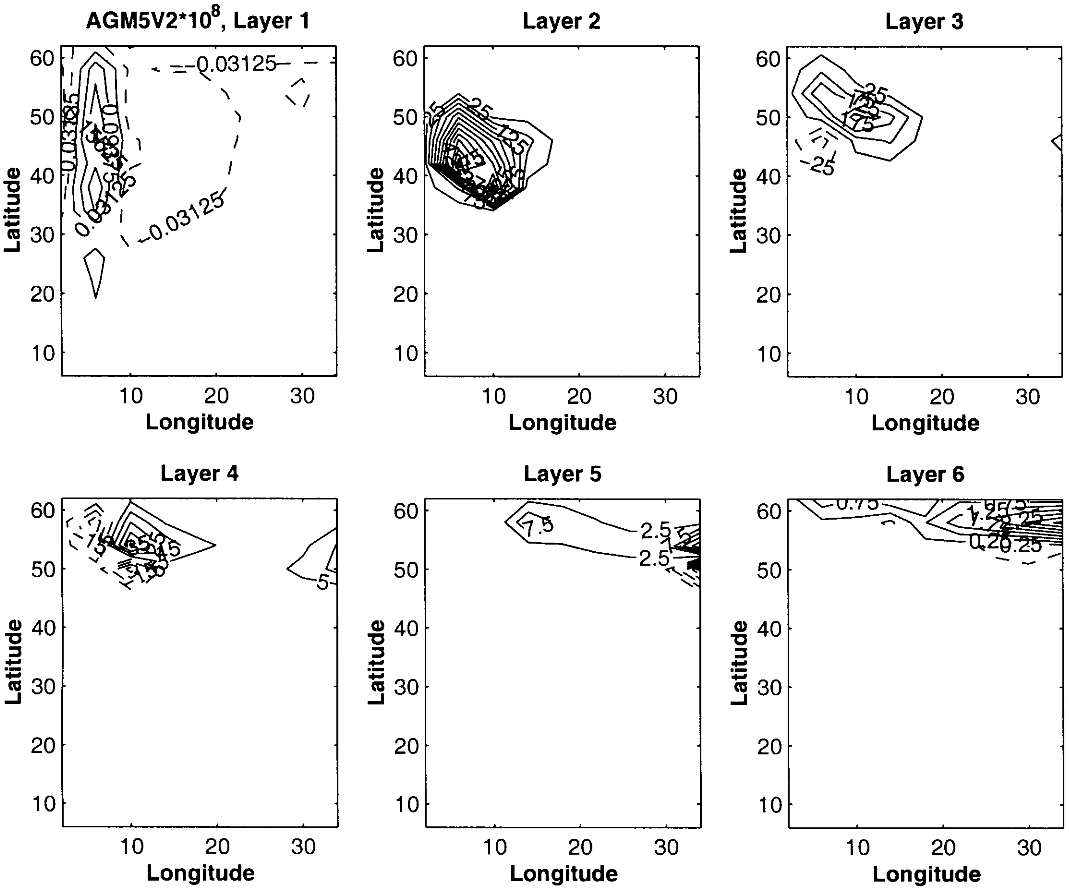

Figure 6-23: Flux divergence. Gent–McWilliams scheme. Experiment AGM5V2 (K_{GM} $=10^2\,[M^2\cdot\mathrm{sec}^{-1}]$, $K_{Tw}=0.3{\cdot}10^{-4}\,[M^2\cdot\mathrm{sec}^{-1}]$). Layers 1 to 6. Variable C.I. in $10^{-8}\,[{}^\circ C\cdot\mathrm{sec}^{-1}]$ units.

For other experiments the geographical distribution of the divergence is similar for deeper layers with the magnitude defined by K_{GM} and K_{Tw} coefficients. In the experiment AGM7V2 (Figure 6-24) low value of the GM mixing coefficient $10\,[M^2\cdot\mathrm{sec}^{-1}]$ leads to insignificant divergence for the upper layer (maximum amplitude is about $10^{-10}\,[{}^\circ C\cdot\mathrm{sec}^{-1}]$) with weaker by about factor of 10 sub–surface values consistent with the decrease in K_{GM} by the same factor.

The experiment AGM5V3 (Figure 6-25) with high background vertical diffusivity of $10^{-4}\,[M^2\cdot\mathrm{sec}^{-1}]$ differs from the experiment with the reference value only for the upper

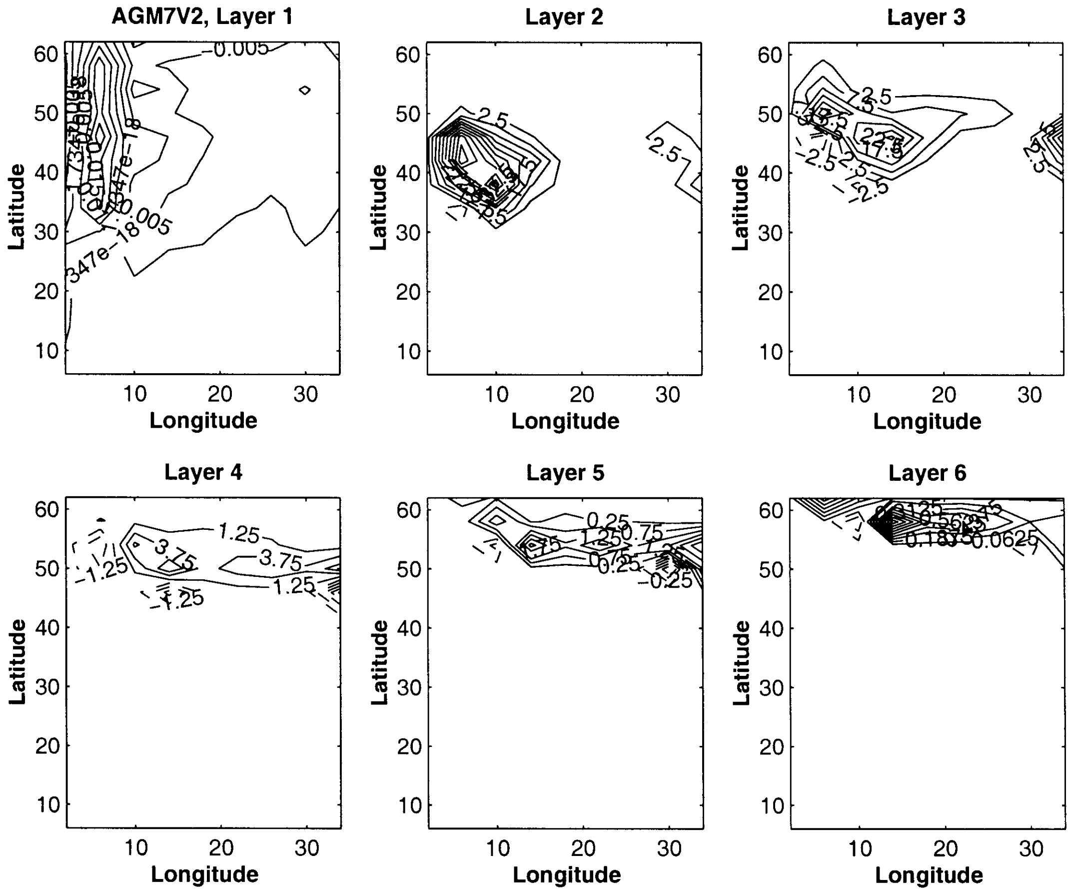

Figure 6-24: Flux divergence. Gent–McWilliams scheme. Experiment AGM7V2 (K_{GM} =10$[M^2 \cdot \sec^{-1}]$, $K_{Tw} = 0.3{\cdot}10^{-4}\,[M^2 \cdot \sec^{-1}]$). Layers 1 to 6. Variable C.I. in $10^{-8}\,[°C \cdot \sec^{-1}]$ units. Divergence for Layer 1 $< 10^{-10}\,[°C \cdot \sec^{-1}]$.

layer where it produces moderate compared with the deeper layers. Large divergence in areas of higher slope dominates distribution and does not allow the intensification in the mid–latitudinal areas near the Western boundary which was observed in the divergence of the reference eddy heat flux.

Summary

The Gent–McWilliams parameterization scheme demonstrated better skills than Fickian diffusivity in the simulation of the climatological properties. In the presence of back-

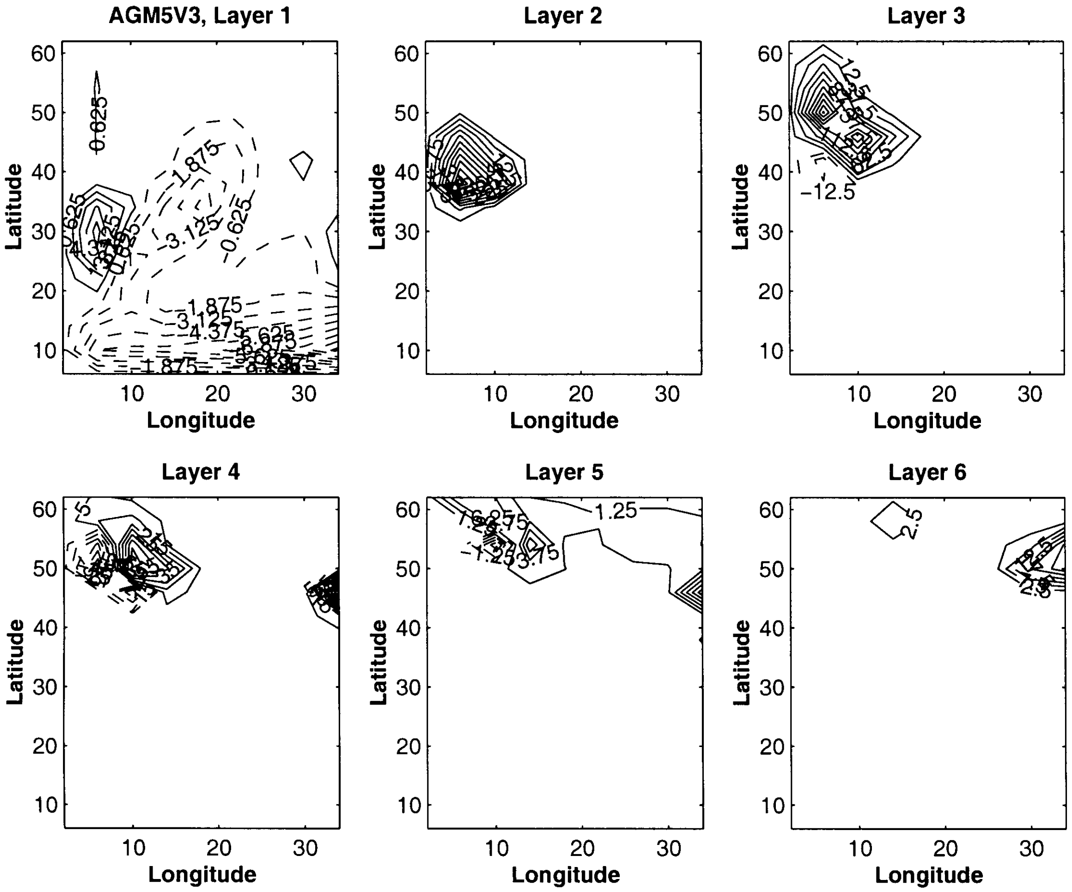

Figure 6-25: Flux divergence. Gent–McWilliams scheme. Experiment AGM5V3 (K_{GM} $=10^2\,[M^2 \cdot \sec^{-1}]$, K_{Tw} $=10^{-4}\,[M^2 \cdot \sec^{-1}]$). Layers 1 to 6. Variable C.I. in $10^{-8}\,[^\circ C \cdot \sec^{-1}]$ units.

ground vertical diffusivity of the same magnitude used in the simulation of the reference state the scheme enhances reproduction of the total heat transport especially in the mid–latitudinal area. The magnitude and the orientation of the main overturning cell is best achieved in the experiment that at the same time produced the best fit in the total heat transport. The respective K_{GM} is $100\,[M^2 \cdot \sec^{-1}]$ a smaller value compared to the traditionally used in coarse resolution experiments, leads to weaker interior mixing for deeper layers.

The Gent–McWilliams scheme performs in a comparable manner to the Green–Stone scheme when evaluating the climatological properties. It has similar performance in simulating the thermal structure of the upper ocean for comparable parameters. There are differences in the deep ocean. The deep ocean is warmer in the case of GS scheme, although the difference is small. While simulating total northward heat transport the GM scheme has better skills in the midlatitudinal area of the basin while GS scheme performs better in the Northern region.

The patterns in the divergence of time–averaged flux $\overline{\vec{F}_{GM}}$ (6.9) do not correspond at all to the distribution of the divergence of the eddy heat flux evaluated in the reference experiment. For the five subsurface layers in three considered experiments the geographical distribution of divergencies is similar with the magnitude defined by the mixing coefficients, even though the climatologies are significantly different. This observation demonstrates little correspondence between a success of the scheme in simulating climatological quantities and reproducing the eddy heat flux divergence term in the thermal balance for the thermocline layers.

6.4 Conclusions

The evaluation of the parameterization schemes in coarse resolution experiments did not identify a unique scheme that provides the best representation of the reference experiment. Given the knowledge of the exact nature of the vertical diffusivity, as the most important process in the simulation of the climatological reference state, all experiments managed to simulate states with similar climatological descriptions; thus, the evaluation was stressed on the reproduction of patterns, such as mid–latitudinal enhancement of the total heat transport or the simulation of the variations in the thermal structure.

The Fickian diffusivity as the most simple and the easiest to visualize scheme demonstrated the least skills in the climatological analysis by significantly overestimating the temperature of the ocean, weaker thermocline and the total heat transport. The Green–Stone scheme provided some improvements in the simulation of the thermal structure due to better representation of the horizontal and vertical mixing process, although it did not succeed in improving heat transport. The Gent–McWilliams scheme performed better in the mid–latitudinal heat transport simulation, although it tends to produces cooler ocean for all vertical layers compared to the reference state and is the worst parameterization for the estimate of flux divergence.

The question of why one scheme performs better than the other is still open. The analysis of the divergencies did not reveal that one scheme succeeds in the reproduction of the divergence of the eddy heat flux. The diabatic schemes, especially the Green–Stone, perform better in the simulations of patterns and in their magnitude. The Gent–McWilliams scheme significantly overestimates/underestimates the divergence for some localities and produces the results that are different from the reference simulation. All schemes fail in identifying the eddy activities associated with the Southern boundary and specifics of the distribution for the Western boundary area.

The proposed eddy parameterization schemes can be tuned to reproduce with some degree of accuracy some of the climatological diagnostic quantities, although the corresponding divergence of parameterized flux is different from the eddy heat flux divergence. Thus, it suggests that the relative success of parameterization schemes in the simulation of the climatological state is due to better reproduction of the overall mixing processes and not to local representation of the heat transport by the mesoscale eddies.

Chapter 7

Conclusions

Some of the difficulties of the modern climate modelling lay in the representation of the oceanic component of the coupled Atmosphere–Ocean system. The major role of the Ocean in the climate is in the storage and redistribution of heat. In order to improve our skills in the representation of the system, it is necessary to model the oceanic circulation and transport properties with a high degree of realism. There is a number of technical and conceptual obstacles in approaching this problem. Among them is the inability of modern computers to integrate the equations governing the dynamical system long enough to establish a realistic climate state and at the same time resolve the mesoscale eddies as one of the major energetic processes of the ocean dynamics. Thus, if one is interested in the modelling of climate system on longer time scales, the mesoscale processes need to be parameterized in terms of large–scale properties.

A number of schemes representing the effects of mesoscale eddies on the transport of heat has been proposed. The three most fundamental ones were evaluated in the thesis: the Fickian diffusivity, the diabatic Green–Stone scheme (*Green, 1970* [26] and *Stone, 1972* [55]) and quasi-adiabatic Gent–McWilliams scheme (*Gent and McWilliams, 1990* [23]). The thesis project explored the properties of the schemes in a systematic way by designing a reference eddy resolving experiment and a series of coarse resolution experiments utilizing the proposed parameterization schemes. The fine resolution reference experiment provided the necessary numerical data to perform the local diagnostic evaluation of the eddy heat flux parameterization schemes. Its climatological state was used to assess the performance of the schemes in coarse resolution experiments. The simulation of the bulk transport properties and the establishment of the thermal structure were some of the criteria of the climatological tests. By comparing the divergence of the parameterized flux in the coarse resolution experiments with the computed divergence of the eddy heat flux in the reference experiment, I have addressed the question of whether the possible improvements in the climatological simulations are actually related to the better representation of the transport properties by mesoscale eddies.

The reference fine resolution simulation in an idealized geometry forced by steady wind stress and the relaxation to an apparent atmospheric temperature was performed using the MIT GCM (*Marshall et. al, 1997* [43], [42]) on the massive parallel computer CM-5. The total length of the reference simulation of 105 years after the initialization was an order of magnitude longer than the majority of the eddy resolving basin scale experiments published to date, thus allowing a more stable estimation of the eddy dynamics.

Because of an apparent complexity in designing and executing an eddy resolving ocean simulation, the total number of wind– and buoyancy–driven basin scale experiments is still very small. Because of this limited experience, researchers can not possibly foresee all potential problems in the design of the calculations. Thus, the ideas about the set–up of the eddy resolving reference experiment, data accumulation strategy and monitoring of the reference simulations presented in the thesis are of outmost importance for future large–scale ocean modelling.

The climatological analysis of the reference fine resolution experiment demonstrated some significant improvements in simulating the climate of the model ocean by overcoming the identified deficiencies of the coarse resolution climate simulations. The thermocline in the fine resolution experiment was sharper and had a more complex structure. The time–averaged thermal state developed a more stable temperature distribution with warmer upper layers and cooler deeper ones. The main overturning cell had a more realistic structure. Although the strength of the cell did not increase, the southward penetration was larger and the deep part of the cell was shallower. The ocean in the reference experiment transported more heat in the mid–latitudinal and northern areas where there was almost a 50% increase compared to the coarse resolution experiments. The better representation of the main overturning cell led to the improvements in the total heat transport of the fine resolution experiment. The success of the reference simulation was attributed to the finer horizontal resolution. The explicit representation of eddies allowed better representation of the mixing processes and the establishment of the climatological thermal state and the associated transports.

One of the most important results in the climatological state of the reference experiment is the significant increase of the total heat transport for the mid–latitude area. Both of the baroclinic components of the heat transport are responsible for this modification. This observation is consistent with the analysis by *Fanning and Weaver, 1997* [21] where they observed a similar increase in the total heat transport resulting from the baroclinic gyre component only. The difference in their case is due to modifications of the wind–driven transport when increasing the horizontal resolution. The wider domain in the Fanning and Weaver experiment of 60° supports in fact a strong wind–driven circulation and a strong western boundary current leading to the increase in the wind–driven gyre component of the heat flux. In the reference experiment of the thesis the strength of the wind–driven circulation is weaker due to the narrow basin of 36°. Thus, the increase in the heat transport requires an additional increase in the baroclinic overturning component.

Through the direct evaluation of the divergence of the eddy heat flux as a term in the time–averaged thermal balance, it was identified that eddies provide a geographically limited contribution to the balance. The three major areas where the divergence of the eddy heat flux was one of the leading terms in the balance were identified. The western mid–latitudinal area with the strongest forcing along the boundary was located from the western boundary to approximately $10°E$ and between latitudes $25°N$ and $50°N$ from the surface to about $1000M$. The northern area occupied the region to the North of $50°N$. The southern area spanned a latitudinal band from $4°N$ to $12°N$. The areas were filled with anomalies of the eddy heat flux divergence of the opposite signs with a typical radius of about $2° - 3°$. Overall they covered a smaller part of the whole basin.

All of the proposed eddy heat flux parameterization schemes are of a local nature; thus, in order to possess some predictive skills, they should reproduce the larger magnitudes where the eddy heat flux divergence is large but not simultaneously introduce some artificial forcing where the eddy heat flux divergence is small. The western mid–latitudinal area where the eddy contribution was the strongest but contained areas with weak eddy heat flux divergence was chosen for the testing of the schemes. A series of specific diagnostic tests was designed comparing the local properties of the eddy heat flux with the parameterized flux diagnosed from the data according to the underlying physical mechanism of the parameterization schemes.

The general distribution of the eddy contribution to the thermal balance is in qualitative agreement with the observed intensification of eddy activity in the vicinity of the western boundary current in the mid–latitude for the upper ocean. The idealized nature of the reference experiment does not allow a detailed quantitative comparison of the eddy heat flux and its divergence with the observations.

When evaluating the Fickian diffusion it was found that the total eddy heat flux was not downgradient to the distribution of temperature in a larger portion of the region. For individual components the horizontal flux was more of a downgradient nature than the vertical. The magnitude of the implied mixing was consistent with the values used in coarse resolution experiments of the order $10^3 - 10^4\,[M^2 \cdot \mathrm{sec}^{-1}]$ for the horizontal coefficients and $10^{-4} - 10^{-5}\,[M^2 \cdot \mathrm{sec}^{-1}]$ for the vertical one. The horizontal mixing was stronger in the upper layers and closer to the western boundary. There was a general anticorrelation between the horizontal and vertical mixing coefficients, resulting in a much smaller area where all three components were downgradient. The test of the scheme performed on averaged fields revealed that a $1° \times 1°$ average sufficiently reproduced the fine resolution results for all three considered layers. The evaluation of a vertical mixing on a $1° \times 1°$ grid showed a large range of coefficients, suggesting that the use of a constant coefficient would significantly change the patterns of the vertical mixing. The vertical mixing coefficient was more uniformly distributed in the lower layers.

A special angle test of the Green–Stone (GS) parameterization was designed in the thesis. It evaluated the relative orientation of the isopycnal surface and the projection of the eddy heat flux on the plane formed by the isopycnal vector and the vertical direction. This test showed some mixed results of the GS scheme. In general, it was shown that the eddy heat flux was more aligned with the isopycnal surfaces for deeper layers, thus suggesting that the associated transfer became more adiabatic.

The evaluation of the Gent–McWilliams (GM) scheme did not demonstrate an overall success in the simulation of the divergence of the eddy heat flux everywhere in the interior and in the western region as well. The adiabatic nature of the scheme was observed in the increase with depth of the area where the GM scheme could diagnose the observed eddy heat flux divergence. There was some anticorrelation between the GS and GM tests. First, the total area, where GS succeeded, decreased with depth. Second, there was some anticorrelation in the distribution of areas of the two tests, which was especially pronounced in the fifth layer of the model corresponding to the mid–thermocline depth.

The comparison of the divergencies predicted with the schemes for typical values of specific parameters in the smaller subdomain of the same western region did not identify any scheme as being superior to the others. For the upper layer the distribution of divergency as predicted by the GS scheme was the best except in the North–East corner, where the scheme overestimated the divergence due to the direct diabatic forcing. In the interior of the fifth layer all three schemes had some skills generally predicting the correct number of anomalies, although with different magnitude. Two of the schemes, GS and GM, failed in the Western boundary current area by predicting the wrong sign of divergencies.

Overall, the transfer of heat associated with the time–dependent motions as diagnosed from the reference experiment was identified as a complicated process that could not be uniquely explained with any one of the proposed local parameterizations. The tests did not demonstrate that the more sophisticated schemes performed better in the representation of the local distribution of the eddy heat flux compared to the Fickian diffusion. The Green–Stone and Gent–McWilliams schemes contain some tunable parameters that could potentially improve the schemes' performance. The diagnostic analysis identified the important requirement for the Green–Stone and Gent–McWilliams schemes to be properly tapered in the areas with larger isopycnal slopes such as the western boundary currents and the mixed layer where they significantly overestimated the eddy heat flux divergence.

The assessment of the parameterizations with the experiments that were formulated in the framework of coarse resolution climate simulations did not succeed in finding a unique scheme that provided the best representation of the reference experiment. A wide range of solutions was obtained by varying the specific parameters within their typical range of values. It shows the importance of having appropriately tuned parameterization schemes in climatological simulations. The Fickian diffusivity demonstrated the least skills in the climatological analysis by significantly overestimating the temperature of the deep ocean, maintaining a weaker thermocline and a weaker total heat transport. The Green–Stone scheme provided some improvements in the simulation of the thermal structure due to better representation of the horizontal and vertical mixing process, although it did not succeed in improving the heat transport. The Gent–McWilliams scheme improved the mid–latitudinal heat transport simulation, although it produced a cooler ocean for all vertical layers compared to the reference state.

The question of why one scheme seems to perform better than the other is still open. The analysis of the divergencies for some typical parameter values in the coarse resolution experiments did not reveal a scheme that succeeded in the reproduction of the averaged divergence of the eddy heat flux. The diabatic schemes, especially the Green–Stone, performed better in the simulations of the patterns and of their magnitude. The Gent–McWilliams scheme significantly overestimated/underestimated the divergence for some localities and was the worst parameterization scheme for the estimate of flux divergences. All schemes failed in identifying enhanced eddy activity associated with the Southern boundary and the specifics of the distribution for the Western boundary area. This result was different from some apparent improvements using these parameterizations identified in some of the published studies (*Visbeck et. al, 1997* [58]; *Treguier, 1999* [57]). The success of the parameterization schemes in these studies essentially repeated the results obtained in the modelling of atmospheric flows. The experimental set–up was in fact the oceanic analog of the periodic zonal atmospheric circulation. Thus, the instability processes associated with the baroclinically unstable jet or the wind–driven zonal channel in these idealized experiments were allowed to develop in isolation. The complex non–linear interactions with essential oceanic features, such as the western boundary currents or the thermohaline circulation, are not present in these studies. Another difference is in the formulation of the coarse resolution experiments. While the two–dimensional zonally averaged models are employed in the referred studies, this thesis project uses a three–dimensional model with a coarse horizontal grid — the set–up actually used in climate modelling with numerical oceanic GCMs. This formulation makes the analysis presented in the thesis to be more consistent with climate studies.

The proposed eddy parameterizations can be tuned to reproduce with some degree of accuracy some of the climatological diagnostic quantities, although the corresponding divergence of parameterized flux is different from the actual eddy heat flux divergence. Thus, it suggests that the relative success of parameterization schemes in the simulation of the climatological state of the reference experiment is due to better reproduction of the overall mixing processes and not to the local representation of the heat transport by the mesoscale eddies.

The proposed local eddy parameterization schemes are based on the assumption that the divergence of the parameterized flux in the coarse resolution experiments should match the eddy heat flux divergence. Only if the balance is satisfied, would the solution of a coarse resolution simulation be a good approximation to the time–averaged reference state. On the other hand, it was demonstrated in the thesis that even if the divergence of the parameterized flux does not correspond to the eddy heat flux divergence, some improvements in the simulation of the integrated properties of the climatological state can be obtained. This suggests that the development of the eddy parameterizations needs to address not only the representation of the eddy flux themselves but also the eddy–induced modifications to the model climatology.

Appendix A

Data Preprocessing

The state of the fine resolution simulation is significantly richer in details as compared to the simulated initial state, which is obtained in a typical coarse resolution experiment. The dynamical processes that are resolved by a high resolution grid create complicated patterns of circulation and density structure. Most of these features are unfeasible to reproduce with a typical coarse resolution grid. To make a fair comparison between the experiments, it is required to project the state of the fine resolution experiment on the grid of the coarse resolution simulation.

The projection is the averaging on the coarse grid. The vertical resolution of both simulations is the same; therefore, it is required to perform averaging only on the horizontal plane.

All state variables can be divided into two groups according to the finite volume discretization scheme. The tracer variables T and S are defined in the center of each individual volume as the average quantity over the volume. The dynamical variables u, v and w are the area variables; therefore, they are defined on the sides of each individual volume. The averaging procedures differ accordingly.

Consider all individual volumes with the sides of 0.2° that are contained in the large ABDC volume with the horizontal dimensions of $4^\circ \times 4^\circ$ (Figure A-1). For the volume

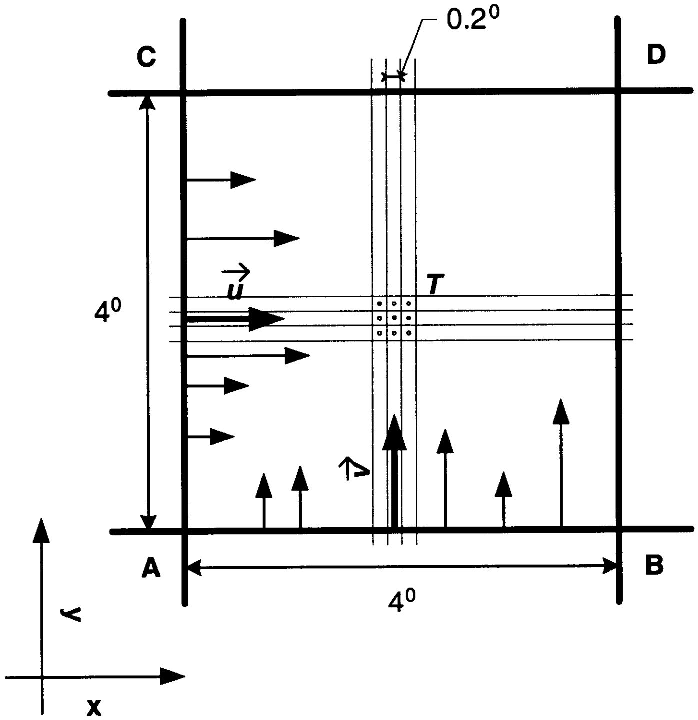

Figure A-1: Horizontal averaging procedure on the coarse resolution grid.

variables, the averaged quantity is the sum of all individual values contained in ABDC divided by the number of volumes. For the area variables, the averaged value over the container is determined on the side where the variable is defined. It is computed as the total incoming flux. For example, consider the volume variable T and the area variable u. The averaged on the 4° coarse grid T_c is equal to the spatial mean value of T of each individual volume with 0.2°:

$$T_C = \frac{1}{N_{ABDC}} \sum_{i \in [AB]} \sum_{j \in [AC]} T_{i,j},$$

where N_{ABDC} equals to the number of volumes of the fine resolution experiment contained in the coarse resolution volume. For the dynamical variable u, the averaged value u_C is an average of all zonal velocities entering the volume:

$$u_C = \frac{1}{N_{AC}} \sum_{j \in [AC]} u_{i_A,j},$$

where N_{AC} is the number of the fine resolution volumes contained in the rectangular with one side equal to the meridional length of the coarse volume and the other equal to the zonal length of the fine volume; subscript i_A indicates the x–coordinate of the zonal velocities on the side AC of a unit volume.

After performing the averaging operation according to these rules, I conserve the total heat content of each volume and incoming and outgoing flows.

Appendix B

Computations of Operators in the Thermal Balance

The discretization of the model's equations is formulated in the finite volume framework. This numerical approach simplifies the calculations of (4.5) by using Gauss's theorem to evaluate divergences and higher order derivatives in (4.5) for any individual volume. The method requires the evaluation of volumes and areas for all terms in (4.5a) and (4.5b). The grid that is used by the model is staggered; thus, T is computed in the center of a volume, and u, v and w on the faces of a unit volume.

Consider the unit volume at the location. The projections of the volume on the (x, y) and (x, z) planes are presented in Figure B-1. The formulae below, which are the expanded versions from *Marshall et al., 1997* [42], provide the rules to compute all necessary operators for a volume at location (n, m, k).

The divergence of flux $\vec{f} = (f_x, f_y, f_z)$ is

$$\begin{aligned}\nabla \cdot \vec{f} &= \frac{1}{V}\left(\delta_x\left(A_x f_x\right) + \delta_y\left(A_y f_y\right) + \delta_z\left(A_z f_z\right)\right) \\ &= \frac{1}{V}\left(\left[(A_x f_x)_E - (A_x f_x)_W\right] + \left[(A_y f_y)_N - (A_y f_y)_S\right] + \left[(A_z f_z)_T - (A_z f_z)_B\right]\right)\end{aligned} \tag{B.1}$$

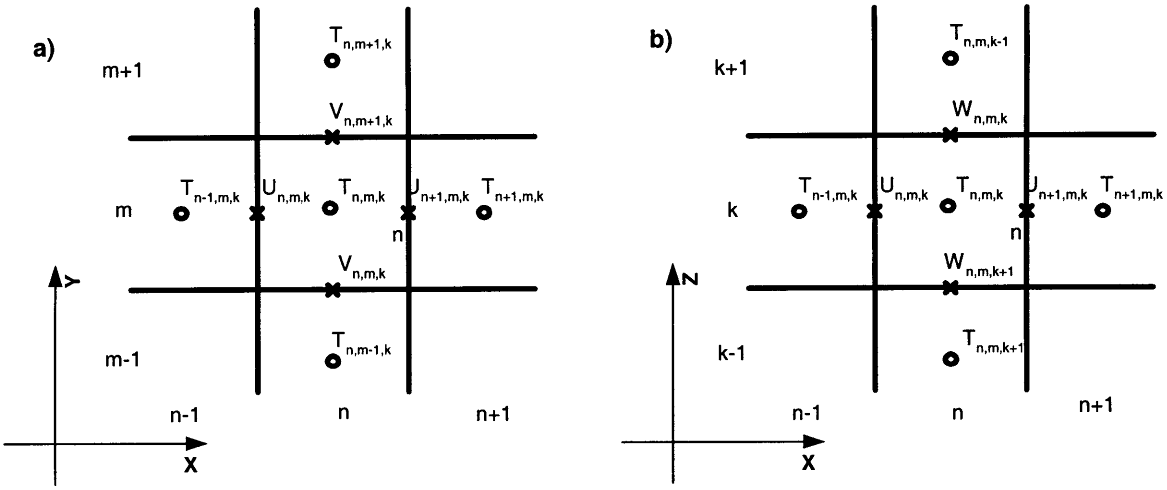

Figure B-1: Definition of the model grid in the horizontal (a) and vertical (b) planes: u, v, w - face quantities, T - zone quantity.

$$\begin{aligned} &= \frac{1}{V}\left(\left[A_x^{n+1,m,k} f_x^{n+1,m,k} - A_x^{n,m,k} f_x^{n,m,k}\right] + \right. \\ &\quad \left[A_y^{n,m+1,k} f_y^{n,m+1,k} - A_y^{n,m,k} f_y^{n,m,k}\right] + \\ &\quad \left.\left[A_z^{n,m,k+1} f_z^{n,m,k+1} - A_z^{n,m,k} f_z^{n,m,k}\right]\right), \end{aligned} \qquad \text{(B.2)}$$

where V, A_x, A_y, A_z are the volume and areas of the respective faces of the volume.

The divergence of the flux of a tracer T over a volume is

$$\begin{aligned} \nabla \cdot \left(\vec{U}T\right) &= \frac{1}{V}\left(\delta_x\left(A_x u \overline{T}^x\right) + \delta_y\left(A_y v \overline{T}^y\right) + \delta_z\left(A_z w \overline{T}^z\right)\right) \\ &= \frac{1}{V}\left(\left[\left(A_x u \overline{T}^x\right)_E - \left(A_x u \overline{T}^x\right)_W\right] + \left[\left(A_y v \overline{T}^y\right)_N - \left(A_y v \overline{T}^y\right)_S\right] + \right. \\ &\quad \left.\left[\left(A_z w \overline{T}^z\right)_T - \left(A_z w \overline{T}^z\right)_B\right]\right) \\ &= \frac{1}{V}\left(\left[A_x^{n+1,m,k} \cdot u^{n+1,m,k}\left(\alpha^{n+1,m,k}T^{n+1,m,k} + \alpha^{n,m,k}T^{n,m,k}\right) - \right.\right. \\ &\quad \left. A_x^{n,m,k} \cdot u^{n,m,k}\left(\alpha^{n,m,k}T^{n,m,k} + \alpha^{n-1,m,k}T^{n-1,m,k}\right)\right] + \qquad \text{(B.3)} \\ &\quad \left[A_y^{n,m+1,k} \cdot v^{n,m+1,k}\left(\beta^{n,m+1,k}T^{n,m+1,k} + \beta^{n,m,k}T^{n,m,k}\right) - \right. \\ &\quad \left. A_y^{n,m,k} \cdot v^{n,m,k}\left(\beta^{n,m,k}T^{n,m,k} + \beta^{n,m-1,k}T^{n,m-1,k}\right)\right] + \end{aligned}$$

$$\left[A_z^{n,m,k} \cdot w^{n,m,k}\left(\gamma^{n,m,k}T^{n,m,k} + \gamma^{n,m,k-1}T^{n,m,k-1}\right) - \right.$$
$$\left. A_z^{n,m,k} \cdot w^{n,m,k+1}\left(\gamma^{n,m,k+1}T^{n,m,k+1} + \gamma^{n,m,k}T^{n,m,k}\right)\right]\Big).$$

The coefficients α, β and γ are the interpolation weights for the transformation of T from the center of a volume to its sides. The computation of the vertical derivative of flux $\vec{U}T$ in (B.3) considers the direction of the velocity w, which is in the coordinate system with the Z-axe pointing downward.

The Laplacian operator, acting on the volume variable T, is

$$\begin{aligned}
\Delta \cdot T &= \frac{1}{V}\nabla \cdot \left(A_x\delta_x T, A_y\delta_y T, A_z\delta_z T\right) \\
&= \frac{1}{V}\nabla \cdot \left(\left[A_x\left(T_E - T_W\right)\right], \left[A_y\left(T_N - T_S\right)\right], \left[A_z\left(T_T - T_B\right)\right]\right) \\
&= \frac{1}{V}\nabla \cdot \left(\left[A_x^{n,m,k}\left(T^{n+1,m,k} - T^{n,m,k}\right)\right] + \right. \qquad\qquad \text{(B.4)} \\
&\quad \left[A_y^{n,m,k}\left(T^{n,m+1,k} - T^{n,m,k}\right)\right] + \\
&\quad \left.\left[A_z^{n,m,k}\left(T^{n,m,k+1} - T^{n,m,k}\right)\right]\right),
\end{aligned}$$

here the divergence is defined in (B.1). The higher order diffusivities, such as horizontal biharmonic diffusivity in (4.6b), are obtained by acting twice with the operator (B.4).

Bibliography

[1] D. Andrews and M. McIntyre. Planetary waves in horizontal and vertical shear: The generalized Eliassen-Palm relation and the mean zonal acceleration. *J. Atmos. Sci.*, 33:2031–2048, 1976.

[2] R. Bleck and D. Boudra. Wind-driven spin-up in eddy-resolving ocean models formulated in isopycnic and isobaric coordinates. *J. Geophys. Res.*, 91:7611–7621, 1986.

[3] C. Boning, F. Bryan, W. Holland, and R. Doscher. Deep-water formation and meridional overturning in a high-resolution model of the North Atlantic. *J. Phys. Oceanogr.*, 23:1142–1164, 1996.

[4] C. Boning and R. Budich. Eddy dynamics in a primitive equation model: sensitivity to horizontal resolution and friction. *J. Phys. Oceanogr.*, 22:361–381, 1992.

[5] C. Boning, R. Doscher, and R. Budich. Seasonal transport variation in the Western subtropical North Atlantic: Experiments with an eddy-resolving model. *J. Phys. Oceanogr.*, 21:1271–1289, 1991.

[6] C. Boning, W. Holland, F. Bryan, G. Danabasoglu, and J. McWilliams. An overlooked problem in model simulations of the thermohaline circulation and heat transport in the North Atlantic Ocean. *J. Climate*, 8:515–523, 1995.

[7] F. Bryan. Parameter sensitivity of primitive equation ocean general circulation models. *J. Phys. Oceanogr.*, 17:970–985, 1987.

[8] F. Bryan and W. Holland. *Parameterization of small-scale processes.*, chapter A high-resolution simulation of the wind- and thermohaline driven circulation in the North Atlantic Ocean., pages 99–115. Spec. Publ., Inst. of Geophys., University of Hawaii, 1989.

[9] K. Bryan. A numerical method for the study of the circulation of the World Ocean. *J. Comput. Phys.*, 3:347–376, 1969.

[10] K. Bryan. Accelerating the convergence to equilibrium of Ocean-Climate models. *J. Phys. Oceanogr.*, 14:666–673, 1984.

[11] K. Bryan. Poleward buoyancy transport in the ocean and mesoscale eddies. *J. Phys. Oceanogr.*, 16:927–933, 1986.

[12] M. Cox. A primitive equation, three-dimensional model of the ocean. Tech. rep. 1, 143 pp, Geophys. Fluid Dyn. Lab. Ocean Group, Princeton, NJ, 1984.

[13] M. Cox. An eddy resolving numerical model of the ventilated thermocline. *J. Phys. Oceanogr.*, 15:1322–1324, 1985.

[14] G. Danabasoglu and J. McWilliams. Sensitivity of the global ocean circulation to parameterizations of mesoscale tracer transports. *J. Climate*, 8:2967–2987, 1995.

[15] G. Danabasoglu, J. McWilliams, and P. Gent. The role of mesoscale tracer transports in the global ocean circulation. *Science*, 264:1123–1126, 1994.

[16] S. Drijfhout. Heat transport by mesoscale eddies in an ocean circulation model. *J. Phys. Oceanogr.*, 24:353–369, 1994.

[17] P. Duffy, K. Caldeira, J. Selvaggi, and M. Hoffert. Effects of subgrid-scale mixing parameterizations on simulated distributions of natural ^{14}C, temperature, and salinity in a three-dimensional ocean circulation model. *J. Phys. Oceanogr.*, 27:498–523, 1997.

[18] E. Eady. Long waves and cyclone waves. *Tellus*, 1:33–52, 1949.

[19] M. England. Using chlorofluorocarbons to assess ocean climate models. *Geophys. Res. Lett.*, 22:3051–3054, 1995.

[20] M. England and A. Hirst. Chlorofluorocarbon uptake in a world ocean model. 2. Sensitivity to surface thermohaline forcing and subsurface mixing parameterizations. *J. Geophys. Res.*, 102(C7):15709–15731, 1997.

[21] A. Fanning and A. Weaver. A horizontal resolution and parameter sensitivity study of heat transport in an idealized coupled climate model. *J. Climate*, 10:2469–2478, 1997.

[22] FRAM Group. An eddy-resolving model of the southern ocean. *EOS Trans. AGU*, 72:169–175, 1991.

[23] P. Gent and J. McWilliams. Isopycnic mixing in ocean circulation models. *J. Phys. Oceanogr.*, pages 150–155, 1990.

[24] A. Gill. *Atmosphere-Ocean Dynamics.* Academic Press, New York, 1982.

[25] S. Gille and R. Davis. The influence of mesoscale eddies on coarsely-resolved density: an examination of subgrid-scale parameterization. *J. Phys. Oceanogr.*, 6:1109–1123, 1999.

[26] J. Green. Transfer properties of the large-scale eddies and the general circulation of the atmosphere. *Quart. J. Roy. Meteor. Soc.*, 96:157–185, 1970.

[27] M. Hall and H. Bryden. Direct estimates and mechanisms of ocean heat transport. *Deep-Sea Res.*, 29:339–359, 1982.

[28] R. Haney. Surface thermal boundary conditions for ocean circulation models. *J. Phys. Oceanogr.*, 1:241–248, 1971.

[29] C. Hill and J. Marshall. Parallel computational fluid dynamics: Implementation and results using parallel computers. chapter Application of a parallel Navier-Stokes model to ocean circulation., pages 545–552. Elsevier Science B.V., 1995.

[30] N. Hogg. Stochastic wave radiation by the Gulf Stream. *J. Phys. Oceanogr.*, 18:1687–1701, 1988.

[31] W. Holland and P. Rhines. An example of eddy-induced ocean circulation. *J. Phys. Oceanogr.*, 10:1010–1030, 1980.

[32] I. Kamenkovich, J. Marotzke, and P. Stone. Factors affecting heat transport in an ocean general circulation model. *Submitted for publication*, 1999.

[33] P. Killworth. On the parameterization of eddy transfer. Part II: Tests with a channel model. *J. Mar. Res.*, 56:349–374, 1998.

[34] V. Larichev and I. Held. Eddy amplitudes and fluxes in a homogeneous model of fully developed baroclinic instability. *J. Phys. Oceanogr.*, 25:2285–2297, 1995.

[35] M.-M. Lee, D. Marshall, and R. Williams. On the eddy transfer of tracers: Advective or diffusive? *J. Mar. Res.*, 55:483–505, 1997.

[36] S. Levitus. Climatological atlas of the world ocean. In *Noaa Professional Paper 13*. US Department of Commerce: National Oceanic and Atmospheric Administration., 1982.

[37] S. Levitus and T. Boyer. *NOAA Atlas NESDIS 3*, chapter World Ocean Atlas 1994 Vol. 3: Temperature., page 117p. NODC, Washington, DC, 1994.

[38] S. Manabe and R. Stouffer. Two stable equilibria of a coupled ocean-atmosphere model. *J. Climate*, 7:5–23, 1988.

[39] J. Marotzke. *Ocean Models in Climate Problems.*, pages 79–109. Kluwer Academic Publishers, 1994.

[40] J. Marotzke and J. Willebrand. Multiple equilibria of the global thermohaline circulation. *J. Phys. Oceanogr.*, 21:1372–1385, 1991.

[41] J. Marshall. On the parameterization of geostrophic eddies in the ocean. *J. Phys. Oceanogr.*, 11:257–271, 1981.

[42] J. Marshall, A. Adcroft, C. Hill, L. Perelman, and C. Heisey. A finite volume, incompressible Navier Stokes model for studies of the ocean on parallel computers. *J. Geophys. Res.*, 102(C3):5753–5766, 1997.

[43] J. Marshall, C. Hill, L. Perelman, and A. Adcroft. Hydrostatic, quasi-hydrostatic, and non-hydrostatic ocean modeling. *J. Geophys. Res.*, 102(C3):5733–5752, 1997.

[44] C. Pakanowski, K. Dixon, and A. Rosati. The GFDL Modular Ocean Model users guide version 1.0. page 46, 1991.

[45] R. Plumb and J. Mahlman. The zonally averaged transport characteristics of the GFDL general circulation/transport model. *J. Atmos. Sci.*, 44:298–327, 1982.

[46] M. Redi. Oceanic isopycnal mixing by coordinate rotation. *J. Phys. Oceanogr.*, 12:1154–1157, 1982.

[47] N. Rix and J. Willebrand. Parameterization of mesoscale eddies as inferred from a high–resolution circulation model. *J. Phys. Oceanogr.*, 26:2281–2285, 1996.

[48] D. Robitaille and A. Weaver. Validation of sub-gridscale mixing schemes using cfcs in a global ocean model. *Geophys. Res. Lett.*, 22:2917–2920, 1995.

[49] J. Sarmiento. A simulation of bomb tritium entry into the Atlantic Ocean. *J. Phys. Oceanogr.*, 13:1924–1939, 1982.

[50] J. Sarmiento and K. Bryan. An ocean transport model for the North Atlantic. *J. Geophys. Res.*, 87:394–408, 1982.

[51] A. Semtner and R. Chervin. Ocean general circulation from a global eddy-resolving model. *J. Geophys. Res.*, 97(C4):5493–5550, 1992.

[52] A. Semtner and Y. Mintz. Numerical simulation of the Gulf Stream and mid-ocean eddies. *J. Phys. Oceanogr.*, 7:208–230, 1977.

[53] H. Solomon. On the representation of isentropic mixing in ocean circulation models. *J. Phys. Oceanogr.*, 1:233–234, 1971.

[54] P. Stone. On non-geostrophic baroclinic stability: Part III. The momentum and heat transport. *J. Atmos. Sci.*, 29:419–426, 1972.

[55] P. Stone. A simplified radiative-dynamical model for the static stability of rotaiting atmospheres. *J. Atmos. Sci.*, 29:405–418, 1972.

[56] P. Stone and M.-S. Yao. Development of a two dimensional zonally averaged statistical-dynamical model. Part III: The parameterization of the eddy fluxes of heat and momentum. *J. Climate*, 3:726–740, 1990.

[57] A. Treguier. Evaluating eddy mixing coefficients from eddy-resolving ocean models: A case study. *J. Mar. Res.*, 57:89–108, 1999.

[58] M. Visbeck, J. Marshall, T. Haine, and M. Spall. Specifications of eddy transfer coefficients in coarse–resolution ocean circulation models. *J. Phys. Oceanogr.*, 27:381–402, 1997.

[59] T. VonderHaar and A. Oort. New estimate of annual poleward energy transport by northern hemisphere oceans. *J. Phys. Oceanogr.*, 3:169–172, 1973.

[60] A. Weaver and E. Sarachik. On the importance of vertical resolution in certain ocean general circulation models. *J. Phys. Oceanogr.*, 20:600–609, 1990.

[61] J. Woods. The world ocean circulation experiment. *Nature*, 314:501–511, 1985.